FOSSIL ENERGY

DOE/BC/15211-21
(OSTI ID: 802152)

INVESTIGATION OF MULTISCALE AND MULTIPHASE FLOW, TRANSPORT AND REACTION IN HEAVY OIL RECOVERY PROCESSES

Annual Report
May 6, 2001-May 5, 2002

By:
Yanis C. Yortsos

Date Published: October 2002

Work Performed Under Contract No. DE-AC26-99BC15211

University of Southern California
Los Angeles, California

National Energy Technology Laboratory
National Petroleum Technology Office
U.S. DEPARTMENT OF ENERGY
Tulsa, Oklahoma

DOE/BC/15211-21
Distribution Category UC-122

Investigation of Multiscale and Multiphase Flow, Transport and Reaction in Heavy Oil Recovery Processes

By
Yanis C. Yortsos

October 2002

Work Performed Under DE-AC26-00BC15211

Prepared for
U.S. Department of Energy
Assistant Secretary for Fossil Energy

Jerry Casteel, Project Manager
National Energy Technology Laboratory
National Petroleum Technology Office
One West Third Street, Suite 1400
Tulsa, OK 74103

Prepared by
Petroleum Engineering Program
Department of Chemical Engineering
University of Southern California
University Park Campus - EDCO 316, USC
Los Angeles, CA 90090-1211

TABLE OF CONTENTS

ABSTRACT

This is the third annual report for contract DE-AC26-99BC15211. The report describes progress made in the various thrust areas of the project, which include internal drives for oil recovery, vapor-liquid flows, combustion and reaction processes and the flow of fluids with yield stress. The report is mainly a compilation of previous topical reports published in the third year of the project, which ended on May 6, 2001. Advances in multiple processes and at various scales are described.

In the area of internal drives, significant progress was made in the modeling of gas-phase growth driven by mass transfer, as in solution-gas drive, and by heat transfer, as in internal steam drives. The works reported here pertain to the continuum scale, although we have also conducted studies at the pore-network scale, to be reported in the final report. In the area of vapor-liquid flows, we develop further a novel method for the mobilization of trapped phases using boundary integral methods. In the area of combustion, we report on the propagation of combustion fronts in heterogeneous (layered) porous media in the presence of heat losses. We show that layering affects significantly the extinction limits of the process, and therefore is a key limiting factor to the application of the process in realistic systems. Finally, we present a study of the flow and displacement of non-Newtonian fluids with Bingham plastic rheology.

EXECUTIVE SUMMARY

This is the third annual report of an investigation of the various multi-phase and multiscale transport and reaction processes associated with heavy oil recovery. As in the past two reports, the thrust areas include the following: Internal drives, vapor-liquid flows, combustion and reaction processes, fluid displacements and the effect of instabilities and heterogeneities and the flow of fluids with yield stress. These find respective applications in foamy oils, the evolution of dissolved gas, internal steam drives, the mechanics of concurrent and countercurrent vapor-liquid flows, associated with thermal methods and steam injection, such as SAGD, the in-situ combustion, the upscaling of displacements in heterogeneous media and the flow of foams, Bingham plastics and heavy oils in porous media and the development of wormholes during cold production.

In many processes associated with heavy oil recovery, internal drives, namely these driven by applied supersaturation in dissolved gases or heat content, are common. The main result is the growth of a gas phase, which is driven by mass or heat transfer, depending on the kind of the applied supersaturation. We have conducted various studies of this multifaceted problem. In this report, we present results in two areas, one associated with the nucleation and growth of a gas phase from a supersaturated liquid, and another on internal steam drives. The first study describes a mathematical model of the dynamics of gas evolution as a function of the rate of application of the supersaturation for solution gas drive. Both constant rate of pressure decline and constant rate of liquid withdrawal are discussed. The second study is an extension of the process to internal steam drives. It is the first time, that such a study is reported in the literature.

The simultaneous flow of vapor and liquid phases is common to steam injection, counter-current flows are encountered in Steam-Assisted-Gravity-Drainage (SAGD), and in steam injection in horizontal wells. Concurrent flows are found in typical displacements, in solution gas-drives near wells, and various other contexts. In this section we report on the dynamics of two-phase flows in heterogeneous media where capillarity induces a trapped phase. We expand and complete a new approach, introduced for the first time in the previous report, based on what we term Darcian Dynamics, to describe the dynamics of the flow of a disconnected phase, in the form of ganglia, in the flow field of a displacing continuous phase. It is a computationally fast approach for the evaluation of quantities in concurrent and counter-current flows, such as the critical capillary number for mobilization, the subsequent movement of the mobilized phase, and its possible stranding and/or coalescence.

A well-established method for the recovery of heavy oils is in-situ combustion. Two particular aspects are analyzed in this project: The description of the process at the pore-network scale, and its upscaling at the large scale for field applications. A detailed pore-network simulator was described in our last report. The effort in this direction is continued. Here, we report on an extension of our previous work using an asymptotic approach to describe the movement of combustion fronts in porous media. This approach is essential for the upscaling of the process at the field scale. We apply this method to the problem of in-situ combustion in a heterogeneous reservoir. We show how heterogeneity, combined with heat losses, can lead to extinction phenomena, otherwise absent in homogeneous systems.

Heavy oils and heavy-oil associated recovery processes involve non-Newtonian rheology. Of specific importance is that of Bingham plastics, which characterize the flow behavior of foams, for enhanced recovery, heavy oils, containing asphaltenes, as well as the rheological behavior during the formation of wormholes in sand production. In this report we present new approaches for the simulation of this type of rheology in flow and displacement including Bingham plastics.

ACKNOWLEDGEMENTS

This research was made possible through the Department of Energy contract DE-AC26-99BC15211, the contribution of which is gratefully acknowledged. The PI would like to express his gratitude to the NPTO Project officers in charge of the contract, Dr. Jerry Casteel and the late Mr. Thomas Reid for their help and support.

INTRODUCTION

This project is an investigation of various multi-phase and multiscale transport and reaction processes associated with heavy oil recovery. The thrust areas of the project include the following: Internal drives, vapor-liquid flows, combustion and reaction processes, fluid displacements and the effect of instabilities and heterogeneities and the flow of fluids with yield stress. These find respective applications in foamy oils, the evolution of dissolved gas, internal steam drives, the mechanics of concurrent and countercurrent vapor-liquid flows, associated with thermal methods and steam injection, such as SAGD, the in-situ combustion, the upscaling of displacements in heterogeneous media and the flow of foams, Bingham plastics and heavy oils in porous media and the development of wormholes during cold production. Funding of the project is for three years, from May 6, 1999 to May 5, 2002. The project was extended at no-cost to the agency to January 5, 2003.

In this report, progress made in the various areas outlined above during the second year of the project is described. Work was conducted in all areas, with progress being greater in some areas compared to others, for a variety of circumstances. During the reporting period, a total of up to 8 students were supported by the project. A number of publications and 13 technical reports have resulted from this effort. A cumulative publication list is given below. The report is essentially, but not exclusively, a compilation of the various topical reports.

This report is organized as follows: For each of the four first thrust areas, namely internal drives, vapor-liquid flows, combustion dynamics, and flow of yield-stress fluids, we provide a brief summary of the work performed, followed by various reports. Work in the thrust area of heterogeneity and upscaling will be reported in the final report, along with other progress reports.

CUMULATIVE PUBLICATION LIST

Refereed Publications

Kechagia, P., Tsimpanogiannis, I.N., Yortsos, Y.C. and Lichtner, P., *On the Upscaling of Reaction-Transport Processes in Porous Media with Fast Kinetics*, Chem. Eng. Sci., in press (2002).

Yang, Z., Yortsos, Y.C., and Salin, D., *Asymptotic Regimes of Unstable Miscible Displacements in Random Porous Media*, Adv. Water Res., special anniversary issue, accepted (2002).

Zhan, L. and Yortsos, Y.C., *The Shape of a Gravity Finger in a Rectangular Channel in a Homogeneous Porous Medium*, Transport in Porous Media, in press (2002).

Tsimpanogiannis, I.N., and Yortsos, Y.C., *An Effective Continuum Model for the Evolution of the Gas-Phase in Porous Media Driven by Solute Diffusion*, AIChEJ, in press (2002).

Akkutlu, I.Y., and Yortsos, Y.C., *The Dynamics of Combustion Fronts in Porous Media*, Combustion and Flame, submitted (2001).

Laroche, C., Chen, M., Yortsos, Y.C., and Kamath, J., *Time Scaling of the Rates of Produced Fluids in Laboratory Displacements*, SPEJ, submitted (2001).

Shariati, M. and Yortsos, Y.C., *Stability of Miscible Displacements Across Stratified Porous Media*, Phys. Fluids **13**, 2245-2257 (2001).

Yortsos, Y.C., Xu, B., and Salin, D., *Delineation of Microscale Regimes in Fully Developed Drainage and Implications for Continuum Models*, Comp. Geosc. **5**, 257-278 (2001).

Yortsos, Y.C., and Stubos, A.K, *Phase Change in Porous Media*, Current Opinions in Colloid and Interface Science **6**, 208-216 (2001).

Kechagia, P., Yortsos, Y.C. and Lichtner, P., *A Non-Local KPZ Equation to Model Interface Growth*, Phys. Rev. E **64**, 016315-1-15 (2001).

Yiotis, A.G., Stubos, A.K., Bountouvis, A., and Yortsos, Y.C., *A 2-D Pore-Network Model of the Drying of Single-Component Liquids in Porous Media*, Adv. Water Res. **24**, 437-458 (2001).

Zhan, L. and Yortsos, Y.C., *A Direct Method for the Identification of the Permeability Field of an Anisotropic Porous Medium*, Water Res. Res. **37**, 1929-1938 (2001).

Lajeunesse, E., Martin J., Rakotomalala, N., Salin, D., and Yortsos, Y.C., *The Threshold of Instability in Miscible Displacements in a Hele-Shaw Cell at High Rates*, Phys. Fluids, **13**, 799 (2001).

Zhan, L. and Yortsos, Y.C., *A Note on the Use of Streamline Coordinates in Porous Media Displacements*, Water Res. Res., submitted (2000).

Yortsos, Y.C., *The Permeability Variogram from Pressure Transients of Multiple Wells*, in "Theory, Modeling, and Field Investigation in Hydrogeology: A Special Volume in Honor of Shlomo P. Neuman's 60th Birthday" (D. Zhang, and C.L. Winter, eds.), Geological Society of America Special Paper {\bf 348}, 19-23 (2000).

Yortsos, Y.C., *Physical Considerations in the Upscaling of Immiscible Displacements in a Fractured Medium*, in "Dynamics of Fluids in Fractured Rock" (B. Faybisenko, P.A. Witherspoon and S.M. Benson, eds.), Geophysical Monograph Series {\bf 122}, American Geophysical Union, 235-251 (2000).

Zhan, L., and Yortsos, Y.C., *Identification of the Permeability Field of a Porous Media from the Injection of a Passive Tracer*, Phys. Rev. E **62**, 863-879 (2000).

Tsimpanogiannis, I.N., Yortsos, Y.C., and Stubos, A.K., *Evaporation of a Stagnant Liquid*, Ind. Eng. Chem. Res. **39**, 1505-1513 (2000).

Conference Papers

Akkutlu, Y.I, and Yortsos, Y.C., *The Effect of Heterogeneity on In-situ Combustion: ThePropagation of Combustion Fronts in Layered Porous Media*, paper SPE 75128, presented at the 13th SPE/DOE Symposium on Improved Oil Recovery, Tulsa, OK (April 13-17, 2002). Also, highlighted in Jour. Pet. Tech., page 56 (June 2002).

Amili, P., and Yortsos, Y. C., *Mobilization of Ganglia in Porous Media Using Darcian Dynamics*, paper SPE 75191, presented at the 13th SPE/DOE Symposium on Improved Oil Recovery, Tulsa, OK (April 13-17, 2002).

Tsimpanogiannis, I.N., and Yortsos, Y.C., *An Effective Continuum Model for the Gas Evolution in Internal Steam Drives*, paper SPE 75242 presented at the 13th SPE/DOE Symposium on Improved Oil Recovery, Tulsa, OK (April 13-17, 2002).

Zeng, J., Yortsos, Y. C., and Salin, D., *On the Brinkman Correction in Hele-Shaw Flows*, paper presented at the APS-DFD meeting, San Diego, CA (Nov. 18-20, 2001).

Amili, P., and Yortsos, Y. C., *Darcian Dynamics*, paper presented at the AIChE Fall Meeting, Reno, NV (November 5-8, 2001).

Lu, C., Kechagia, P., Yortsos, Y. C., and Lichtner, P., *Non-Local Upscaling of Reaction-Transport in Porous Media Using a Hybrid Algorithm*, paper presented at the AIChE Fall Meeting, Reno, NV (November 5-8, 2001).

Yiotis, A., Stubos, A. K., Bountouvis, A., and Yortsos, Y. C., *A Pore-Network Model of Drying in Porous Media*, paper presented at the AIChE Fall Meeting, Reno, NV (November 5-8, 2001).

Tsimpanogiannis, I.N., and Yortsos, Y.C., *A Continuum Model for the Evolution of Gas During Solution-Gas Drive*, paper SPE 71502 presented at the 75th SPE Annual Fall Meeting, New Orleans, LA (Oct. 1-3, 2001).

Sudaryanto, B., and Yortsos, Y.C., *Optimization of Displacements in Porous Media Using Rate Control*, paper SPE 71509 presented at the 75th SPE Annual Fall Meeting, New Orleans, LA (Oct. 1-3, 2001).

Laroche, C., Chen, M., Kamath, J., and Yortsos, Y.C., *Determining Relative Permeability Exponents Near the Residual Saturation*, paper SPE 71489 presented at the 75th SPE Annual Fall Meeting, New Orleans, LA (Oct. 1-3, 2001).

Lu, C., and Yortsos, Y.C., *A Pore-Network Model of Combustion in Porous Media*, paper SPE 69705 presented at the International Thermal Operations and Heavy Oil Symposium (ITOHOS), Margarita Island, Venezuela (March 12-14, 2001).

Lu, C., and Yortsos, Y. C., *A Pore-Network Model of Smoldering Combustion*, paper presented at the AIChE Fall Meeting, Los Angeles, CA (November 12-17, 2000).

Shariati, M., and Yortsos, Y. C., *A Study of Miscible Displacement in the Gap of a Hele-Shaw Cell with a Non-Monotonic Viscosity Profile*, paper presented at the AIChE Fall Meeting, Los Angeles, CA (November 12-17, 2000).

Kechagia, P., Yortsos, Y. C. and Lichtner, P., *On the Constraint of Local Equilibrium in the Upscaling of Reaction and Transport Problems in Heterogeneous Porous Media*, paper presented at the AIChE Fall Meeting, Los Angeles, CA (November 12-17, 2000).

Laroche, C., Kamath, J., Nakagawa, F. and Yortsos, Y.C., *Gas Relative Permeability Reduction Due to Waterblocking - A Laboratory-Based Analysis*, paper presented at the 2000 SCA conference, Abu Dhabi (Oct. 18-22, 2000).

Akkutlu, I., and Yortsos, Y.C., *The Dynamics of Combustion Fronts in Porous Media*, paper SPE 63225 proceedings of the 74th SPE Annual Fall Meeting, Dallas, TX (Oct. 1-4, 2000).

Zhan, L. and Yortsos, Y.C., *A Direct Method for the Identification of the Permeability Field of an Anisotropic Porous Medium*, paper SPE 62976 proceedings of the 74th SPE Annual Fall Meeting, Dallas, TX (Oct. 1-4, 2000).

Lu, C. and Yortsos, Y.C., *The Dynamics of Combustion in Porous Media at the Pore-Network Scale*, paper presented at the 7th European Conference on the Mathematics of Oil Recovery, Baveno, Lago Maggiore, Italy (Sept. 5-8, 2000).

Laroche, C., Yortsos, Y.C., and Kamath, J., *Time-Scaling of the Rates of Produced Fluids in Laboratory Displacements in Porous Media*, paper presented at the 7th European Conference on the Mathematics of Oil Recovery, Baveno, Lago Maggiore, Italy (Sept. 5-8, 2000).

Zhan, L., and Yortsos, Y.C., *Identification of Permeability Heterogeneity from Tracer Displacement: Sensitivity Analysis*, proceedings of Conference Tracers and Modeling in Hydrogeology, Tram 2000, Liege, Belgium, pp. 63-73 (May 23-26, 2000).

Zhan, L., and Yortsos, Y. C., *The Identification of the Permeability Heterogeneity of Porous Media from the Displacement of a Passive Tracer*, paper presented at the APS (DFD) Fall Meeting, New Orleans, LA (November 21-23, 1999).

Amili, P. and Yortsos, Y. C., *Stability of Heat Pipes in Vapor-Dominated Systems*, paper presented at the ASME Fall Meeting, Nashville, TN (November 14-19, 1999).

Shariati, M., and Yortsos, Y. C., *Effect of Heterogeneity on the Stability of Displacement Processes in Porous Media with Non-Monotonic Viscosity*, paper presented at the AIChE Fall Meeting, Dallas, TX (November 1-5, 1999).

Zhan, L., and Yortsos, Y. C., *Identification of the Permeability Heterogeneity of Porous Media from the Displacement of a Passive Tracer*, paper presented at the AIChE Fall Meeting, Dallas, TX (November 1-5, 1999).

Kechagia, P., and Yortsos, Y. C., *A Model Stochastic Equation for Convection-Diffusion Equation in Evolving Porous Media*, paper presented at the AIChE Fall Meeting, Dallas, TX (November 1-5, 1999).

Zhan, L., and Yortsos, Y.C., *Identification of the Permeability Heterogeneity of Porous Media from the Displacement of a Passive Tracer*, proceedings of the 10th European Symposium on Improved Oil Recovery, Brighton, UK (August 18-20, 1999).

I. INTERNAL DRIVES

In many processes associated with heavy oil recovery, internal drives, namely these driven by applied supersaturation in dissolved gases or heat content, are common. These include, but are not limited to the evolution of gas in foamy oils, internal steam drives, the evaporation of volatile components during gas injection or the injection of steam, and other processes. The main result is the growth of a gas phase, which is driven by mass or heat transfer, depending on the kind of the applied supersaturation. We have conducted various studies of this multifaceted problem. In this report, we present results in two areas, one associated with the nucleation and growth of a gas phase from a supersaturated liquid, and another associated with internal steam drive. The first study describes a mathematical model of the dynamics of gas evolution as a function of the rate of application of the supersaturation for solution gas drive. The two problems of constant rate of pressure decline and constant rate of liquid withdrawal are treated. This part is the final version of a report, a preliminary version of which was presented in our report last year. The second study is an extension of the same approach to the problem of internal steam drive, which is driven by heat transfer. This problem refers to the phase change of liquid to vapor in single-component systems, and appears in processes where the production of high-temperature liquid leads to a supersaturated condition and the subsequent phase change. It is also related to boiling in porous media, under these conditions. Both applications emphasize the role of nucleation on the onset of phase change, and the subsequent mass or heat transfer on the growth of the resulting new phase. They find applications in foamy oil flow as well as in steam injection and "blowdown" for the production of oils from fractured reservoirs. We need to mention that work in this area has also been conducted at the pore-network scale. It will be reported in the final report of this project.

A Model for the Gas Evolution in a Porous Medium Driven by Solute Diffusion

By

Ioannis N. Tsimpanogiannis and Yannis C. Yortsos

I. INTRODUCTION

The liquid-to-gas phase change in a porous medium and the subsequent growth of the gas phase is encountered in many applications driven by mass or heat transfer. These span various fields of scientific interest and a range of length scales. Examples include the solution gas-drive process for the recovery of oil from oil reservoirs (Sheng et al., 1999a, 1999b), boiling in porous media (Thome, 1990; Satik and Yortsos, 1996), thermal methods for oil recovery (Prats, 1982), nuclear waste disposal (Doughty and Pruess, 1990), soil remediation (Ho and Udell, 1995) and others. In this chapter, we focus on the isothermal gas phase growth from a supersaturated, slightly compressible, binary liquid in a porous medium. This is driven by mass transfer, the extent of which is controlled by the application of either a constant-rate decline of the system pressure or the withdrawal of the liquid at a constant rate.

Consider the removal of an initially supersaturated liquid from a porous medium of a fixed volume (Fig. 1). As the pressure continuously declines, due to liquid expansion, the bubble point of the liquid is eventually reached. Then, nucleation of a gas phase starts, at rates depending on the nucleation properties of the medium. Nucleation is manifested either in the release of pre-existing gas bubbles, trapped in hydrophobic cavities, or in the form of heterogeneously nucleated nuclei. Emphasis will be placed on the former mechanism, although the conventional model will also be used. Because of the competing processes of bubble growth, which depletes the solute from the liquid, thus reducing the supersaturation, and the liquid withdrawal, which reduces the pressure, thus increasing the supersaturation, a supersaturation maximum is attained, following which, nucleation terminates. Identifying the maximum supersaturation and its dependence on process parameters is a key issue. The subsequent gas evolution is controlled by the available supersaturation, the solute mass transfer from the liquid to the gas and the capillary characteristics of the porous medium. The gas phase appears first in the form of small bubbles growing within the confines of single pores (Fig. 2a), but ultimately takes the form of large clusters, spanning a number of pores (Fig. 2b). Competition for mass transfer between the growing bubbles or clusters, capillary effects at pore constrictions, viscous and gravity forces, and the possibility of coalescence or the snap-off of gas-liquid interfaces are important factors in determining the gas-phase evolution.

Eventually, gas flows as a bulk phase. The onset of flow is signaled when the gas pore-volume fraction, S_g, becomes equal to the so-called critical gas saturation, S_{gc}, a value which depends on the underlying growth and flow mechanisms. If viscous or gravity gradients are negligible, gas flow occurs for the first time when isolated gas clusters connect to form a sample-spanning (percolation) cluster (Yortsos and Parlar, 1989). If they do not, gas flow and production occur through the continuous motion of finite-size gas clusters, subject to various mechanisms of interaction, including coalescence. This simultaneous flow of gas and liquid is quite complex, particularly under strong pressure gradients, for example in the case of high-viscosity oils, where "foamy" oil flow takes place (Smith, 1988; Maini, 1996, 1999). In this chapter, we will only consider the stage before the onset of gas flow, however, and in the absence of significant gravity or viscous gradients.

A number of studies have been reported on this problem. A review of the early literature can be found in Li and Yortsos (1995a, 1995b). Experimental work for the case of constant pressure decline rate in consolidated porous media using light oils was reported by Moulu and Longeron (1989), Moulu (1989) and Scherpenisse et al. (1994). Sheng et al. (1999b), Wong et al. (1999) and Urgelli et al. (1999) conducted experiments with heavy oils. Visualization experiments with light oils were reported by Li and Yortsos (1995a), Hawes et al. (1997), Mackay et al. (1998) and Dominguez et al. (2000). Bora et al. (2000) reported experiments with heavy oils. These studies have shown that the critical gas saturation is an increasing function of the liquid withdrawal rate, a finding explained by the increasing number of nucleation centers at larger depletion rates. Scherpenisse et al. (1994) provided useful, but qualitative, scaling arguments showing that maximum supersaturation and critical gas saturation are power-law functions of the depletion rate. A theoretical analysis of bubble growth by solute diffusion in which mass transfer and porous medium capillarity dominate, was provided by Li and Yortsos (1995a, 1995b). The authors conducted visualization experiments in glass micromodels and pore-network simulations to explain patterns and rates of growth of the gas phase at the pore-network scale. Along similar lines, Du and Yortsos (1999) provided a pore-network analysis of the critical gas saturation, in the absence of gravity/viscous gradients. They confirmed an earlier hypothesis by Yortsos and Parlar (1989) that in the absence of spatial gradients, the onset of critical gas saturation coincides with the percolation threshold of an invasion percolation process, originating from multiple nucleation centers. They also showed that S_{gc} is a power law of the final nucleation fraction (defined more precisely below), f_{qf}, namely

$$S_{gc} = f_{qf}^{1-D_f/E} \tag{1}$$

Here, E (equal to 2 or 3) is the (Euclidean) dimension of the pore network and D_f is the mass fractal dimension of the percolation cluster (equal to 1.82 for 2-D Invasion Percolation (IP) with trapping, and 2.53 for 3-D IP with or without trapping, Feder, 1988). The dependence in (1) was established regardless of the nucleation sequence (instantaneous or sequential) or the particular regime of bubble growth (see Li and Yortsos, 1995a, 1995b).

The presence of gradients will affect the above scaling. Pore-network simulations conducted by McDougal and Sorbie (1999) and Wang and Mohanty (1999) in the related topic of gas condensation, showed that S_{gc} decreases as the hydrostatic pressure gradient increases, a trend also anticipated in Scherpenisse et al. (1994). In a parallel study (Tsimpanogiannis and Yortsos, 2002), we have analyzed the effect of gravity and/or viscous forces on S_{gc}, and developed scaling laws for the dependence of S_{gc} on f_{qf} and on two dimensionless parameters, the Bond and capillary numbers, defined respectively as

$$B = \frac{\Delta\rho g k}{\gamma} \quad \text{and} \quad Ca = \frac{q\mu}{\gamma} \tag{2}$$

Here $\Delta\rho$ denotes the density difference between liquid and gas, k is permeability, γ the liquid-gas interfacial tension, q the liquid flow rate and μ the liquid viscosity. Equation (1) is obtained in the limits $B \ll 1$ and $Ca \ll 1$ (more specifically, $B \leq 10^{-5}$ and $Ca \leq 10^{-5}$), which are the regions of interest of this chapter.

In many practical cases, pressure depletion is due to liquid withdrawal at a constant flow rate. Experimental work in consolidated porous media with light oils was reported by

Firoozabadi et al. (1992), Firoozabadi and Aronson (1999) and Egermann and Vizika (2000). These studies focused on the critical gas saturation, which was found to be an increasing function of the liquid withdrawal rate. As before, this finding was explained by the increasing number of nucleation centers, from which gas clusters grow, at larger depletion rates. Sheng et al. (1999a) and Renard et al. (2000) in two recent reviews focused on aspects of solution gas drive related to the primary recovery of heavy oil.

A modeling attempt to capture the gas phase growth, but not the preceding nucleation period, in an experiment at a constant rate of withdrawal, was made by Firoozabadi and Kashchiev (1997). These authors used an effective continuum model with bubble growth driven by diffusion. The gas phase is modeled as a collection of effective bubbles, mass transfer to which is approximated by simple expressions. Although the paper discusses rate-dependent nucleation using classical expressions (see also below), the nucleation issue is in fact bypassed, in that nucleation fraction, the maximum supersaturation, or the effect of depletion rate on the number of bubbles nucleated, are not actually predicted or calculated. Rather, the latter quantities are inferred from the experimental results, and subsequently used as parameters for the gas phase growth following the nucleation period.

Experiments on pressure depletion driven by constant liquid withdrawal rate, particularly with heavy oils, were reported by Pooladi-Darvish and Firoozabadi (1999), Tang and Firoozabadi (1999), Kumar et al. (2000), Andarcia et al. (2001), Arora and Kovscek (2001) and Kamp et al. (2001a, 2001b). In two very recent studies, which appeared at the same time this work was being written, Kamp et al. (2001a) and Arora and Kovscek (2001) presented effective continuum models to interpret the pressure depletion of heavy oils, focusing, in particular, on the foamy oil issue. Because of the high viscous forces in these experiments, these models must also account for two-phase flow, which was done using conventional relative permeability functions. In the present context, these studies are of interest insofar as nucleation is concerned. The latter is incorporated in the form of rate-dependent nucleation in Kamp et al. (2001a), and in the form of activated cavities in Arora and Kovscek (2001). Nucleation parameters were estimated to match experimental data (see more discussion below).

The objective of this chapter is to provide a comprehensive model both of the nucleation and the gas-phase growth periods, until the onset of the critical gas saturation. For this purpose, an effective continuum model will be developed. If used to model the later stages of bubble growth, where gas occupies several pores and is influenced by the pore geometry, topology and capillarity (e.g. see Li and Yortsos, 1995a, 1995b), effective continuum models have obvious drawbacks. However, they may be adequate for describing nucleation and the early stages of bubble growth. The last two, particularly the nucleation sequence, are the main areas of interest of this chapter. We focus on the effect of the nucleation characteristics on the maximum supersaturation, the nucleation fraction and the critical gas saturation, and provide an analysis of the effect of various parameters, such as pressure decline rate, on these quantities. Results for the gas phase growth following the conclusion of nucleation are also presented.

The chapter is organized as follows: First, we formulate the problem. A scaling analysis allows to recast the problem in a more useful form, to be used for direct predictions. Then, numerical results are analyzed. It turns out that for their interpretation, a simplified model of the nucleation and growth periods can be developed. We use the simpler model to obtain expressions for the maximum supersaturation as a function of geometric, thermodynamic and process parameters. This allows to obtain useful relations for the dependence of the final nucleation fraction and the critical gas saturation on process parameters. The theoretical predictions are then compared against experimental results.

II. MATHEMATICAL FORMULATION

Consider the heterogeneous nucleation and growth of multiple bubbles from a binary liquid, within an effective porous medium. The process is driven by the continuous increase in the supersaturation of the system, $KC_\infty(t) - P_l(t)$, where we have assumed for simplicity linear thermodynamic equilibria using Henry's law

$$P_g = KC_\infty(t) \tag{3}$$

Here, K is the solubility constant, $C_\infty(t)$ the time-varying mass concentration, P stands for pressure, and subscripts g and l denote gas and liquid, respectively. More complex thermodynamics can certainly be incorporated, but the salient features are manifested with the simpler model (3). As noted above, the change in supersaturation can be imposed in two different ways, one in which the pressure declines at a constant rate, and another in which the liquid is withdrawn at a constant rate. Because gravitational and/or viscous effects are not included, the pressure is spatially uniform. Instead, emphasis is placed on nucleation and on the effect of the increase of supersaturation on the growth of the gas phase.

a. Nucleation

As the liquid pressure declines, nucleation sets in. Yortsos and Parlar (1989) reviewed the gas-liquid phase change in porous media and concluded that heterogeneous nucleation is the most plausible mechanism in solution gas drives (see also more recent reviews by Laaksonen et al., 1995, and Jones et al., 1999). In one model, nucleation occurs when a gas bubble, either pre-existing or nucleated inside a cavity at the pore walls, becomes unstable and detaches or otherwise occupies the host pore body (Fig. 3). This type of mechanism is in agreement with visual observations from micromodel experiments (Li and Yortsos, 1995a; El Yousfi et al., 1991, 1997; Bora et al., 2000, and Dominguez et al., 2000). In the cavity model, the condition for the activation of a nucleation site is when the trapping capillary forces are overcome for the first time (Fig. 3). This occurs when the following condition is satisfied between the radius of the nucleation cavity, r_c, and supersaturation,

$$\frac{2\gamma\cos\theta}{r_c} = KC_\infty(t) - P_l(t) \tag{4}$$

where θ is the contact angle ($0 < \theta < \pi/2$). In this model, the onset of nucleation is not kinetically related to the degree of supersaturation, as for example, in conventional approaches (Firoozabadi and Kashchiev, 1997), but rather depends on the size distribution, $\alpha_c(r_c)$, of the nucleation cavities.

Consider, now, the activation of nucleation sites. With the decrease in the liquid pressure, the right-hand side of (4) increases, eventually becoming positive. Then, various cavities satisfying (4) become activated and their corresponding host pore bodies occupied by gas. At any time, the current nucleation fraction, f_q, defined as the number fraction of pores that contain sizes which have been activated, is

$$f_q = \int_{r_c}^{\infty} \alpha_c(r)dr \tag{5}$$

where r_c is an implicit function of time, through (4). Equation (5) implies a zero nucleation fraction at zero supersaturation ($r_c \rightarrow \infty$) and a nucleation fraction of one at infinite supersaturation ($r_c \rightarrow 0$). The cavity size distribution, α_c, pertains only to the largest cavity in any given pore (as this cavity will be activated first). The actual number of bubbles contained in a given pore may be larger. We will assume that a number of bubbles, n_B, are contained in each activated pore. Parameter n_B will be taken equal to 1, for the cavity model, as this is suggested in the micromodel experiments, but will be kept arbitrary for rate-dependent heterogeneous nucleation. Equation (5) slightly overestimates the true nucleation fraction, since pores containing sites to be activated later, may already be occupied by gas, due to the growth of gas clusters from neighboring pores. A more appropriate expression in such a case would be

$$\frac{df_q}{dt} = (1 - S_g)\frac{d}{dt}\left[\int_{r_c}^{\infty} \alpha_c(r)dr\right] \tag{6}$$

where S_g is the gas saturation. However, in most cases, nucleation terminates well before gas bubble growth has occurred to any substantial degree ($S_g \ll 1$), thus (5) should be an excellent approximation.

It is interesting to illustrate the dependence of f_q on the various cavity size distributions. For a Rayleigh distribution

$$\alpha_c(r) = \frac{\pi r}{2r_c^{*2}}\exp\left(-\frac{\pi r^2}{4r_c^{*2}}\right) \tag{7}$$

where r_c^* is a characteristic (here the mean) cavity size, equation (5) reads

$$f_q = \exp\left(-\frac{\pi r_c^2}{4r_c^{*2}}\right) = \exp\left[-\frac{\pi\gamma^2}{r_c^{*2}(KC_\infty - P_l)^2}\right] \tag{8}$$

This exponential relation bears a superficial resemblance to classical nucleation (see below), a result, however, which is purely due to the form of the Rayleigh distribution. Different distributions will result in different functionals. For example, we will also consider stretched-exponential or log-normal expressions of the form

$$f_q = \exp\left(-\frac{r_c^n}{\sigma r_c^{*n}}\right) \quad \text{or} \quad f_q = \frac{1}{2}\text{erfc}\left(\frac{\ln\frac{r_c}{r_c^*}}{\sqrt{2}\sigma}\right) \tag{9}$$

respectively, where n is a positive exponent and σ is a measure of the variance. The type of assumed distribution influences the results to be obtained, as will be demonstrated below. In comparing with the experimental results, we postulated a size distribution and then determined its parameters by fitting with the experimental data

As long as the level of supersaturation increases with time, the right-hand-side of equation (8) also increases, implying that additional sites become activated, and the nucleation fraction continuously rises. This is consistent with experimental evidence of sequential nucleation reported by Li and Yortsos (1995a), Hawes et al. (1997), Mackay et al. (1998) and Bora et al. (2000). After the supersaturation reaches a maximum (local or global), equation (8) predicts a decreasing f_q, which is unphysical. Therefore, in segments of decreasing supersaturation the nucleation fraction is assumed constant. When the supersaturation goes through a global maximum, it signals the end of the nucleation period, in which case the fraction of pores ultimately activated, f_{qf}, will be given by equations (8) or (9) at the time of the maximum supersaturation.

The fraction f_{qf} can be directly related to the number of bubbles nucleated per unit pore volume, N_f, a quantity used in Firoozabadi and Kashchiev (1997) to quantify nucleation. Assuming $n_B = 1$, we have

$$qN_f = \frac{f_{qf} N_T}{V_p} \tag{10}$$

q where N_T is the total number of pores and V_p is the total pore volume. By noting that $V_p = N_T V_s$, where V_s is a typical volume of a pore (site), we can further write

$$qN_f = \frac{f_{qf}}{V_s} \tag{11}$$

q This allows us to relate the nucleation fraction to experimental values of N_f (see below). We note, in advance, that in typical experiments, f_{qf} is very small, of the order of $10^{-9} - 10^{-6}$.

A different approach is to use rate-dependent heterogeneous nucleation. Consider the nucleation rate expression

$$\frac{dN_f}{dt} = K_{het}\exp\left[-\frac{16\pi\gamma^3 f}{3k_B T(KC_\infty - P_l)^2}\right] \tag{12}$$

where K_{het} is a heterogeneous rate constant, f is a dimensionless number expressing the wettability of the medium vis-a-vis nucleation (ranging between 1 and 0 for perfectly homogeneous and perfectly heterogeneous rate-dependent nucleation, respectively), and k_B is Boltzmann's constant. Both K_{het} and f can be determined from the matching of experimental data. Using the equivalent of (11) we can express (12) in terms of the nucleation fraction f_q,

$$\frac{df_q}{dt} = \frac{K_{het}V_s}{n_B}\exp\left[-\frac{16\pi\gamma^3 f}{3k_B T(KC_\infty - P_l)^2}\right] \tag{13}$$

Compared to (8), equation (13) contains an explicit rate dependence, while the dependence on parameters, such as γ, is different from the previous, as expected. Both these models will be considered below.

Through the nucleation process, nucleation centers are activated sequentially, giving rise to evolving gas clusters, which grow by mass transfer from the liquid to the gas. Sequential nucleation results into clusters of different ages (the time passed since a particular class of gas clusters has been nucleated/activated). Let $\omega(\tau)$ be the number density of clusters nucleated per total number of pores. Then, $\omega(\tau)d\tau$ is the number of new clusters per total number of pores that become activated in the time interval between τ and $\tau + d\tau$. Evidently,

$$\omega(\tau)d\tau = n_B df_q \tag{14}$$

This relation will be used below to simplify the expressions for the gas phase growth.

b. Gas phase growth

During the growth of the gas phase we can roughly distinguish two periods, one in which the growth is within single pores and another corresponding to gas clusters spanning several pores (Figs. 2a, 2b, respectively). The first period extends throughout and following the nucleation stage, the second is the later stage of growth. In either, growth is driven by diffusive mass transfer of the dissolved gas. During the first period, mass transfer results mostly in the increase of the volume of the gas. During the second, it also leads to an increase in the gas pressure, in case the interface becomes pinned at pore throats (Fig. 2), until the time when the smallest capillary threshold at the throats is overcome. Following this, the gas cluster volume expands accordingly. In general, different clusters compete for the available solute in the liquid, the relative mass transfer rates depending on their geometry and relative position. These dynamics were analyzed in Li and Yortsos (1995a, 1995b).

In the absence of competition between adjacent clusters, an isolated cluster j grows at a rate which is proportional to its effective radius, $R_j(t,\tau)$, and the driving force $C_\infty - C_i$, where C_∞ is the far-field concentration and C_i the equilibrium concentration at the gas-liquid interface. We will proceed, therefore, by assuming that mass transfer is by quasi-steady-state diffusion and that the gas is ideal. Then, we can write the following mass balance for a growing cluster

$$\left(\frac{M_w}{R_g T}\right)\frac{d}{dt}(P_l V_g) \approx 4\pi\lambda R_j \mathcal{D}(C_\infty - C_i) \tag{15}$$

where M_w is the molecular weight of the gas, R_g the ideal gas constant, T the temperature, V_g the gas cluster volume and $\mathcal{D}$ the diffusion coefficient. The mass transfer term in (15) was obtained assuming quasi-steady-state diffusion to a spherical bubble. This is true even for ramified fractal clusters, as was verified by Satik and Yortsos (1996) for a percolation cluster. Dimensionless parameter λ is an $O(1)$ geometric constant to account for possible corrections to the mass transfer model depending on the growth period (see below). In equation (15) we have neglected the capillary pressure, P_c, which in typical applications is small compared to the liquid pressure. From Henry's law, we also have

$$C_i = \frac{P_v}{K} = \frac{P_l + P_c}{K} \approx \frac{P_l}{K} \tag{16}$$

where the second equality is again an excellent approximation in the typical applications examined here.

The gas volume V_g takes a different expression in the two different periods. For growth within a single pore, $V_g \approx V_c\left(\frac{R_j}{r_c^*}\right)^3$, where V_c is a characteristic cavity volume (defined here as $\frac{4}{3}\pi r_c^{*3}$). For growth of a cluster spanning several pores, we have $V_g \approx A^* V_s \left(\frac{R_j}{r_s^*}\right)^{D_f}$, where

V_s is the average site volume, r_s^* is a characteristic pore body size, D_f is the mass fractal dimension, equal approximately to 2.5 for a 3-D cluster, and A^* is a dimensionless geometric prefactor. To capture both periods with the same equation we write

$$\left(\frac{AV_cM_w}{R_gT}\right)\frac{d}{dt}\left[P_l\left(\frac{R_j}{r_c^*}\right)^{D_f}\right] = 4\pi\lambda R_j\mathcal{D}(C_\infty - C_i) \tag{17}$$

with the understanding that D_f varies between 3 and 2.5, and A between 1 and $\frac{A^*V_s}{V_c}\left(\frac{r_c^*}{r_s^*}\right)^{D_f}$, during the nucleation period and growth periods, respectively.

The nucleation period and the early part of the growth period are adequately represented by equation (17). However, growth during the later stages of the second period, where gas clusters span several pores, cannot in reality be captured by (17). Competing clusters affect growth rates in a non-trivial manner. The latter would still be proportional to a mean driving force, $C_\infty - C_i$, where now C_∞ is the volume-averaged concentration in the liquid, and R_j stands for the average size of a cluster. However, the mass transfer coefficient λ may be variable in time and space, while coalescence of clusters will also occur. Accounting for these complexities is a difficult problem, the solution of which requires a pore-network approach (Li and Yortsos 1995a, 1995b).

Under the above assumptions, the gas phase will be described as a collection of clusters of size $R(t,\tau)$, the dynamics of each of which is described by equation (17), with R_j replaced by R, namely

$$\left(\frac{AV_cM_w}{R_gT}\right)\frac{\partial}{\partial t}\left[P_l\left(\frac{R}{r_c^*}\right)^{D_f}\right] = 4\pi\lambda R\mathcal{D}(C_\infty - C_i) \tag{18}$$

subject to the initial condition $R(\tau,\tau) = r_c(\tau)$, where r_c satisfies (4). In the formulation of Firoozabadi and Kashchiev (1997), the equivalent of equation (18) was integrated under a number of simplifying assumptions to obtain an explicit dependence of R on time. Such an approximation will not be used here.

Consider, next, the mass balance for the solute in the liquid phase. We have

$$\frac{d}{dt}\left[V_p(1-S_g)C_\infty\right] = -4\pi\lambda\mathcal{D}(C_\infty - C_i)N_T\int_0^t R(t,\tau)\omega(\tau)d\tau - C_\infty Q(t) \tag{19}$$

where the integration is over all existing clusters and $Q(t)$, the volumetric flow rate of the liquid out of the porous medium, is in general a function of time. Equivalently, we can rewrite (19) as

$$\frac{d}{dt}\left[V_p(1-S_g)C_\infty\right] = -4\pi\lambda\mathcal{D}(C_\infty - C_i)N_T n_B \int_0^{f_q} \hat{R}(t,f)df - C_\infty Q(t) \tag{20}$$

where we introduced the notation $\hat{R}(t,f(\tau)) \equiv R(t,\tau)$, for the radius of a cluster at time t, nucleated when the nucleation fraction was $f(\tau)$. For the case of instantaneous nucleation, e.g. as postulated in Firoozabadi and Kashchiev (1997), $\hat{R}(t,f_q) = R(t)\delta(f_q - f_{qf})$, where f_{qf} is the final nucleation fraction and δ is the Dirac delta function. Then, the above integral reduces to $R(t)f_{qf}$. However, f_{qf} is the very quantity we must determine, is not known a priori, and needs to be computed as part of the overall process, as discussed in detail below.

The volumetric flow rate $Q(t)/V_p$ is related to the pressure decline rate through the mass balance on the liquid, which reads

$$\frac{d}{dt}\left[\rho_l(1-S_g)\right] = -\rho_l\frac{Q(t)}{V_p} \tag{21}$$

where ρ_l is the liquid density. For a slightly compressible liquid,

$$\rho_l = \rho_b \exp[c(P_l - P_b)] \tag{22}$$

where the liquid compressibility, c, takes values in the range $1.45\times10^{-4} - 1.45\times10^{-3}\mathrm{MPa}^{-1}$. Then,

$$\frac{Q(t)}{V_p} = -(1-S_g)c\frac{dP_l}{dt} + \frac{dS_g}{dt} \tag{23}$$

Finally, the gas saturation is related to the radius of the growing clusters and the nucleation fraction through the relation

$$S_g = Av\int_0^t \left(\frac{R(t,\tau)}{r_c^*}\right)^{D_f}\omega(\tau)d\tau = Avn_B\int_0^{f_q}\left(\frac{\hat{R}(t,f_q)}{r_c^*}\right)^{D_f}df_q \tag{24}$$

where we introduced the volume ratio $v \equiv \frac{V_c}{V_s}$. This parameter can be calculated from knowledge of the average cavity and pore sizes. Subject to the relevant initial conditions, the system of equations (18), (20), (23) and (24) can be integrated. Integration proceeds until the time when the critical gas saturation (1) is reached.

c. Dimensionless formulation and scaling

For the solution of the problem, we recast the equations in dimensionless form. Denote dimensionless quantities by subscript D and scale concentrations by $C_b = \frac{P_b}{K}$, pressure by P_b, where subscript b refers to the bubble point, and cluster size by r_c^*. The choice of the characteristic time depends on the process. We will take $t^* = \frac{P_b}{a}$, where a is the pressure decline rate, for the case of constant pressure decline rate and $t^* = \frac{V_p}{Q}$, for the case of liquid withdrawal at constant volumetric flow rate Q.

For the case of constant pressure decline rate, the dimensionless mass balances for the solute in the gas and liquid phases read

$$(1-t_D)\frac{\partial \hat{R}_D^{D_f}}{\partial t_D} = \frac{\Pi_2}{A\Pi_1}(C_{D\infty} - P_{Dl})\hat{R}_D + \hat{R}_D^{D_f} \tag{25}$$

and

$$(1-S_g)\frac{dC_{D\infty}}{dt_D} = -\frac{1}{\Pi_1}(C_{D\infty} - P_{Dl})\int_0^{f_q} \hat{R}_D(t_D, f_q)df_q - \Pi_3(1-S_g)C_{D\infty} \tag{26}$$

where we used the equilibrium relationship

$$C_{Di} = P_{Dl}(t_D) \tag{27}$$

and assumed that the process begins ($t_D = 0$) when the pressure is at the bubble point. In the above, we have defined three dimensionless groups,

$$\Pi_1 = \frac{V_p a}{4\pi\lambda\mathcal{D}P_b N_T r_c^*} = \frac{V_s a}{4\pi\lambda\mathcal{D}P_b n_B r_c^*}, \quad \Pi_2 = \frac{R_g T}{v n_B M_w K} \quad \text{and} \quad \Pi_3 = cP_b \tag{28}$$

Parameter Π_1 expresses the ratio of the characteristic times for diffusion at the pore scale to that for the decline of pressure. Although a small number in typical applications (see Table 1), it plays a key role in determining the nucleation fraction and the critical gas saturation. Parameter Π_2 is the product of the geometric constant vn_B with a thermodynamic constant, expressing the ratio of the equilibrium concentrations in the liquid and the gas phases. These parameters are either known or can be estimated from comparison with experimental data.

For the case of constant liquid withdrawal rate the analogous equations read

$$P_{Dl}(t_D)\frac{\partial \hat{R}_D^{D_f}}{\partial t_D} + \hat{R}_D^{D_f}\frac{dP_{Dl}}{dt_D} = \frac{\Pi_2}{A\Pi_4}(C_{D\infty} - P_{Dl})\hat{R}_D \tag{29}$$

and

$$(1 - S_g)\frac{dC_{D\infty}}{dt_D} = -\frac{1}{\Pi_4}(C_{D\infty} - P_{Dl})\int_0^{f_q} \hat{R}_D(t, f_q)df_q - C_{D\infty} + C_{D\infty}\frac{dS_g}{dt_D} \tag{30}$$

where

$$\Pi_4 = \frac{Q}{4\pi\lambda\mathcal{D}N_T n_B r_c^*} = \frac{V_s Q}{4\pi\lambda\mathcal{D}V_p n_B r_c^*} \tag{31}$$

Here, parameter Π_4 expresses the ratio of the characteristic time for diffusion to that for the emptying of the pore volume. Typically, this is also a small number (Table 1). As will be shown below, Π_4/Π_3 plays a role equivalent to Π_1.

Finally, in both cases, we have the following relations: The liquid mass balance becomes

$$\frac{dP_{Dl}}{dt_D} = \frac{1}{\Pi_3(1 - S_g)}\left(\frac{dS_g}{dt_D} - 1\right) \tag{32}$$

The gas saturation is

$$S_g = Avn_B\int_0^{f_q} \hat{R}(t_D, f_q)^{D_f}df_q \tag{33}$$

The cavity size that becomes activated at a given time is

$$r_{Dq} = \frac{\Pi_c}{C_{D\infty}(t_D) - P_{Dl}(t_D)} \tag{34}$$

where we introduced the dimensionless cavity capillary pressure threshold, $\Pi_c = \frac{2\gamma\cos\theta}{r_c^* P_b}$. The latter is an important parameter in the overall dynamics. In terms of the supersaturation

$$s \equiv C_{D\infty}(t_D) - P_{Dl}(t_D) \tag{35}$$

or, more conveniently, in terms of the rescaled supersaturation

$$s_D \equiv \frac{s}{\Pi_c} \tag{36}$$

equation (34) can be further expressed as $r_{Dq} = s_D^{-1}$. The nucleation fraction is then given by the various expressions

$$f_q = \exp\left(-\frac{\pi}{4s_D^2}\right), \quad f_q = \exp\left(-\frac{1}{\sigma s_D^n}\right), \quad f_q = \frac{1}{2}\text{erfc}\left(-\frac{\ln s_D}{\sqrt{2}\sigma}\right) \tag{37}$$

depending on the size distribution used, or by

$$\frac{df_q}{dt_D} = h_1 \exp\left(-\frac{h_2}{s^2}\right) \tag{38}$$

in the rate-dependent nucleation case. In the latter we introduced the dimensionless parameters

$$h_1 = \frac{K_{het} t^* V_s}{n_B} \quad \text{and} \quad h_2 = \frac{16\pi\gamma^3 f}{3P_o^2 k_B T} \tag{39}$$

Parameter h_1 is inversely proportional to Π_1 or Π_4. If this dependence is extracted, then equation (39) reads as

$$h_1 = \frac{\zeta}{\Pi_1} \quad \text{or} \quad h_1 = \frac{\zeta}{\Pi_4}, \quad \text{where} \quad \zeta \equiv \frac{K_{het} V_s^2}{4\pi\lambda\mathcal{D} n_B^2 r_c^*} \tag{40}$$

The initial conditions for the simulations were $C_{D\infty} = 1$, $P_{Dl} = 1$ and $R_D(\tau, \tau) = s_D^{-1}(\tau)$.

The above system contains one key parameter, Π_1 or Π_4, describing the effect of the rate of increase of the supersaturation. Because it is small, a further rescaling of the nucleation fraction and the cluster size is necessary. After some analysis, it is not difficult to show that for the cavity nucleation model, the following scaling is valid (for example, for the constant pressure decline rate), $f_q \sim \Pi_1^{\frac{D_f}{D_f - 1}}$ and $f_q R^{D_f} \sim O(1)$ (where, given that the nucleation fraction varies only during the first period, $D_f = 3$). This scaling contains the main effect of the pressure decline rate on the nucleation fraction. Thus, we may define a rescaled nucleation fraction

$$\phi_q = f_q \Pi_1^{-\frac{3}{2}} \quad \text{or} \quad \phi_q = f_q \left(\frac{\Pi_4}{\Pi_3}\right)^{-\frac{3}{2}} \tag{41}$$

and rescaled cluster sizes

$$\rho_D = \Pi_1^{\frac{1}{2}} \hat{R}_D \quad \text{or} \quad \rho_D = \left(\frac{\Pi_4}{\Pi_3}\right)^{\frac{1}{2}} \hat{R}_D \tag{42}$$

in the two different cases. In the new notation, the governing equations become as follows:

For the case of constant rate of pressure decline,

$$(1 - t_D)\frac{\partial \rho_D^{D_f}}{\partial t_D} = \frac{\Pi_2}{A} s \rho_D + \rho_D^{D_f} \tag{43}$$

and

$$(1 - S_g)\frac{ds}{dt_D} = -s \int_0^{\phi_q} \rho_D(t_D, \phi_q) d\phi_q - (s + 1 - t_D)\left[\Pi_3(1 - S_g)\right] + 1 - S_g \tag{44}$$

while for the constant liquid withdrawal rate,

$$\Pi_3 P_{Dl}(t_D)\frac{\partial \rho_D^{D_f}}{\partial t_D} + \Pi_3 \rho_D^{D_f} \frac{dP_{Dl}}{dt_D} = \frac{\Pi_2}{A} s \rho_D \tag{45}$$

and

$$\Pi_3(1 - S_g)\frac{ds}{dt_D} = -s \int_0^{\phi_q} \rho_D(t_D, \phi_q) d\phi_q + \left(\frac{dS_g}{dt_D} - 1\right)\left[\Pi_3(P_{Dl} + s) - 1\right] \tag{46}$$

The last two equations are also accompanied by equation (32). The gas saturation expression for either case becomes

$$S_g = A v n_B \int_0^{\phi_q} \rho(t_D, \phi_q)^{D_f} d\phi_q \tag{47}$$

For the case of rate-dependent nucleation, the rescaled nucleation fraction reads as

$$\frac{d\phi_q}{dt_D} = h_1^* \text{exp}\left(-\frac{h_2}{s^2}\right) \tag{48}$$

where $h_1^* = h_1 \Pi_1^{-\frac{3}{2}}$ or $h_1^* = h_1 \left(\frac{\Pi_4}{\Pi_3}\right)^{-\frac{3}{2}}$ in the respective cases. The solution of the system of the rescaled equations will be sought numerically in the following sections.

III. NUMERICAL RESULTS

The system of differential equations was solved numerically using a fourth-order Runge-Kutta method (Press et al., 1994). A typical calculation requires the time to be marched forward. A difficulty is that the total number of classes of gas clusters is not known *a priori*, but it is an outcome of the computation during the nucleation process. In theory, this number is infinite, and the problem becomes one of solving an infinite system of differential equations. In practice, the number of equations is constrained by the size of the time step. At each time step we examine whether nucleation of a new class of gas clusters is possible, namely whether the supersaturation is increasing. If so, a new class of gas clusters is added. Then, the simultaneous growth of all different classes of clusters is computed. When the supersaturation reaches a maximum, further nucleation stops. Computations during the nucleation process were also facilitated with an asymptotic analysis, to be described in more detail later.

a. Constant Pressure Decline Rate

In the typical case, parameters which can vary over a significant range are Π_1 and Π_c (and possibly Π_2). An additional variable is the type of the cavity size distribution used in the calculation of the nucleation fraction. The sensitivity to these parameters was examined in the simulations.

The effect of Π_1 and Π_c on the rescaled nucleation fraction, ϕ_q, the mean rescaled radius, $\rho_{D,m}$, the rescaled supersaturation, s_D, and the gas saturation, S_g, is shown in Figs. 4-7. In these calculations, we used a Rayleigh size distribution, Π_2 and Π_3 were kept constant to the values 2.33×10^6 and 8.7×10^{-3}, respectively, while Π_1 varied over several orders of magnitude (from 10^{-8} to 10^{-2}).

The variation of ϕ_q as a function of the dimensionless time, t_D, and of the parameters Π_1 and Π_c is shown in Fig. 4. It is found that ϕ_q increases very rapidly in a small time interval, and then stabilizes to a final value at the conclusion of nucleation. Such behavior is characteristic of nucleation processes, and has features similar to those reported by El Yousfi et al. (1991, 1997). It is demonstrated here for the first time for the case of nucleation from pre-existing, trapped gas. The rapid variation of ϕ_q is approximately a stretched exponential of the form

$$\phi_q \sim \exp\left(-\frac{\pi \Pi_c^2}{4t_D^2}\right), \quad \phi_q \sim \exp\left(-\frac{\Pi_c^n}{\sigma t_D^n}\right), \quad \phi_q \sim \operatorname{erfc}\left(\frac{\ln \frac{\Pi_c}{\sigma t_D}}{\sqrt{2}\sigma}\right) \qquad (49)$$

for the different cases, as during the early nucleation period we have $s \sim t_D$ (see below). Equation (49) suggests that, e.g. for the Rayleigh distribution case, a plot of $-\ln\phi_q$ vs. t_D^{-2} is linear with slope $\frac{\pi \Pi_c^2}{4}$. Because of the resulting very sharp rise, this process can be interpreted as instantaneous nucleation (IN). However, proceeding with such an assumption does not allow for the computation of the final nucleation values. Instead, we must consider the details of the approach to the final values using the progressive nucleation model, used here. Fig. 4a shows that for constant Π_c, the effect of Π_1 on the rescaled nucleation fraction is not very significant at small Π_1, but that it becomes stronger (roughly a power law) as Π_1 takes larger values. The relatively weak dependence on Π_1 verifies the correctness of the scaling (41). At the same time, the stronger dependence at larger Π_1 is significant, and as shown below, is needed in order to explain experimental data. In terms of the actual nucleation fraction, these findings imply that an increase in Π_1 leads to an increase in the final fraction, f_{qf}, according to a power law scaling, namely $f_{qf} \sim \Pi_1^{\frac{3}{2}}$ at very small Π_1, and $f_{qf} \sim \Pi_1$ at larger Π_1. The effect of Π_c is also significant. As Π_c increases, the final nucleation fraction ϕ_{qf} (hence f_{qf}) decreases (Fig. 4b). The increase of f_{qf} with an increase in Π_1 and a decrease in Π_c is expected. Larger values of Π_1 result from a faster decline rate, a greater departure from equilibrium, the establishment of a greater supersaturation, hence the activation of more nucleation sites. Likewise, smaller Π_c imply that nucleation is facilitated at increasingly smaller supersaturations, as larger size cavities can be activated. An approximate analysis shown below will provide an explanation of the behavior observed.

Fig. 5 shows the corresponding effects on the mean rescaled size ρ_{Dm}. There are two regions, one corresponding to the nucleation period, and another to growth after nucleation. The two periods can be roughly approximated as power-law regimes (as a function of time) with slopes approximately equal to 1 and 0.63, respectively. The effect of Π_1 is relatively insignificant at small Π_1, confirming the validity of the scaling (41). The effect of Π_c is more significant. Smaller values of Π_c lead to an increase in the nucleation fraction, and a corresponding decrease in the size of the gas clusters at the conclusion of nucleation.

Fig. 6a shows plots of the rescaled supersaturation s_D as a function of time for different

Π_1 and Π_c. At the beginning of the process and during nucleation, the supersaturation increases with time almost linearly, suggesting that $C_{D\infty}$ does not vary significantly in that period. As nucleation and growth take place, the rate of supersaturation increase slows down and, at some point, s_D reaches a maximum value, s_{Dm}. It is at that point where nucleation terminates. Following this point, the supersaturation decreases monotonically. The value s_{Dm} is plotted in Fig. 6b as a function of Π_1 and Π_c. Note that s_{Dm} is in general of the order of 10^{-1}. The dependence on the parameters is weak at small Π_1 and large Π_c, but becomes stronger at larger Π_1 and smaller Π_c. This behavior is consistent with that of the nucleation fraction discussed above. From a compilation of experimental results, Scherpenisse et al. (1994) suggested that s_{Dm} behaves roughly as a power law of the pressure decline rate with exponent 1/4. Our analysis indicates that such a power law is not universally valid, although it may apply in a certain range of Π_1. It is interesting that the sensitivity of s_{Dm} to Π_c and Π_1 (and in particular to the latter) is not as large as one might have intuitively anticipated. Nonetheless, its effect on the nucleation fraction can be significant, due to the exponential dependence, as can be seen for example in the following expression (for a Rayleigh distribution)

$$\phi_q = \exp\left[-\frac{\pi}{4s_D^2} - \frac{D_f}{(D_f-1)}\ln\Pi_1\right] \tag{50}$$

Because of the exponential dependence on s_D^{-2} and because s_{Dm} is of the order of 10^{-1}, even small changes in s_D have a very large effect on the nucleation fraction. This large sensitivity enhances the weak sensitivity of s_{Dm} on Π_1 and β and leads overall to a non-trivial effect.

The evolution of the gas saturation is shown in Fig. 7. It follows that of f_q, during the nucleation period, and that of ρ_{Dm}, during the period of growth. The latter gives a power-law segment of slope 0.63. The effect of Π_c is indirect, in that smaller values of Π_c promote larger values of S_g due to an increase in both f_{qf} and ρ_D. The difference between equilibrium and actual curves depends on the value of Π_1, increasing as the latter increases, but remaining constant following the end of nucleation. Fig. 8 shows the effects of Π_1 and Π_c on the critical gas saturation S_{gc}. In our work, the latter pertains to the formation of a sample-spanning cluster, in the absence of viscous or gravity effects. Thus, Fig. 8 actually reflects the variation of f_{qf}. Fig. 8 shows that S_{gc} can be considered a power-law both of Π_1 and of Π_c with exponents that vary between 0.16 and 0.25 with respect to Π_1 and between -0.33 and -0.22, with respect to Π_c, respectively. The trends are consistent with the experimental evidence (Scherpenisse et al., 1994; Bora et al., 2000). In Fig. 8 we allowed S_{gc} to take values that may be larger than what is required for the validity of our model. This was done only for the shake of parametric sensitivity.

b. Constant Rate of Liquid Withdrawal

Except for the evolution of pressure with time, similar results are obtained for the case of constant rate of liquid withdrawal. The effect of the parameters is also very similar to the constant pressure decline rate, subject to the change $\Pi_1 \rightarrow \Pi_4/\Pi_3$ and to the rescaling of time by Π_3. Thus, we anticipate a scaling of the form: $f_{qf} \sim \Pi_4^{\frac{3}{2}}$ at small Π_4, and $f_{qf} \sim \Pi_4$ at larger Π_4; and of the form: $f_{qf} \sim \Pi_c^{-2}$ at large Π_c, and $f_{qf} \sim \Pi_c^{-1.3}$ at smaller Π_4. The critical gas saturation has the analogous scaling: $S_{gc} \sim \Pi_4^{0.25}$ at small Π_4, and $S_{gc} \sim \Pi_4^{0.16}$ at larger Π_4; and $S_{gc} \sim \Pi_c^{-0.22}$ at large Π_c, and $S_{gc} \sim \Pi_c^{-0.33}$ at smaller Π_4. The discussion and interpretation of the findings is similar to the case of constant pressure decline rate and will not elaborated further. Additional figures and discussion are presented in Tsimpanogiannis (2002).

What is different in the case of constant rate of liquid withdrawal, is the evolution of pressure with time (Fig. 9). In the calculations, shown in Fig. 9 we used a Rayleigh size distribution, Π_2 and Π_3 were kept constant to the values 6.84×10^5 and 1.5×10^{-2}, respectively, while Π_4 varied over several orders of magnitude (from 10^{-12} to 10^{-6}). During the nucleation period, the pressure declines almost linearly with time, $P_{Dl} \approx 1 - \frac{t_D}{\Pi_3}$, following equation (32). This decrease slows down as nucleation sets in, and when the maximum supersaturation is approached, the pressure reaches a local minimum. Following this minimum, the pressure increases, reaches a maximum and subsequently decreases, roughly paralleling the equilibrium curve. The pressure minimum decreases as Π_4 increases (Fig. 9), the dependence being roughly the same as that of s_{Dm}, namely weak at small Π_4 and stronger at larger Π_4 (where the 1/4 power law may be applicable).

The non-equilibrium behavior reflects the competition between mass transfer and solute availability and can be explained as follows. The ideal gas law requires $P_g V_g = n R_g T$. The rate of change, dn/dt, of the moles in the gas phase is dictated by the mass transfer rate. At the end of the nucleation period, near s_{Dm}, this rate is the highest. Now, if the rate by which the gas volume expands, dV_g/dt (which is almost equal to Q), is not sufficiently large, the increase in volume due to mass transfer cannot be compensated, thus the pressure, P_g, must increase. An increasing pressure leads to a successively decreasing supersaturation (since C_i increases), thus to a continuous decrease of the mass transfer rate. Eventually, this decrease becomes sufficiently large for the volume expansion rate to balance mass transfer. Then, the pressure goes through a maximum, following which it begins to decline.

In the above, we used the cavity-based nucleation model. We must stress that qualitatively similar results were obtained for the model based on rate-dependent nucleation. These will not be shown. In a subsequent section, the numerical solutions obtained will be compared against available experimental results. However, before doing so it is beneficial to provide an interpretation of the main findings, using a simpler model.

IV. INTERPRETATION USING A SIMPLER MODEL

To interpret the results obtained we consider a simpler model that captures the essential features of the problem. Consider, first, the nucleation period.

A. Nucleation

a. Constant Pressure Decline Rate

To approximately describe the nucleation period, we simplify as follows the equations for the gas phase growth and the supersaturation

$$\frac{\partial \rho_D^3}{\partial t_D} \approx \Pi_2 s \rho_D \tag{51}$$

and

$$\frac{ds}{dt_D} \approx 1 - s \int_0^{\phi_q(s)} \rho_D d\phi_q \tag{52}$$

respectively. These are subject to the initial conditions

$$s(0) = 0 \quad \text{and} \quad \rho_D(\tau,\tau) = \frac{\Pi_1^{\frac{1}{2}}}{s_D(\tau)} \tag{53}$$

At early times and for small Π_1, the approximate solution of (51)-(53) is

$$s \approx t_D \quad \text{and} \quad \rho_D \approx \left[\frac{\Pi_1 \Pi_c^2}{s^2(\tau)} + \frac{\Pi_2[s^2 - s(\tau)^2]}{3}\right]^{\frac{1}{2}} \tag{54}$$

The dimensionless supersaturation is equal to the dimensionless time and the mean cluster size becomes eventually a power-law of time with exponent 1. These results are consistent with the numerical results during the nucleation period (Figs. 5 and 6).

We will use (52) to approximate the approach to the maximum supersaturation. The latter is reached when $\frac{ds}{dt_D} = 0$, namely when

$$s \int_0^{\phi_q} \rho_D d\phi_q \approx 1 \tag{55}$$

From (54) we approximately read, $\rho_D \approx \left(\frac{\Pi_2}{3}\right)^{\frac{1}{2}} s(t_D)$. Then, using the definition of ϕ_q leads to an algebraic equation for the rescaled maximum supersaturation, s_{Dm}. For example, for the case of Rayleigh distribution we have the equation

$$\frac{\pi}{4s_{Dm}^2} - 2\ln s_{Dm} \approx \ln\Lambda - \frac{1}{2}\ln 3 - \frac{3}{2}\ln\Delta \tag{56}$$

where we introduced the combination of variables

$$\Delta \equiv \Pi_1 \Pi_c^{-\frac{4}{3}} \Pi_2^{-\frac{1}{3}} \tag{57}$$

and for the case of constant pressure decline rate, $\Lambda \equiv 1$. Likewise for the case of a stretched exponential, and of a log-normal distribution, we have

$$\sigma^{-1} s_{Dm}^{-n} - 2\ln s_{Dm} \approx \ln\Lambda - \frac{1}{2}\ln 3 - \frac{3}{2}\ln\Delta \tag{58}$$

$$s_{Dm}^2 \operatorname{erfc}\left(\frac{\ln\frac{1}{s_{Dm}}}{\sqrt{2}\sigma}\right) \approx 2\sqrt{3}\Delta^{\frac{3}{2}}\Lambda^{-1} \tag{59}$$

where, again, for the constant pressure decline rate, $\Lambda = 1$. Equations (56)-(59) represent key findings of this chapter. First, they suggest that the dependence of the maximum supersaturation on the various parameters, other than the thermodynamic ones, enters only through Δ. The solution of (56) for the Rayleigh distribution is plotted in Fig. 10, as a function of Δ. We see that s_{Dm} varies weakly, in the range $0.1 - 1$, as Δ varies over several orders of magnitude (between 10^{-10} and 10^{3}). For small Δ, the maximum supersaturation is practically constant. As Δ takes larger values, s_{Dm} increases weakly and eventually more strongly, as Δ approaches the order of one (compare also with Fig. 6). Also shown in the logarithmic coordinates of Fig. 10 is a line with slope 1/4, corresponding to the 1/4 power law postulated by Scherpenisse et al. (1994) to describe several experimental data. Although the power law does not capture the overall behavior, it can approximate the results in a certain window of Δ. Plotted in the same figure are also the results of the numerical solution of the full problem for a number of different parameter values. The agreement between the numerical results and the simple analytical model is remarkable and demonstrates the validity of the simple equation (56). For the stretched exponential nucleation model, the variation is much stronger in the logarithmic plot. The solution of (56), (58) and (59) corresponding to different distributions was investigated in detail in Tsimpanogiannis (2002). As the tail of the cavity size distribution becomes longer (which occurs for smaller values of $n > 0$ and/or for larger σ) the dependence of s_{Dm} on Δ becomes stronger. In addition, the region where a power-law scaling with exponent $\approx 1/4$ tentatively fits the results, increases and also corresponds to a range with smaller values of Δ.

Equations (56)-(59) can be used to approximate the final nucleation fraction, ϕ_{qf}, and the time (or pressure) at the end of nucleation. For all cases we have

$$\phi_{qf} \approx s_{Dm}^{-2} \Pi_c^{-2} \left(\frac{\Pi_2}{3}\right)^{-\frac{1}{2}} \Lambda^{-1} \tag{60}$$

thus, the final nucleation fraction reads

$$f_{qf} \approx s_{Dm}^{-2} \Pi_1^{\frac{3}{2}} \Pi_c^{-2} \left(\frac{\Pi_2}{3}\right)^{-\frac{1}{2}} \Lambda^{-1} \tag{61}$$

This equation represents another important result of this chapter and leeds to the following conclusions:

(a) In the region where s_{Dm} varies weakly with Δ (at small Δ) the final nucleation fraction varies as a power law of Π_1, with slope equal to 3/2. This is consistent with the anticipated increase in the nucleation fraction as the rate of pressure decline increases. The equation suggests a power-law dependence on the capillary properties of the cavity. One should interpret this carefully, however, since information on the cavity properties is included in all three parameters Π_1, Π_2 and Π_c (through r_c^* and v). For example, if we were to consider only the dependence on r_c^*, we would find the power-law scaling $f_{qf} \sim r_c^{*2}$, indicating a smaller nucleation fraction as the cavity size decreases. This is as expected.

(b) In the region where s_{Dm} may be approximated by a power-law dependence on Δ, e.g. as $s_{Dm} \sim \Delta^m$, we have the scaling

$$f_{qf} \sim \Delta^{\frac{3}{2}-2m} \tag{62}$$

Such a dependence on Δ leads to a decrease in the exponent in the power-law scaling of f_{qf} on Π_1. For example, if we take $m \approx 1/4$ (as suggested by Scherpenisse et al., 1994), we read

$$f_{qf} \sim \Pi_1 \qquad \text{and} \qquad f_{qf} \sim r_c^{*\frac{4}{3}} \tag{63}$$

A linear dependence of the rate on Π_1 was postulated in Scherpenisse et al. (1994) and McDougal and Sorbie (1999), to fit available experimental data.

(c) The time, hence the pressure, P_m, when nucleation ends can be approximated using (54). We find

$$\frac{P_b - P_m}{P_b} \approx \Pi_c s_{Dm} \tag{64}$$

thus, the supersaturation at the end of nucleation is directly related to s_{Dm}. It follows that in the region where s_{Dm} is insensitive to Δ, the pressure supersaturation varies only linearly with Π_c. A rate dependence, observed experimentally in some cases, enters only insofar as s_{Dm} varies with Δ. Assuming again a power-law variation with $m \approx 1/4$, the maximum pressure supersaturation varies as follows

$$\frac{P_b - P_m}{P_b} \sim \Pi_1^{\frac{1}{4}} \qquad \text{and} \qquad \frac{P_b - P_m}{P_b} \sim r_c^{-\frac{2}{3}} \tag{65}$$

The 1/4 power-law dependence was found to fit well experimental data (see below). It is interesting that the maximum supersaturation relative to the bulk bubble point is only weakly dependent on the rate of pressure decline, for example varying by only a factor of 2 when the pressure decline rate varies by two orders of magnitude, in the range considered.

b. Constant Rate of Liquid Withdrawal

A similar analysis applies for the case of constant liquid withdrawal. After various simplifications, the equations for the gas phase growth and the supersaturation read

$$\Pi_3 \frac{d\rho_D^3}{dt_D} \approx \Pi_2 s \rho_D \tag{66}$$

and

$$\Pi_3 \frac{ds}{dt_D} \approx 1 - \left(1 + \frac{\kappa}{\Pi_3} - \kappa\right) s \int_0^{\phi_q} \rho_D d\phi_q \tag{67}$$

respectively, where we have introduced the thermodynamic parameter $\kappa \equiv \frac{R_g T}{M_w K}$. These are subject to the initial conditions

$$s(0) = 0 \quad \text{and} \quad \rho_D(\tau, \tau) = \frac{\left(\frac{\Pi_4}{\Pi_3}\right)^{\frac{1}{2}}}{s_D(\tau)} \tag{68}$$

At early times and for small $\frac{\Pi_4}{\Pi_3}$, the solution is

$$s \approx \frac{t_D}{\Pi_3} \quad \text{and} \quad \rho_D \approx \left[\frac{\Pi_4}{\Pi_3}\frac{\Pi_c^2}{s^2(\tau)} + \frac{\Pi_2\left[s^2 - s(\tau)^2\right]}{3}\right]^{\frac{1}{2}} \tag{69}$$

The early-time behavior is identical to the constant pressure decline rate, if t_D is replaced by t_D/Π_3 and Π_1 with $\frac{\Pi_4}{\Pi_3}$. We note again, that the linear scaling of the cluster size with time is consistent with the full numerical solution.

Proceeding as previously we find that the maximum rescaled supersaturation, s_{Dm}, is now given by

$$s \rho_D \phi_q \approx \frac{\Pi_3}{\kappa} \tag{70}$$

where ρ_D satisfies Eq. (69). Thus, the solution of (70) is the same as that obtained for the constant pressure decline rate problem, except that one must replace Π_1 with $\frac{\Pi_4}{\Pi_3}$, and take $\Lambda \equiv \kappa/\Pi_3$. For exactly the same reasons, the final nucleation fraction can be directly obtained from (61). The previous analysis for the constant pressure decline rate applies directly to the constant rate of liquid withdrawal, subject to the aforementioned substitution.

A comparison between the solution of the full problem (for the cases of the Rayleigh distribution and a stretched exponential with $n = 0.5$ and $\sigma = 1.0$) and of the approximate equation (70) is also shown in Fig. 10. We note an excellent agreement. The scalings obtained are also consistent with the solution of the full equations. Additional comparisons with stretched exponential cavity distribution, which have lower values of n and σ, will be presented below.

As noted above, a difference for the problem involving a constant rate of liquid withdrawal, is that the pressure reaches a local minimum. To identify it, we will proceed as follows. Integrating equation (32), we obtain

$$\Pi_3 P_{Dl} \approx Av\phi_q \rho_D^3 - t_D + \Pi_3 \tag{71}$$

where we made the same approximation for the integral, as in (67). Finding the minimum in pressure requires equating the derivative of (71) to zero. Using (69) for ρ_D, it is not difficult to show that the following equation is satisfied by s_{Dn} at that point,

$$\phi_q \left(3s_{Dn}^2 + \frac{\pi}{2}\right) \approx \frac{\Pi_3}{Av}\left(\frac{3}{\Pi_2}\right)^{\frac{3}{2}}\left(\frac{1}{\Pi_c}\right)^2 \tag{72}$$

where we used a Rayleigh distribution. For the stretched exponential case we have,

$$\phi_q \left(3s_{Dn}^2 + \frac{ns_{Dn}^{2-n}}{\sigma}\right) \approx \frac{\Pi_3}{Av}\left(\frac{3}{\Pi_2}\right)^{\frac{3}{2}}\left(\frac{1}{\Pi_c}\right)^2 \tag{73}$$

Based on these equations, one can show that the pressure reaches its local minimum before the supersaturation reaches its maximum, suggesting that nucleation continues slightly after the minimum in pressure, albeit for a very brief period of time. We can solve the above to determine the pressure minimum. For the Rayleigh distribution, we approximately find

$$\frac{P_b - P_n}{P_b} \approx \Pi_c s_{Dn} \left(\frac{2s_{Dn}^2 + \frac{\pi}{2}}{3s_{Dn}^2 + \frac{\pi}{2}} \right) \tag{74}$$

and for the stretched exponential,

$$\frac{P_b - P_n}{P_b} \approx \Pi_c s_{Dn} \left(\frac{2\sigma s_{Dn}^n + n}{3\sigma s_{Dn}^n + n} \right) \tag{75}$$

Given that s_{Dn} is generally of the order of 0.1, equations (74) and (75) are very similar to those for the maximum supersaturation in the constant-pressure decline rate case (equation (64)). Furthermore, because of the closeness of s_{Dn} to s_{Dm}, we may use the sensitivity analysis we conducted before to assess the dependence of $\frac{P_b - P_n}{P_b}$ to the various parameters. Thus, in the region where s_{Dm} is insensitive to Δ, the supersaturation $\frac{P_b - P_n}{P_b}$ varies linearly with Π_c. When s_{Dm} is more sensitive, with an assumed power-law variation with an exponent 1/4, the supersaturation at the minimum pressure varies roughly as

$$\frac{P_b - P_m}{P_b} \sim \left(\frac{\Pi_4}{\Pi_3} \right)^{\frac{1}{4}} \Pi_c^{\frac{2}{3}} \Pi_2^{-\frac{1}{12}} \tag{76}$$

Such a dependence can be used to guide the matching of the experimental data, as discussed below.

c. The Rate-Dependent Nucleation Model

We close this section by applying a similar analysis, but now for the rate-dependent nucleation model. We recall the rescaled expression

$$\frac{d\phi_q}{dt_D} = h_1^* \exp\left(-\frac{h_2}{s^2} \right) \tag{77}$$

where $h_1^* = h_1 \Pi_1^{-\frac{3}{2}}$. We proceed as before to evaluate the time when the maximum supersaturation is reached. For this, we first use the relation $s \approx t_D$, to obtain

$$\frac{d\phi_q}{ds} \approx h_1^* \exp\left(-\frac{h_2}{s^2} \right) \tag{78}$$

the solution of which is readily found

$$\phi_q = h_1^* \left[s\exp\left(-\frac{h_2}{s^2}\right) - \sqrt{\pi h_2}\mathrm{erfc}\left(\frac{\sqrt{h_2}}{s}\right)\right] \tag{79}$$

The maximum supersaturation occurs when the right-hand-side of (52) vanishes, which in this model approximately occurs when the following equation is satisfied

$$s_{Dm}^{*3}\exp\left(-\frac{1}{s_{Dm}^{*2}}\right) - s_{Dm}^{*2}\sqrt{\pi}\mathrm{erfc}\left(\frac{1}{s_{Dm}^{*}}\right) = \Delta_h^{\frac{3}{2}}\Lambda^{-1} \tag{80}$$

Here, we defined the reduced supersaturation $s_D^* = s/\sqrt{h_2}$ and the dimensionless parameter

$$\Delta_h = \Pi_1 h_1^{-\frac{2}{3}} h_2^{-1}\Pi_2^{-\frac{1}{3}} \quad \left(= \Pi_1^{\frac{5}{3}}\zeta^{-\frac{2}{3}} h_2^{-1}\Pi_2^{-\frac{1}{3}} \quad \text{or} \quad = \frac{\Pi_4}{\Pi_3}^{\frac{5}{3}}\zeta^{-\frac{2}{3}} h_2^{-1}\Pi_2^{-\frac{1}{3}}\right) \tag{81}$$

For relatively small s_{Dm}^*, the solution of the above reads

$$\frac{1}{s_{Dm}^{*2}} - 5\ln s_{Dm}^* \approx \ln\Lambda - \frac{1}{2}\ln 3 - \ln 2 - \frac{3}{2}\ln\Delta_h \tag{82}$$

A plot of the solution of (80) is shown in Fig. 11. We note features very similar to the cavity nucleation model, namely a region of weak sensitivity at small Δ_h and of stronger sensitivity at higher Δ_h. The rescaled supersaturation for the rate-dependent nucleation model is slightly higher in the region of small Δ_h, but its rate of increase at higher Δ_h is weaker than for the cavity model. Given the dependence of Δ_h on rate, the dependence of the maximum supersaturation could, at first, be considered stronger. For example, for s_{Dm}^* to vary as a power-law of the rate with exponent m, it suffices for it to follow a power law with respect to Δ_h with exponent $3m/5$. Interestingly, however, this higher sensitivity is counterbalanced by the lower sensitivity to Δ_h at higher values of Δ_h, compared to the cavity model. For example, if we were to demand $m = 1/4$, then we should consider a range of Δ_h in Fig. 11 where the exponent is of the order of 3/20. As shown in the Figure, this roughly corresponds to the same range as that of Δ, for the cavity model (Fig. 10).

The nucleation fraction at the time of the maximum supersaturation can be estimated as before. We find

$$f_{qf} = s_{Dm}^{*-2} h_2^{-1}\left(\frac{\Pi_2}{3}\right)^{-\frac{1}{2}}\Pi_1^{\frac{3}{2}}\Lambda^{-1} \tag{83}$$

As expected, the nucleation rate increases with a decreasing h_2, namely with smaller values of the interfacial tension γ and the nucleation parameter f. The combination $h_1^{\frac{1}{2}} h_2^{\frac{3}{4}}$ plays here the role of Π_c. For the same reasons as before, the pressure at the end of nucleation, which is also approximately the minimum pressure, is given by

$$\frac{P_b - P_m}{P_b} \approx \sqrt{h_2 s^*_{Dm}} \tag{84}$$

In matching experimental data using this model, we would need to infer two parameters, the rate constant K_{het} and the heterogeneous parameter f. This is discussed below.

Working likewise for the case of constant liquid withdrawal rate we find that the previous equations are valid if we replace Π_1 with $\frac{\Pi_4}{\Pi_3}$, and take $\Lambda \equiv \kappa/\Pi_3$.

B. Gas cluster growth

The modeling of the growth regime, where nucleation has terminated, can also be simplified if we consider only one class of clusters. For the case of constant pressure decline rate we approximate

$$\frac{dC_{D\infty}}{dt_D} \approx -(C_{D\infty} - 1 + t_D)z - C_{D\infty}\Pi_3 \tag{85}$$

and

$$(1 - t_D)\frac{dz^{D_f}}{dt_D} = k_1^{-1}(C_{D\infty} - 1 + t_D)z + z^{D_f} \tag{86}$$

where, we introduced the variable

$$z \equiv \phi_{qf}\rho_D \tag{87}$$

and the parameter

$$k_1 = \frac{\phi_{qf}^{1-D_f}}{\Pi_2} \tag{88}$$

The final value of the rescaled nucleation fraction, ϕ_{qf}, as well as the initial values for $C_{D\infty}$ and ρ_D needed for the calculations, are obtained from the previous analysis. Likewise, for the case of constant liquid withdrawal rate, we have similar equations

$$\frac{dC_{D\infty}}{dt_D} \approx -\frac{1}{\Pi_3}(C_{D\infty} - P_{Dl})z - C_{D\infty} + C_{D\infty}\kappa k_2 \frac{dz^{D_f}}{dt_D} \tag{89}$$

and

$$\Pi_3 P_{Dl}\frac{dz^{D_f}}{dt_D} + z^{D_f}\left(\kappa k_2 \frac{dz^{D_f}}{dt_D} - 1\right) = k_2^{-1}(C_{D\infty} - P_{Dl})z \tag{90}$$

along with

$$\frac{dP_{Dl}}{dt_D} \approx \frac{1}{\Pi_3}\left(\kappa k_2 \frac{dz^{D_f}}{dt_D} - 1\right) \tag{91}$$

and where we defined

$$k_2 = \frac{\phi_{qf}^{1-D_f}}{\Pi_2} \tag{92}$$

To use the simplified growth model, we take initial values for $C_{D\infty}$, ρ_D, P_{Dl}, and ϕ_{qf} corresponding to the time the local minimum pressure is reached. Note that P_{Dl} might be known experimentally, while one can take $C_{D\infty} \approx 1$ without introducing significant error.

Comparison of the full solution with the approximate model is shown in Fig. 12. We note a good agreement. In particular, the approximate model captures well the pressure increase, following the minimum, its subsequent leveling and the gradual decline paralleling the equilibrium curve. The system in consideration has parameters corresponding to the Berea sandstone experiments of Firoozabadi et al. (1992) with $Q = 1.44\ cm^3/day$. This system will be discussed in further detail in the next section.

V. COMPARISON WITH EXPERIMENTS

a. Constant Pressure Decline Rate

The above models were subsequently checked against published experimental results. We attempted to match the following quantities and their dependence on parameters, particularly on rate: the final nucleation fraction, the maximum supersaturation, s_{Dm}, the critical gas saturation, S_{gc}, and the evolution of pressure or saturation as a function of time.

Experimental data for the maximum supersaturation, for the case of constant pressure decline rate, were reported by Moulu and Longeron (1989) and Scherpenisse et al. (1994). In these experiments, the maximum estimated value for the capillary number was approximatelly 10^{-8} which is well within the range of the validity of the model. In addition, the macroscopic capillary number, $Ca_m = Ca\frac{L}{\sqrt{k}}$, where L is the length of the core, was of the order of 10^{-3} indicating negligible viscous pressure gradients. Matching the results requires the use of a window in the s_{Dm} vs. Δ relationship, where a 1/4 power-law is approximately observed. The corresponding windows were identified in Fig. 11 both for the rate-dependent nucleation model and the cavity model. The combination Δ contains a number of geometric variables, which are not known a priori. The cavity size distribution is also unknown. We used best estimates for V_s and a range of values for the cavity size characteristics, to indicate the range of Δ where the various experimental results fall for various size distributions considered. Theory and experiments for the mixture C1/C5 in the Berea sandstone experiments by Scherpeniesse et al. (1994) match well, assuming a stretched exponential distribution with values $n = 0.215$ and $\sigma = 0.045$. In these experiments we used for r_s^* and r_c^* the suggested values by the authors. For the experiments involving the mixture C1/C3/C10 in a limestone core, reported by Moulu and Longeron (1989), the corresponding best-fit values were $n = 0.152$ and $\sigma = 0.049$, respectively. These indicate a significantly stretched (long-tailed) cavity-size distribution, with small characteristic sites (see also Table 2 for additional data regarding the experiments).

The predictions of the rate-dependent nucleation model were also tested. Here, the parameters to be estimated include f and the heterogeneous nucleation rate K_{het}, since

$$\Delta_h \sim K_{het}^{-\frac{2}{3}} f^{-1} \tag{93}$$

Matching of the experiments of Scherpenisse et al. (1994) required the following parameter values: $f = 2. \times 10^{-4}$ and $K_{het} = 0.02119\ (cm^3 s)^{-1}$ (Fig. 11). Correspondingly, for the experiments by Moulu and Longeron (1989) the following best-fit parameter values were found: $f = 3.6 \times 10^{-6}$ and $K_{het} = 6.45 \times 10^{-6}\ (cm^3 s)^{-1}$. Both these sets of values are extreme for the heterogeneous model considered.

Estimates for the final nucleation fraction for the experiments by Scherpenisse et al.

(1994) are shown in Fig. 13. The final nucleation fraction in the experiments was estimated as suggested by Scherpenisse et al. (1994). Then, f_{qf} was calculated using equation (11). As anticipated, f_{qf} is quite small, of the order of 10^{-10}-10^{-7}. The power-law scaling with exponent 1, predicted by the theory in this range, is well supported by the data. Finally, a comparison of the evolution of the gas saturation, S_g, as a function of the dimensionless pressure $P_{Dl} = P/P_b$, using the full solution for the Berea sandstone experiments of Scherpenisse et al. (1994) is presented in Fig. 14. Good agreement is observed for the early part of the curve, namely before the gas saturation starts to approach an asymptotic value. The latter stage corresponds to flow of gas out of the sample, which the present theory does not take into account. The dependence of S_{gc} on f_{qf} was tested against the data of Scherpenisse et al. (1994). Shown in Fig. 15 are predictions for both the critical gas saturation as a function of Δ from the simpler model and from the full solution. Although there is a slight tendency for the theory to underestimate the data, we note a quite good agreement. In particular, the power-law scaling with exponent 0.16, predicted by the theory, is well supported by the data.

One of the most interesting effects is that of the pressure decline rate. Quantifying its effect is significant, as one can then control the extent of nucleation, the value of the critical gas saturation, and the time of the onset of bulk gas flow, which for practical purposes signifies the end of the liquid production. An important result of this work has been the derivation of simple algebraic equations (for example (56)-(59), (80)) that relate the critical supersaturation to a combination of dimensionless parameters, which involve the rate, given the particular nucleation characteristics of the system. The model developed shows that the effect on the nucleation fraction, hence on the critical gas saturation, is a power law, with an exponent which is equal 3/2 at low rates, decreases to 1 at higher rates, and ultimately becomes zero at very high rates. The critical supersaturation was predicted to be independent of the rate at small rates and to depend as a weak power law (with an exponent equal to 1/4 or larger) at higher rates. It can be also readily shown that for very large depletion rates, the maximum supersaturation is insensitive to the particular size distribution, scaling as a power law with exponent 3/4. In that limit, the final nucleation fraction is also independent of the rate of depletion.

It interesting that for the experimentally reported rate effect to be matched requires a considerably stretched (long-tailed) cavity size distribution and small cavity sizes. Equivalently, if the heterogeneous, rate-dependent nucleation model is used, matching the experiments requires very small values of the wetability parameter and of the nucleation rate constant. A long-tailed cavity size distribution leads to a larger nucleation fraction, provided that the decline rate is not extremely large. Then, more cavity sizes are nucleated at the early stages of the process, as (large) sizes are available for activation even under very small supersaturations. It is possible that this is due to the nucleation of large cavities, exposed at the openings of the core for which a very small supersaturation is needed. Because of the existence of nucleated bubbles early during the process, the maximum supersaturation obtained for a long-tailed distribution is smaller than for a narrow distribution (such as a Rayleigh), when the rates are not too large. Because as the rate of depletion becomes very large, the supersaturation becomes eventually the same for all distributions, there is a large window in the rate dependence, where the behavior is like the experimentally reported 1/4 power law. A similar explanation holds for the case of the rate-dependent heterogeneous nucleation model, where a very small value of the wetability parameter favors the nucleation of bubbles even at small supersaturation.

b. Constant Rate of Liquid Withdrawal

The model was also compared against experimental results for the case of constant rate of liquid withdrawal. We matched the local minimum pressure and the related the maximum supersaturation, P_n and s_{Dn} respectively, the critical gas saturation, S_{gc}, and the evolution of pressure as a function of time.

Consider, first, matching the minimum pressure and its rate-dependence. Using the simpler model, this can be done by fitting parameters r_c^*, r_s^* (if not available) and the cavity size distribution. We first performed this matching for the mixture C1/C10 in the Berea sandstone experiments of Firoozabadi et al. (1992). In these experiments, the estimated values for Ca and Ca_m were 10^{-9} and 10^{-3}, respectively, well within the assumptions of our theory.

Best-fit values $r_s^* = 1.0 \times 10^{-2} cm$, $r_c^* = 2.0 \times 10^{-3} cm$, $n = 0.1014$ and $\sigma = 0.0339$ (for a stretched exponential cavity distribution) were found for a good match. The calculated minimum pressures, P_n, using the full solution and the above parameters are very close to the experimental, as shown in Table 3. Comparison of the evolution of the system pressure as a function of the dimensionless time, $t_n = t_D$, using the full solution, and the Berea experiments of Firoozabadi et al. (1992) is presented in Fig. 16. A good agreement is also observed.

A comparison with the chalk experiments of Firoozabadi et al. (1992), for two different reported volumetric flow rates, was also undertaken. Again, $Ca \simeq 10^{-8}$ and $Ca_m \simeq 10^{-2}$ are within the assumptions of our model. Here, the effect of rate is rather weak, and a Rayleigh distribution was found to be adequate. Based on $r_s^* = 1.0 \times 10^{-4} cm$, a value of $r_c^* = 1.98 \times 10^{-6} cm$ is needed to match the minimum pressure supersaturation. Figure 17 shows a comparison of the evolution of the liquid pressure as a function of the dimensionless time, $t_n = t_D$, using the full solution. Again good agreement is observed for the pressure evolution, while an excellent match is achieved for the minimum pressures (see Table 3). In both Figs. 16 and 17, the predictions from the simpler model closely follow the full solution.

Finally, the theory was tested against the sand-pack experiments of Kumar et al. (2000). In contrast to the previous, the estimated values for Ca and Ca_m are considerably higher (equal to about 10^{-4} and 10, respectively). This sugests that our model may not adequately capture the physical processes particularly at later times Using the best-fit values of $r_s^* = 1.0 \times 10^{-2} cm$ and $r_c^* = 1.0 \times 10^{-3} cm$, and a stretched exponential cavity distribution, with parameters $n = 0.3466$ and $\sigma = 0.0134$, provides for good matching. With these parameters, the ability of the full problem to predict the minimum pressure is good, as can be seen in Table 4. The evolution of the pressure as a function of dimensionless time, t_n, and for different flow rates is shown in Fig. 18, based on the simpler growth model. With the exception of the high rate curve, which is not perfectly matched, agreement is good, considering the scatter of the experimental data.

A feature that is not well matched in either of these experiments, however, are the values of S_{gc}. The predicted values, using the full solution, are shown in Tables 3-4 respectively. The theory systematically over-predicts the experimental data. This disagreement may be due to the different definition of S_{gc}. In this chapter, the critical gas saturation is defined as the gas saturation, when a sample spanning cluster is formed, in the absence of gravity or viscous gradients in the system (which will result in increasing S_{gc}). In the experiments, however, bubbles can be mobilized due to the presence of gradients before the onset of a sample-spanning cluster. The disagreement is more profound for the cases of the Berea sandstone or the sand-pack, than it is for the chalk. It is also very pronounced in the Kumar et al. (2000) experiments, as explained above. This is consistent, since chalk is a tighter porous medium, the capillary and Bond numbers are smaller and the earlier mobilization of the gas bubbles is less likely.

For completeness, we also estimated the wetability parameter, f, and the heterogeneous nucleation rate, K_{het}, assuming a rate-dependent nucleation model. We found the following: for the Berea sandstone experiments (Firoozabadi et al., 1992), $f = 3.305 \times 10^{-5}$ and $K_{het} = 7.219 \times 10^{-7}$ $(cm^3s)^{-1}$; for the chalk experiments (Firoozabadi et al., 1992), $f = 1.240 \times 10^{-5}$ and $K_{het} = 2.299 \times 10^{4}$ $(cm^3s)^{-1}$; and for the sand-pack experiments (Kumar et al., 2000), $f = 1.790 \times 10^{-5}$ and $K_{het} = 1.683 \times 10^{-4}$ $(cm^3s)^{-1}$.

As in the case of constant pressure decline rate and with the exception of the experiments in chalk, matching of the experimental results with the theory required the use of either stretched, long-tailed cavity size distributions, or very small wetability parameters in the rate-dependent nucleation model. Such distributions offer the ability to nucleate bubbles even at small supersaturations, and can provide the reported experimental dependence on rate.

VI. CONCLUSIONS

In this chapter we developed an effective continuum model to describe the nucleation and subsequent growth of a gas phase from a supersaturated, slightly compressible binary liquid in a porous medium, driven by solute diffusion. The evolution of the gas results either from the reduction of the system pressure at a constant rate, or from the withdrawal of the liquid at constant rate. The model addresses two stages before the onset of bulk gas flow, nucleation and gas phase growth. We assume negligible gradients due to gravity or viscous forces, thus the critical gas saturation, which signals the onset of bulk gas flow, is only a function of the nucleation fraction.

We showed that the important quantities characterizing the process, such as the fraction of pores that host activated sites, the deviation from thermodynamic equilibrium, the maximum supersaturation in the system and the critical gas saturation depend crucially on the nucleation characteristics of the medium. We used a heterogeneous nucleation models primarily in the form of pre-existing gas, trapped in hydrophobic cavities, but also in terms of a rate-dependent nucleation, to investigate in detail the nucleation behavior. Using scaling analysis and a simpler analytical model we showed that the relevant quantities during nucleation can be expressed in terms of a simple combination of dimensionless parameters, which include rate effects, for either type of nucleation model.

The theory predicts that the maximum supersaturation in the system is a weakly increasing function of rate, which in the region of typical experimental parameters, can be approximated as a power law with a small exponent. This function depends sensitively on the probability density function of the nucleation cavity sizes. It also predicts that the final nucleation fraction, thus the critical gas saturation, is a power law of the decline rate (or the withdrawal rate). The theoretical exponents were shown to fit the experimental data provided that a stretched exponential distribution for the cavity size distribution is used.

References

[1] Andarcia, L., Kamp, A.M., and P. Vaca, "Heavy Oil Solution Gas Drive in the Venezuelan Orinoco Belt: Laboratory Experiments and Field Simulation" paper *SPE 69715*, presented at the SPE International Thermal Operations and Heavy Oil Symposium, Margarita Island, Venezuela (12-14 March 2001).

[2] Arora, P., and A.R. Kovscek, "Mechanistic Modeling of Solution-Gas Drive in Viscous Oils," paper *SPE 69717*, presented at the SPE International Thermal Operations and Heavy Oil Symposium, Margarita Island, Venezuela (12-14 March 2001).

[3] Bora, R., Maini, B.B., and A. Chakma, "Flow Visualization Studies of Solution Gas Drive Process in Heavy Oil Reservoirs Using a Glass Micromodel," *SPE Res. Eval. Eng.*, **3**, 224 (2000).

[4] Dominguez, A., Bories, S., and M. Prat, "Gas Cluster Growth by Solute Diffusion in Porous Media. Experiments and Automaton Simulation on Pore Network," *Int. J. Multiphase Flow*, **26**, 1951 (2000).

[5] Doughty, C. and K. Pruess, "A Similarity Solution for Two-Phase Fluid and Heat Flow Near High-Level Nuclear Waste Packages Emplaced in Porous Media," *Int. J. Heat Mass Transfer*, **33**, 1205 (1990).

[6] Du, C., and Y.C. Yortsos, "A Numerical Study of the Critical Gas Saturation in a Porous Medium," *Transport in Porous Media*, **35**, 205 (1999).

[7] Egermann, P., and O. Vizika, "Critical Gas Saturation and Relative Permeability During Depressurization in the Far Field and the Near-Wellbore Region," paper *63149*, presented at the SPE Annual Technical Conference and Exhibition, Dallas, TX, 1-4 October 2000.

[8] El Yousfi, A., Zarcone, C., Bories, S. and R. Lenormand, "Mècanismes de Formation d'une Phase Gazeuse par détente d'un liquide en Milieu Poreux," *C.R. Acad. Sci. Paris, Série II,* **313**, 1093 (1991).

[9] El Yousfi, A., Zarcone, C., Bories, S. and R. Lenormand, "Physical Mechanisms for Bubble Growth During Solution Gas Drive," paper *SPE 38921* presented at the SPE Annual Technical Conference and Exhibition, San Antonio, TX (5-8 October 1997).

[10] Feder, J., *Fractals,* Plenum, New York (1988).

[11] Firoozabadi, A., and A. Aronson, "Visualization and Measurement of Gas Evolution and Flow of Heavy and Light Oil in Porous Media," *SPE Res. Eval. Eng.*, **2**, 550 (1999).

[12] Firoozabadi, A., and D. Kashchiev, "Pressure and Volume Evolution During Gas Phase Formation in Solution Gas Drive Processes," *SPE Journal*, **1**, 219 (1997).

[13] Firoozabadi, A, Ottesen, B, and M. Mikkelsen, "Measurements of Supersaturation and Critical Gas Saturation," *SPE Form. Eval.*, 337 (December 1992).

[14] Jones, S.F., Evans, G.M., and K.P. Galvin, "Bubble Nucleation from Gas Cavities - A Review," *Adv. Colloid Interface Sci.*, **80**, 27 (1999).

[15] Hawes, R.I., Dawe, R.A., and R.N. Evans, "The Release of Solution Gas from Waterflood Residual Oil," *SPE Journal*, **2**, 379 (1997).

[16] Ho, C.K., and K.S. Udell, "Mass Transfer Limited Drying of Porous Media Containing an Immobile Binary Liquid Mixture," *Int. J. Heat Mass Transfer*, **38**, 339 (1995).

[17] Kamp, A.M., Joseph, D.D., and R. Bai, "A New Modeling Approach for Heavy Oil Flow in Porous Media," paper *SPE 69720*, presented at the SPE International Thermal Operations and Heavy Oil Symposium, Margarita Island, Venezuela (12-14 March 2001a).

[18] Kamp, A.M., Heny, C., Andarcia, L., Lago, M. and A. Rodriguez, "Experimental Investigation of Foamy Oil Solution Gas Drive," paper *SPE 69725*, presented at the SPE International Thermal Operations and Heavy Oil Symposium, Margarita Island, Venezuela (12-14 March 2001b).

[19] Kumar, R., Pooladi-Darvish, M., and T. Okazawa, "An Investigation Into Enhanced Recovery Under Solution Gas Drive in Heavy Oil Reservoirs," paper *SPE 59336*, presented at the SPE/DOE Improved Oil Recovery Symposium, Tulsa, OK (3-5 April 2000).

[20] Laaksonen, A., Talanquer, V., and D.W. Oxtoby, "Nucleation: Measurements, Theory, and Applications," *Annu. Rev. Phys. Chem.*, **46**, 489 (1995).

[21] Li, X., and Y.C. Yortsos, "Visualization and Simulation of Bubble Growth in Pore Networks," *AIChE J.*, **41**, 214 (1995a).

[22] Li, X., and Y.C. Yortsos, "Theory of Multiple Bubble Growth in Porous Media by Solute Diffusion," *Chem. Eng. Sci.*, **50**, 1247 (1995b).

[23] Mackay, E.J., Henderson, G.D., Tehrani, D.H., and A. Danesh, "The Importance of the Interfacial Tension on Fluid Distribution During Depressurization," *SPE Res. Eva. Eng.*, **1**, 408 (1998).

[24] McDougall, S.R., and K.S. Sorbie, "Estimation of Critical Gas Saturation During Pressure Depletion in Virgin and Water-flooded Reservoirs," *Petroleum Geoscience*, **5**, 229 (1999).

[25] Maini, B., "Foamy Oil Flow in Primary Production of Heavy Oil Under Solution Gas Drive," paper *SPE 56541*, presented at the SPE Annual Technical Conference and Exhibition, Houston, TX (3-6 October 1999).

[26] Maini, B., "Foamy Oil Flow in Heavy Oil Production," *J. Canadian Petroleum Technology*, **35**(6), 21 (1996).

[27] Moulu, J.C., "Solution-Gas Drive: Experiments and Simulation," *J. Pet. Sci. Eng.*, **2**, 379 (1989).

[28] Moulu, J.C., and D.L. Longeron, "Solution-Gas Drive: Experiments and Simulation," *Proc.,* Fifth European Symposium on Improved Oil Recovery, Budapest, Hungary (April 1989).

[29] Pooladi-Darvish, M., and A. Firoozabadi, "Solution-gas Drive in Heavy Oil Reservoirs," *J. Canadian Petroleum Technology*, **38**(4), 54 (1999).

[30] Prats, M., *Thermal Recovery,* SPE Monograph, Dallas, TX, 1982.

[31] Press, W.H., Teukolsky, W.T., Vettering, S.A., and B.P. Flannery, *Numerical Recipes,* 2nd ed. Cambridge University Press, (1992).

[32] Renard, G., Nauroy, J.-F., Deruyter, Ch., Moulu, J.-C., Sarda, J.-P., and J.-F. Le Romancer, "Production Froide des Huiles Visqueuses," *Oil & Gas Science and Technology - Rev. IFP*, **55**, 35 (2000).

[33] Scherpenisse, W., Wit, K., Zweers, A.E., Shoei, G., and A. van Wolfswinkel, "Predicting Gas Saturation Buildup during Depressurization of a North Sea Oil Reservoir," paper *SPE 28842*, presented at the European Petroleum Conference, London, UK (25-27 October 1994).

[34] Satik, C., and Y.C. Yortsos, "A Pore Network Study of Bubble Growth in Porous Media Driven by Heat Transfer," *ASME J. of Heat Transfer*, **118**, 155 (1996).

[35] Sheng, J.J., Maini, B.B., Hayes, R.E., and W.S. Tortike, "Critical Review of Foamy Oil Flow," *Transport in Porous Media*, **35**, 157 (1999a).

[36] Sheng, J.J., Hayes, R.E., Maini, B.B., and W.S. Tortike, "Modeling Foamy Oil Flow in Porous Media," *Transport in Porous Media*, **35**, 227 (1999b).

[37] Smith, G.E., "Fluid Flow and Sand Production in Heavy-Oil Reservoirs Under Solution-Gas Drive," *SPE Prod. Eng.*, **3**, 169 (1988).

[38] Tang, G.-Q., and A. Firoozabadi, "Gas and Liquid-Phase Relative Permeabilities for Cold Production from Heavy Oil," paper *SPE 56540* presented at the SPE Annual Technical Conference and Exhibition, Houston, TX (3-6 October 1999).

[39] Thome, J.R., *Enhanced Boiling Heat Transfer,* Hemisphere Publishing Co., New York (1990).

[40] Tsimpanogiannis, I.N. , PhD Dissertation, Univ. of Southern California, In preparation (2002).

[41] Tsimpanogiannis, I.N., and Y.C. Yortsos, "A Numerical Study of the Critical Gas Saturation in a Porous Medium in the Presence of Viscous or Gravity Gradients," In preparation (2002).

[42] Urgelli, D., Durandeau, M., Foucault, H., and J.-F. Besnier, "Investigation of Foamy Oil Effect from Laboratory experiments," paper *SPE 54083* presented at the SPE International Thermal Operations and Heavy Oil Symposium, Bakersfield, CA, 17-19 March 1999.

[43] Wang, X., and K.K. Mohanty, "Critical Condensate Saturation in Porous Media," *J. Colloid Interface Sci.*, **214**, 416 (1999).

[44] Wong, R.C.K., Guo, F., Weaver, J.S., and W.E. Barr, "Heavy Oil Flow Under Solution-Gas Drive: Pressure Depletion Tests," *J. Canadian Petroleum Technology*, **38**, 31 (1999).

[45] Yortsos, Y.C., and M. Parlar, "Phase Change in Binary Systems in Porous Media: Application to Solution Gas Drive," paper *SPE 19697*, presented at the SPE Annual Technical Conference and Exhibition, San Antonio, TX (8-11 October 1989).

Parameter	*CPDR*	*CLWR*
MW (g/mol)	18.6	16.0
D (cm^2/s)	2.40×10^{-5}	1.35×10^{-5}
γ (mN/m)	8.2	13.0
T (K)	314.6	314.6
P_b (MPa)	6.0	7.384
K ($MPa\, m^3/kg$)	8.604×10^{-3}	1.537×10^{-1}
c (MPa^{-1})	1.45×10^{-3}	2.17×10^{-3}
r_s (cm)	9.0×10^{-4}	1.0×10^{-2}
r_c (cm)	8.0×10^{-6}	2.0×10^{-3}
A^*	1.	1.
n_B	1.	1.
λ	1.	1.
a (Pa/s)	26.82	-
Q (cm^3/s)	-	1.67×10^{-5}
V_p (cm^3)	-	132.24
Π_1	5.859×10^{-6}	-
Π_2	2.327×10^{6}	1.330×10^{3}
Π_3	8.700×10^{-3}	1.603×10^{-2}
Π_4	-	1.559×10^{-6}
Π_c	3.417×10^{-2}	1.760×10^{-4}

Table 1: Characteristic values of the various parameters. *CPDR*: Constant Pressure Decline Rate; *CLWR*: Constant Liquid Withdrawal Rate

parameter	*I*	*II*	*III*	*IV*	*V*
porous medium	Berea Sandstone	St. Maxim Limestone	Berea Sandstone	Chalk	Quartz sand-pack
fluid system	C_1/C_5	$C_1/C_3/C_{10}$	C_1/C_{10}	C_1/C_{10}	$C_1/PAO-100$
Length (cm)	~ 15	5	49.04	50.495	60
Diameter (cm)	~ 5	5	3.9116	3.759	na
porosity %	23.0	29.3	22.3	40.4	38.6
permeability (m^2)	1.20×10^{-12}	2.08×10^{-13}	5.97×10^{-13}	2.66×10^{-15}	1.16×10^{-12}
pore volume (cm^3)	na	na	132.24	225.16	487.00
P_b (MPa)	6.0	2.844	7.384	7.627	3.964

Table 2: Fluid and porous medium properties for experiments reported by: *(I)* Scherpenisse et al., (1994); *(II)* Moulu and Longeron, (1989); *(III)*, *(IV)*, Firoozabadi et al., (1992); *(V)* Kumar et al. (2000). *(na)*: not available.

System	Q (cm^3/day)	P_n^{calc} (MPa)	P_n^{exp} (MPa)	S_{gc}^{calc} (%)	S_{gc}^{exp} (%)	Δ	Π_2	Π_3	Π_4	Π_c
Berea	1.44	6.99664	6.98621	10.8	1.3-2.0	0.30×10^0	$.851 \times 10^4$	0.16×10^{-1}	0.62×10^{-5}	0.70×10^{-3}
Berea	7.20	6.64871	6.60689	12.7	1.3-2.0	0.15×10^1	$.851 \times 10^4$	0.16×10^{-1}	0.31×10^{-4}	0.70×10^{-3}
Chalk	7.20	7.63703	7.62966	1.6	0.6-1.2	0.38×10^{-7}	$.683 \times 10^6$	0.15×10^{-1}	0.46×10^{-8}	0.16×10^0
Chalk	12.96	7.63326	7.62137	1.9	0.6-1.2	0.68×10^{-7}	$.683 \times 10^6$	0.15×10^{-1}	0.83×10^{-8}	0.16×10^0

Table 3: Comparison between the full solution and the experiments of Firoozabadi et al. (1992).

Q (cm^3/day)	P_n^{calc} (MPa)	P_n^{exp} (MPa)	S_{gc}^{calc} $(\%)$	S_{gc}^{exp} $(\%)$	Δ	Π_4
1.92	3.68040	3.80689	9.9	3.0	0.13×10^0	0.11×10^{-5}
8.88	3.57088	3.58621	12.7	3.4	0.61×10^0	0.52×10^{-5}
72.00	3.31097	3.31034	17.7	4.2	0.49×10^1	0.42×10^{-4}
288.00	2.95306	3.05517	22.6	7.0	0.19×10^2	0.17×10^{-3}

Table 4: Comparison between the full solution and the sand-pack experiments of Kumar et al. (2000). For $\Pi_c = 0.655 \times 10^{-3}$, $\Pi_2 = 0.395 \times 10^3$ and $\Pi_3 = 0.205 \times 10^{-1}$.

FIGURE CAPTIONS

Figure 1: Schematic of a gas cluster growth in a porous medium, driven by the decline of pressure at constant rate.

Figure 2: Micromodel snapshots indicating: **(a)** Gas bubbles confined within single pore throats/bodies; **(b)** a gas bubble spanning several pore bodies.

Figure 3: Schematic of a nucleation cavity in a host pore body.

Figure 4: The variation of the rescaled nucleation fraction, ϕ_q, as a function of the dimensionless time, t_D. **(a)** Effect of $\Pi_1 = 5.86 \times 10^{-m}$, for $\Pi_c = 3.41 \times 10^{-2}$, $\Pi_2 = 2.33 \times 10^6$ and $\Pi_3 = 8.7 \times 10^{-3}$. **(b)** Effect of $\Pi_c = 0.34 \times 10^{-m}$, for $\Pi_1 = 5.86 \times 10^{-4}$ and $\Pi_3 = 8.7 \times 10^{-3}$.

Figure 5: The variation of the mean rescaled dimensionless radius, ρ_{Dm}, as a function of the dimensionless time, t_D. Effect of $\Pi_1 = 5.86 \times 10^{-m}$, for $\Pi_c = 3.41 \times 10^{-2}$, $\Pi_2 = 2.33 \times 10^6$ and $\Pi_3 = 8.7 \times 10^{-3}$.

Figure 6: Numerical results for: **(a)** The variation of the rescaled supersaturation, s_D, as a function of the dimensionless time, t_D. Effect of $\Pi_1 = 5.86 \times 10^{-m}$, for $\Pi_c = 3.41 \times 10^{-2}$, $\Pi_2 = 2.33 \times 10^6$ and $\Pi_3 = 8.7 \times 10^{-3}$. **(b)** The effect of the dimensionless parameter Π_1 on the maximum rescaled supersaturation, s_{Dm}, for $\Pi_c = 0.34 \times 10^{-m}$. Points correspond to the full numerical solution, solid lines correspond to the simpler model.

Figure 7: The variation of the gas saturation, S_g, as a function of the dimensionless time, t_D. Effect of $\Pi_1 = 5.86 \times 10^{-m}$, for $\Pi_c = 3.41 \times 10^{-2}$, $\Pi_2 = 2.33 \times 10^6$ and $\Pi_3 = 8.7 \times 10^{-3}$.

Figure 8: The effect of the dimensionless parameter Π_1 on the critical gas saturation, S_{gc}, for $\Pi_c = 0.34 \times 10^{-m}$. Points denote the full numerical solution, solid lines correspond to the simpler model.

Figure 9: The variation of the dimensionless pressure, P_{Dl}, as a function of the dimensionless time, t_D, for the case of constant liquid withdrawal rate. Effect of $\Pi_4 = 0.4631 \times 10^{-m}$, for $\Pi_c = 1.67 \times 10^{-1}$, $\Pi_2 = 6.84 \times 10^5$ and $\Pi_3 = 1.52 \times 10^{-2}$. Shown in dashed-dotted line is the thermodynamic equilibrium curve.

Figure 10: The maximum rescaled supersaturation, s_{Dm}, as a function of Δ for the cases of constant pressure decline rate (dotted lines) and constant liquid withdrawal rate (solid lines). Comparison between the simpler model (dotted or solid lines) and the full numerical

solution (denoted by triangles for the stretched exponential cavity size distribution with $n = 0.5$ and $\sigma = 1.0$, and by squares for the Rayleigh cavity size distribution).

Figure 11: The maximum rescaled supersaturation, s^*_{Dm}, as a function of Δ_h for the simpler model (solid line). Triangles denote s^*_{Dm} values calculated using experimental data from Scherpenisse et al. (1994). Also plotted are the predictions based on the cavity model (dashed lines for the simpler model, squares denoting s_{Dm} values for the same experimnets).

Figure 12: Comparison of the full numerical results (denoted by solid lines) with the approximate model (denoted by triangles) for the case of constant liquid withdrawal rate. Shown in dashed-dotted line in the last panel is the thermodynamic equilibrium curve.

Figure 13: The final nucleation fraction, f_{qf}, as a function of Δ, for a stretched exponential ($n = 0.215$ and $\sigma = 0.045$) cavity size distribution. The solid line corresponds to the simpler model, squares denote values calculated using experimental data from Scherpenisse et al. (1994).

Figure 14: The evolution of the gas saturation as a function of the dimensionless pressure for three depletion rates for the Berea sandstone experiments of Scherpenisse et al. (1994). Points denote experimental values, solid lines correspond to the full numerical solution, the dashed-dotted line corresponds to the thermodynamic equilibrium curve.

Figure 15: The critical gas saturation, S_{gc}, as a function of Δ, for a stretched exponential ($n = 0.215$ and $\sigma = 0.045$) cavity size distributions. The solid line corresponds to the simpler model, triangles denote the full solution, squares denote experimental data (constant pressure decline rate) from Scherpenisse et al. (1994).

Figure 16: Evolution of pressure as a function of time for the Berea stone experiments of Firoozabadi et al. (1992) for two different withdrawal rates. Solid lines denote the full solution, dotted lines denote the simpler growth model, the dashed-dotted line denotes the thermodynamic equilibrium curve, symbols denote the experimental results.

Figure 17: Evolution of pressure as a function of time for the Chalk experiments of Firoozabadi et al. (1992) for two different withdrawal rates. Solid lines (both coincide) denote the full solution, dotted lines denote the simpler growth model, the dashed-dotted line denotes the thermodynamic equilibrium curve, symbols denote the experimental results.

Figure 18: Evolution of pressure as a function of time for the sand-pack experiments of

Kumar et al. (2000) for four different withdrawal rates. Solid lines denote the simpler growth model, the dashed-dotted line denotes the thermodynamic equilibrium curve, symbols denote the experimental results.

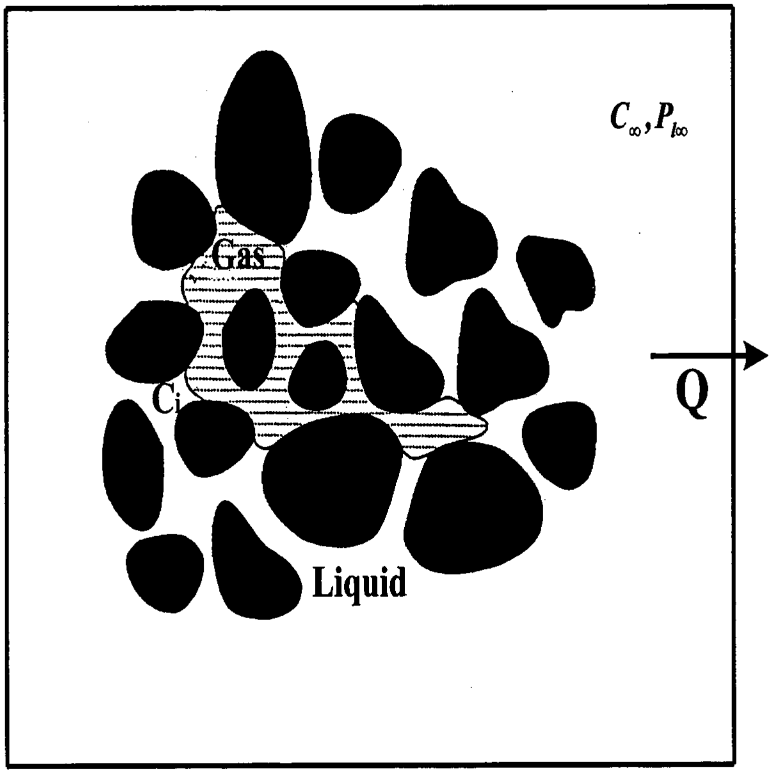

Figure 1: Schematic of a gas cluster growth in a porous medium, driven by the decline of pressure at constant rate.

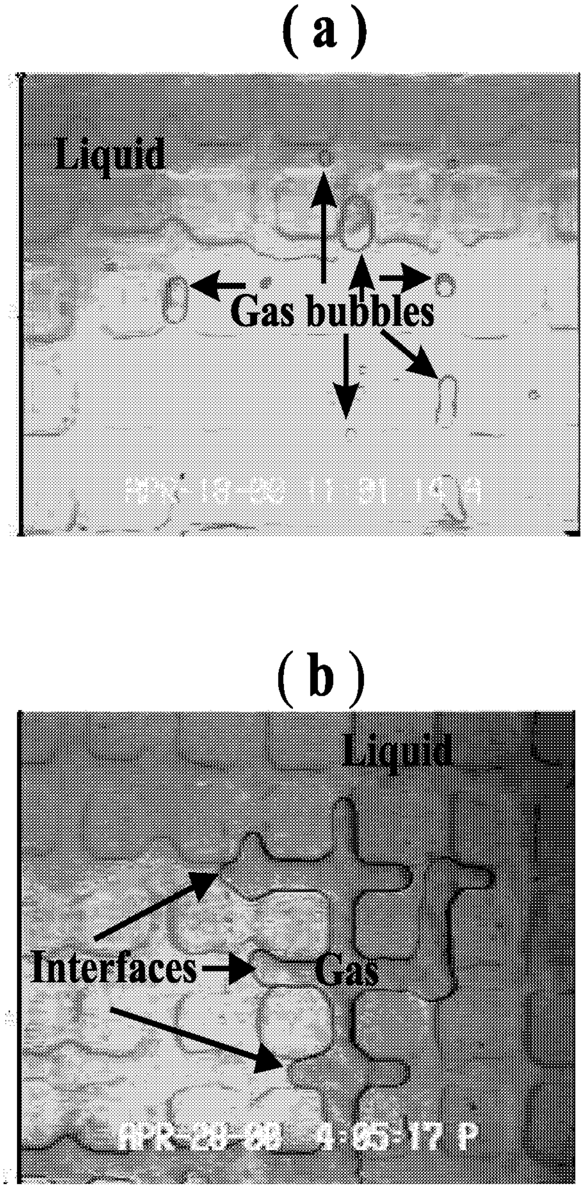

Figure 2: Micromodel snapshots indicating: **(a)** Gas bubbles confined within single pore throats/bodies; **(b)** a gas bubble spanning several pore bodies.

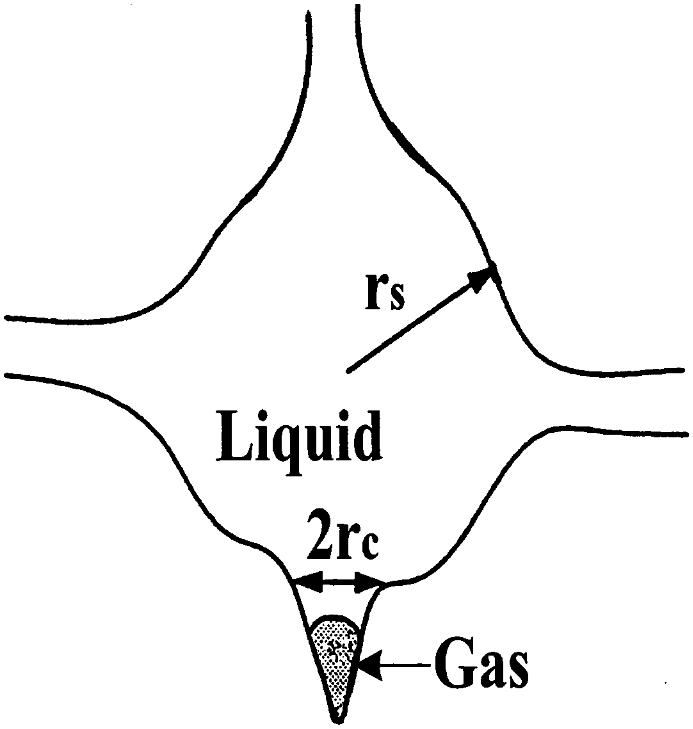

Figure 3: Schematic of a nucleation cavity in a host pore body.

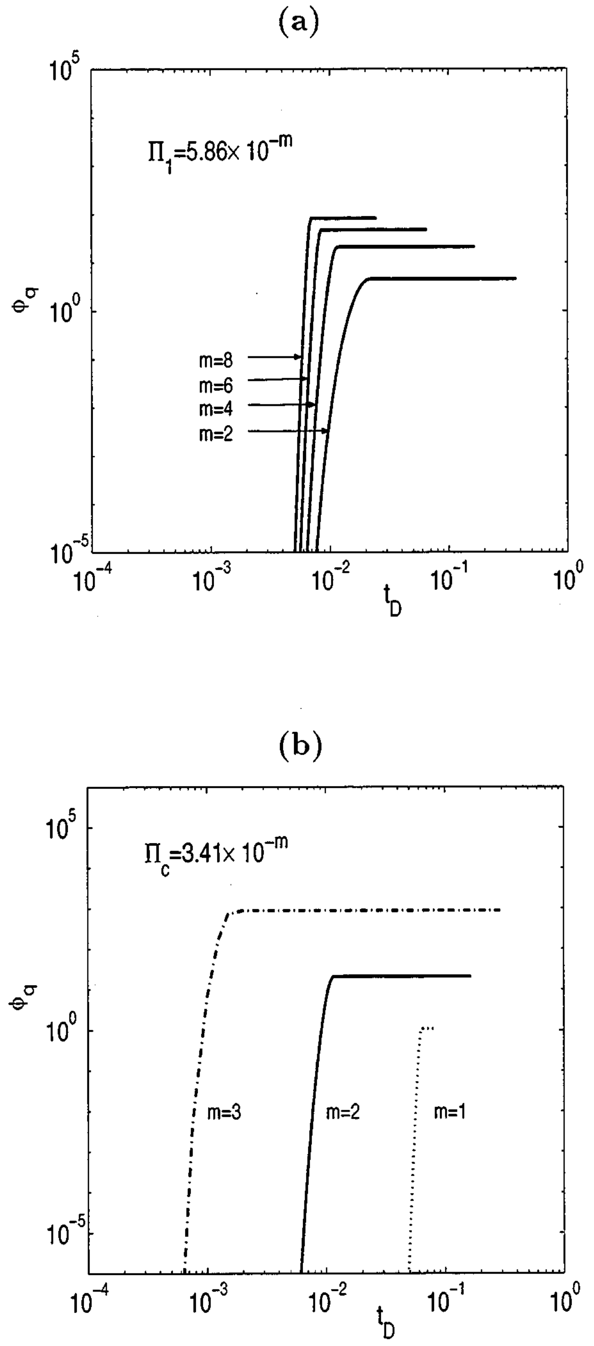

Figure 4: The variation of the rescaled nucleation fraction, ϕ_q, as a function of the dimensionless time, t_D. (**a**) Effect of $\Pi_1 = 5.86 \times 10^{-m}$, for $\Pi_c = 3.41 \times 10^{-2}$, $\Pi_2 = 2.33 \times 10^6$ and $\Pi_3 = 8.7 \times 10^{-3}$. (**b**) Effect of $\Pi_c = 0.34 \times 10^{-m}$, for $\Pi_1 = 5.86 \times 10^{-4}$ and $\Pi_3 = 8.7 \times 10^{-3}$.

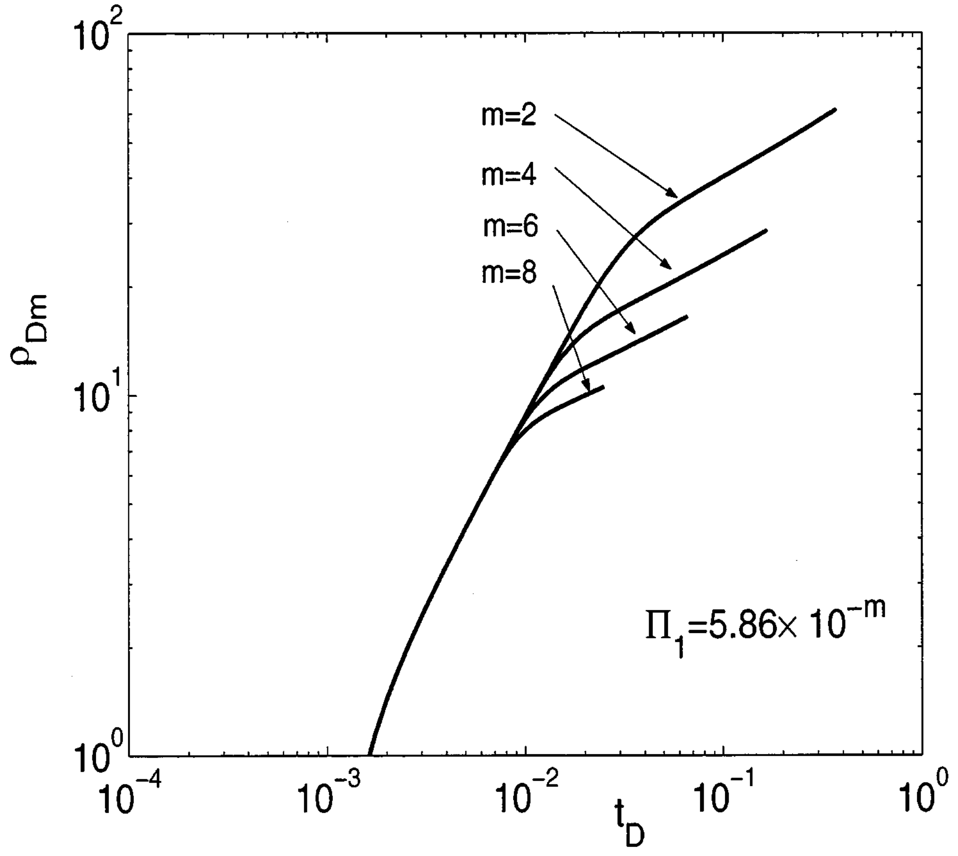

Figure 5: The variation of the mean rescaled dimensionless radius, ρ_{Dm}, as a function of the dimensionless time, t_D. Effect of $\Pi_1 = 5.86 \times 10^{-m}$, for $\Pi_c = 3.41 \times 10^{-2}$, $\Pi_2 = 2.33 \times 10^6$ and $\Pi_3 = 8.7 \times 10^{-3}$.

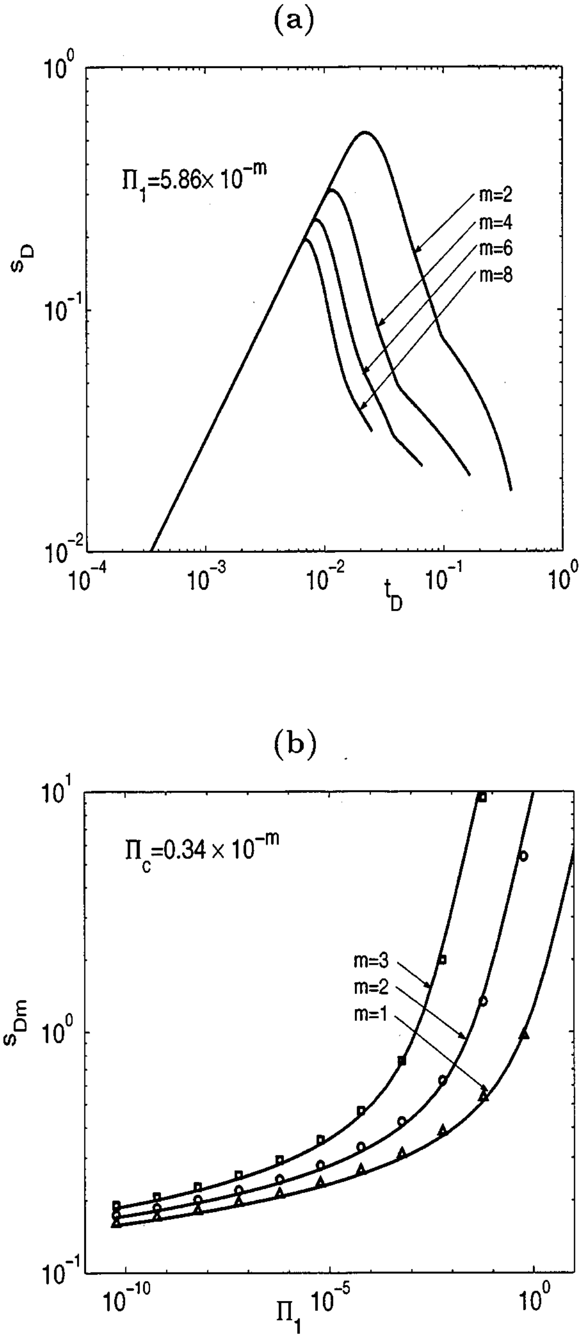

Figure 6: Numerical results for: (**a**) The variation of the rescaled supersaturation, s_D, as a function of the dimensionless time, t_D. Effect of $\Pi_1 = 5.86 \times 10^{-m}$, for $\Pi_c = 3.41 \times 10^{-2}$, $\Pi_2 = 2.33 \times 10^6$ and $\Pi_3 = 8.7 \times 10^{-3}$. (**b**) The effect of the dimensionless parameter Π_1 on the maximum rescaled supersaturation, s_{Dm}, for $\Pi_c = 0.34 \times 10^{-m}$. Points correspond to

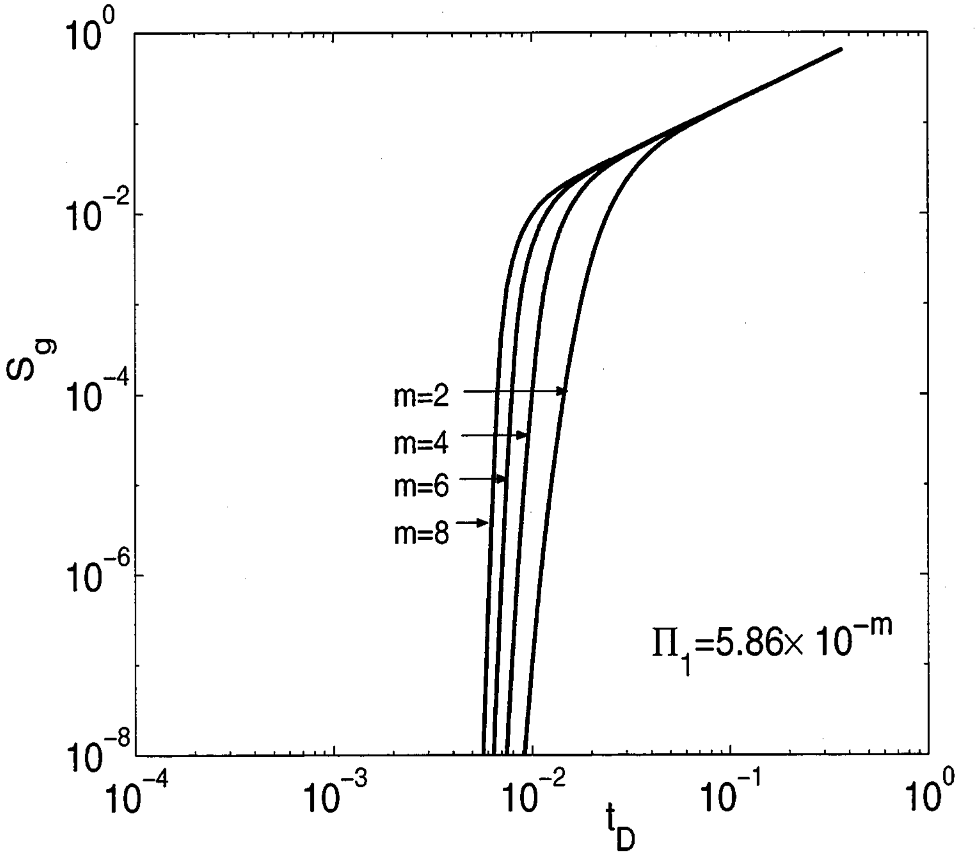

Figure 7: The variation of the gas saturation, S_g, as a function of the dimensionless time, t_D. Effect of $\Pi_1 = 5.86 \times 10^{-m}$, for $\Pi_c = 3.41 \times 10^{-2}$, $\Pi_2 = 2.33 \times 10^6$ and $\Pi_3 = 8.7 \times 10^{-3}$.

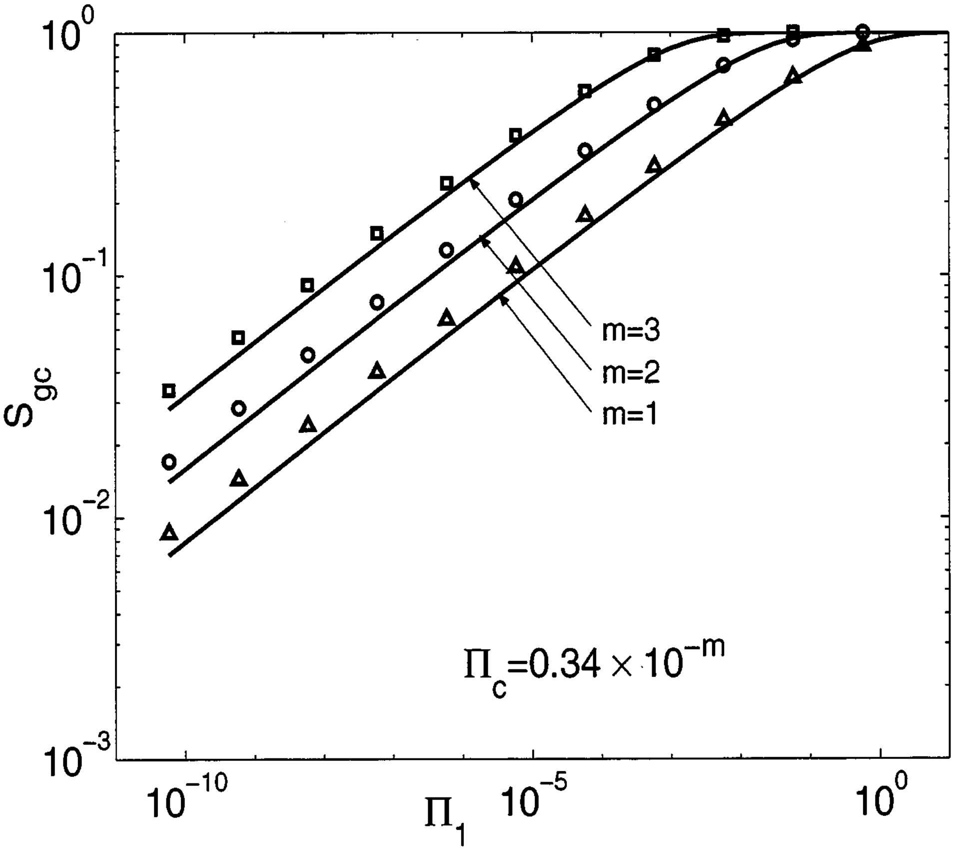

Figure 8: The effect of the dimensionless parameter Π_1 on the critical gas saturation, S_{gc}, for $\Pi_c = 0.34 \times 10^{-m}$. Points denote the full numerical solution, solid lines correspond to the simpler model.

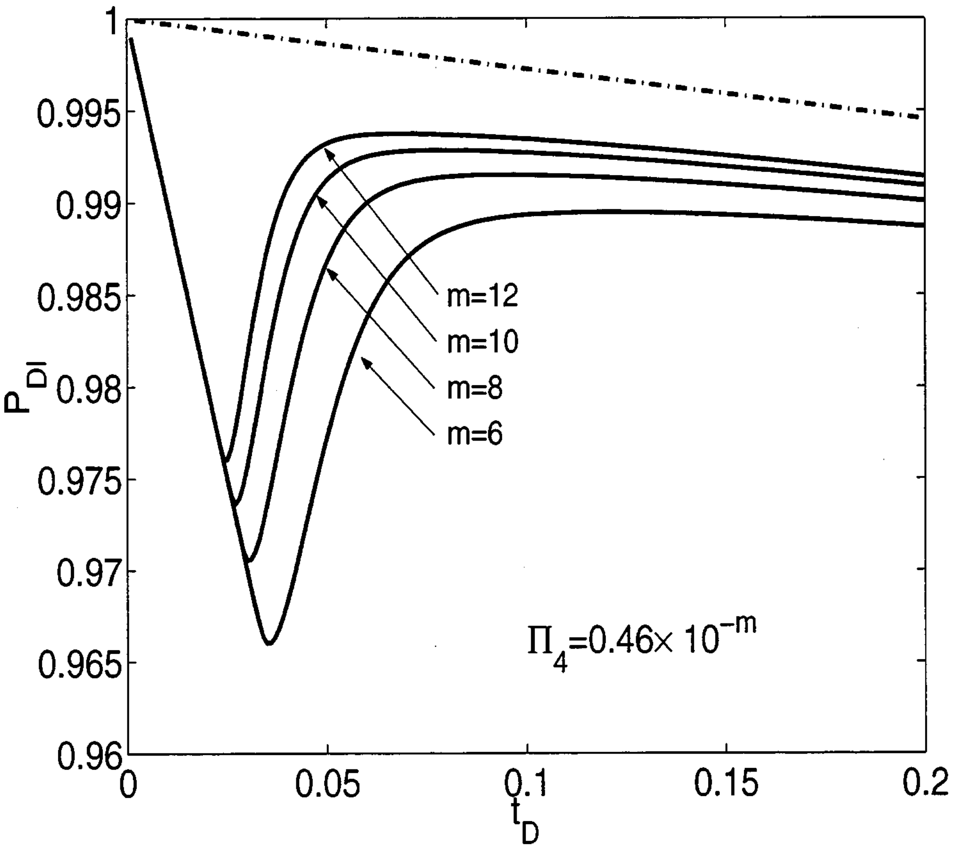

Figure 9: The variation of the dimensionless pressure, P_{Dl}, as a function of the dimensionless time, t_D, for the case of constant liquid withdrawal rate. Effect of $\Pi_4 = 0.4631 \times 10^{-m}$, for $\Pi_c = 1.67 \times 10^{-1}$, $\Pi_2 = 6.84 \times 10^5$ and $\Pi_3 = 1.52 \times 10^{-2}$. Shown in dashed-dotted line is the thermodynamic equilibrium curve.

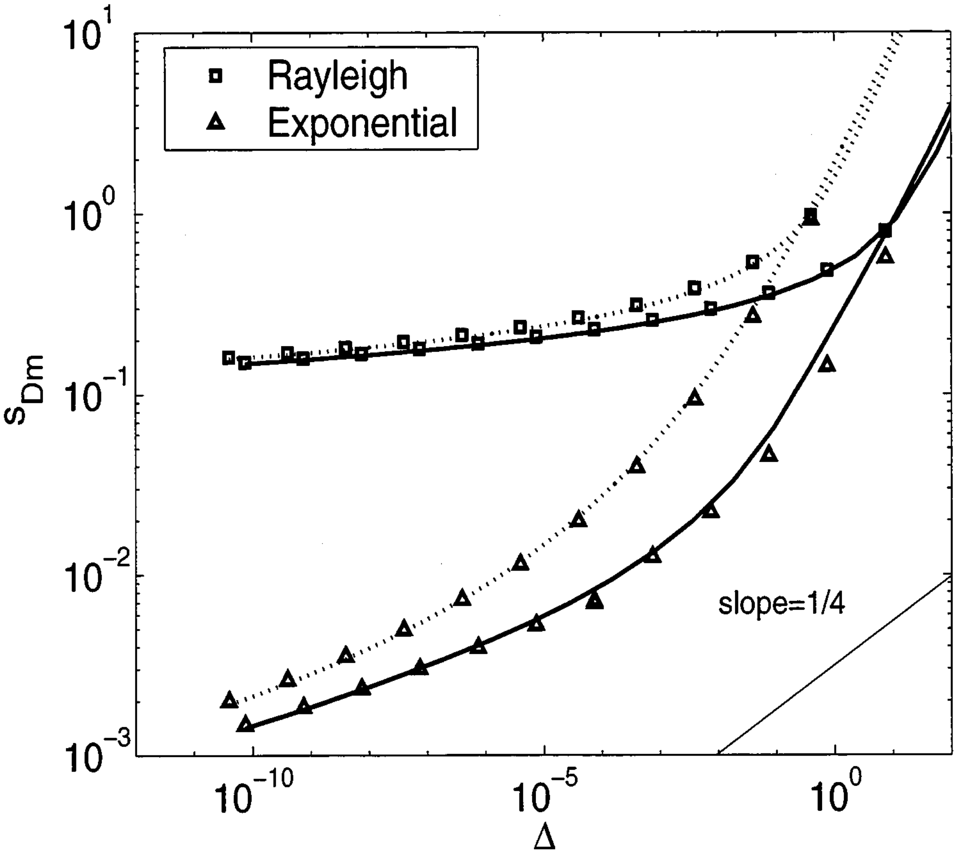

Figure 10: The maximum rescaled supersaturation, s_{Dm}, as a function of Δ for the cases of constant pressure decline rate (dotted lines) and constant liquid withdrawal rate (solid lines). Comparison between the simpler model (dotted or solid lines) and the full numerical solution (denoted by triangles for the stretched exponential cavity size distribution with $n = 0.5$ and $\sigma = 1.0$, and by squares for the Rayleigh cavity size distribution).

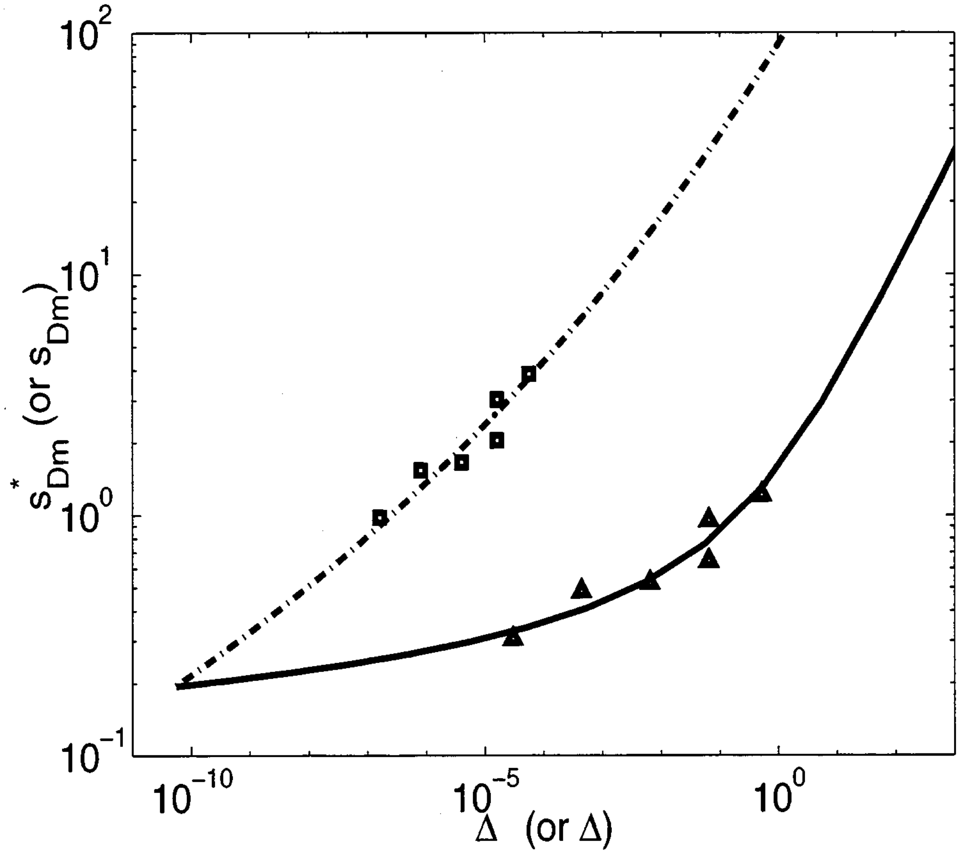

Figure 11: The maximum rescaled supersaturation, s^*_{Dm}, as a function of Δ_h for the simpler model (solid line). Triangles denote s^*_{Dm} values calculated using experimental data from Scherpenisse et al. (1994). Also plotted are the predictions based on the cavity model (dashed lines for the simpler model, squares denoting s_{Dm} values for the same experimnets).

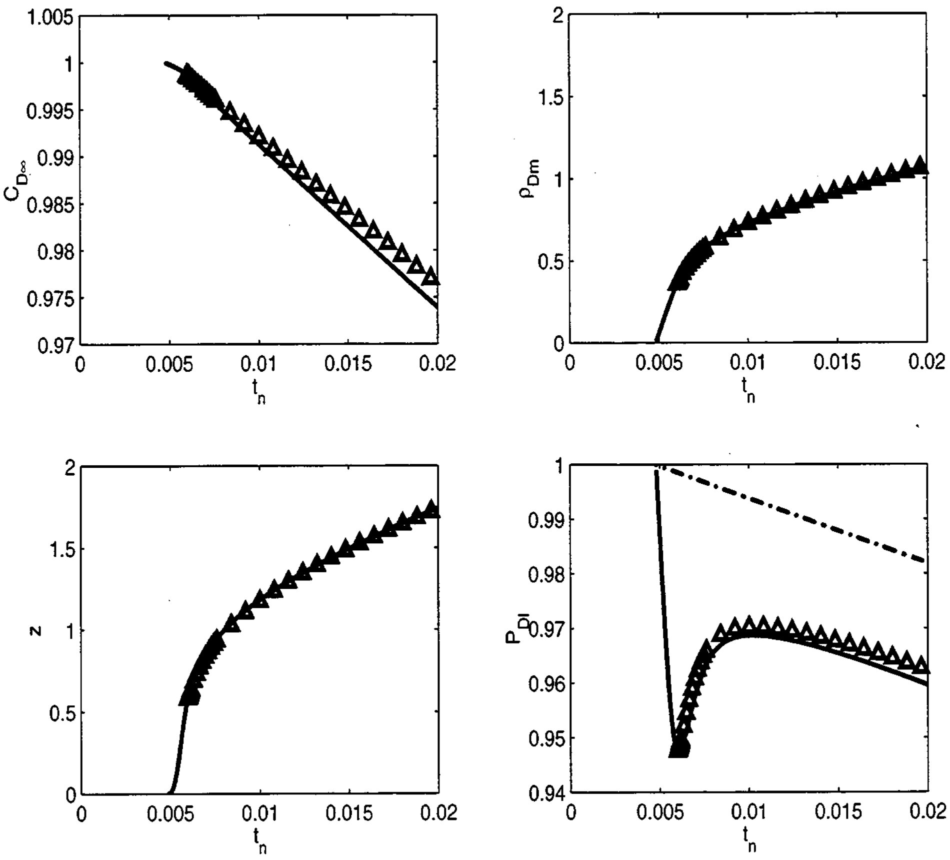

Figure 12: Comparison of the full numerical results (denoted by solid lines) with the approximate model (denoted by triangles) for the case of constant liquid withdrawal rate. Shown in dashed-dotted line in the last panel is the thermodynamic equilibrium curve.

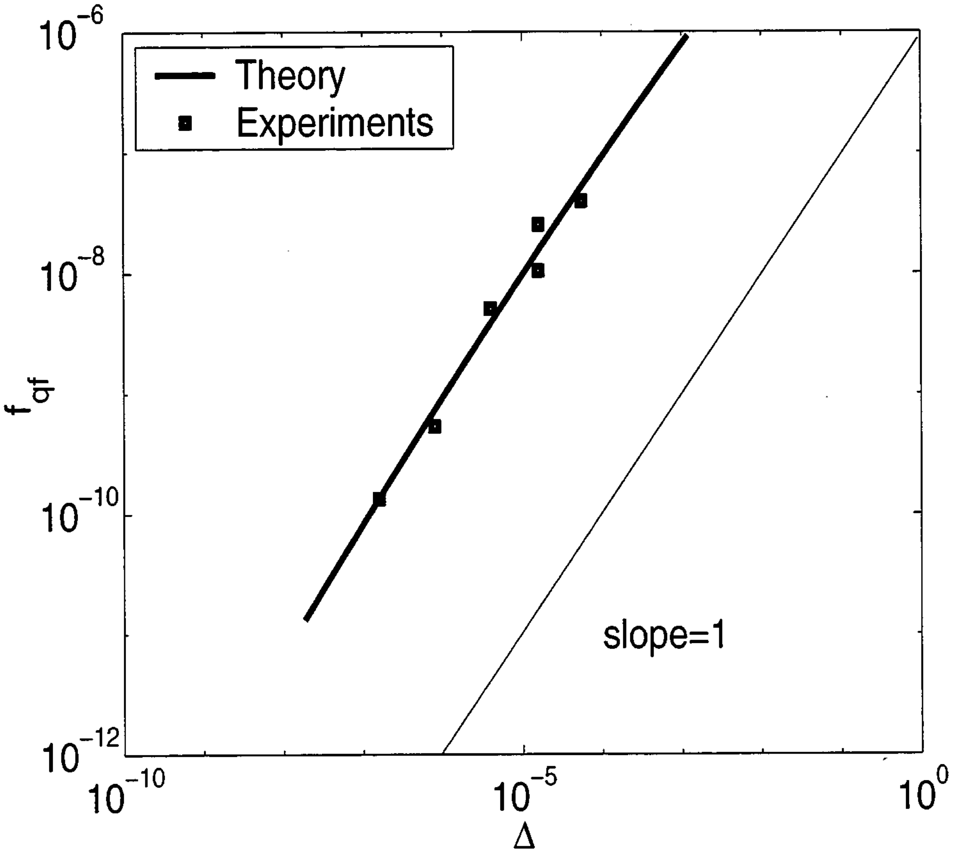

Figure 13: The final nucleation fraction, f_{qf}, as a function of Δ, for a stretched exponential ($n = 0.215$ and $\sigma = 0.045$) cavity size distribution. The solid line corresponds to the simpler model, squares denote values calculated using experimental data from Scherpenisse et al. (1994).

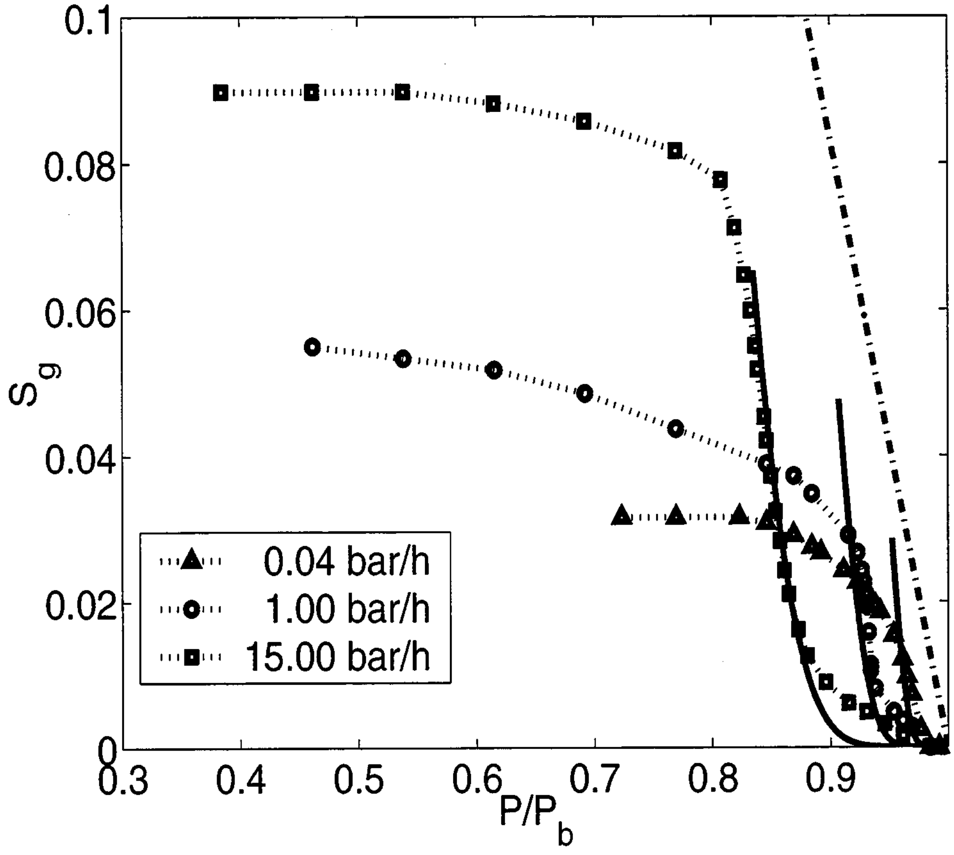

Figure 14: The evolution of the gas saturation as a function of the dimensionless pressure for three depletion rates for the Berea sandstone experiments of Scherpenisse et al. (1994). Points denote experimental values, solid lines correspond to the full numerical solution, the dashed-dotted line corresponds to the thermodynamic equilibrium curve.

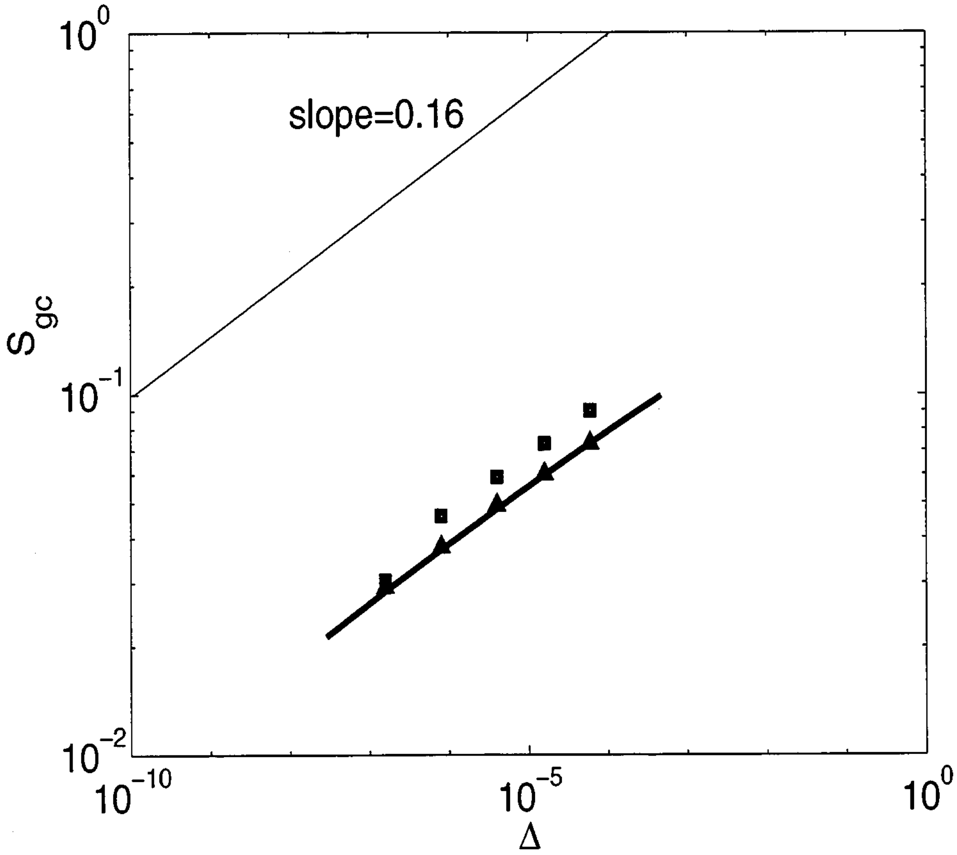

Figure 15: The critical gas saturation, S_{gc}, as a function of Δ, for a stretched exponential ($n = 0.215$ and $\sigma = 0.045$) cavity size distributions. The solid line corresponds to the simpler model, triangles denote the full solution, squares denote experimental data (constant pressure decline rate) from Scherpenisse et al. (1994).

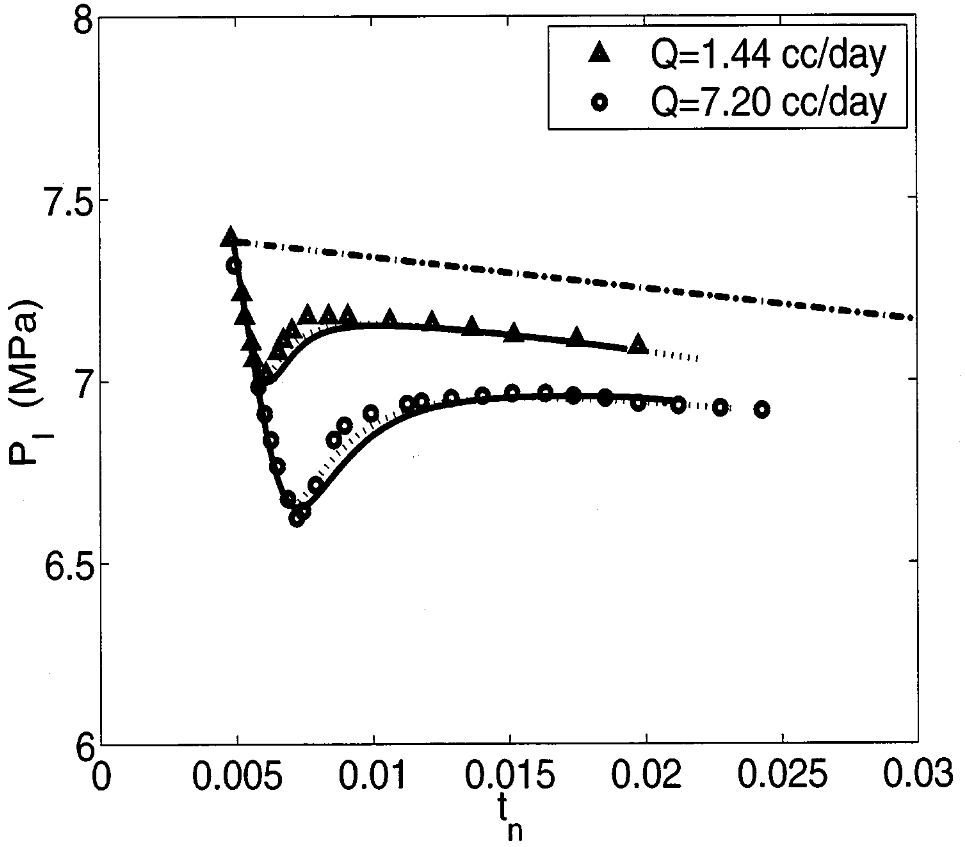

Figure 16: Evolution of pressure as a function of time for the Berea stone experiments of Firoozabadi et al. (1992) for two different withdrawal rates. Solid lines denote the full solution, dotted lines denote the simpler growth model, the dashed-dotted line denotes the thermodynamic equilibrium curve, symbols denote the experimental results.

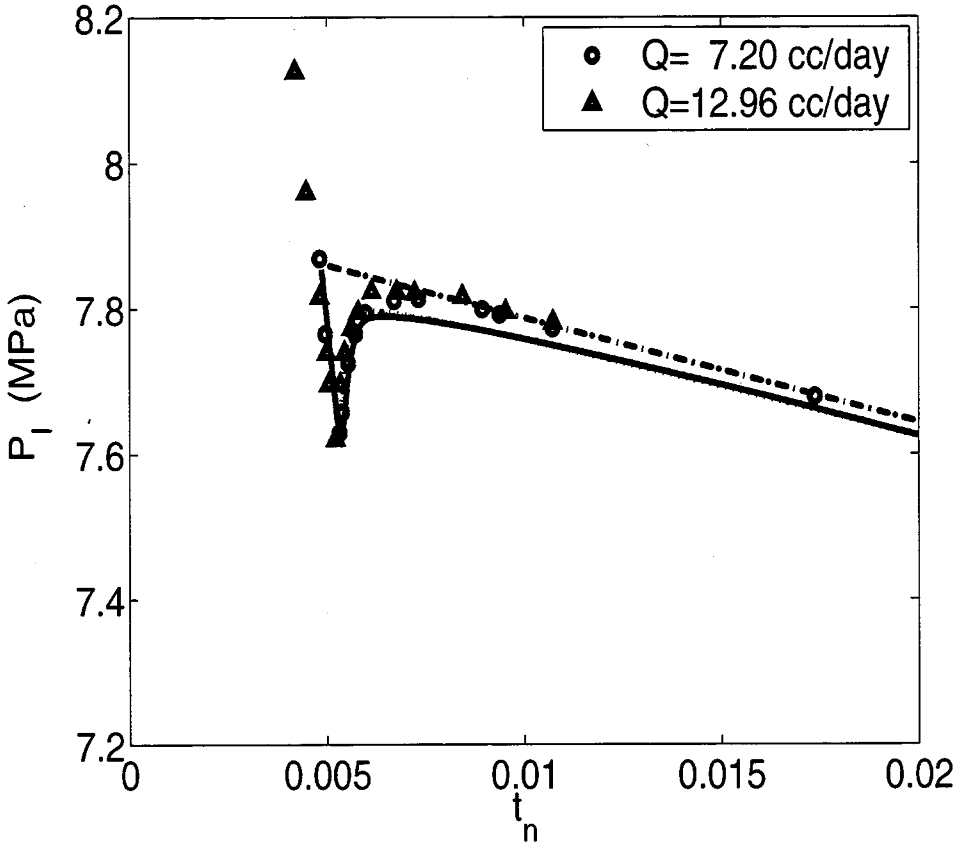

Figure 17: Evolution of pressure as a function of time for the Chalk experiments of Firoozabadi et al. (1992) for two different withdrawal rates. Solid lines (both coincide) denote the full solution, dotted lines denote the simpler growth model, the dashed-dotted line denotes the thermodynamic equilibrium curve, symbols denote the experimental results.

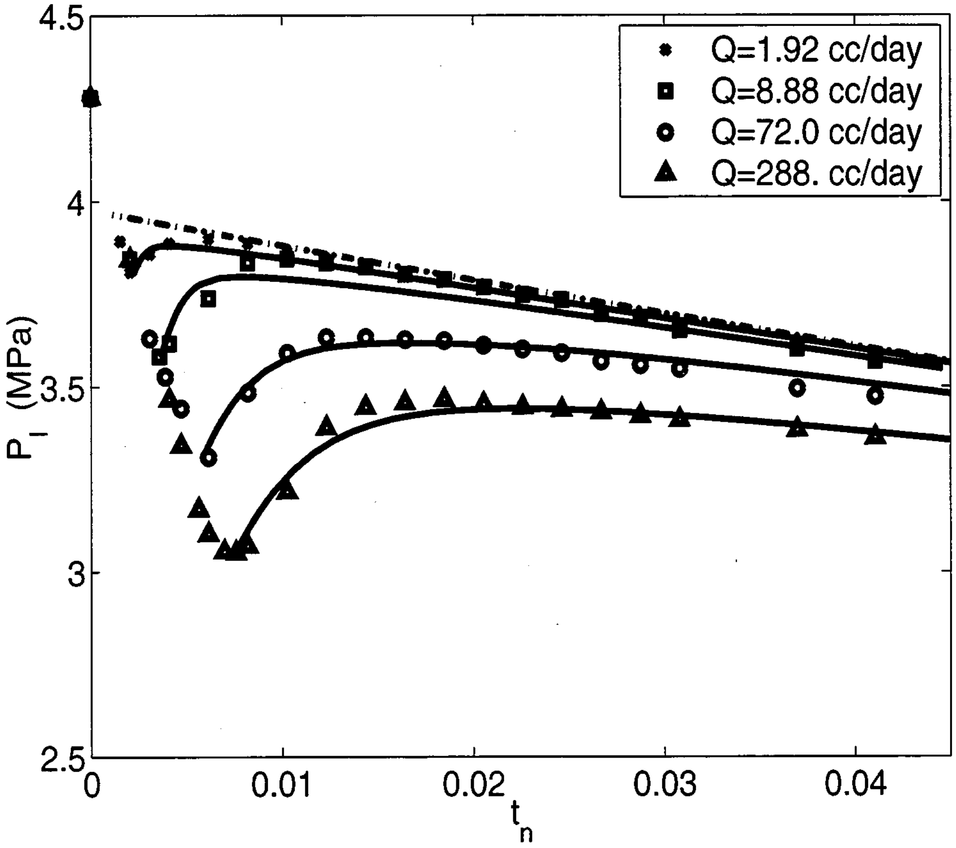

Figure 18: Evolution of pressure as a function of time for the sand-pack experiments of Kumar et al. (2000) for four different withdrawal rates. Solid lines denote the simpler growth model, the dashed-dotted line denotes the thermodynamic equilibrium curve, symbols denote the experimental results.

An Effective Continuum Model for the Gas Evolution in Internal Steam Drives

By

Ioannis N. Tsimpanogiannis and Yannis C. Yortsos

I. INTRODUCTION

The liquid-to-gas phase change in a porous medium and the subsequent growth of the gas phase is encountered in a plethora of applications driven by mass or heat transfer. Typical examples include the solution gas-drive process for the recovery of oil from oil reservoirs, boiling in porous media, thermal methods for oil recovery, nuclear waste disposal, soil remediation and others. In this report, we examine the gas phase growth from a supersaturated, slightly compressible, liquid in a porous medium, driven by heat transfer and controlled by the application of a constant-rate decline of the system pressure. A characteristic example of such a process occurs dyring cyclic steaming for the recovery of oil from low permeability reservoirs through hydraulic or natural fractures (Dehghani et al., 1997). During injection and soaking, steam condenses in the fracture and hot water imbibes into the matrix. During production, the pressure of the system constantly declines, and when it falls sufficiently below the vapor pressure, it results in the appearence of steam in the matrix (in-situ boiling). The in-situ production and subsequent growth of the steam phase inside the matrix are of interest because they result in expelling additional oil from the matrix.

Dehghani et al. (1997) conducted a series of core experiments in order to study the effect of in-situ steam drive on fluid displacement in porous media. Subsequently, Dehghani and Kamath (1999) conducted experiments with a vuggy carbonate core using a recombined oil to study the contribution of the various recovery mechanisms (thermal expansion, thermally enhanced solution gas drive, dry distillation, and in-situ steam drive) during steam injection, followed by pressure reduction.

While of interest both from theoretical and applied viewpoints, a more fundamental understanding of the basic aspects of this process has not been obtained, to our knowledge. It is the objective of this report to bridge this gap, by providing a model both of the nucleation and of the gas-phase growth periods. Internal steam drive has many similarities with the process of solution gas-drive. They both describe the evolution of a gas phase due to the increase of the supersaturation of the system, through a relatively slow pressure decline. Nucleation and subsequent phase growth play a key role in both processes. An important difference is that solution gas drive involves a binary system and it is controlled by mass transfer, while internal steam drive is fundamentally a single-component system, controlled by heat transfer. In two recent publications (Tsimpanogiannis and Yortsos, 2001a,b) we developed a comprehensive effective continuum model to model solution gas-drive under various conditions. In this report, we extend that approach to the specific problem of internal steam drive.

As discussed in Tsimpanogiannis and Yortsos (2001a,b), the effective continuum model is best suited during the early part of the process, where nucleation and the early stages of bubble growth are dominant. The latter two, particularly the nucleation sequence, are the main areas of interest of this report. We focus on the effect of the nucleation characteristics on the maximum supersaturation and the nucleation fraction (and the critical gas saturation) and provide an analysis of the effect of various parameters, such as pressure decline rate, on these quantities. Results for the gas phase growth following the conclusion of nucleation are also presented. It is assumed that the pressure decline rates are sufficiently slow so that inertia and spatial gradient effects on bubble growth are negligible. Under the same conditions, the model can in principle be applied to describe the onset of boiling in porous media, driven by the application of a constant heat flux. This application is left for a future study, however.

At later stages of bubble growth, where the various gas clusters compete with each other through a combination of pore geometrical and topological effects, the present continuum model will have obvious drawbacks. In the latter stages, a pore-network model should instead be used. Pore-network models of bubble growth in single-component systems, driven by heat transfer w ere developed by Satik and Yortsos (1996). In principle, these contain all the necessary physics for a rigorous modeling of the process, particularly when significant spatial gradients develop. Such an effort can be pursued in parallel.

The report is organized as follows: First, we formulate the problem closely following Tsimpanogiannis and Yortsos (2001a,b). A scaling analysis of the resulting equation allows to recast the problem in a more useful form, to be used for direct predictions. The numerical results are analyzed. It turns out that for their interpretation, a simplified model of the nucleation and growth periods can be developed. We use the simpler model to obtain expressions for the maximum supersaturation as a function of geometric, thermodynamic and process parameters. This allows us to obtain useful relations for the dependence of the final nucleation fraction (and the critical gas saturation) on process parameters. The theoretical predictions are then compared against experimental results.

II. MATHEMATICAL FORMULATION

Consider an effective porous medium occupied by a single-component liquid. At the beginning of the process, the system is subcooled at the initial temperature, T_o, and pressure, P_o, where $P_o > P^{sat}(T_o)$ and $P^{sat}(T)$ denotes the equilibrium vapor pressure at temperature T. In the practical application discussed by Dehghani and Kamath (1999) this state is achieved by steam injection, followed by steam condensation. Then, the pressure of the system is slowly decreased. Nucleation and subsequent bubble growth are driven by the continuous increase in the supersaturation, $P^{sat}(T_\infty) - P_l(t)$, where T_∞ is the far-field system temperature and subscript l denotes liquid. To describe phase equilibria, we will assume a Clausius-Clapeyron equation

$$\frac{d\ln\left[P^{sat}(T_\infty)\right]}{dT_\infty} = \frac{L_v}{R_g T_\infty^2} \tag{1}$$

where R_g is the ideal gas constant and L_v the molar latent heat of vaporization. Equation (1) does not include Kelvin vapor pressure lowering effects. However, these can be readily incorporated by replacing L_v in (1) by $L_v + P_c v_m$, where P_c is the capillary pressure and v_m the molar liquid volume. More complex thermodynamics can certainly be incorporated (Reid et al., 1986), but the salient features are manifested with the simpler model (1). Conversely, at a specified liquid pressure, P_l, a degree of superheat is present in the system, given by the difference

$$\Delta T = T_\infty - T^{sat}(P_l) \tag{2}$$

where $T^{sat}(P_l)$ denotes the equilibrium temperature corresponding to P_l. The change in supersaturation (or superheat) is here driven by a constant rate of pressure decline. As mentioned, we will proceed with the assumption that the rate of decline is sufficiently slow, so that inertia effects as well as effects of spatial gradients (gravitational and/or viscous) are negligible. This requires sufficiently small Rayleigh, Bond, capillary and Peclet numbers. Instead, emphasis will be placed on nucleation and on the effect of the increase of supersaturation on the growth of the gas phase.

a. Nucleation

As the liquid pressure declines, nucleation sets in. Yortsos and Parlar (1989) reviewed the gas-liquid phase change in porous media and concluded that heterogeneous nucleation is the most plausible mechanism under sufficiently slow rates of supersaturation. In one model, nucleation occurs when a gas bubble, either pre-existing or nucleated inside a cavity at the pore walls, becomes unstable and detaches or otherwise occupies the host pore body. This type of mechanism is in agreement with visual observations from micromodel experiments in solution gas drive (Li and Yortsos, 1995a, El Yousfi et al., 1991, 1997, Bora et al., 2000 and Dominguez et al., 2000) and will also be assumed here. In the cavity model, the activation of a nucleation site occurs when the trapping capillary forces are overcome for the first time. Then, the following condition is satisfied between the radius of the nucleation cavity, r_c, and the (local) supersaturation,

$$P_c \equiv \frac{2\gamma \cos\theta^*}{r_c} = P^{sat}(T_\infty) - P_l(t) \tag{3}$$

where θ^* is the contact angle ($0 < \theta^* < \pi/2$). In the present model, the onset of nucleation is not kinetically related to the degree of supersaturation, as for example, in conventional approaches for solution gas drive (Firoozabadi and Kaschiev, 1997), but rather depends on the size distribution, $\alpha_c(r_c)$, of the nucleation cavities.

Consider, now, the activation of nucleation sites. With the decrease in the liquid pressure, the right-hand side of (3) increases, eventually becoming positive. Then, various cavities satisfying (3) become activated and their corresponding host pore bodies are occupied by gas. At any time, the current nucleation fraction, f_q, defined as the number fraction of pores that contain sizes which have been activated, is

$$f_q = \int_{r_c}^{\infty} \alpha_c(r) dr \tag{4}$$

where r_c is an implicit function of time, through (3). Equation (4) implies a zero nucleation fraction at zero supersaturation ($r_c \to \infty$) and a nucleation fraction of one at infinite supersaturation ($r_c \to 0$). As elaborated in Tsimpanogiannis and Yortsos (2001a), the cavity size distribution, α_c, pertains only to the largest cavity in any given pore (as this cavity will be activated first). Also, equation (4) slightly overestimates the true nucleation fraction, since pores containing sites to be activated later, may already be occupied by gas, due to the growth of gas clusters from neighboring pores. However, in most cases, nucleation terminates well before gas bubble growth has occurred to any substantial degree ($S_g \ll 1$), thus (4) should be an excellent approximation.

It is apparent that f_q will have a different dependence on parameters, depending on the assumed cavity size distribution. In the present report, we will consider distribution of the Rayleigh type,

$$f_q = \exp\left(-\frac{\pi r_c^2}{4 r_c^{*2}}\right) = \exp\left[-\frac{\pi \gamma^2}{r_c^{*2}[P^{sat}(T_\infty) - P_l]^2}\right] \tag{5}$$

where r_c^* is a characteristic (here the mean) cavity size, as well as a stretched-exponential

$$f_q = \exp\left(-\frac{r_c^n}{\sigma r_c^{*n}}\right) \tag{6}$$

where n is a positive exponent and σ is a measure of the variance. The type of distribution influences significantly the results to be obtained, as will be demonstrated below.

As long as the level of supersaturation increases with time, the right-hand-side of equation (5) also increases, implying that additional sites become activated, and the nucleation fraction continuously rises. This is consistent with experimental evidence of sequential nucleation reported by Satik and Yortsos (1996). After the supersaturation reaches a maximum (local or global), equation (5) predicts a decreasing f_q, which is unphysical. Therefore, in segments of decreasing supersaturation the nucleation fraction is assumed constant. When the supersaturation goes through a global maximum, it signals the end of the nucleation period, in which case the fraction of pores ultimately activated, f_{qf}, will be given by equations (5) or (6) at the time of the maximum supersaturation. We note that in typical solution gas-drive experiments, f_{qf} is very small, of the order of $10^{-9} - 10^{-6}$.

Through this process, nucleation centers are activated sequentially, giving rise to evolving gas clusters, which grow by heat transfer from the liquid to the gas. Sequential nucleation results into clusters of different ages (the time passed since a particular class of gas clusters has been nucleated/activated). Let $\omega(\tau)$ be the number density of clusters nucleated per total number of pores. Then, $\omega(\tau)d\tau$ is the number of new clusters per total number of pores that become activated in the time interval between τ and $\tau + d\tau$. Evidently,

$$\omega(\tau)d\tau = df_q \tag{7}$$

This relation will be used below to simplify the expressions for the gas phase growth.

b. Gas phase growth

During the growth of the gas phase we can roughly distinguish two periods, one in which the growth is within single pores and another corresponding to gas clusters spanning several pores (Tsimpanogiannis and Yortsos, 2001a). The first period extends throughout and following the nucleation stage, the second is the later stage of growth. In either, growth is driven by heat transfer. In general, different clusters compete for the available heat in the liquid, the relative heat transfer rates depending on their geometry and relative position.

In the absence of competition between adjacent clusters and under the assumption that heat transfer is conduction-controlled (namely that the Peclet number is sufficiently small), an isolated cluster j grows at a rate which is proportional to its effective radius, $R_j(t,\tau)$, and the driving force $T_\infty - T^{sat}(P_l)$ where T_∞ is the far-field temperature. This is true even for ramified fractal clusters, as was verified by Satik and Yortsos (1996) for a percolation cluster. Assuming that the gas is ideal, we can write the following mass balance for a growing cluster

$$\left(\frac{M_w}{R_g T_g}\right) \frac{d}{dt}\left[(P_l + P_c)V_g\right] \approx 4\pi R_j \frac{k_{eff}}{\tilde{L}_v}(T_\infty - T^{sat}(P_l)) \tag{8}$$

where M_w is the molecular weight of the gas, T_g the temperature in the gas phase, V_g the gas cluster volume, k_{eff} an effective conductivity and $\tilde{L}_v$ the mass latent heat of vaporization ($L_v = \tilde{L}_v M_w$). In equation (8) we have also included the capillary pressure, P_c, which in the application of interest can be significant. To simplify, we linearize the phase equilibria around P_o,

$$T^{sat}(P_l) \approx T^{sat}(P_o) + \frac{dT^{sat}}{dP}(P_l - P_o) \tag{9}$$

and take without significant loss $T_g \approx T_o$.

The gas volume V_g takes a different expression in the two different periods (Tsimpanogiannis and Yortsos, 2001a). For growth within a single pore, $V_g \approx V_c \left(\frac{R_j}{r_c^*}\right)^3$, where V_c is a characteristic cavity volume (defined here as $\frac{4}{3}\pi r_c^{*3}$). For growth of a cluster spanning several pores, we have $V_g \approx A^* V_s \left(\frac{R_j}{r_s^*}\right)^{D_f}$, where V_s is the average site volume, r_s^* is a characteristic pore body size, D_f is the mass fractal dimension, equal approximately to 2.5 for a 3-D cluster, and A^* is a dimensionless geometric prefactor. To capture both periods with the same equation we write

$$\left(\frac{AV_c M_w}{R_g T_o}\right) \frac{d}{dt}\left[(P_l + P_c)\left(\frac{R_j}{r_c^*}\right)^{D_f}\right] = 4\pi R_j \frac{k_{eff}}{\tilde{L}_v}(T_\infty - T^{sat}) \tag{10}$$

with the understanding that D_f varies between 3 and 2.5, and A between 1 and $A = \frac{A^* V_s}{V_c}\left(\frac{r_c^*}{r_s^*}\right)^{D_f}$, during the nucleation period and growth periods, respectively.

Under the above assumptions, the gas phase will be described as a collection of clusters of size $R(t, \tau)$, the dynamics of each of which is described by equation (10), with R_j replaced by R, namely

$$\left(\frac{AV_c M_w}{R_g T_o}\right) \frac{\partial}{\partial t}\left[(P_l + P_c)\left(\frac{R}{r_c^*}\right)^{D_f}\right] = 4\pi R \frac{k_{eff}}{\tilde{L}_v}(T_\infty - T^{sat}) \tag{11}$$

subject to the initial condition $R(\tau, \tau) = r_c(\tau)$, where r_c satisfies (3).

Consider, next, the heat balance for the entire system. We have

$$\begin{aligned} V_p\left[\phi(1 - S_g)\rho_l C_{pl} + (1 - \phi)\rho_r C_{pr}\right]\frac{dT_\infty}{dt} &= -\ 4\pi\phi k_{eff}(T_\infty - T^{sat}) N_T \int_0^t R(t, \tau)\omega(\tau)d\tau \\ &+\ hA_{surf}(T_o - T_\infty) \end{aligned} \tag{12}$$

where the integration is over all existing clusters, C_p denotes heat capacity per unit mass, ϕ is porosity, h is the heat transfer coefficient to the surroundings, assumed at temperature T_o, and A_{surf} is the corresponding surface area through which heat is exchanged.

The gas saturation is related to the radius of the growing clusters and the nucleation fraction through the relation

$$S_g = Av \int_0^{f_q} \left(\frac{\hat{R}(t, f_q)}{r_c^*} \right)^{D_f} df_q \tag{13}$$

where we introduced the volume ratio $v \equiv \frac{V_c}{V_s}$ and the notation $\hat{R}(t, f(\tau)) \equiv R(t, \tau)$, for the radius of a cluster at time t, nucleated when the nucleation fraction was $f(\tau)$. Note that the liquid mass balance can also be expressed and reads as

$$\frac{Q(t)}{V_p} = -(1 - S_g)c\frac{dP_l}{dt} + \frac{dS_g}{dt} \tag{14}$$

where c takes values in the range of $1.45 \times 10^{-4} - 1.45 \times 10^{-3}\mathrm{MPa}^{-1}$. However, in the present problem it is not used. Subject to the relevant initial conditions, the system of equations (11), (12), (14) and (13) can be integrated. Integration proceeds until the time when the critical gas saturation is reached. In the present approach, we assume that the critical gas saturation, S_{gc}, can be predicted given the nucleation fraction and the capillary and Bond numbers (Du and Yortsos, 1999, Tsimpanogiannis and Yortsos, 2001a,b, Tsimpanogiannis and Yortsos, 2002). Therefore, for the purposes of estimating S_{gc}, it only suffices to model well the events during the nucleation period.

c. Dimensionless formulation and scaling

For the solution of the problem, we recast the equations in dimensionless form. Denote dimensionless quantities by subscript D and scale temperature by T_o, pressure by P_o, cluster size by r_c^*, and time by $t^* = \frac{P_o}{a}$, where a is the constant pressure decline rate. The dimensionless mass balance for the gas phase is given by

$$(1 - t_D + \Pi_c)\frac{\partial \hat{R}_D^{D_f}}{\partial t_D} = \frac{\Pi_2}{A\Pi_1}(T_{D\infty} - T_D^{sat})\hat{R}_D + \hat{R}_D^{D_f} \tag{15}$$

while the dimensionless heat balance for the system reads

$$\begin{aligned}(1-S_g)\left(\Pi_\rho+\frac{1-\phi}{\phi}\right)\frac{dT_{D\infty}}{dt_D} &= -\ \frac{1}{\Pi_1}(T_{D\infty}-T_D^{sat})\int_0^{f_q}\hat{R}_D(t_D,f_q)df_q \\ &+\ \Pi_H(1-T_{D\infty})\end{aligned} \tag{16}$$

In the above, we have defined the dimensionless groups

$$\begin{aligned}&\Pi_1=\frac{V_s\rho_r C_{pr}a}{4\pi P_o k_{eff}r_c^*}=\frac{V_p\rho_r C_{pr}a}{4\pi P_o N_T k_{eff}r_c^*},\\ &\Pi_2=\frac{R_gT_o^2}{vM_w\tilde{L}_v}\frac{\rho_rC_{pr}}{P_o},\qquad \Pi_H=\frac{hA_{surf}P_o}{V_p\rho_rC_{pr}a\phi},\\ &\Pi_\rho=\frac{\rho_lC_{pl}}{\rho_rC_{pr}}\quad\text{and}\quad \Pi_c=\frac{2\gamma\cos\theta^*}{r_c^*P_o}\end{aligned} \tag{17}$$

Parameter Π_1 expresses the ratio of the characteristic times for heat diffusion at the pore scale to that for the decline of pressure. Although a small number in typical applications, it plays a key role in determining the nucleation fraction and the critical gas saturation.

In addition, we have the following relations: The gas saturation is

$$S_g=Av\int_0^{f_q}\hat{R}(t_D,f_q)^{D_f}df_q \tag{18}$$

Using the linearized phase equilibria, the dimensionless superheat is

$$\theta\equiv T_{D\infty}-T_D^{sat}=T_{D\infty}-(1-\psi t_D) \tag{19}$$

where $\psi\equiv\frac{R_gT_o}{L_v}$ or $\psi\equiv\frac{R_gT_o}{L_v+P_cv_m}$, when Kelvin effects are important. The cavity size that becomes activated at a given time and temperature can be expressed in terms of the supersaturation

$$s\equiv P_D^{sat}(T_{D\infty},t_D)-P_{Dl}(t_D)=t_D-\frac{1-T_{D\infty}}{\psi} \tag{20}$$

or, more conveniently, in terms of the rescaled supersaturation

$$s_D\equiv\frac{s}{\Pi_c} \tag{21}$$

Then, the nucleation fraction is

$$f_q = \exp\left(-\frac{\pi}{4s_D^2}\right), \quad f_q = \exp\left(-\frac{1}{\sigma s_D^n}\right) \tag{22}$$

depending on the size distribution used. In the solution of the problem, we assumed that the process begins ($t_D = 0$) when the pressure is at the bubble point corresponding to T_o. Initial conditions for the simulations were $T_{D\infty} = 1$, $P_{Dl} = 1$ and $R_D(\tau, \tau) = s_D^{-1}(\tau)$.

The above system contains one key parameter, Π_1, describing the effect of the rate of increase of the supersaturation. Because it is small, a further rescaling of the nucleation fraction and the cluster size is necessary. After some analysis (Tsimpanogiannis and Yortsos, 2001a), it is not difficult to show that for the cavity nucleation model, the following scaling is valid, $f_q \sim \Pi_1^{\frac{D_f}{D_f-1}}$ and $f_q R^{D_f} \sim O(1)$ (where, given that the nucleation fraction varies only during the first period, $D_f = 3$). This scaling contains the main effect of the pressure decline rate on the nucleation fraction. Thus, we define a rescaled nucleation fraction and rescaled cluster sizes

$$\phi_q = f_q \Pi_1^{-\frac{3}{2}} \quad \text{and} \quad \rho_D = \Pi_1^{\frac{1}{2}} \hat{R}_D \tag{23}$$

In this notation, the governing equations become

$$(1 - t_D + \Pi_c)\frac{\partial \rho_D^{D_f}}{\partial t_D} = \frac{\Pi_2}{A}\theta \rho_D + \rho_D^{D_f} \tag{24}$$

and

$$(1 - S_g)\left(\Pi_\rho + \frac{1-\phi}{\phi}\right)\frac{dT_{D\infty}}{dt_D} = -\theta \int_0^{\phi_q} \rho_D(t_D, \phi_q)\, d\phi_q + \Pi_H(1 - T_{D\infty}) \tag{25}$$

while

$$S_g = Av \int_0^{\phi_q} \rho(t_D, \phi_q)^{D_f}\, d\phi_q \tag{26}$$

The numerical solution of the system of the rescaled equations is described below.

III. NUMERICAL RESULTS

The system of differential equations was solved numerically using a fourth-order Runge-Kutta method (Press et al., 1994). At each time step we examine whether nucleation of a new class of gas clusters is possible, namely whether the supersaturation is increasing. If so, a new class of gas clusters is added. Then, the simultaneous growth of all different classes of clusters is computed. When the supersaturation reaches a maximum, further nucleation stops. In the typical case, parameters which can vary over a significant range are Π_1 and Π_c (and possibly Π_2). An additional important variable is the type of the cavity size distribution used in the calculation of the nucleation fraction. The sensitivity to these parameters was examined in the simulations.

The effect of Π_1 and Π_c on the rescaled nucleation fraction, ϕ_q, the mean rescaled radius, $\rho_{D,m}$, the rescaled supersaturation, s_D, and the gas saturation, S_g, is shown in Figs. 1-4. In these calculations, we used a stretched exponential ($n = 1.0$ and $\sigma = 1.0$) cavity size distribution, Π_2 was kept constant to the value 0.9697×10^8, we assumed an adiabatic system ($\Pi_H = 0$), while Π_1 varied over several orders of magnitude (from 10^{-14} to 10^{-5}).

The variation of ϕ_q as a function of the dimensionless time, t_D, and of the parameters Π_1 and Π_c is shown in Fig. 1. The nucleation fraction increases rapidly in a small time interval, and then stabilizes to a final value at the conclusion of nucleation. Such behavior is characteristic of nucleation processes, and has features similar to those reported by Tsimpanogiannis and Yortsos (2001a, b) for solution gas drive. There is a slight effect of Π_1, which basically demonstrates the correctness of the scaling (23). The effect of Π_c is significant. As Π_c increases, the final nucleation fraction ϕ_{qf} (hence f_{qf}) decreases, while the onset of nucleation is delayed (Fig. 1b). The increase of f_{qf} with an increase in Π_1 and a decrease in Π_c is expected. Larger values of Π_1 result from a faster decline rate, a greater departure from equilibrium, the establishment of a greater supersaturation in the system, hence the activation of more nucleation sites. Likewise, smaller Π_c imply that nucleation is facilitated at increasingly smaller supersaturations, as larger size cavities can be activated more easily.

Fig. 2 shows the corresponding effects on the mean rescaled size ρ_{Dm}. There are two different regions, corresponding to the nucleation period, and another to growth after nucleation. The first period can be approximated as a linear function of time. The effect of Π_1 is relatively insignificant at small Π_1, confirming the validity of the scaling (23). The effect of Π_c (not shown) is more significant. Smaller values of Π_c lead to an increase in the nucleation fraction, and a corresponding decrease in the size of the gas clusters at the conclusion of nucleation.

Fig. 3 shows plots of the rescaled supersaturation s_D as a function of time for different Π_1 and Π_c. During the nucleation period (straight line segment in Fig. 3a), the supersaturation increases with time almost linearly, suggesting that $T_{D\infty}$ does not vary significantly in that period. Eventually, the rate of supersaturation increase slows down and, at some point, s_D reaches a maximum, s_{Dm}, at which point nucleation terminates. Following this point, the supersaturation decreases monotonically. The maximum value s_{Dm} is plotted in Fig. 3b as a function of Π_1 for two different values of Π_c. Note that s_{Dm} is in general of the order of $10^{-3} - 10^{-1}$. The dependence on the parameters becomes stronger at larger Π_1 and smaller Π_c.

The evolution of the gas saturation is shown in Fig. 4. It follows that of f_q, during the nucleation period, and that of ρ_{Dm}, during the period of growth. The effect of Π_c is indirect, in that smaller values of Π_c promote larger values of S_g due to an increase in both f_{qf} and ρ_D. All these trends are similar to the case of solution gas drive, as explained in Tsimpanogiannis and Yortsos (2001a, b). We refer the reader to these publications for other effects, including the effect of Π_1 and Π_c on the critical gas saturation S_{gc}. Because the latter pertains to the formation of a sample-spanning cluster, in the absence of viscous or gravity effects, S_{gc} actually reflects the variation of f_{qf}. Thus, S_{gc} can be considered a power-law both of Π_1 and of Π_c with exponents that vary between 0.16 and 0.25 with respect to Π_1 and between -0.33 and -0.22, with respect to Π_c, respectively (see Tsimpanogiannis and Yortsos, 2001a, b).

The effect of Π_H on the rescaled nucleation fraction, ϕ_q and the gas saturation, S_g, is shown in Figs. 5-6. In these calculations, we used a stretched exponential ($n = 0.2233$ and $\sigma = 0.1364$) cavity size distribution. As Π_H increases, the level of superheat and thus the level of the supersaturation in the system is higher. This leads to an earlier onset of nucleation, as well as a higher degree of nucleation. Note, however, that the effect of Π_H on the maximum superheat and on the rescaled final nucleation fraction, ϕ_{qf}, is not significant.

A change of Π_H by three orders of magnitude, results in a change of ϕ_{qf} by a factor of less than 2. The gas saturation increases faster as the heat transfer coefficient increases. This is due to the maintaining of a higher level of superheat, therefore a larger driving force for gas volume growth. Interestingly, as the heat transfer coefficient decreases the gas saturation growth slows down at larger values of the gas saturation. A noticeable difference, however, at higher values of Π_H, is that the superheat is not be completely depleted before the gas saturation becomes equal to one, as happens with the lower values of Π_H.

The numerical solutions obtained will be compared against available experimental results. However, before doing so it is beneficial to provide an interpretation of the numerical findings, using a simpler model.

IV. INTERPRETATION USING A SIMPLER MODEL

To interpret the results obtained we will consider a simpler model that captures the essential features of the problem, just like in Tsimpanogiannis and Yortsos (2001a, 2001b). Consider, first, the nucleation period.

a. Nucleation

We use the following equations for the gas phase growth and the superheat

$$(1+\Pi_c)\frac{\partial \rho_D^3}{\partial t_D} \approx \Pi_2 \theta \rho_D \tag{27}$$

and

$$\left(\Pi_\rho + \frac{1-\phi}{\phi}\right)\frac{d\theta}{dt_D} \approx \psi\left(\Pi_\rho + \frac{1-\phi}{\phi}\right) - \theta\int_0^{\phi_q(s)} \rho_D d\phi_q + \Pi_H(\psi t_D - \theta) \tag{28}$$

These are subject to the initial conditions

$$\theta(0) = 0 \quad \text{and} \quad \rho_D(\tau,\tau) = \frac{\Pi_1^{\frac{1}{2}}}{s_D(\tau)} \tag{29}$$

At early times and for small Π_1, the solution is approximately

$$\theta \approx \psi t_D \quad \text{and} \quad \rho_D \approx \left[\frac{\Pi_2}{3(1+\Pi_c)}\frac{\theta^2}{\psi}\right]^{\frac{1}{2}} \tag{30}$$

Note that the heat transfer term does not affect the early behavior (compare also with Figs. 5-6). The dimensionless superheat is linearly proportional to the dimensionless time and the mean cluster size becomes evantually proportional to time. Both are consistent with the numerical results during the nucleation period (Figs. 2 and 3).

We will use (28) to approximate the approach to the maximum superheat. The latter is reached when $\frac{d\theta}{dt_D} = 0$, namely when

$$\theta \int_0^{\phi_q} \rho_D d\phi_q \approx \left(\Pi_\rho + \frac{1-\phi}{\phi}\right)\psi \tag{31}$$

Following a similar approach as in Tsimpanogiannis and Yortsos (2001a, b) we can combine (30) and (30) with the definition of ϕ_q to obtain an approximate algebraic equation for the rescaled maximum supersaturation, s_{Dm}. For example, for the case of Rayleigh distribution we have the equation

$$\frac{\pi}{4s_{Dm}^2} - 2\ln s_{Dm} \approx \frac{1}{2}\ln\psi - \ln\left(\Pi_\rho + \frac{1-\phi}{\phi}\right) - \frac{1}{2}\ln 3 - \frac{3}{2}\ln\Delta \tag{32}$$

where we introduced the combination of variables

$$\Delta \equiv \Pi_1 \Pi_c^{-\frac{4}{3}} \left(\frac{\Pi_2}{1+\Pi_c}\right)^{-\frac{1}{3}} \tag{33}$$

Likewise for the case of a stretched exponential we get

$$\sigma^{-1} s_{Dm}^{-n} - 2\ln s_{Dm} \approx \frac{1}{2}\ln\psi - \ln\left(\Pi_\rho + \frac{1-\phi}{\phi}\right) - \frac{1}{2}\ln 3 - \frac{3}{2}\ln\Delta \tag{34}$$

These equations suggest that the dependence of the maximum supersaturation (hence the maximum superheat since $\theta = \psi\Pi_c s_D$) on the various parameters. The solutions of (32) for the Rayleigh distribution and of (34) for two different cases of a stretched exponential are plotted in Fig. 7, as a function of Δ. For the Rayleigh distribution, s_{Dm} varies weakly, in the range $0.1 - 1$, as Δ varies over several orders of magnitude (between 10^{-14} and 10^{-5}). For small Δ, the maximum supersaturation is practically constant. As Δ takes larger values, s_{Dm} increases weakly and eventually much more strongly, as Δ approaches the order of one (compare also with Fig. 3). On the other hand, for the stretched exponential, the variation is much stronger in the logarithmic plot, and almost approximates a straight line. Stronger dependence on Δ is observed for the case when the tail of the cavity size distribution becomes longer (smaller values for n). Plotted in the same figure are also the results of the numerical solution of the full problem for a number of different parameter values. The agreement between the numerical results and the simple analytical model is very good and demonstrates the validity of the simple model.

Equations (32)-(34) can be used to approximate the final nucleation fraction. For all cases we have

$$f_{qf} \approx s_{Dm}^{-2} \Lambda \Pi_1^{\frac{3}{2}} \Pi_c^{-2} \left[\frac{\Pi_2}{3(1+\Pi_c)} \right]^{-\frac{1}{2}} \tag{35}$$

where

$$\Lambda = \left(\Pi_\rho + \frac{1-\phi}{\phi} \right) \psi^{-\frac{1}{2}} \tag{36}$$

The behavior of the maximum supersaturation as a function of the parameter Δ is very similar to that in solution gas drive (Tsimpanogiannis and Yortsos, 2001a, b). In particular,

(a) In the region where s_{Dm} varies weakly with Δ (at very small Δ) the final nucleation fraction varies as a power law of Π_1, with exponent equal to 3/2.

(b) In the region where s_{Dm} may be approximated by a power-law dependence on Δ, e.g. as $s_{Dm} \sim \Delta^m$, we have the scaling

$$f_{qf} \sim \Lambda \Delta^{\frac{3}{2}-2m} \tag{37}$$

Such a dependence on Δ leads to a decrease in the exponent in the power-law scaling of f_{qf} on Π_1. For example, if we take $m \approx 1/4$ (a value examined in more detail in Tsimpanogiannis and Yortsos, 2001a, b), we read

$$f_{qf} \sim \Pi_1 \qquad \text{and} \qquad f_{qf} \sim r_c^* \tag{38}$$

b. Gas cluster growth

The modeling of the growth regime, where nucleation has terminated, can be simplified if we consider only one class of clusters and simplify the heat and mass balances as follows

$$\frac{d\theta}{dt_D} \approx \frac{-\theta z + \Pi_H(\psi t_D - \theta)}{(\Pi_\rho + \frac{1-\phi}{\phi})(1 - \upsilon \Pi_2 k_1 z^{D_f})} + \psi \tag{39}$$

and

$$\frac{dz^{D_f}}{dt_D} = \frac{k_1^{-1}\theta z + z^{D_f}}{(1 - t_D + \Pi_c)} \tag{40}$$

Here, we introduced the variable

$$z \equiv \phi_{qf}\rho_D \tag{41}$$

and the parameter

$$k_1 = \frac{\phi_{qf}^{1-D_f}}{\Pi_2} \tag{42}$$

The final value of the rescaled nucleation fraction, ϕ_{qf}, as well as initial values for $T_{D\infty}$ and ρ_D needed for the above calculation, are obtained from the previous analysis.

V. COMPARISON WITH EXPERIMENTS

The theoretical model was next compared to the experimental results of Dehghani et al. (1997). In these experiments, the pressure at the open end of a Colton sandstone core, saturated with water and embedded in a constant temperature bath, was slowly reduced at the rate of 0.7448 bar/h (10.8 psi/h). The other end of the core was kept closed to flow. Properties of the core of interest to this report were taken as follows: $r_s = 3.0 \times 10^{-5}$ cm, $r_c = 3.0 \times 10^{-7}$ cm. Additional physical parameters and values of the dimensionless parameters used in the calculations are shown in Table 1.

The gas saturation as a function of time for the single-component experiment and for various axial positions along the core are shown in Fig. 8. It is worth noting that the evolution of the gas saturation is slower as the distance from the entrance of the core increases. In a way, this reflects a reduced rate of pressure decline, or a decrease in the heat transfer coefficient as the distance from the open end increases. For a better comparison of the data, we attempted to collapse all data into a single curve. By replotting the data using as time origin the time the boiling point in the bulk is reached (which is $t_o = 84$ minutes), and by rescaling time by a factor $b(L)$, where L is the distance from the open end, we were able to collapse satisfactorily all data in a single curve, as shown in Fig. 9. The less satisfactory collapse of the data at the early times could be the result of poor CT-scan resolution in the low porosity sandstone used in the experiments (Dehghani et al., 1997). The variation of the factor $b(L)$ which allows this collapse is shown in Fig. 10. It is a linear function of the dimensionless distance and the best fit line describing the data is given by: $b(L) = 1.0106 + 5.1513\left(\frac{L}{L_o}\right)$, where L_o is the core length. We then attempted to match this universal curve using our model. As shown in Fig. 9, a very good match was obtained, using a stretched exponential cavity size distribution with $n = 0.35$ and $\sigma = 1.0$.

VI. CONCLUSIONS

In this report we developed an effective continuum model to describe the nucleation and subsequent growth of a gas phase from a supersaturated liquid in a porous medium, driven by heat transfer. The evolution of the gas results from the reduction of the system pressure at a constant rate. The model addresses two stages before the onset of bulk gas flow, nucleation and gas phase growth.

We used heterogeneous nucleation models in the form of pre-existing gas, trapped in hydrophobic cavities to investigate the nucleation behavior. Using scaling analysis and a simpler analytical model we showed that the relevant quantities during nucleation can be expressed in terms of a simple combination of dimensionless parameters, which include rate effects. The subsequent evolution of the gas phase were also described using numerical and analytical models.

The theory predicts that the maximum supersaturation in the system is a weakly increasing function of the decline rate. This function depends sensitively on the probability density function of the nucleation cavity sizes. It also predicts that the final nucleation fraction, thus the critical gas saturation, is a power law of the decline rate. The theory was then compared with available experimental data of internal steam drives, such as the blowdown experiments in carbonate rocks (Dehghani et al., 1997) and a good match is obtained by appropriate fitting of the nucleation characteristics of the medium.

References

[1] Bora, R., Maini, B.B., and A. Chakma, "Flow Visualization Studies of Solution Gas Drive Process in Heavy Oil Reservoirs Using a Glass Micromodel," *SPE Reservoir Eval. Eng.*, **3**, 224-229 (2000).

[2] Dehghani, K., Kumar, M., deZabala, E.F., Meyer, R.F., and H. Duran, "An Experimental and Numerical Study of In-Situ Stemadrive During Cyclic Steaming," *SPERE*, 144-150 (May 1997).

[3] Dehghani, K., and J. Kamath, "High Temperature Blow-Down Experiments in a Vuggy Carbonate Core," paper *SPE 56542* presented at the SPE Annual Technical Conference and Exhibition, Houston, TX (3-6 October 1999).

[4] Dominguez, A., Bories, S., and M. Prat, "Gas Cluster Growth by Solute Diffusion in Porous Media. Experiments and Automaton Simulation on Pore Network," *Int. J. Moultiphase Flow*, **26**, 1951-1979 (2000).

[5] Du, C., and Y.C. Yortsos, "A Numerical Study of the Critical Gas Saturation in a Porous Medium," *Transport in Porous Media*, **35**, 205-225 (1999).

[6] El Yousfi, A., Zarcone, C., Bories, S. and R. Lenormand, "Mècanismes de Formation d'une Phase Gazeuse par détente d'un liquide en Milieu Poreux," *C.R. Acad. Sci. Paris, Série II,* **313**, 1093-1098 (1991).

[7] El Yousfi, A., Zarcone, C., Bories, S. and R. Lenormand, "Physical Mechanisms for Bubble Growth During Solution Gas Drive," paper *SPE 38921* presented at the SPE Annual Technical Conference and Exhibition, San Antonio, TX (5-8 October 1997).

[8] Firoozabadi, A., and D. Kashchiev, "Pressure and Volume Evolution During Gas Phase Formation in Solution Gas Drive Processes," *SPE Journal*, **1**, 219-227 (1997).

[9] Li, X., and Y.C. Yortsos, "Visualization and Simulation of Bubble Growth in Pore Networks," *AIChE J.*, **41**, 214-222 (1995a).

[10] Li, X., and Y.C. Yortsos, “Theory of Multiple Bubble Growth in Porous Media by Solute Diffusion,” *Chem. Eng. Sci.*, **50**, 1247-1271 (1995b).

[11] Press, W.H., Teukolsky, W.T., Vettering, S.A., and B.P. Flannery, *Numerical Recipies,* 2nd ed. Cambridge University Press, (1992).

[12] Reid, R.C., Prausnitz, J.M., and B.E. Poling, *The Properties of Gases and Liquids,* 4th ed. McGraw-Hill, New York, (1986).

[13] Satik, C., and Y.C. Yortsos, A Pore Network Study of Bubble Growth in Porous Media Driven by Heat Transfer,” *ASME J. of Heat Transfer*, **118**, 155-462 (1996).

[14] Tsimpanogiannis, I.N., and Y.C. Yortsos, “An Effective Continuum Model for the Liquid-to-Gas Phase Change in a Porous Medium Driven by Solute Diffusion: I. Constant Pressure Decline Rates,” paper *SPE 71502* presented at the SPE Annual Technical Conference and Exhibition, New Orleans, LA (30th September-3rd October 2001); also AIChEJ, submitted (2001a).

[15] Tsimpanogiannis, I.N., and Y.C. Yortsos, “An Effective Continuum Model for the Liquid-to-Gas Phase Change in a Porous Medium Driven by Solute Diffusion: II. Constant Liquid Withdrawal Rates,” AIChEJ, submitted (2001b).

[16] Tsimpanogiannis, I.N., and Y.C. Yortsos, “A Numerical Study of the critical Gas Saturation in a Porous medium in the Presence of Viscous or Gravity Gradients,” In preparation (2002).

[17] Yortsos, Y.C., and M. Parlar, “Phase Change in Binary Systems in Porous Media: Application to Solution Gas Drive,” paper *SPE 19697*, presented at the SPE Annual Technical Conference and Exhibition, San Antonio, TX (8-11 October 1989).

$Parameter$	$Value$
a (bar/h)	0.7448
C_{pl} $(J/(KgK))$	5954.7
C_{pr} $(J/(KgK))$	850.0
k (μm^2)	4.145×10^{-4}
k_{eff} $(W/(mK))$	1.0
L_o (cm)	11.354
L_v (J/mol)	37294.8
MW (g/mol)	18.016
P_o (bar)	9.276
r_c (cm)	3.0×10^{-7}
r_s (cm)	3.0×10^{-5}
T_o (K)	449.4
γ (mN/m)	55.0
Π_1	1.333×10^{-10}
Π_2	9.697×10^{7}
Π_c	3.901×10^{1}
Π_H	2.697×10^{2}
Π_ρ	2.981×10^{0}
ρ_r $(Kg/(m^3))$	2350.0
υ	$1. \times 10^{-6}$
ϕ	0.111
ψ	1.002×10^{-1}

Table 1: Characteristic values for the various parameters.

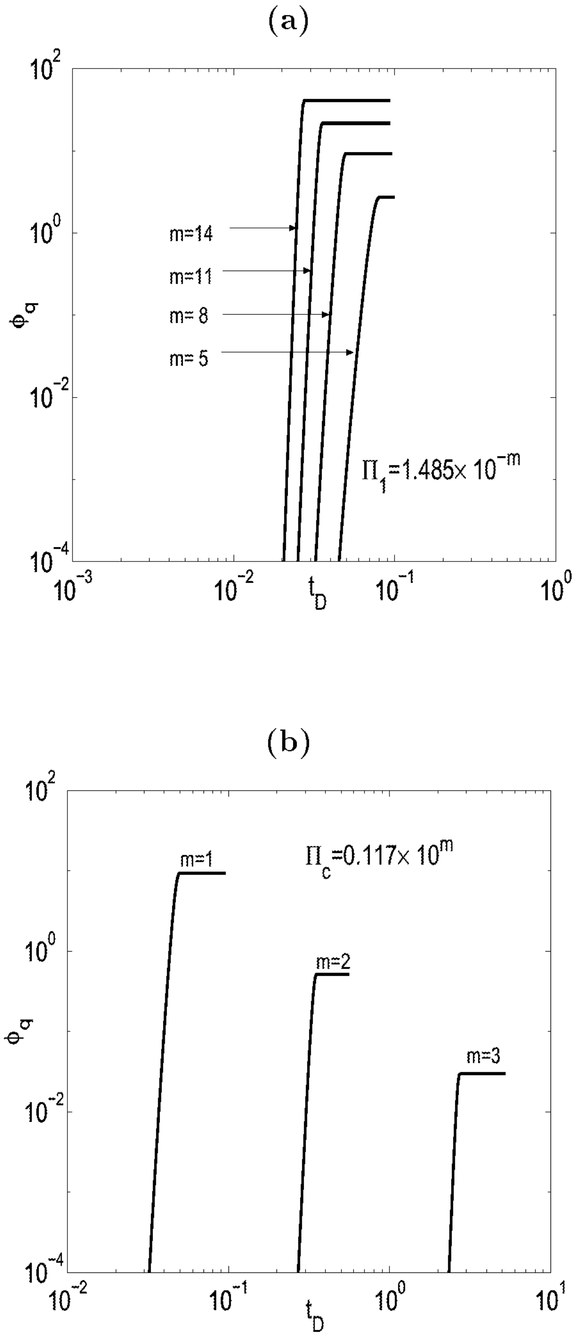

Figure 1: Variation of the rescaled nucleation fraction, ϕ_q, as a function of the dimensionless time, t_D. **(a)** Effect of $\Pi_1 = 1.485 \times 10^{-m}$, for $\Pi_2 = 9.6972 \times 10^7$, $\Pi_\rho = 2.981$ and $\Pi_H = 0$. **(b)** Effect of $\Pi_c = 0.117 \times 10^m$, for $\Pi_1 = 1.485 \times 10^{-8}$, $\Pi_2 = 9.6972 \times 10^7$, $\Pi_\rho = 2.981$ and $\Pi_H = 0$.

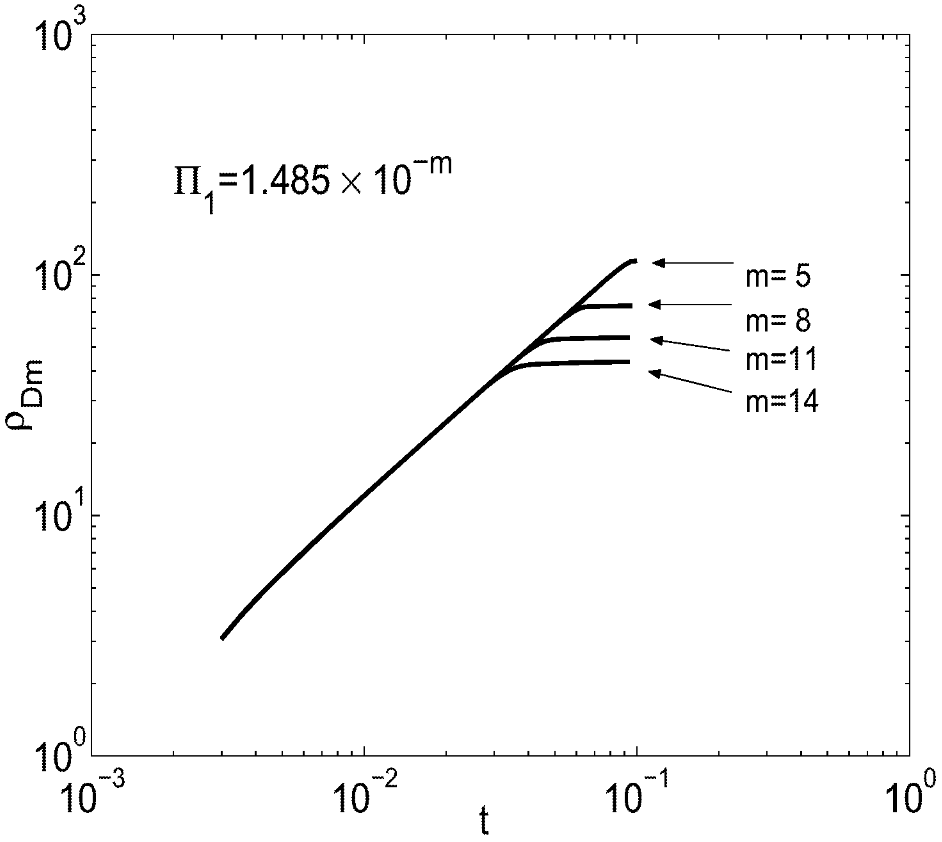

Figure 2: Variation of the mean rescaled dimensionless radius, ρ_{Dm}, as a function of dimensionless time, t_D. Effect of $\Pi_1 = 1.485 \times 10^{-m}$, for $\Pi_2 = 9.6972 \times 10^7$, $\Pi_\rho = 2.981$, $\Pi_c = 0.117 \times 10^1$ and $\Pi_H = 0$.

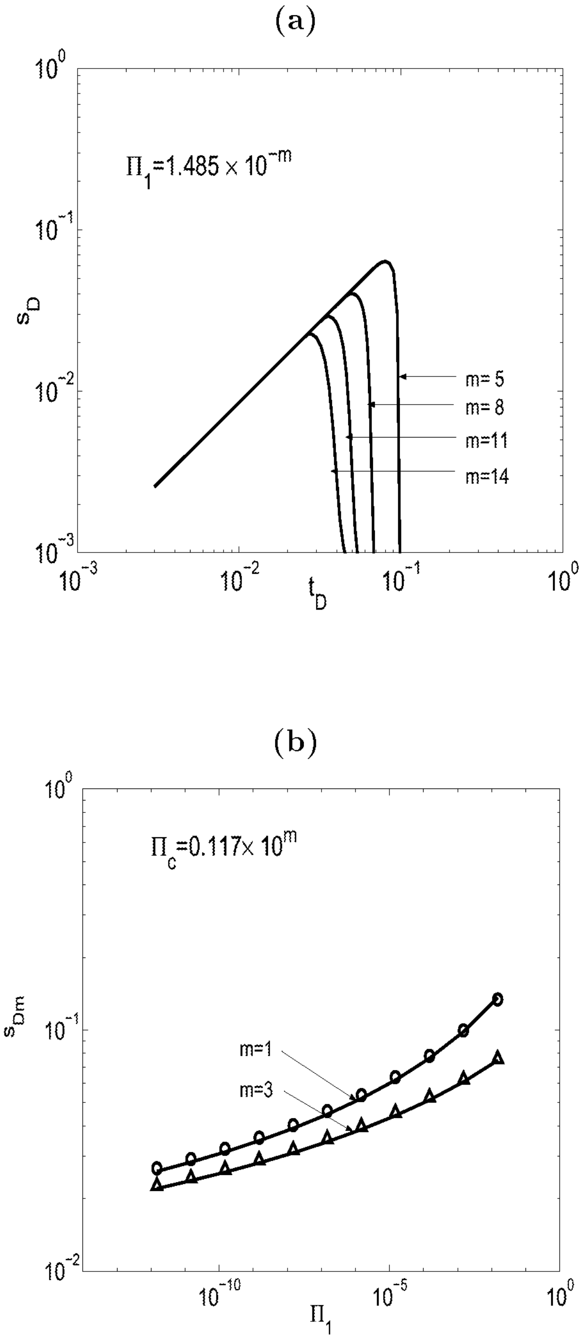

Figure 3: Numerical results for the rescaled supersaturation, s_D: **(a)** Variation as a function of dimensionless time, t_D. Effect of $\Pi_1 = 1.485 \times 10^{-m}$, for $\Pi_2 = 9.6972 \times 10^7$, $\Pi_\rho = 2.981$ and $\Pi_H = 0$. **(b)** Effect of the parameter Π_1 on the maximum rescaled supersaturation, s_{Dm}, for $\Pi_c = 0.117 \times 10^m$. Points correspond to the full numerical solution, solid lines correspond to the simpler problem.

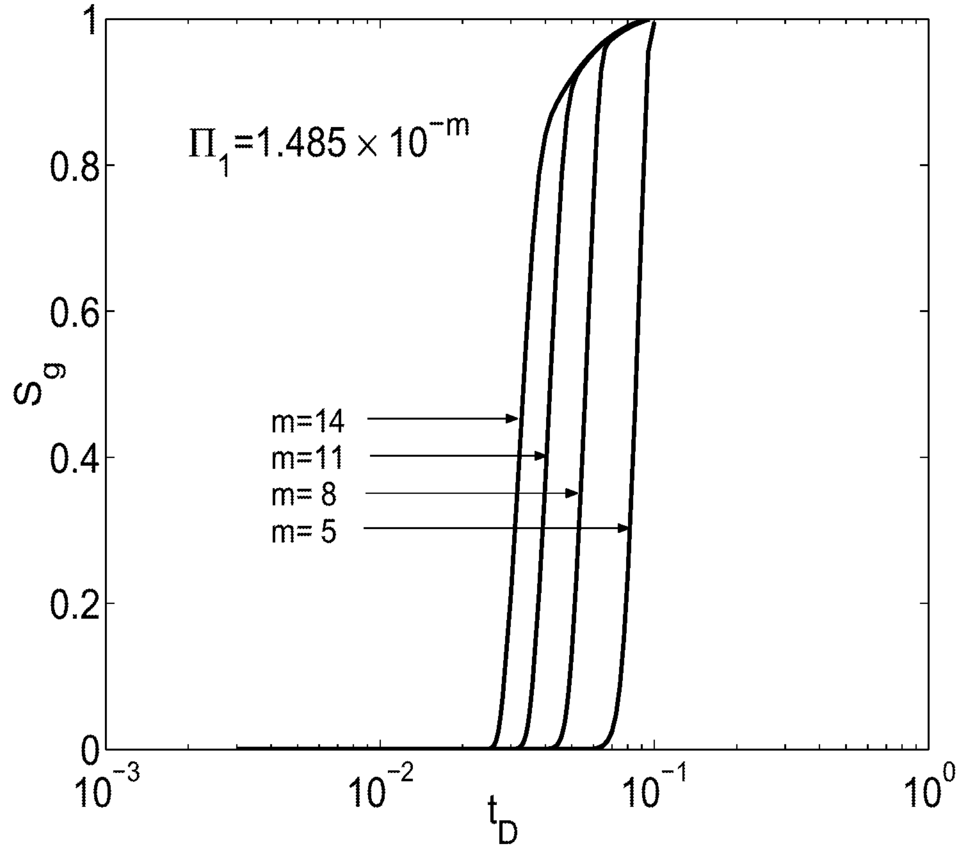

Figure 4: Variation of the gas saturation, S_g, as a function of dimensionless time, t_D. Effect of $\Pi_1 = 1.485 \times 10^{-m}$, for $\Pi_2 = 9.6972 \times 10^7$, $\Pi_\rho = 2.981$, $\Pi_c = 0.117 \times 10^1$ and $\Pi_H = 0$.

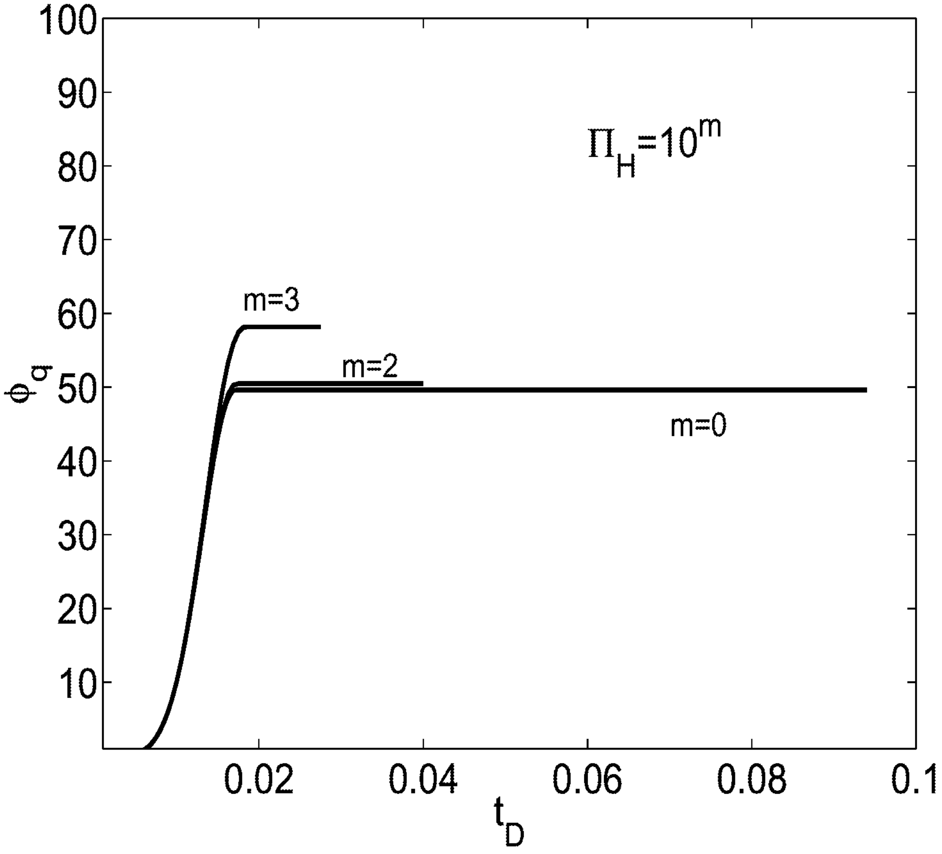

Figure 5: Variation of the rescaled nucleation fraction, ϕ_q, as a function of dimensionless time, t_D. Effect of $\Pi_H = 10^m$, for $\Pi_1 = 1.485 \times 10^{-8}$, $\Pi_2 = 9.6972 \times 10^7$, $\Pi_c = 0.117 \times 10^1$ and $\Pi_\rho = 2.981$.

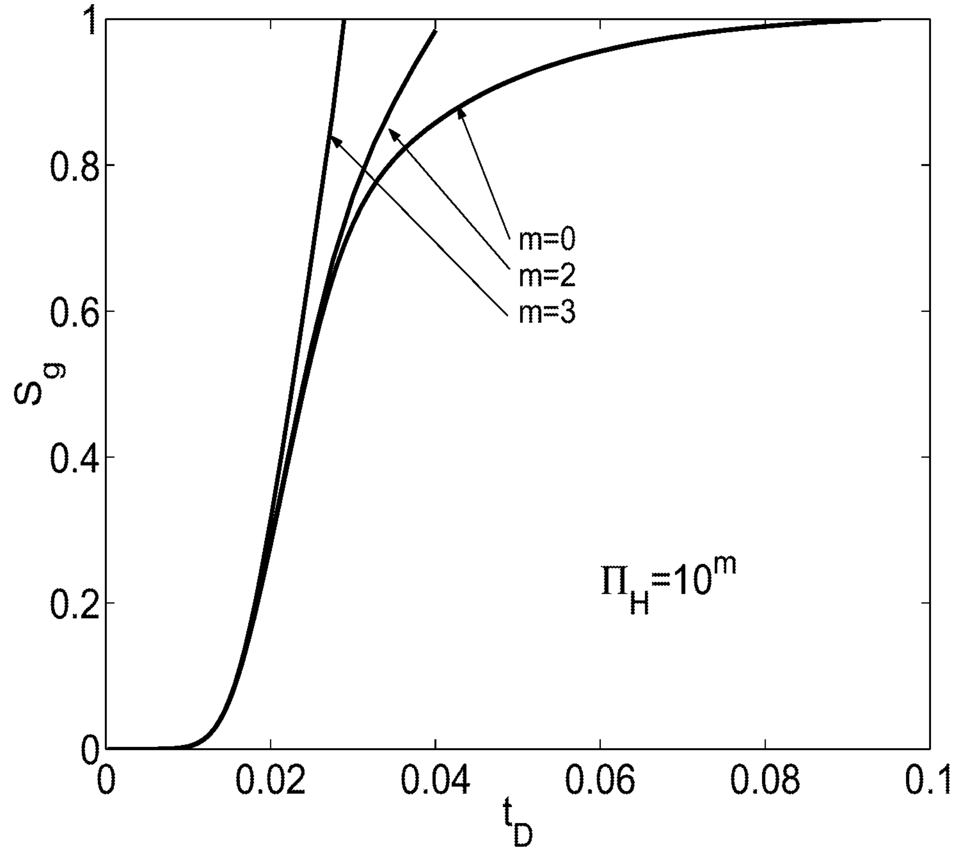

Figure 6: Variation of the gas saturation, S_g, as a function of dimensionless time, t_D. Effect of $\Pi_H = 10^m$, for $\Pi_1 = 1.485 \times 10^{-8}$, $\Pi_2 = 9.6972 \times 10^7$, $\Pi_c = 0.117 \times 10^1$ and $\Pi_\rho = 2.981$.

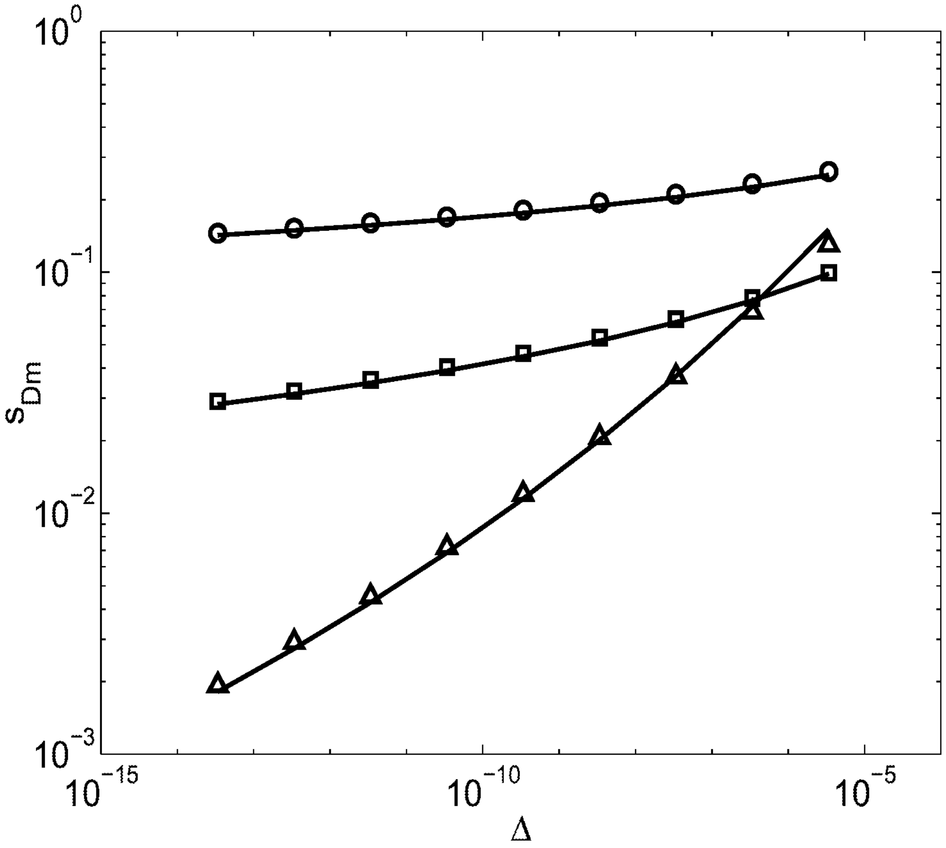

Figure 7: Maximum rescaled supersaturation, s_{Dm}, as a function of Δ for various cavity size distributions. Solid lines correspond to the simpler problem, points correspond to the full numerical solution [denoted by circles for the Rayleigh cavity size distribution, by triangles for a stretched exponential ($n = 0.2233$ and $\sigma = 0.1364$) and by squares for a stretched exponential ($n = 1.0$ and $\sigma = 1.0$)].

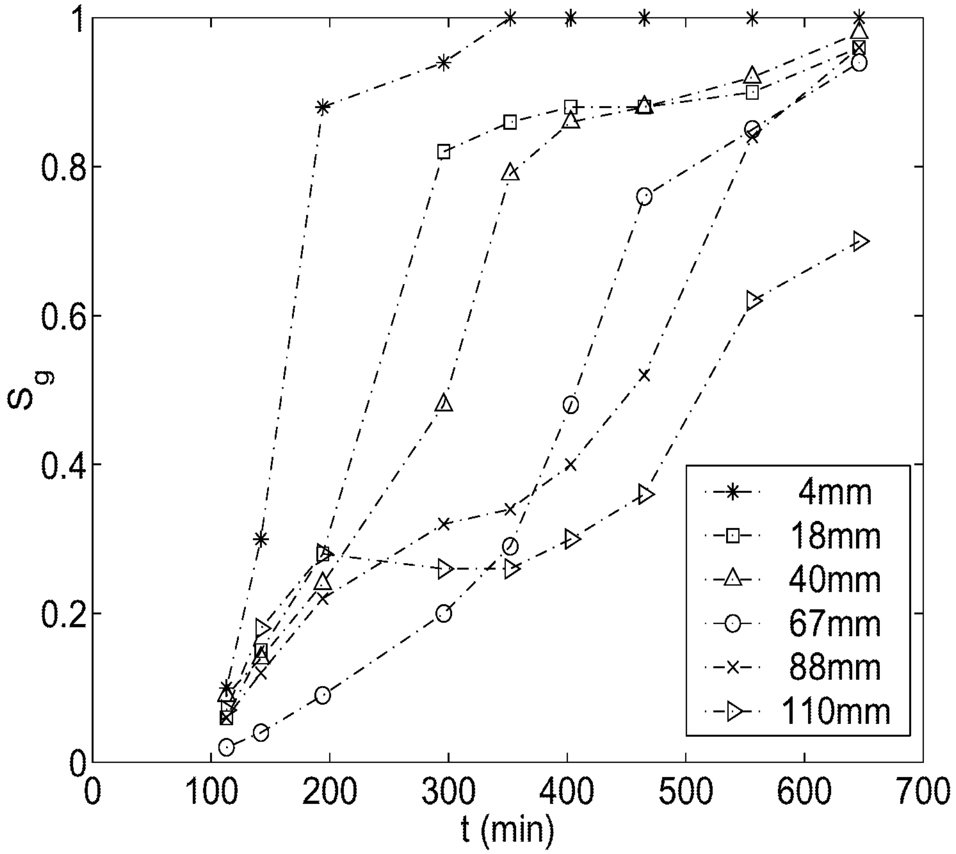

Figure 8: Gas saturation profiles for single-phase flash experiment as a function of time and for various axial positions along the core, L. Experimental data from Dehghani et al., (1997).

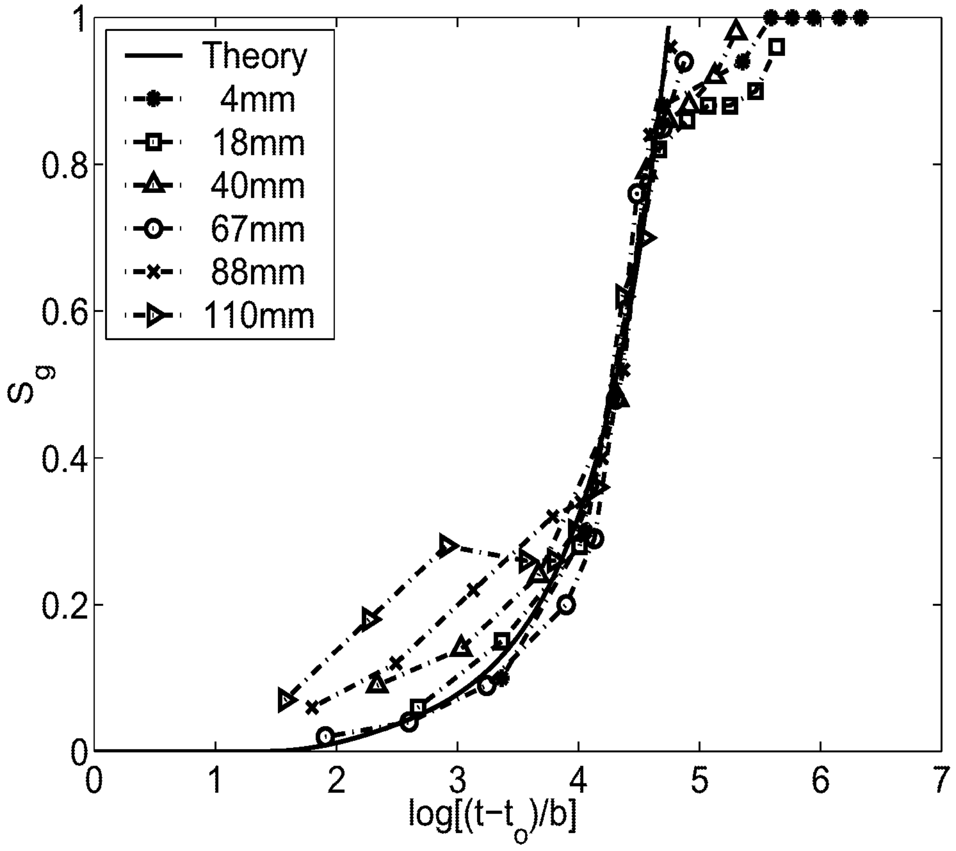

Figure 9: The evolution of the gas saturation as a function of a rescaled time for the experiments of Dehghani et al., (1997). Points denote experimental values and the solid line corresponds to the full numerical solution.

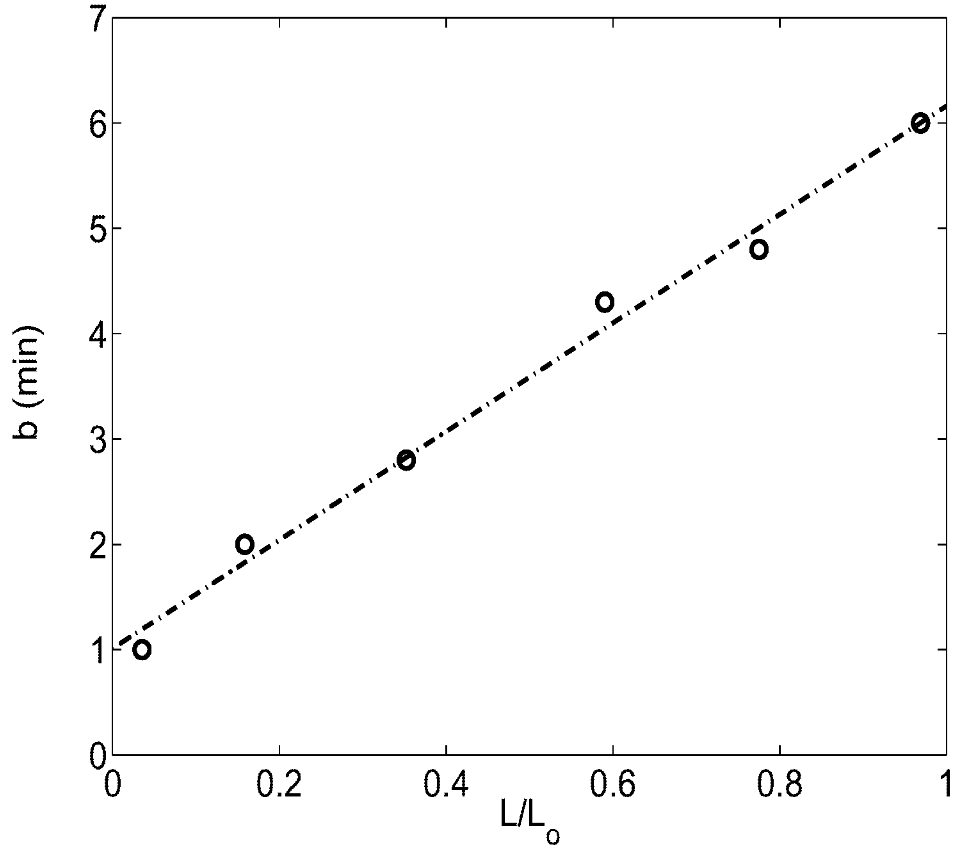

Figure 10: Variation of the rescaling factor, b, as a function of the dimensionless axial position along the core, L/L_o.

II. VAPOR-LIQUID FLOWS

The simultaneous flow of vapor and liquid phases is common to steam injection. Counter-current flows are encountered in Steam-Assisted-Gravity-Drainage (SAGD), and in steam injection in horizontal wells. They also appear in the context of heat pipes in a variety of processes (from geothermal to high-level nuclear waste disposal). Concurrent flows are found in typical displacements, in solution gas-drives near wells, and various other contexts. The interaction between heat transfer, heat flux, buoyancy and fluid flow affects the occupancy of phases and the flow characteristics, such as relative permeabilities. In this section we report on one specific study, based on what we term Darcian Dynamics, to describe the dynamics of the flow of a disconnected phase, in the form of ganglia, in the flow field of a displacing continuous phase. This effort parallels the analogous effort in Stokes flows, called Stokesian Dynamics. It was first described in last year's report. The method was further developed during the period elapsed, and the findings are described in detail in the section that follows. The method provides a computationally fast approach for the evaluation of quantities such as the critical capillary number for mobilization, the subsequent movement of the mobilized phase, and its possible stranding and/or coalescence. The study does not address phase-change or heat transfer issues, which are currently under consideration.

Darcian Dynamics: A New Approach for the Mobilization of Ganglia in Porous Media

Pouya Amili and Yanis C. Yortsos

INTRODUCTION

Two-phase flow in porous media has been the subject of many studies due to its importance in applications such as oil recovery, geothermal reservoirs, nuclear waste repositories and so on. The original motivation for this study was the modeling of co-current and counter-current vapor-liquid flows in porous media[1]. In many of these applications, due to capillary forces, one of the phases (and particularly the gas phase) becomes disconnected. The resulting bubbles (generically referred to here as ganglia) can be mobilized, if the flow rate of the other phase is sufficiently large, otherwise they become stranded. The existence of trapped ganglia perturbs the flow, which in turn affects trapping and mobilization conditions of other ganglia.

Modeling of trapping, mobilization, and or coalescence of disconnected ganglia in porous media has been investigated using two models, percolation theory and pore-network simulations. Percolation models[2,3,4,5] are computationally fast, however they only apply to very small flow rates where the process is quasi-static. In fact, they theoretically correspond to a zero capillary number. On the other hand, pore-network simulations do not have this disadvantage and apply to general dynamic flow conditions[6,7,8]. However, they can be computationally intensive.

In this work, we provide an alternative approach, which utilizes the fact that at the small scale, fluid flow is in fact described by Poiseuille's equation, which then leads to a Darcy law macroscale description. We use homogeneous flow conditions to describe the flow of the flowing phase, and account for the pore microstructure only in so far as capillary forces are concerned. In this approach, therefore, the governing equation is the Laplace equation, for the solution of which we can use the many advances made in potential theory. Specifically, the linear character of the equation allows us to apply a boundary integral method in which all the relevant flow information is mapped onto the boundaries of the two phases. (We should note that pore-network models essentially solve the same equation, except that they can also account for heterogeneity in the pore conductances. This cannot be captured by the present method.)

An analogous situation arises in the bulk flow of a suspension of particles, droplets or bubbles, where viscous forces predominate. A significant advance for the understanding of the flow properties of such systems is the method of Stokesian Dynamics, developed by Brady and Bossis[9]. Stokesian Dynamics is based on the linearity of the problem at small Reynolds numbers, where Stokes equations apply, and relies on a boundary integral method to compute the hydrodynamic forces between hydrodynamically interacting particles, as transmitted through the flowing fluid. In fluids in the bulk, these forces are driven by viscous shear, which compete with thermal and interparticle forces. In fluid flow through porous media, on the other hand, the relevant forces are pressure forces, expressed through Darcy's law, and capillary forces. Their competition determines the mobilization, coalescence, break-up and stranding of the various ganglia. The method we propose in this study, and which we will term *Darcian Dynamics*, is the analogue of Stokesian Dynamics to flow in porous media.

The use of a boundary integral technique enables us to investigate with relatively small computational requirements the interaction in a porous medium between flowing and dispersed phases, held trapped by capillary forces. With this approach, the pressure distribution on the interface of the various ganglia is directly obtained as a function of parameters, such as ganglion size and shape, their position and relative distance, and their population. Thus, the net effect of the viscous forces on each ganglion can be calculated and compared to the capillary forces to determine the possibility of mobilization and the subsequent movement. Effects of gravity can be included in a straightforward manner. Thus, Darcian Dynamics provides a fast way to model the flow behavior and its dependence on the various geometric and flow parameters.

The report is organized as follows: First, we present the theoretical foundation and the development of the Darcian Dynamics approach. Then, a numerical technique is introduced to solve the resulting boundary integral equation. Numerical results are presented that test the validity of the method and subsequently address the conditions for ganglia mobilization, probabilities of break-up and stranding, the effect of gravity and the effects of ganglia interaction.

DARCIAN DYNAMICS

1. Boundary integral formulation

We consider the flow of a fluid in a homogeneous porous medium in the presence of another phase, which is disconnected in the form of ganglia. We assume that the flowing fluid is an incompressible viscous liquid, while the disconnected phase is an inviscid fluid (e.g. vapor or gas). Under the assumptions noted above, the governing equation for the flowing fluid is described by the Laplace equation

$$\nabla^2 p = 0 \tag{1}$$

As pointed out above, pore-network simulators also solve a discrete form of the above equation. Hence, with the exception of the fact that in pore-network simulation the flow conductance can be heterogeneous, the fundamental premises of the two approaches are identical in this respect.

In this report, we consider the solution of Eqn. (1) in a two-dimensional geometry, in which the injected fluid flows with a far-field velocity $\mathbf{u}_0$ aligned, with no loss of generality, along the direction of the x-axis. The existence of the ganglia of the other phase perturbs the flow, thus, we will take the pressure and flow velocity as the superposition of a base flow and a perturbation

$$\begin{aligned} p_t &= p_d + p_o \\ \mathbf{u}_t &= \mathbf{u}_d + \mathbf{u}_o \end{aligned} \tag{2}$$

where $p_d = -\mathbf{u}_o x\mu / k$ and subscript d denotes the perturbation due to the presence of the ganglia. At the far field the perturbed flow rate and pressure vanish

$$p_d \rightarrow 0,\ \mathbf{u}_d \rightarrow 0 \quad \text{and} \quad \mathbf{u}_t \rightarrow \mathbf{u}_o\ ,$$

while at the ganglia interface, the normal flow velocity is zero

$$\mathbf{u}_t \cdot \mathbf{n} = 0$$

where **n** is the outer normal to the ganglia interface (see Figure 1). In appropriate dimensionless notation, the above can be rewritten as follows

$$\nabla^2 p_d = 0 \tag{3}$$

$$\begin{cases} \dfrac{\partial p_d}{\partial n} = \cos\theta & \text{on the interface} \\ \mathbf{u}_t = 1 & \text{at far-field} \end{cases} \tag{4}$$

and where θ is the angle between the normal **n** and the x-direction.

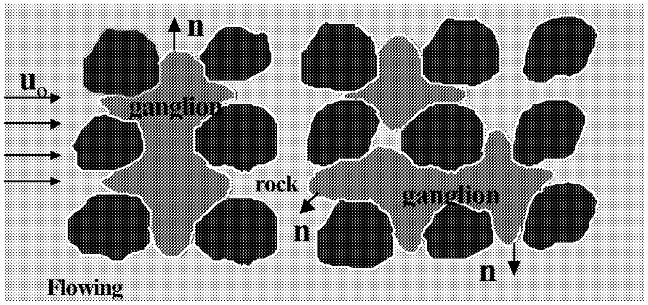

Figure 1. Schematic of the problem considered.

To solve (3) we will use an integral equation approach following advances from electrostatic potential theory. In that terminology, the free-space 2-D potential at location $\boldsymbol{\rho}$ due to a point sink (source) at $\boldsymbol{\rho}'$ is

$$\phi(\boldsymbol{\rho}) = \frac{1}{2\pi} \ln |\boldsymbol{\rho} - \boldsymbol{\rho}'| \tag{5}$$

For sources or sinks distributed on any contour C (here the ganglia interface) with density Q_l, the potential at point $\boldsymbol{\rho}$ is then given by superposition

$$p_d(\boldsymbol{\rho}) = \int_C \frac{Q_l(\boldsymbol{\rho}')}{2\pi} \ln |\boldsymbol{\rho} - \boldsymbol{\rho}'| \, dl_{\boldsymbol{\rho}'} \tag{6}$$

Differentiating the above equation by carefully accounting for the removable singularities[1] and using the boundary condition (4) results in

$$\lim_{\boldsymbol{\rho} \to C^+} \frac{\partial p_d}{\partial n_{\boldsymbol{\rho}}} = \frac{1}{2} Q_l(C) + \int_{C_0} Q_l(\boldsymbol{\rho}') \frac{\cos(\boldsymbol{\rho} - \boldsymbol{\rho}', \mathbf{n})}{2\pi |\boldsymbol{\rho} - \boldsymbol{\rho}'|} dl_{\boldsymbol{\rho}'} = \cos\theta \tag{7}$$

This is a Fredholm integral equation of the second kind for Q_l. For its numerical solution we apply the method of moments[1] which reduces the equation into a linear matrix equation. From the calculated Q_l, the pressure follows readily using Eqn. (6).

The Green's function in Eqn. (5) is based on an infinite system. For different geometries, the appropriate Green's functions must be used instead. For example, for flow confined between two impermeable boundaries parallel to the x-axis, the corresponding Green's function is[1]

$$\phi(x,y;x_0,y_0)=\frac{1}{4\pi}\ln\frac{1}{2}\left[\cosh\frac{\pi}{d}(x-x_0)-\cos\frac{\pi}{d}(y-y_0)\right]+ \\ \frac{1}{4\pi}\ln\frac{1}{2}\left[\cosh\frac{\pi}{d}(x-x_0)-\cos\frac{\pi}{d}(y+y_0-d)\right] \tag{8}$$

where d is the distance between two boundaries. This equation provides the potential at (x, y) caused by a point source at (x_0, y_0). If the system is periodic in the flow direction, we have[1]

$$\phi(x,y;x_0,y_0)=\frac{1}{4\pi}\ln\frac{1}{2}\left[\cosh\frac{2\pi}{a}(y-y_0)-\cos\frac{2\pi}{a}(x-x_0)\right] \tag{9}$$

where a is the period length. This geometry is useful when the number of ganglia is large and a periodic distribution along the flow direction may be assumed. Results will be provided for a number of cases in the various geometries, in the next section of this report.

2. Mobilization Conditions

To simulate the flow behavior in a system containing a dispersed and a disconnected phase, conditions for ganglia mobilization must be formulated. Specifically, we need to know if the pressure difference across a ganglion is sufficient to overcome the capillary forces, which hold it trapped. The pore microstructure gives rise to capillary thresholds, which are in general randomly distributed, following the distribution of the pore throats. Thus, we can assign dimensionless capillary pressure thresholds to all ganglia segments, which in the present notation will be expressed in terms of the capillary number of the problem. We find that the capillary threshold at any segment is[1]

$$p_{cD}=\frac{\beta}{Ca\, r_D} \tag{10}$$

where parameter $\beta = -\frac{16\ln(p_c)}{226F}$ is related to the percolation threshold of the lattice, p_c, and the formation factor, F, and we defined the capillary number $Ca = u_o\mu/\gamma$, where γ is the interfacial tension. The dimensionless radius r_D is in general a random variable, which in the following illustrations was distributed using the Rayleigh distribution

$$\alpha(r) = r\exp(-\frac{r^2}{2}) \tag{11}$$

The movement of a ganglion is decided by the difference between the viscous pressure and the capillary pressure threshold. At every step of the simulation, we first determine the segments of the ganglia subject to mobilization. For this, we form the pressure difference between pairs of ganglia segments i and j, belonging to the same ganglion, and subtract the capillary pressure threshold of the segment with the smallest pressure,

$$\Delta p_{i,j} = p_j - p_i - p_{cDi} \tag{12}$$

For a given ganglion, the maximum of $\Delta p_{i,j}$ over all i and j is found. If it is positive, segments i and j are advanced one pore, such that segment i moves outward and segment j inward. Otherwise the ganglion remains stationary. The procedure is repeated at every step, leading to new ganglia configuration, with different shapes, geometry and orientation, from which the fluid pressure can be comouted again. We note that this approach is essentially a quasi-static one, in that only one set of interfaces is advanced at any step. Given that time is not explicit in these calculations, however, this limitation is not significant.

The above were obtained in the absence of gravity. Buoyancy forces can play an equally important role to viscous, however. In the presence of gravity acting along the x-direction, the determination of the pressure field is as above, except that the base pressure must also include the hydrostatic contribution. The effect of gravity actually enters in the mobilization condition (12), which must now include the gravity contribution $l_{i,j}$ Ng_x, where we introduced the gravity number

$$Ng_x = \frac{\Delta\rho\, k\, g_x}{u_o \mu} \tag{13}$$

and $l_{i,j}$ is the projection of the distance between the two segments along the x-axis. The gravity number is also equal to the ratio between the Bond number, $Bo = \Delta\rho g k / \gamma$, and the capillary number. Gravity effects will be analyzed below.

NUMERICAL RESULTS

Using the method of moments, the integral equation was solved for a variety of situations of interest. In this section we first demonstrate the validity of the method by comparison with an analytical solution. Then, we consider the conditions for the mobilization of a single ganglion as a function of its size, confinement, flown rate, capillary environment and gravity. We analyze the sensitivity of the critical capillary number, above which a ganglion is mobilized to various parameters. We also investigate the effect of ganglia interaction.

1. Validity of the Method

To test the validity of the method, we compared the numerical predictions with some analytical results. In 2-D, analytical solutions exist for potential flow around a cylinder in an unbounded domain. Then, the dimensionless pressure at the interface is given by the simple equation

$$p=-\cos\theta. \tag{14}$$

(see Lamb[10]). Figure 2 shows a comparison between

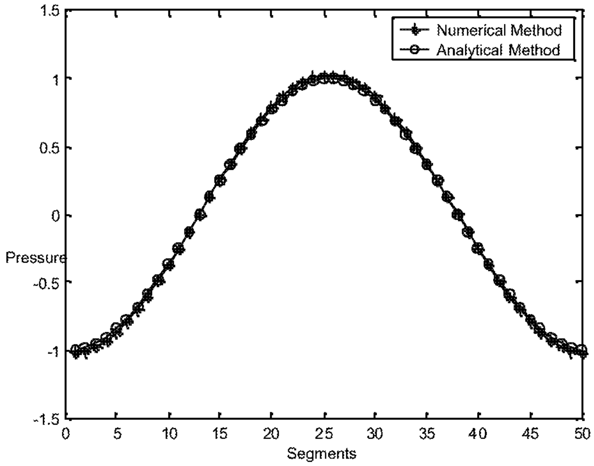

Figure 2. Comparison between analytical and numerical solutions for flow around a circular ganglion.

analytical and numerical results, using Darcian Dynamics, in which the circle was discretized in 50 segments. In Figure 2 the ordinate indicates the location of a segment, numbered clockwise from the downstream end. An excellent agreement is observed. Similar agreement was found for the case of an elliptical shape ganglion, for which an analytical solution is also possible[1]. Having confirmed the validity of the method, we then proceeded to investigate the sensitivity of the flow to various parameters.

2. Single Ganglion

First, we studied the mobilization and subsequent movement of a single ganglion. The first parameter studied was the ganglion size.

Ganglion size

The mobilization of a ganglion depends principally on its size. Increasing the size, increases the pressure gradient across the ganglion, resulting in a higher probability of mobilization. Figure 3 shows the variation of the critical capillary number as a function of size for a square-shaped ganglion of size nxn in a homogeneous capillary environment with the same capillary thresholds in each segment. As expected, there exists a critical capillary number for ganglia mobilization, which is of the order of 10^{-3}. This value is consistent with what is typically assumed regarding the importance of viscous forces in porous media. The critical capillary number decreases as the ganglion size increases, and becomes asymptotically inversely proportional to the linear ganglion size (and in Figure 3 inversely proportional to the square root of the ordinate, except for the periodic geometry case, which limits the ganglion size). The effect of confinement is also apparent. When the flow is confined, the critical capillary number decreases, due to the increased viscous pressure. This is more clearly illustrated in Figure 4. It is shown that the spacing of the confinement has a significant effect as long as it is smaller than a value, which is about 5 times the ganglion size. For larger spacings, the effect is not significant and the critical capillary number approaches its value in an infinite system. We add that the above behavior is qualitatively similar for ganglia of different shapes, although the shape and orientation of a ganglion does affect the numerical value of the critical capillary number.

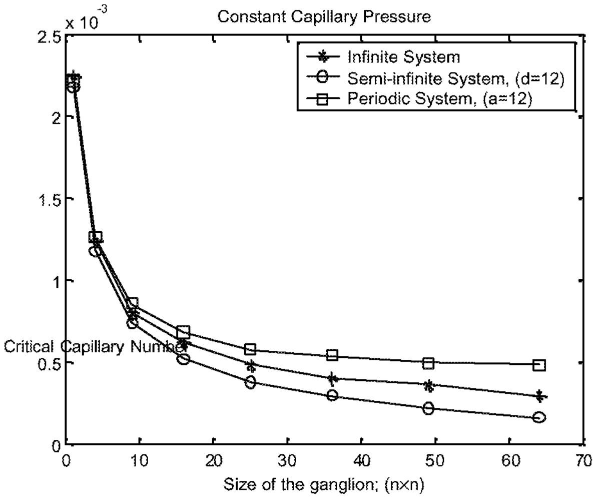

Figure 3. The dependence of the critical capillary number for mobilization on ganglion size for three different geometries: infinite, semi-infinite and periodic.

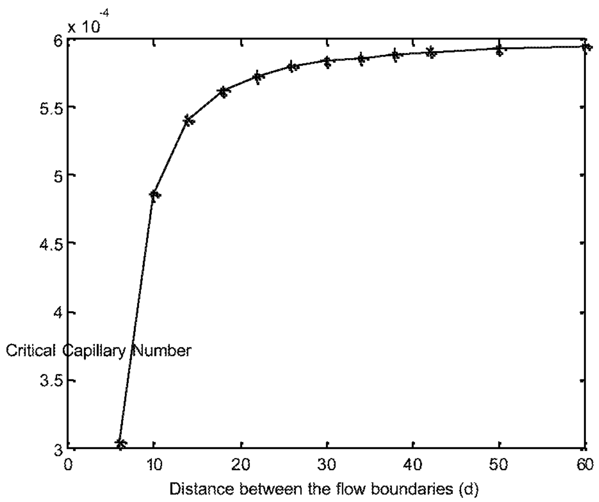

Figure 4. Critical capillary number for the mobilization of a square-shaped ganglion of size 4×4 confined between two parallel plates, plotted versus the distance between the plates.

Effect of flow rate

Following the onset of mobilization, ganglia undergo shape changes, break-up, coalescence and/or stranding. The applied flow rate (capillary number), the capillary threshold distribution and the original ganglion shape are important variables for these events. Figure 5 illustrates successive snapshots of the movement of a ganglion in a random capillary environment for a capillary number equal to $8x10^{-4}$, which is larger than the critical for this size. It is apparent that the mobilization and subsequent motion is accompanied by deformation, break-up and stranding of daughter ganglia of smaller size. The resulting ganglia interaction is quite complex and dynamic. Typically, ganglia movement occurs in a random capillary threshold environment, due to the randomness in the pore structure. In a random domain, the critical capillary number is also a random variable. Equivalently, we may define a probability of mobilization, given a value of the applied capillary number. Likewise, we can determine probabilities for break-up, stranding of all ganglia generated, etc. as a function of the capillary number. Figure 6 shows the curves obtained by simulating the motion of a ganglion of size 45, for several realizations of the random capillary thresholds. The key features of the curves obtained are as follows: (i) mobilization, break-up and stranding are stochastic processes; (ii) the variation of the probabilities for these events vary in a rather narrow interval of the capillary number, of the order of 10^{-4}-10^{-3}, the width of which also depends on the variance of the threshold distribution; (iii) the probability of break-up becomes one for sufficiently large capillary numbers; (iv) the probability of stranding becomes negligible if the flow rate is sufficiently large. It is important to mention here that although a ganglion can go through several break-ups during its movement, the data presented correspond to the first break-up only. It is also important to mention that a value of unity for the probability of stranding in this case means the stranding of all daughter ganglia. Similarly, a value of zero means that at least one daughter ganglion is still mobile before leaving the domain of the simulation.

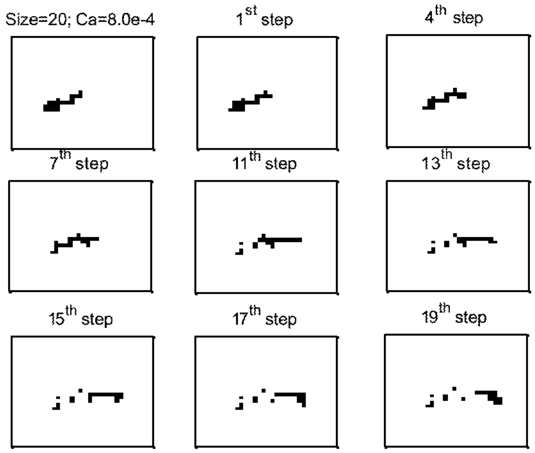

Figure 5. Snapshots of the movement of a ganglion of size 20 in a random capillary threshold environment for Ca=8.0e-4.

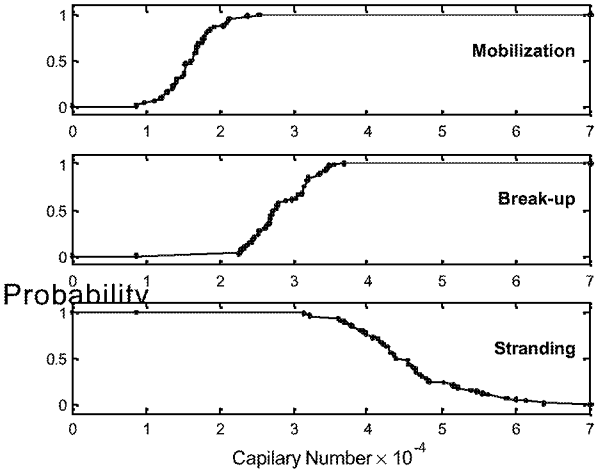

Figure 6. Probabilities of mobilization, break-up, and stranding after the mobilization of a single ganglion of size 45 in a heterogeneous medium, plotted as a function of the capillary number.

Effect of gravity

When buoyancy forces are considered, both the magnitude and the direction of the gravity vector are important. If gravity aids viscous forces, mobilization is facilitated, and the critical capillary number decreases with an increase in the Bond number. In such cases, the critical capillary number is a decreasing linear function of the Bond number, as can be readily shown. Figure 7 shows the corresponding relationship, obtained from simulations in a homogeneous capillary threshold environment, with a ganglion of size 45. There exists a critical Bond number of the order of about 3×10^{-4}, above which the ganglion is mobilized by gravity forces alone. In the opposite case, when gravity opposes mobilization (for example, when flow and gravity act in the same direction), the situation is a bit more complex. Now, the critical capillary number increases with the Bond number. Furthermore, when the velocity is small, for sufficiently large Bond numbers, the ganglion is mobilized in the direction opposite to the flow. In other words, there exists now a critical Bond number, which depends in a straight-line relationship on the capillary number. In-between the two lines is the regime where the ganglion remains stationary. The two lines intersect at a critical point, beyond which a single line separates two regimes, one in which mobilization is in the direction of flow (higher Ca) and another in which it is in the opposite direction (lower *Ca*). Subsequent to mobilization, the ganglion undergoes a sequence of events similar to the previous, except that when gravity effects are significant, there is a preference for the ganglion to elongate along the gravity direction[1].

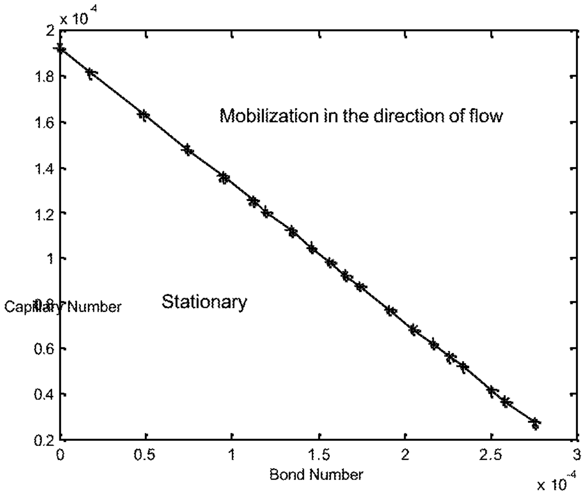

Figure 7. Regimes of mobilization in a diagram involving the capillary and the Bond numbers, for the case when gravity aids the mobilization.

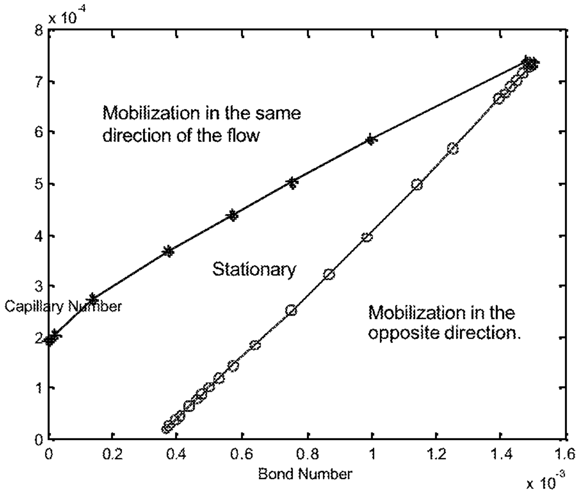

Figure 8. Regimes of mobilization in a diagram involving the capillary and the Bond numbers, for the case when gravity aids the mobilization.

3. Ganglia interaction

The mobilization and subsequent evolution of a ganglion depends also on the presence of neighboring ganglia. A "crowding" effect has been postulated by previous authors[11], in which the increase of the population density of ganglia increases the viscous forces on the system, thus making it easier to mobilize ganglia, even at relatively small capillary numbers, where viscous effects are not expected to be significant. To investigate such phenomena, we considered the effect of distance and orientation of one ganglion on the mobilization of another identical ganglion. For simplicity, we assumed two identical circular ganglia confined between two parallel plates, as shown in the insets of Figures 9 and 10. First, we examined the case in which the ganglia are stacked in a direction perpendicular to the boundaries (Figure 9).

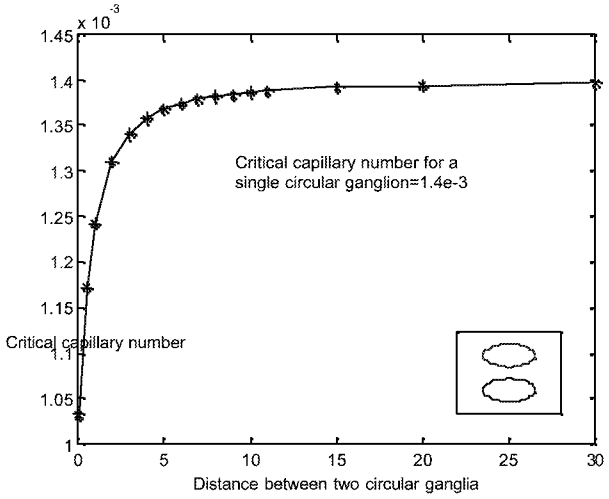

Figure 9. Critical capillary number for ganglia mobilization plotted versus the distance between the two ganglia confined between two parallel plates and stacked perpendicular to the plates (see inset). Homogeneous capillary environment.

Figure 9 shows the critical capillary number for the mobilization of the ganglia (both are mobilized simultaneously due to the symmetrical location) as a function of the distance between them. In this configuration, it is apparent that the presence of the neighboring ganglion increases the viscous forces in the system, thus making the mobilization of the other ganglion (and itself) easier. Indeed, there is approximately a 40% reduction in the value of the critical capillary number as the two ganglia approach one another. A crowding effect is indeed present, leading to enhanced viscous forces.

When the configuration was changed, however, such that the two ganglia were aligned along the flow direction, parallel to the plates, the effect was in fact opposite to the previous (Figure 10). In this case, increasing the distance between the ganglia resulted in a decrease of the critical capillary number, which asymptotically approached the critical capillary number for a single ganglion as the distance becomes sufficiently large. It appears that as the ganglia approach each other, such configurations lead to a better streamlined object, which offers smaller viscous resistance, hence an increase in the critical capillary number. This unexpected effect is opposite to the conventional crowding effect. The effect was confirmed using a different numerical technique, as well. One concludes that not only the density, but also the relative position and orientation of the ganglia are important factors in ganglia mobilization.

An illustration of the non-trivial aspects of these effects is shown in Figure 11, where the effect of the orientation of the two ganglia on the critical number for the mobilization of the upstream ganglion is portrayed. As in Figure 10, the critical capillary number of a single isolated circular ganglion in this geometry is 1.4×10^{-3}. The second ganglion is then rotated counter-clockwise around the reference one, while maintaining the same distance. Clearly, the configuration in which the ganglia are stacked perpendicular to the flow is the one with the strongest crowding effect, while the alignment along the flow direction in fact favors the trapping of the ganglion. Additional work in this direction, including the subsequent evolution of the mobilized ganglion is discussed in Amili[1] and is also actively pursued at this time.

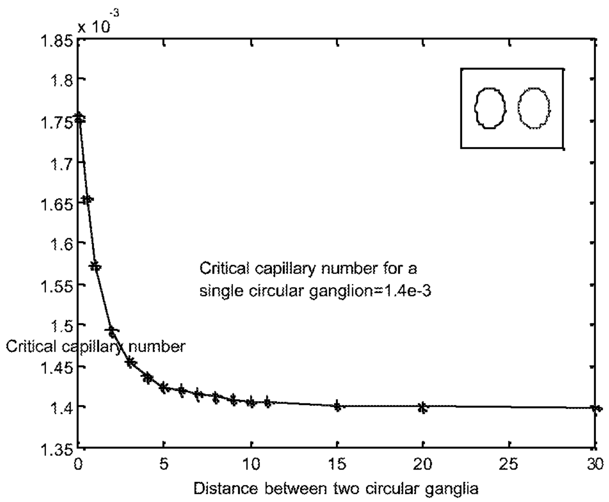

Figure 10. Critical capillary number for ganglia mobilization plotted versus the distance between the two ganglia confined between two parallel plates and stacked perpendicular to the plates (see inset). Homogeneous capillary environment.

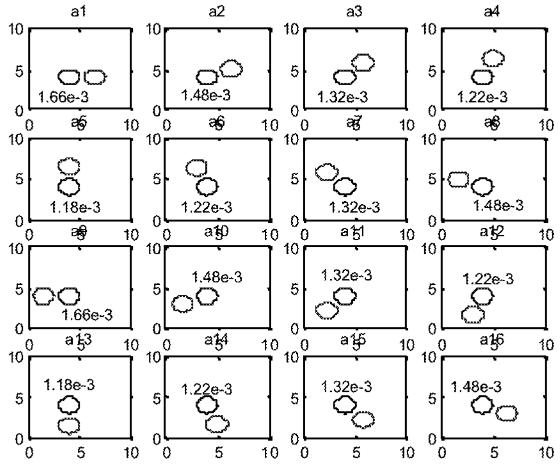

Figure 11. The critical capillary number for the mobilization of the upstream ganglion for different positions of the two ganglia. (Note that the lower two panels are mirror images of the top two.) Homogeneous capillary environment.

CONCLUSIONS

In this report we developed a new method, which we termed Darcian Dynamics, in analogy with Stokesian Dynamics for flow of bulk fluids, to study and simulate two-phase (liquid-gas) flow in porous media, when the gas phase is disconnected in the form of ganglia. The method assumes homogeneous flow conditions for the flowing liquid phase, but heterogeneous capillary thresholds. Using techniques from potential theory, we describe the hydrodynamic interaction in terms of the solution of an integral equation, valid over the ganglia interfaces. We use this method to explore the conditions for the onset of ganglia mobilization and their subsequent motion. Break-up, coalescence and stranding are simulated. The interaction between ganglia and the flowing phase is influenced by many parameters, several of which have been studied in this work. In particular, we examined effects of size, orientation, gravity, and ganglia interaction. The latter does not always enter as a crowding effect, as intuitively expected. The technique is currently being further developed in order to address a variety of interesting problems.

REFERENCES

1. Amili, P.: "Two Studies in Simultaneous Two-Phase Flow in Porous Media: I. Heat Pipe Stability, II. Darcian Dynamics" Ph.D. dissertation, University of Southern California, Los Angeles, California (2002).
2. Melrose, J. C. and Brander, C. F.: "Role of Capillary Forces in Determining Microscopic Displacement Efficiency for Oil Recovery by water Flooding," *Can. J. Pet. Tech.* **13,** 54-62 (1974).
3. Scriven, L. E. Larson, R. G. and Davis, H. T.: "Percolation Theory of Residual Phases in Porous Media," *Nature* **268,** 409-413 (1977).
4. Lerman ,K. Chandler, R. Koplik, J. and Willemsen, J. F.: "Capillary Displacement and Percolation in Porous Media," *J. Fluid Mech.* **119,** 249-267 (1982).
5. Wilkinson, D. and Willemsen, J.: "Invasion Percolation: A New Form of Percolation Theory," *J. Phys. A* **16,** 3365-3376 (1983).

6. Dias, M. M. and Payatakes, A. C.: “Network Models for Two-Phase Flow in Porous Media. Part 1. Immiscible Microdisplacement of Non-Wetting Fluids,” *J. Fluid Mech.* **164,** 305-336 (1986).
7. Dias, M. M. and Payatakes, A. C.: “Network Models for Two-Phase Flow in Porous Media. Part 2. Motion of Oil Ganglia,” *J. Fluid Mech.* **164,** 337-358 (1986).
8. Constantinides, G. N. and Payatakes, A. C.: “Network Simulation of Steady-State Two-Phase Flow in Consolidated Porous Media,” *AIChE Journal* **42,** 369-382 (1996).
9. Brady, J. F. and Bossis, G.: “Stokesian Dynamics,” *Ann. Rev. Fluid Mech.* **20,** 111-157 (1988).
10. Sir H. Lamb. *Hydrodynamics*. Dover, New York (1945).
11. Valavanides, M.S. Constantinides, G.N. Payatakes, A.C.: “Mechanistic Model of Steady-State Two-Phase Flow in Porous Media Based on Ganglion Dynamics,” *Transp. Porous Media* **30**, 267-299 (1998).

III. DYNAMICS OF IN-SITU COMBUSTION AT VARIOUS SCALES

A well-established method for the recovery of heavy oils is in-situ combustion. Despite its long history, however, many aspects of the process are not well understood. In our previous report we described two particular aspects: The description of the process at the pore-network scale, and its upscaling at the large scale for field applications. In particular, we applied an asymptotic approach to describe the movement of combustion fronts in porous media as gas-dynamic discontinuities and in the presence of heat losses, but only for homogeneous systems. This approach is essential for the upscaling of the process at the field scale and for the assessment of the effect of macrcoscale heterogeneity on issues such as sustained front propagation, extinction, efficiency, etc. In this report, we extend the effort to account for the effect of heterogeneity in the form of a layered reservoir on the propagation of combustion fronts. It is found that heterogeneity plays an important role in setting extinction criteria for combustion and should be very carefully considered in the design of combustion projects. These findings were also supported by pore-network simulations, which will be reported in the final report. Progress was also made to the upscaling of reaction fronts using hybrid algorithms. This will also be reported in the final report.

The Effect of Heterogeneity on In-situ Combustion: The Propagation of Combustion Fronts in Layered Porous Media

I. Yücel Akkutlu and Yanis. C. Yortsos

1 Introduction

The sustained propagation of a combustion front is necessary for the recovery of oil using in situ combustion. Compared to other methods, in situ combustion involves the complexity of exothermic reactions and temperature-dependent reaction kinetics. The combustion dynamics are influenced by the fluid flow of injected and produced gases, the heat transfer in the porous medium and the surroundings, the rate of combustion reaction(s) and the heterogeneity of the porous medium. In the presence of heat losses, the possibility exists of extinction (quenching) as well as the necessity of ignition for sustained propagation.

Combustion fronts in porous media have been studied extensively in the context of filtration combustion. Analytical treatments of the combustion front dynamics is possible, by using methods similar to the analysis of laminar flames (gaseous phase combustion in the absence of porous medium). Using the property that the activation energy of the overall reaction is large in comparison with the thermal enthalpy [1], Britten and Krantz [2, 3] provided an asymptotic analysis in one-dimensional systems of reverse combustion in coal gasification. In detailed works, Schult *et al.* [4, 5] investigated the adiabatic combustion of a homogeneous porous medium, in the contexts of fire safety and the synthesis of compacted metal powders (SHS processes). More recently, forward and reverse filtration combustion in a non-reacting porous medium was studied using a pore-network model by Chuan and Yortsos [6]. In parallel, a detailed analysis of the propagation of planar combustion fronts in porous media was undertaken by the present authors [7]. They addressed the issue of steady-state propagation under both adiabatic and non-adiabatic conditions, but emphasized the effect of heat losses to the surroundings. The latter were modeled both by conduction (for subsurface applications) and by convection (for laboratory applications). A number of important results were obtained, which are briefly summarized in the next section.

In this chapter, we consider the use of the same type of approach in an attempt to answer the important question of the effect of the porous medium heterogeneity on the sustained propagation of combustion fronts. As in other contexts, a simple representation of heterogeneity is through the use of layers. For example, layered systems have been employed to investigate heterogeneity effects on processes such as miscible and immiscible displacement [8]. In the latter processes, the effect of heterogeneity typically enters through fluid mobility (where the displacement in a more permeable layer is further accelerated in the case of unfavorable mobility ratio, and conversely retarded in the case of a favorable mobility ratio). In the combustion case of interest here, however, the coupling enters through the heat transfer between the layers, to be expressed by a simple convective-type model. The assumption is rigorously valid if the layers are sealed from one another, or if the fluid mobility remains constant through the process, which is a good assumption, when the net rate of gas generation is small. Then, the injection rate in each layer is constant in time, and proportional to the layer permeability. The analysis will be conducted for two simple geometries, a two-layer system and a symmetric three-layer system, under both adiabatic and non-adiabatic conditions. Our emphasis is on understanding how the heat transfer coupling affects the front propagation in the different layers, on whether or not a state of coherent traveling fronts develops and on whether or not a sufficiently sharp permeability contrast can lead to the extinction of the process. Throughout the chapter, we will use methods similar to the single-layer problem of [7]. Because of the relevance of those results to the present problem, they are briefly summarized below.

2 Preliminaries: Combustion in a Single Layer

Under adiabatic conditions, it is found that there is always sustained propagation, where the front temperature is given by

$$\theta_f \equiv T_f/T_o \approx 1 + q, \quad \text{where} \quad q = \frac{Q\rho_f^o}{(1-\phi)c_s\rho_s T_o} \tag{1}$$

we denoted the heat of reaction by Q, the initially available fuel content per total volume by ρ_f^o and the volumetric heat capacity of the porous medium by $(1-\phi)c_s\rho_s$. Clearly, equation (1) shows that the front temperature is practically independent of the front velocity.

Under non-adiabatic conditions, however, front temperature and front velocity are coupled. When the heat losses are modeled by heat conduction in semi-infinite surroundings, the temperature of the front is obtained from the different equation

$$\theta_f = 1 + \frac{q}{\omega^{2/3} z_1 - \omega^{4/3}\sqrt{z_1}} \qquad \text{where} \qquad \omega = \frac{2\alpha_s}{H v_i} \tag{2}$$

and z_1 is the positive root of the algebraic equation

$$\frac{\bar{\mu}^2}{z_1} = (1 + \bar{\mu} z_1)^2, \qquad \text{with} \qquad \bar{\mu} = -\left(\frac{\omega}{V_D}\right)^{2/3}. \tag{3}$$

In (2), H is the thickness of the porous medium, v_i the injection velocity, $V_D = V/v_i$ is the dimensionless front velocity normalized with the injection velocity, and $\alpha_s = \lambda/(1-\phi)c_s$ is the effective thermal diffusion coefficient. A similar equation applies for the convective heat losses case.

In all cases, the front velocity is related to the front temperature through the following equation

$$V_D^2 = \mathcal{A}\theta_f \text{exp}\left(-\frac{\gamma}{\theta_f}\right)\left(\frac{1-\mu V_D}{1+\mu_g V_D}\right) \tag{4}$$

where $\gamma = E/RT_o$ is the Arrhenius number, E is the activation energy, R the universal gas constant, μ and $\mu_g = \mu_{gp} - \mu$ are dimensionless stoichiometric coefficients for oxygen and produced gas due to reaction, respectively (see [7] for more details), and

$$\mathcal{A} = \frac{a_s \alpha_s k_o Y_i p_i}{q E I_\eta v_i^2} \qquad \text{where} \qquad I_\eta = \int_0^1 \frac{(1-\eta)}{\psi(\eta)} d\eta. \tag{5}$$

In addition, in Equation (5), a_s is the specific surface area per unit volume, k_o the pre-exponential factor, p_i the initial gas pressure, $\eta = 1 - \rho_f/\rho_f^o$ the extent of fuel conversion depth and $\psi(\eta)$ is a dimensionless function representing the dependence of reaction on η.

In the adiabatic case, there is always a solution for the front velocity as a function of the injection velocity. This relation is plotted in Figure 1 for typical parameter values. It shows that the front velocity is proportional to the injection velocity at sufficiently small injection rates, and increases more slowly as the injection velocity becomes larger. In thermally decoupled layers, under adiabatic conditions, we should expect, therefore, that combustion fronts in high permeability layers would travel faster, according to the dynamics portrayed in Figure 1, for example.

On the other hand, in the non-adiabatic case, the coupling between velocity and temperature has significant implications. Figures 2 and 3 show results obtained for the front temperature versus the injection velocity for a varying thickness of the porous medium. The corresponding variation of the front velocity with the injection velocity is shown in Figure 4. For fixed thickness and injection velocity, the system typically shows multiplicity in the solutions, and for sufficiently thin layers, extinction and ignition points, E_c and I_c, exist in temperature (Figures 3, 2). As H decreases, the extinction threshold rapidly increases, namely it requires an increasingly larger injection velocity for the reaction to be sustained, as shown in the Figures. Between these thresholds, there exist three separate solutions for given injection and reservoir parameters, consisting of a stable low temperature (and velocity) branch in the vicinity of the initial conditions, a stable high temperature (and velocity) branch, where rigorous combustion takes place, and an unstable intermediate branch connected to the latter. Such behavior is typical of multiple solutions in other areas in reaction engineering. The upper branch is the solution corresponding to a proper combustion front. It approaches and runs parallel to the adiabatic solution. For a given H, the sensitivity of the front variables to the injection velocity is very large near the threshold, but becomes almost negligible above it. Likewise, the sensitivity of the extinction threshold E_c to the reservoir thickness is significant for values of H the order of 1 m or less, for the parameters assumed here. As H decreases, the extinction threshold rapidly increases, namely it requires an increasingly larger injection velocity for the reaction to be sustained, as shown in the Figures. Conversely, at larger H, the threshold decreases, and for sufficiently large values, multiplicity disappears altogether.

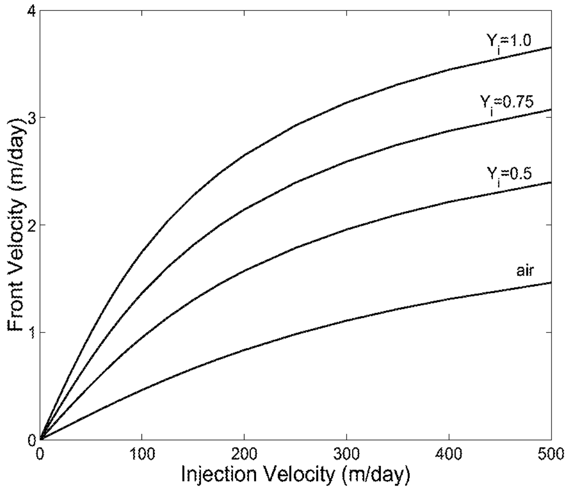

Figure 1: Steady-state front velocity versus injection velocity for different injected oxyen concentration for a single layer porous medium under adiabatic conditions.

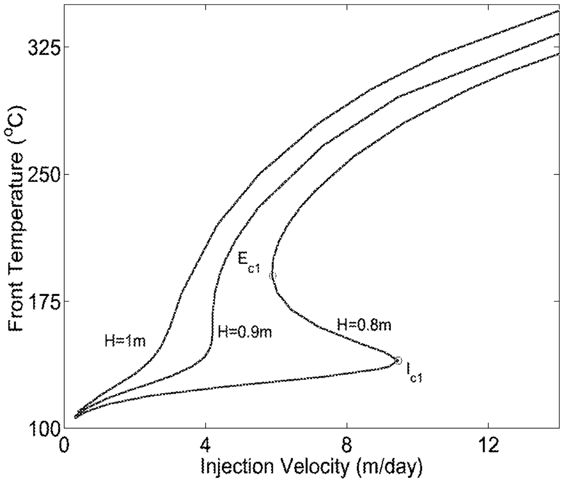

Figure 2: Front temperature versus injection velocity for a single layer under non-adiabatic conditions. I_{c1}=(9.45,140.0), E_{c1}=(5.9,190.0).

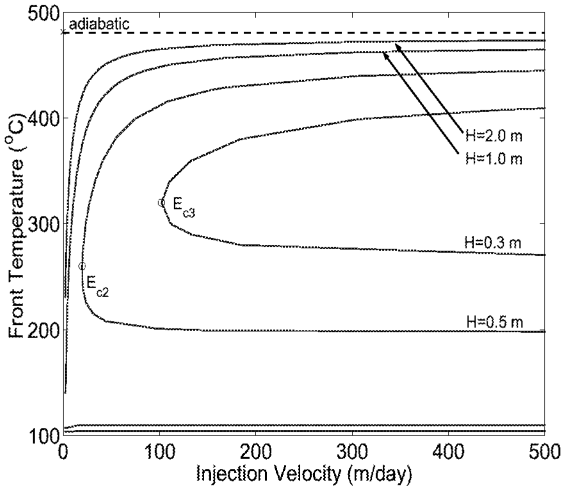

Figure 3: Front temperature versus injection velocity for a single layer under non-adiabatic conditions. E_{c2}=(19.7,260.0), E_{c3}=(102.1,320.0).

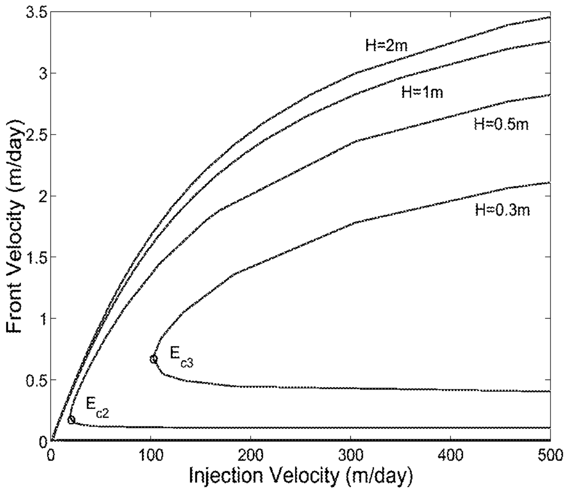

Figure 4: Front velocity versus injection velocity for a single layer under non-adiabatic conditions. E_{c2}=(19.7,260.0), E_{c3}=(102.1,320.0).

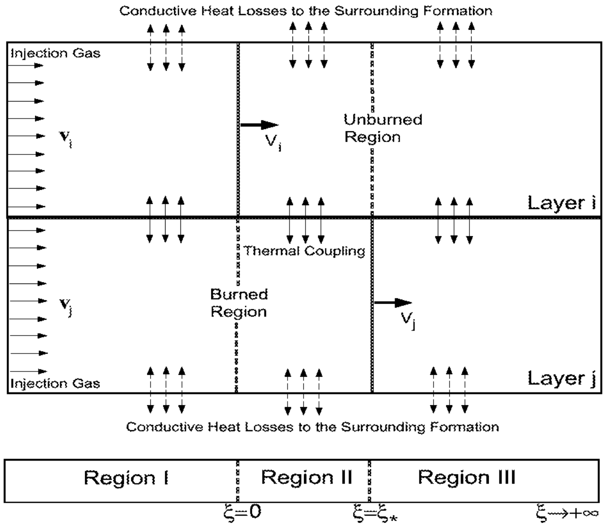

Figure 5: Schematic of the notation used for the propagation of combustion fronts in a two-layered porous medium.

Analogous results are obtained when the heat losses are of the convective type, which would be appropriate for a laboratory application. In fact, in such cases, the system equations are simpler. One can combine the two applications [7], to obtain an expression for the effective heat transfer coefficient $\tilde{h}$ in a system controlled by heat conduction. In terms of the Nusselt number, we have

$$\mathrm{Nu} \equiv \frac{\tilde{h}H}{\lambda} = \frac{HV}{2\alpha_s}\left(\omega_i^{1/3} z_i^2 + 2\omega_i z_i^{3/2} + \omega_i^{5/3} z_i - \omega_i^{-1}\right) \tag{6}$$

Further details can be found in [7].

3 Combustion in a Two-Layered Porous Medium

Consider, now, the application of the same approach to a layered porous medium. The first geometry to be considered is a two-layered system, as shown in the schematic of Figure 5.

The steady-state propagation of combustion in the two layers i and j is considered. The layers are homogeneous, but with different permeabilities (with layer j being more permeable), and hence different injection velocities. In the absence of mobility variation effects, these are proportional to the layer permeability. We assume only thermal coupling across the layers, which will be expressed in terms of a convective-type heat model. Due to thermal coupling, it is apparent that isolated front propagation in each layer with front velocities dictated, e.g. by Figure 4, cannot take place. Indeed, we expect that the faster traveling front in layer j will slow down due to heat losses to layer i the front of which will accelerate until a coherent state is reached and the front velocities are the same in each layer. In the moving coordinate with respect to the combustion front, $\xi = x - V_D t$, where $x = \tilde{x}/l_*$ and $t = \tilde{t}/t_*$ are the dimensionless space and time variables with $l_* = \alpha_s/v_i$ and $t_* = l_*/v_i$, the dimensionless thermal energy balances for the two layers read

$$A_i\theta_i' = \theta_i'' + \sigma(\theta_j - \theta_i) - h_i(\theta_i - 1) \tag{7}$$

$$A_j\theta_j' = \theta_j'' + \sigma(\theta_i - \theta_j) - h_j(\theta_j - 1) \tag{8}$$

where prime denotes derivatives, and we have introduced

$$A_i = a\rho v_i - V_D \cong -V_D, \qquad A_j = a\rho v_j - V_D \cong -V_D \tag{9}$$

The dimensionless parameter $a \ll 1$ represents the ratio of the volumetric heat capacity of the gas to the solid matrix, σ is the non-dimensional coefficient for the heat exchange between the two neighboring points in the direction transverse to the propagation, and we have also allowed for heat loss to the surroundings using the heat loss coefficients

$$h_i = \mathrm{Nu}\left(\frac{\alpha_s}{H_i v_i}\right)^2, \qquad h_j = \mathrm{Nu}\left(\frac{\alpha_s}{H_j v_j}\right)^2 \tag{10}$$

The solution of this problem will be considered in the two different cases of adiabatic and non-adiabatic conditions.

3.1 Adiabatic conditions

In the adiabatic case, equation (8) simplifies to

$$\theta_i = \theta_j + \frac{1}{\sigma}(A_j\theta_j' - \theta_j''). \tag{11}$$

Inserted into equation (7) this gives the following differential equation

$$\theta_j^{(iv)} - B\theta_j''' + D\theta_j'' + \sigma B\theta_j' = 0, \tag{12}$$

where we defined

$$B = A_i + A_j, \qquad D = A_iA_j - 2\sigma \tag{13}$$

Its solution is readily obtained,

$$\theta_j = \tilde{c}_o + \tilde{c}_1 e^{r_1\xi} + \tilde{c}_2 e^{r_2\xi} + \tilde{c}_3 e^{r_3\xi} \tag{14}$$

where $r_1 > 0$, $r_2, r_3 < 0$ are the real roots of

$$r^3 - Br^2 + Dr + \sigma B = 0 \tag{15}$$

The solution for θ_i follows using equation (11), namely

$$\begin{aligned}\theta_i = {} & \tilde{c}_o + \tilde{c}_1 e^{r_1\xi} + \tilde{c}_2 e^{r_2\xi} + \tilde{c}_3 e^{r_3\xi} \\ & + \frac{1}{\sigma}\left(A_j\left(\tilde{c}_1 r_1 e^{r_1\xi} + \tilde{c}_2 r_2 e^{r_2\xi} + \tilde{c}_3 r_3 e^{r_3\xi}\right)\right. \\ & \qquad \left. - \tilde{c}_1 r_1^2 e^{r_1\xi} - \tilde{c}_2 r_2^2 e^{r_2\xi} - \tilde{c}_3 r_3^2 e^{r_3\xi}\right)\end{aligned} \tag{16}$$

Because of the jump conditions at the two combustion fronts, it is convenient to consider three different regions, as shown in Figure 5. Using the far-field boundary conditions

$$\xi \to -\infty \quad : \quad \theta_i = \theta_j = \theta_I, \tag{17}$$

$$\xi \to \infty \qquad : \quad \theta_i = \theta_j = 1 \tag{18}$$

we then have

I. Region I

$$\theta_i = \theta_I + c_1 e^{r_1 \xi} + \frac{1}{\sigma}\left(A_j c_1 r_1 e^{r_1 \xi} - c_1 r_1^2 e^{r_1 \xi}\right) \tag{19}$$

$$\theta_j = \theta_I + c_1 e^{r_1 \xi} \tag{20}$$

II. Region II

$$\begin{aligned} \theta_i = {} & c_o + c_2 e^{r_1 \xi} + c_3 e^{r_2 \xi} + c_4 e^{r_3 \xi} \\ & + \frac{1}{\sigma}\left(A_j \left(c_2 r_1 e^{r_1 \xi} + c_3 r_2 e^{r_2 \xi} + c_4 r_3 e^{r_3 \xi}\right)\right. \\ & \qquad \left. - c_2 r_1^2 e^{r_1 \xi} - c_3 r_2^2 e^{r_2 \xi} - c_4 r_3^2 e^{r_3 \xi}\right) \end{aligned} \tag{21}$$

$$\theta_j = c_o + c_2 e^{r_1 \xi} + c_3 e^{r_2 \xi} + c_4 e^{r_3 \xi} \tag{22}$$

III. Region III

$$\begin{aligned} \theta_i = {} & 1 + c_5 e^{r_2 \xi} + c_6 e^{r_3 \xi} + \frac{1}{\sigma}\left(A_j \left(c_5 r_2 e^{r_2 \xi} + c_6 r_3 e^{r_3 \xi}\right)\right. \\ & \left. - c_5 r_2^2 e^{r_2 \xi} - c_6 r_3^2 e^{r_3 \xi}\right) \end{aligned} \tag{23}$$

$$\theta_j = 1 + c_5 e^{r_2 \xi} + c_6 e^{r_3 \xi}. \tag{24}$$

To complete the problem requires formulating jump conditions across the combustion fronts. These read as follows:

At $\xi = 0$:

$$[\theta_i]_{\xi=0^-}^{\xi=0^+} = [\theta_j]_{\xi=0^-}^{\xi=0^+} = \left[\theta_j'\right]_{\xi=0^-}^{\xi=0^+} = 0, \tag{25}$$

$$[\theta'_i]_{\xi=0^-}^{\xi=0^+} = -qV_{Di}, \tag{26}$$

and at $\xi = \xi_*$:

$$[\theta_i]_{\xi=\xi_*^-}^{\xi=\xi_*^+} = [\theta_j]_{\xi=\xi_*^-}^{\xi=\xi_*^+} = [\theta'_i]_{\xi=\xi_*^-}^{\xi=\xi_*^+} = 0, \tag{27}$$

$$\left[\theta'_j\right]_{\xi=\xi_*^-}^{\xi=\xi_*^+} = -qV_{Dj}. \tag{28}$$

Because the fronts travel with the same speed ($V_i = V_j$), both the front *and* the distance ξ_*between them must be determined. In essence, these constants are the eigenvalues of this system of ten equations (seven integration constants, ξ_*, V_D, and θ_I). In general, the system is non-linear, due to the intricate dependence between front velocity and heat transfer. The ten equations required for its solution consist of the 8 jump conditions, and the application of the expression (4) for the front velocity twice (note that this equation remains valid, regardless of the coupling between the two layers). Details for the solution are given in [9]. Numerical results will be discussed in a later section.

3.2 Non-adiabatic conditions

Working likewise, we can formulate the problem in the presence of heat losses. Now, additional terms describing the interaction with the surroundings must be included. Using equation (8) to substitute θ_i in terms of θ_j, we have

$$\theta_i = (1 + \frac{h_j}{\sigma})\theta_j + \frac{1}{\sigma}\left(A_j\theta'_j - \theta''_j - h_j\right) \tag{29}$$

Inserting into (7) and re-arranging we get

$$\theta_j^{(iv)} - B\theta'''_j + E\theta''_j + F\theta'_j + G\theta_j - G = 0 \tag{30}$$

where

$$
\begin{aligned}
E &= A_i A_j - 2\sigma - (h_i + h_j) \\
F &= A_i(\sigma + h_j) + A_j(\sigma + h_i) \\
G &= h_i h_j + \sigma(h_i + h_j)
\end{aligned} \tag{31}
$$

the general solution of which is

$$
\theta_j = 1 + \tilde{c}_1 e^{r_1 \xi} + \tilde{c}_2 e^{r_2 \xi} + \tilde{c}_3 e^{r_3 \xi} + \tilde{c}_4 e^{r_4 \xi} \tag{32}
$$

where we have identified the real roots r_1, r_2 >0 and r_3, r_4 <0 of

$$
r^4 - Br^3 + Er^2 + Fr + G = 0. \tag{33}
$$

Again, we have to distinguish different expressions in different regimes, which are as follows:

I. <u>Region I</u>

$$
\begin{aligned}
\theta_i = 1 &+ \left(1 + \frac{h_j}{\sigma}\right)\left(c_1 e^{r_1 \xi} + c_2 e^{r_2 \xi}\right) + \frac{1}{\sigma}\Big(A_j \Big(c_1 r_1 e^{r_1 \xi} \\
&+ c_2 r_2 e^{r_2 \xi}\Big) - c_1 r_1^2 e^{r_1 \xi} - c_2 r_2^2 e^{r_2 \xi} - h_j\Big)
\end{aligned} \tag{34}
$$

$$
\theta_j = 1 + c_1 e^{r_1 \xi} + c_2 e^{r_2 \xi} \tag{35}
$$

II. <u>Region II</u>

$$
\begin{aligned}
\theta_i = 1 &+ \left(1 + \frac{h_j}{\sigma}\right)\left(c_3 e^{r_1 \xi} + c_4 e^{r_2 \xi} + c_5 e^{r_3 \xi} + c_6 e^{r_4 \xi}\right) \\
&+ \frac{1}{\sigma}\Big(A_j \Big(c_3 r_1 e^{r_1 \xi} + c_4 r_2 e^{r_2 \xi} + c_5 r_3 e^{r_3 \xi} + c_6 r_4 e^{r_4 \xi}\Big) \\
&- c_3 r_1^2 e^{r_1 \xi} - c_4 r_2^2 e^{r_2 \xi} - c_5 r_3^2 e^{r_3 \xi} - c_6 r_4^2 e^{r_4 \xi} - h_j\Big)
\end{aligned} \tag{36}
$$

$$\theta_j = 1 + c_3 e^{r_1 \xi} + c_4 e^{r_2 \xi} + c_5 e^{r_3 \xi} + c_6 e^{r_4 \xi} \tag{37}$$

III. Region III:

$$\begin{aligned} \theta_i = 1 &+ \left(1 + \frac{h_j}{\sigma}\right)\left(c_7 e^{r_3 \xi} + c_8 e^{r_4 \xi}\right) + \frac{1}{\sigma}\Bigl(A_j \bigl(c_7 r_3 e^{r_3 \xi} \\ &+ c_8 r_4 e^{r_4 \xi}\bigr) - c_7 r_3^2 e^{r_3 \xi} + c_8 r_4^2 e^{r_4 \xi} - h_j\Bigr) \end{aligned} \tag{38}$$

$$\theta_j = 1 + c_7 e^{r_3 \xi} + c_8 e^{r_4 \xi} \tag{39}$$

Application of the same jump conditions as before gives rise to a set of ten equations in terms of the ten unknowns (integration constants, the distance between the fronts and the front velocity). Details of the solution are found in [9].

3.3 Non-adiabatic, symmetric, three-layered porous medium

The same approach can be applied to the solution of a symmetric three-layered medium, when the two outer layers have the same properties. This type of geometry is useful in the investigation of the effect of a middle layer that plays the role of a permeable thief zone. Because of the symmetry assumed, velocity and temperature of the outer reaction fronts are taken to be identical, as shown in Figure 6.

Then, the governing energy balances become

$$A_i \theta_i' = \theta_i'' + \sigma_i(\theta_j - \theta_i) - h_i(\theta_i - 1) \tag{40}$$

$$A_j \theta_j' = \theta_j'' + \sigma_j(\theta_i - \theta_j) \tag{41}$$

Working as before, equation (41) gives θ_i,

$$\theta_i = \theta_j + \frac{1}{\sigma_j}(A_j \theta_j' - \theta_j'') \tag{42}$$

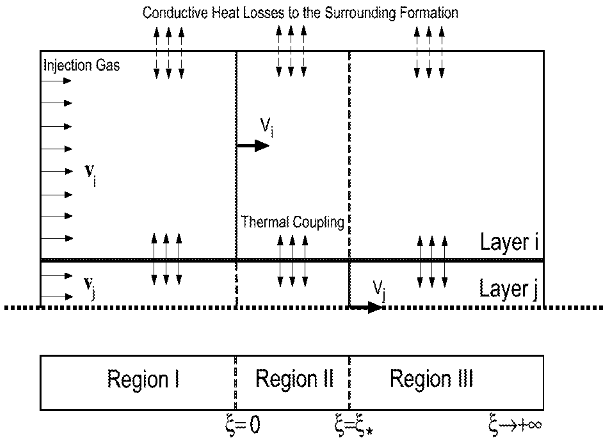

Figure 6: Schematic of the notation used for the propagation of combustion fronts in a two-layered porous medium.

Inserted into (40) gives

$$\theta_j^{(IV)} - B\theta_j''' + \bar{E}\theta_j'' + \bar{F}\theta_j' + \sigma h_i\theta_j - \sigma h_i = 0 \tag{43}$$

where

$$\begin{aligned} \bar{E} &= A_iA_j - \sigma_i - \sigma_j - h_i \\ \bar{F} &= B\sigma_j + A_jh_i \end{aligned}$$

the solution of which is obtained as before, in terms of a combination of exponentials, with exponents the real roots r_1, r_2 >0 and r_3, r_4 <0 of the characteristic equation

$$r^4 - Br^3 + \bar{E}r^2 + \bar{F}r + \sigma_jh_i = 0. \tag{44}$$

The mathematical procedure is similar to the previous and will not be repeated (see [9] for more details).

4 Results

The numerical solution was studied using typical in situ combustion data [7, 9]. Results were obtained for the temperature T_f and velocity V of the fronts as well as their distance $\tilde{\xi}_* = \xi_* \times l_*$, in terms of the velocity (hence, permeability) ratio $R = v_i/v_j$, the thermal coupling coefficient σ, the velocity of the layers, and, in the non-adiabatic cases, the layer thicknesses H_i and H_j. We considered two velocity cases, one in which the larger velocity is fixed to v_j=100m/day (case j), and another in which lower velocity v_i is fixed to v_i=100m/day (case i). In either case R was varied between its limits 0 and 1.

4.1 Adiabatic Two-layer Case

The procedure applied during the calculations is explained in detail in [9]. Figures 7 and 8 show the effect of R on the temperature profiles and the front velocity for constant σ, and case j. We note the following: The system recovers the single-layer solution (with V=1.7346 m/day) in the single-layer case $R = 1$ (Figure 7). Here the two fronts collapse, and their distance is nil. When $R = 0.5$ (Figure 8), the separation between the fronts is clear. The front in layer j has slowed down, and has a lower temperature than that of layer i, which has accelerated to a common velocity (equal to V=1.0033 m/day). The temperature profile is more diffuse than in the single-layer case, with heat being transferred from layer j to layer i downstream and from i to j upstream. Interestingly, the temperature profile in the lower-permeability layer has a peak, which is not present in the single-layer problem. Nonetheless, the far-field temperature upstream is equal to the adiabatic temperature. The common front velocity is much closer to the single-layer velocity for the lower-permeability layer (corresponding to an injection velocity of 50m/day, rather than the arithmetic average injection velocity of 75m/day). This reflects strong non-linear coupling effects. The effect of the thermal coupling parameter σ is shown in Figure 9. Interestingly, as σ decreases the coupling is not weakened, but rather enhanced. Clearly, the front separation has increases, the temperature peaks increased, while the common front velocity has further increased (V=1.0161 m/day).

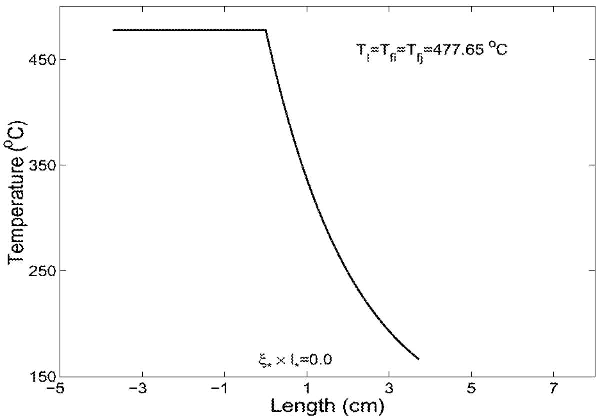

Figure 7: Temperature profiles for the two-layer adiabatic case. R=1.0, σ=0.01.

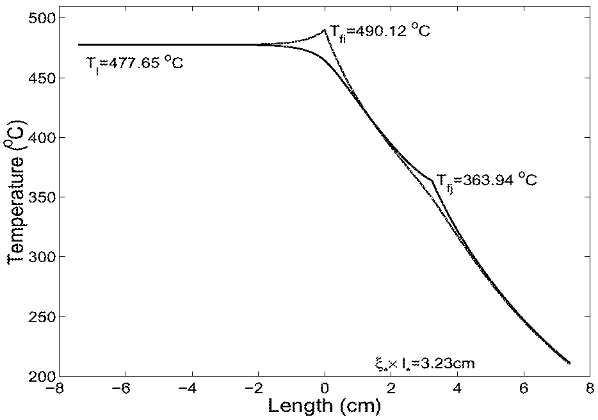

Figure 8: Temperature profiles for the two-layer adiabatic case. R=0.5, σ=0.01.

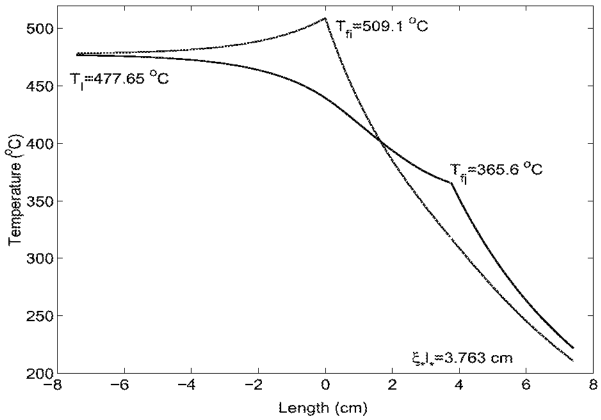

Figure 9: Temperature profiles for the two-layer adiabatic case. R=0.5, σ=0.001.

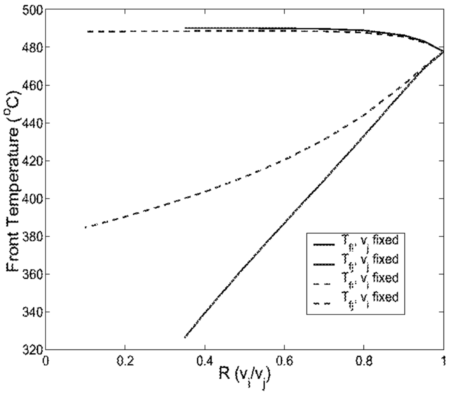

Figure 10: Front temperatures versus R for the two-layer adiabatic case. Solid lines denote case j, dashed lines denote case i.

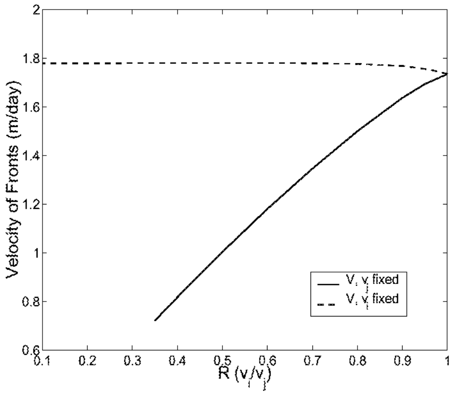

Figure 11: Front velocity versus R for the two-layer adiabatic case. Solid lines denote case j, dashed lines denote case i.

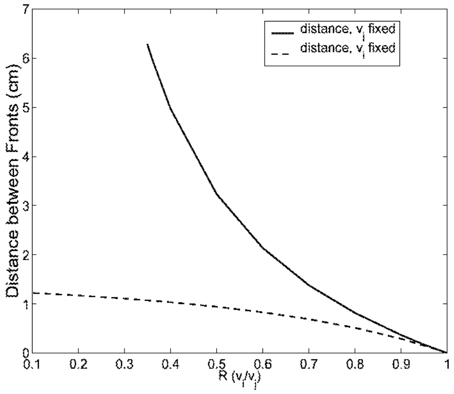

Figure 12: Distance between the fronts versus R for the two-layer adiabatic case. Solid lines denote case j, dashed lines denote case i.

While these results point out to an important effect of R, the latter also depends on the actual velocity values. Figures 10-12 show two sets of the front temperatures, front velocities and front distance, as a function of R for σ=0.01 and the two cases j and i, respectively. Recall that case j corresponds to fixed v_j=100 m/day, while case i to fixed v_i=100 m/day. Of course, ideally one would like to have a three-dimensional plot with v_i and v_j as the independent variables. However, these computations can be time consuming and in the present we will restrict ourselves to only a few slices of this diagram.

It is clear from Figure 10 that the effect of the actual velocity levels is not great on the front temperatures (except for that of the leading front at small values of R). In fact, the far-field temperature behind the two fronts is not influenced at all by the variations in R or σ as its value is always the adiabatic temperature, as pointed out above. Thus, for the adiabatic case, the temperature is roughly only a function of R. However, the effect is significant on the front velocities and the front distance. In case j, where it is the larger injection velocity which is kept fixed, the front velocity decreases as the smaller injection velocity decreases, almost proportionally to it, while in case i, where the smallest velocity is fixed, the variation is insignificant. Analogous is the effect on the front distance.

These results suggest that essentially the behavior of the system is controlled by the layer with the smallest injection velocity, with the front velocity in particular almost being a slave of that variable. The implications of this finding are important. For the adiabatic case they simply affect the rate of front propagation. However, for the non-adiabatic case, discussed below, they may have more dramatic consequences, regarding the possibility of process extinction.

4.2 Non-adiabatic Two-layer Case

Using the formulation described in the previous sections, numerical results were obtained for the non-adiabatic case in the two-layer system. Now, in addition to the previous, an important additional parameter is the layer thickness, which was taken in all simulations shown as the same for the two layers.

When the layer thickness is sufficiently large (approximately 2m, for the parameters shown here) the solution of the problem and its sensitivity to R and the velocities is qualitatively the same as in the adiabatic case. Unique solutions exist and the main difference is that the temperature profile is more spread out, has somewhat more structure and, of course, asymptotically tends to the initial value. Characteristic examples are shown in Figures 13-15. The observed similarity of the non-adiabatic model results when H=2m to the results of the adiabatic case is consistent with the results of single layer analysis – the combustion fronts propagate as if the system is in the adiabatic mode, given that sufficient gas is injected into the layers.

On the other hand, when the thickness becomes small, the qualitative picture changes. As in the single-layer case, the possibility of multiplicity arises. Figures 16 and 17 show features very similar to the single layer. Thus, for case j, where the lower injection velocity can become sufficiently small in magnitude, extinction and ignition limits arise. The multiplicity arises simultaneously in both fronts, and both fronts ignite and get extinct simultaneously. The corresponding curves for case j are similar both qualitatively and quantitatively to the single layer case. The results for case i are somewhat different. Here, because the lowest velocity remains fixed (at 100 m/day), multiplicity does not arise until the layer thickness is sufficiently small (contrast Figures 16 and 17). By comparing with the single-layer results, this effect is somewhat unexpected. If we were to assume that the front basically follows the front velocity corresponding to the lower injection velocity, the curves corresponding to case i could be interpreted from the single-layer results as those corresponding to the upper branch. This would mean that intermediate and lower branches would also exist. These do not appear in Figure 16, although they do in Figure 17, which corresponds to a smaller thickness layer. One infers that when the velocities are sufficiently large, the composite, two-layer system behaves as one with an effectively larger thickness, compared to the case when the layer velocities are relatively small. This interpretation is also supported in the velocity and front distance curves shown in Figures 18 and 19. However, and contrary to the adiabatic case, another effect is also present here, namely, an intrinsic heterogeneity effect through the parameter R. For example, the above figures illustrate through case i, that by increasing the heterogeneity of the layers, extinction will eventually set in, even though the lower-permeability layer has a fixed injection velocity. This effect is non-trivial and unexpected. For completeness, we examined the sensitivity of these results to the thermal parameter σ. Very small differences were found as σ was decreased by a factor of 10.

The implications of these results are important. They point out that increasing the permeability contrast between the layers can have dramatic effects on the propagation of a combustion front. Namely, given an overall injection rate, and for sufficiently small layer thickness, there is a sufficiently large permeability contrast, such that the process becomes extinct. Depending on the parameters, this contrast can be as low as 10. Strongly layered (and by extension, strongly heterogeneous) systems may thus be not good candidates for in-situ combustion. The above results gave only one indication of the ballpark values for this to occur. A more systematic analysis would require the development of 3-D plots using the two velocities as coordinates and the resulting identification of extinction and ignition limits.

4.3 Non-adiabatic Three-layer Case

For completeness, we also analyzed the symmetric, three-layer geometry. Now, the middle layer is shielded and does not lose heat directly to the surroundings. The results obtained were qualitatively similar to the previous non-adiabatic problem. In this geometry, we investigated the sensitivity of the results to the ratio of the thickness of the two layer, which here were taken unequal. In the calculations, we also kept the injection velocity of the surrounding layers fixed, and varied v_j (case i). Front temperature results are shown in Figure 20. It is shown that when the shielding layers are thick enough (dashed lines in Figure 20) the behavior approaches the adiabatic case, where there exists a unique solution. If the layer thickness decreases, then multiplicity sets in, with characteristics similar to the ones discussed above.

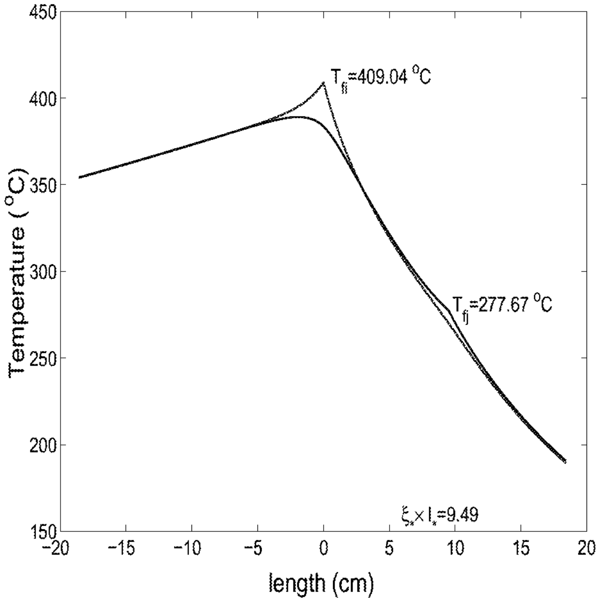

Figure 13: Temperature profiles for the non-adiabatic two-layer model. H_i=H_j=2m, R=0.20, σ=0.01, calculated V=0.4070 m/day.

5 Concluding Remarks

In this chapter we extended the approach of [7] to heterogeneous systems, by considering the simpler case of in-situ combustion in layered porous media. Two simple geometries were considered, a two-layer model and a symmetric three-layer model. Analytical models were developed to delineate the combined effects of fluid flow, reaction and heat transfer on the dynamics of combustion fronts in the layers, using as parameters the thermal coupling between the layers, the heat transfer to the surroundings and the permeability contrast. We find that in layered systems, the thermal coupling between layers leads to coherent traveling fronts, propagating at the same velocity. This coupling retards greatly fronts in the more permeable layer and accelerates only slightly those in the less permeable one, until a common front velocity is attained. In essence, the problem becomes slave to the injection velocity in the lower permeability layer. As in the single-layer case, there exists a unique solution, under adiabatic conditions, and multiple steady-state solutions, under non-adiabatic conditions. The latter lead to ignition and extinction conditions. Importantly, for a sufficiently large permeability contrast, relatively small layer thickness and under non-adiabatic conditions, steady-state

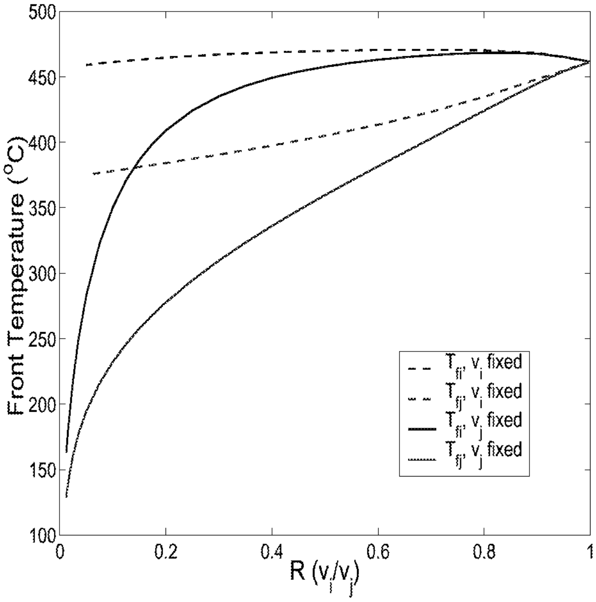

Figure 14: Front temperatures versus R for the non-adiabatic two-layer model. Solid lines denote case j, dashed lines denote case i. H_i=H_j=2m., σ=0.01.

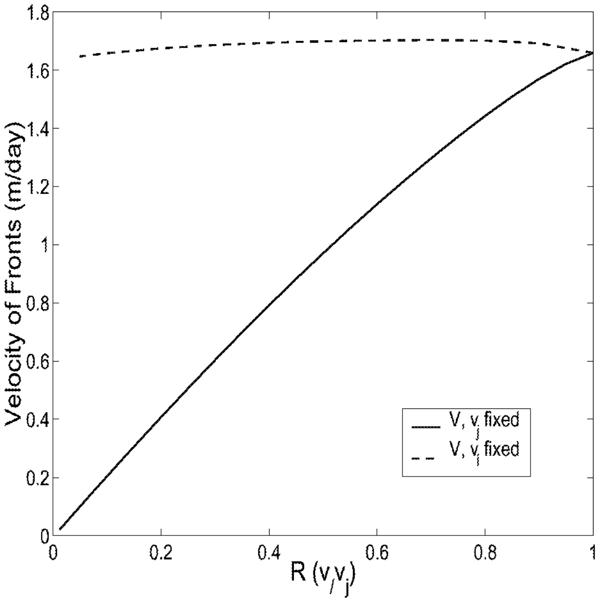

Figure 15: Velocity of the fronts versus R for the non-adiabatic two-layer model. Solid lines denote case j, dashed lines denote case i. H_i=H_j=2m., σ=0.01.

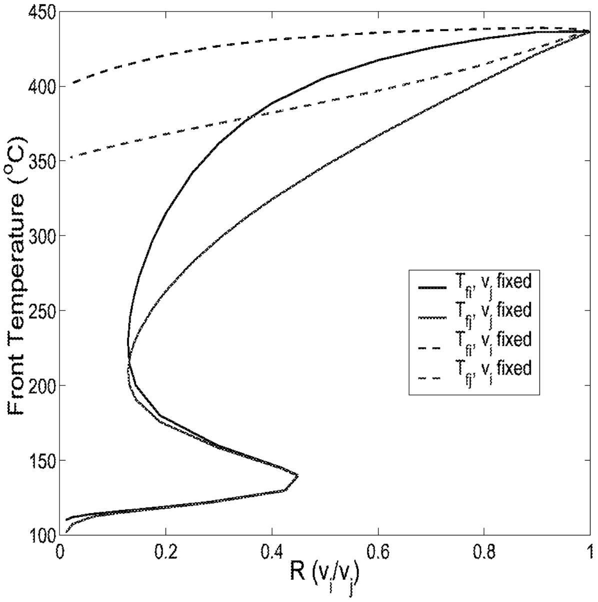

Figure 16: Nonadiabatic front temperatures for layers i and j versus R. Solid lines denote case j, dashed lines denote case i. H_i=H_j=0.8m., σ=0.1.

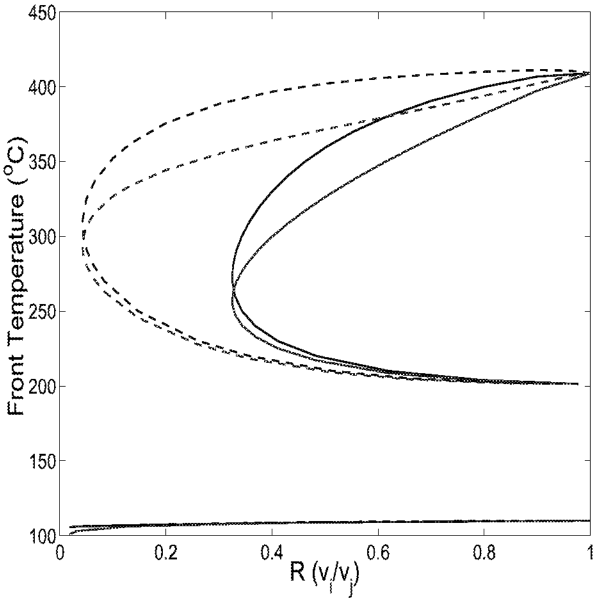

Figure 17: Nonadiabatic front temperatures for layers i and j versus R. Solid lines denote case j, dashed lines denote case i. H_i=H_j=0.5m., σ=0.1.

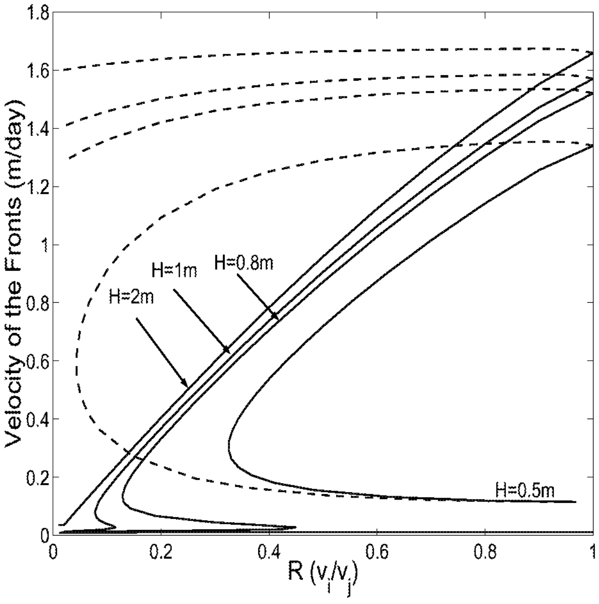

Figure 18: Nonadiabatic front velocity for layers i and j versus R for varying H. Solid lines denote case j, dashed lines denote case i. σ=0.1.

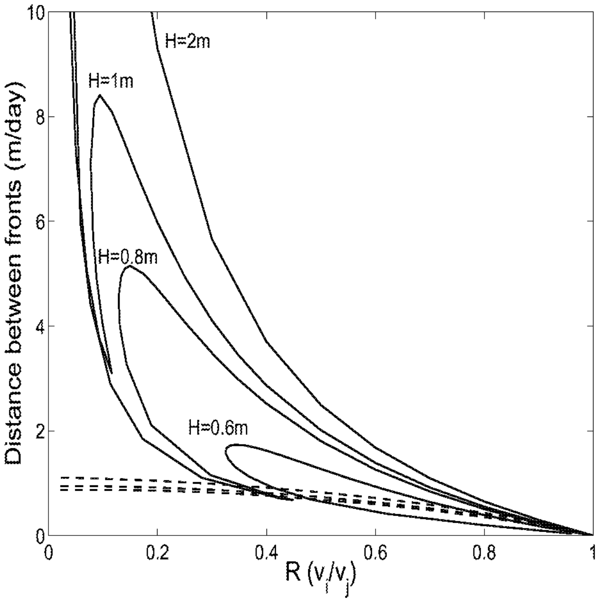

Figure 19: Distance between the fronts in layers i and j versus R for varying H and the non-adiabatic case. Solid lines denote case j, dashed lines denote case i. σ=0.1.

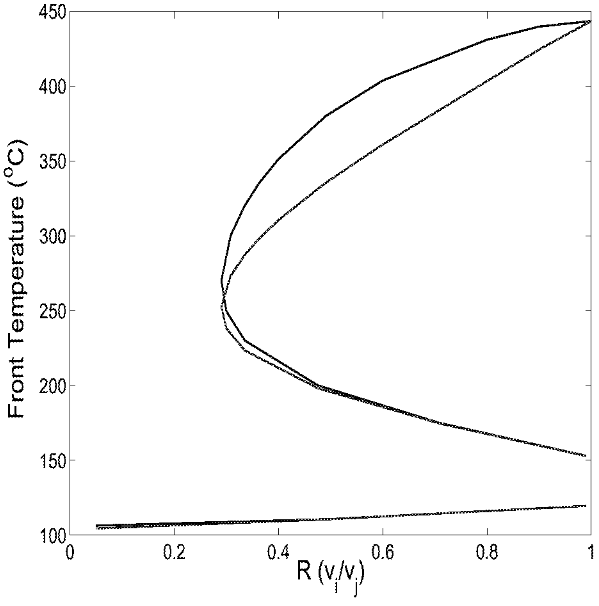

Figure 20: Front temperature versus R for the non-adiabatic symmetric, three-layer case. Solid line denotes thickness of the shielding layers equal to 0.5 m, dashed lines denote thickness equal to 2 m. σ_i=0.1

propagation in the two layers cannot be sustained, and the process becomes extinct, even though, under the same conditions, sustained propagation would have been predicted for the equivalent single-layer problem with the average injection velocity. In a sense, the problem becomes controlled by the extremes of the permeability distribution. Such behavior can be detrimental to the success of in-situ combustion in highly heterogeneous layered media. In addition, it raises serious questions on the ability of conventional reservoir simulators to capture it. Conventional models average flow and kinetic behavior over substantially large distances, where effects, such as the above, which are dominated by the extremes of the permeability field, cannot be adequately represented. Precise conditions for the delineation of the above behavior need to be further developed. We anticipate that similar conclusions will hold in the case of heterogeneous media. Work in this direction is currently in progress.

References

[1] Williams, F.A. *Combustion Theory*, Benjamin and Cummings Publishing Company Inc. (1985).

[2] Britten, J.A. and Krantz, W.B., *Combust. Flame*, 60:125 (1985).

[3] Britten, J.A. and Krantz, W.B., *Combust. Flame*, 65:151 (1986).

[4] Schult, D.A., Matkowsky, B.J., Volpert, V.A., and Fernandez-Pello, A.C., *Combust. Flame*, 104:1 (1996).

[5] Schult, D.A., Bayliss, A. and Matkowsky, B.J., *SIAM J. Appl. Math.*, 58:806 (1998).

[6] Chuan, L. and Yortsos, Y.C. *A Pore-Network Model of In Situ Combustion in Porous Media*, paper SPE 69705 presented at the Society of Petroleum Engineers International Thermal Operations and Heavy Oil Symposium, Santa Margarita, Venezuela, March 15-17 (2001).

[7] Akkutlu, I.Y. and Yortsos, Y.C. *Combust. Flame*, submitted (2001).

[8] Willhite, G.P. *Waterflooding*, SPE Textbook Series Vol. 3 (1986)

[9] Akkutlu, I.Y. *Dynamics of Combustion Fronts in Porous Media*, PhD Dissertation, U. of Southern California (2002, expected).

IV. FLOW AND DISPLACEMENT OF FLUIDS WITH YIELD STRESS

Many applications with heavy oils involve a non-Newtonian rheology. Specifically, the flow and displacements of fluids with yield stress are common. Examples include the flow of foams for oil recovery, where the mobilization of foam lamellae requires that a pressure threshold is exceeded; the flow of heavy oils containing asphaltenes, where a Bingham plastic-like behavior is exhibited; and the formation of wormholes during cold heavy oil production, where the flow of sand particles also requires that limiting yield stresses are overcome. In this section we report on our going efforts to understand these processes at the pore-network scale and to provide the necessary information for their representation at the macroscopic scale. The work reported builds on our previously developed models, including the algorithm of Invasion Percolation with Memory. We utilize this algorithm in order to facilitate the simulation of flow and displacements of Bingham plastics.

Mobilization and Displacement of Fluids with Yield Stress

Min Chen and Yannis C. Yortsos

Introduction

The flow or displacement of fluids with yield stress is an important research area of non-Newtonian fluid studies, which is also encountered in a variety of industry applications. Examples include the flow of heavy oils, which can be often represented as Bingham plastics, the production of sand during cold heavy oil production, and the flow and mobilization of foams in porous media.

Foams are a typical fluid of engineering interest appear to exhibit yield behaviors, which are widely used in the oil industry in various applications, to improve reservoir sweep efficiency, block swept channels, and in gas storage and acidizing operations. These applications rely on the substantial reduction of the gas mobility in rocks obtained in the presence of foams. Some issues in this regard include whether there exists a minimum pressure gradient or a critical gas velocity, above which the porous medium can be mobilized and the relation between the pressure gradient and the flow velocity

In the context of the flow of Bingham fluid, similar problems arise. Typical Bingham fluids include paint, slurries, pastes and food substances like margarine, mayonnaise and ketchup. Bingham fluids possess nonzero yield stresses, so that they flow when an applied stress exceeds some levels of stress, and they show little or no deformation up to the stresses. Because of the complex property of this kind of fluids, much effort has been made to study the flow and mobilization processes of these fluids. In addition, due to the complexity brought out by the combination of the non-Newtonian fluid rheology with the porous media geometry, the state of the art of Bingham fluid flow is not complete.

Many authors in the Russian literature have approximated the rheology of heavy oils as that of a Bingham fluid [1, 2]. Some other studies were also carried out, including flow of foams [3], ground water flow in certain clayey solids, and drilling and hydraulic-fracturing fluids [4]. Rossen and Mamun [5] proposed a percolation approach, consisting of occupying elements with thresholds below a certain value. In the study of the foam flow, Rossen and Gauglitz [3] developed a model for foam mobilization in porous media, for both continuous and discontinuous gas regimes. In the process, they employed percolation theory to find the cluster size, and verified the fact that a minimum pressure gradient is needed to displace lamellae out of a pore throat. Because of lack of data and also the complexity of the system, their conclusions are not complete.

Wu et al. [4] investigated the transient flow of Bingham fluids in porous media, including single- and multiphase flow, using an ad-hoc extrapolation of the single-capillary expressions for the Bingham flow. In the context of reservoir engineering, most existing studies are phenomenological and consist of solving effective continuum equations.

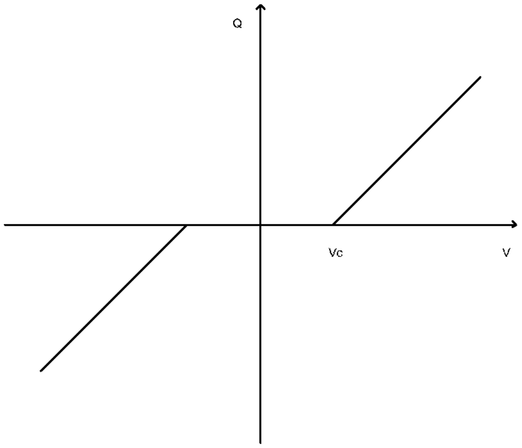

Fig. 1 Voltage – current relation of an individual resistor

A fundamental and now widely accepted work was done by Roux and Herrmann [6]. They used a 2-D network, which is composed of resistors. Each of the resistors has a threshold below which it becomes an insulator. The resistors are distributed randomly in a network. Their results show that the relation between current and the voltage is non-linear. The macroscopic current Q has the following relation with V and V_c,

$$Q \sim (V - V_c)^{\delta} \qquad (1)$$

where $\delta = 2$ or $\delta \sim 0.5$ for intermediate part (if for each of the resistor, Q is linearly determined by V when $|V|$ is larger than threshold, as shown in Fig. 1, and V_c is the minimum voltage to have current in the network. In their studies, the thresholds of the resistors are distributed between 0 and 1.

Sahimi [7] used EMA to predict that in a certain range, Q depends quadratically on V. His Monte Carlo simulation results agree with the prediction quite well. Zhou and Stenby [8] studied the displacement of oil trapped in water-wet reservoirs using percolation theory. They obtained the CDC curve based on pore structure of the medium, which is in good agreement with the measured data.

Kharabaf et al. [9,10,11] developed a different algorithm for the construction of the minimum threshold path (MTP), based on which its properties can be studied, such as the connection of the threshold-lattice problem to percolation and also the relation of the MTP with the minimum path of percolation. The algorithm has a similar simulation process as that of an invasion process; the difference is that the advance of the front depends on the front history. It is referred as Invasion Percolation with Memory (IPM). They studied the mobilization of Bingham fluid, immiscible displacement of Bingham fluid by Newtonian fluid and also displacement of Bingham fluid by another kind of Bingham fluid. The same algorithm is used in the study of foam formation and propagation in porous media.

Even though some work has been done, the understanding of single- and multiphase flow of fluids with yield stress in porous media is still limited. In considering and simulating mobilization of fluids with yield stress, Kharabaf used a static model, which will be modified further here. In his work, the potential of a pore is only determined by thresholds, and the pressure distribution effect of the flowing fluid was not considered. In this paper, a new dynamic algorithm for mobilizing fluids with yield stress based on IPM is developed, in which the contribution of flowing fluid is taken into account. Simulation results for different yield stress distributions are compared and discussed. The difference between the new algorithm and Kharabaf's static model is shown.

Algorithm

1) Invasion Percolation with Memory (IPM)

Because the IPM process is the basis of the new algorithm, the algorithm of IPM is described with some details [9].

A network composed of bonds and pores are used, in which bonds have thresholds, τ_i, randomly assigned from a distribution in (0,1). The invading front invades one site at a time. An arbitrary site currently on the front is denoted by F, a site which is a neighbor of F by F', the site from which the front will advance by F_G, the site which will actually be invaded by F'_G. Each site that has been invaded has a value of $V_1(F)$. For a site F on the front and one of its neighbors F', a sum $S = V_1(F) + \tau_{FF'}$ can be formed.

The minimum one of all possible S can easily be found, the corresponding F and F' become F_G and F_G', respectively, and $V_1(F_G') = V_1(F_G) + \tau_{F_G F'_G}$. If the boundary condition $V_1(R) = 0$ for all sites R on the right boundary is applied, the first site invaded on the left boundary has the MTP value, which is $\sum_i \tau_i$. By this method, the MTP of the lattice can be found, and V_1 of each site is its smallest resistance to the starting side. The patterns before and after a growth step are shown in Fig. 2.

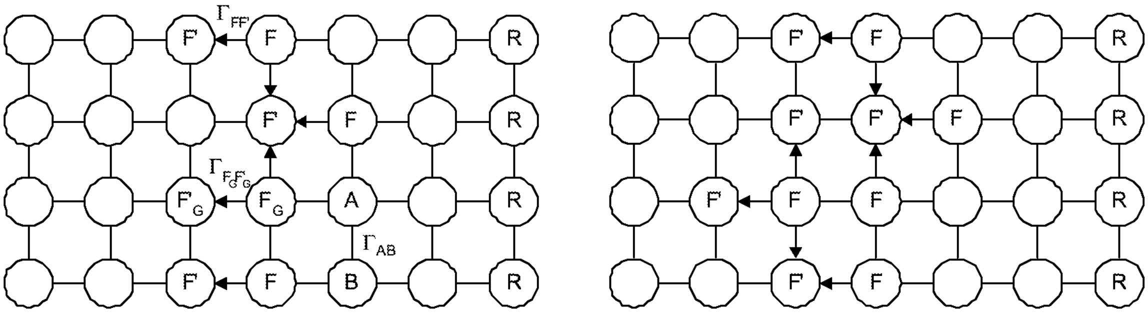

(a) (b)

Fig. 2 Description of the invasion rule, before (a) and after (b) a growth step.

2) New algorithm on mobilization of fluids with yield stress

Fluid with yield stress is a kind of special one, belonging to non-Newtonian fluids. A typical example is Bingham fluids, which exhibit a finite yield stress at zero shear rate and they correspond to the extreme case of pseudoplasticity. Bingham model is the most often used model for a Bingham material. The behavior of this kind of fluid described by Bingham model is shown in Fig. 3. For low stress values, the fluid does not deform, and above the critical value τ_0, it flows like an inelastic non-Newtonian fluid.

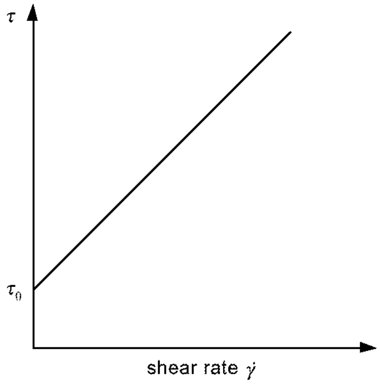

Fig. 3 Behavior of Bingham Fluid

$\tau = \tau_0 - \mu_p \dot{\gamma}$, when $\tau > \tau_0$

and

$\dot{\gamma} = 0$, when $\tau < \tau_0$

If the viscous forces are neglected for single-phase flow of a Bingham fluid, yield stress is the only force affecting its flow. While for Newtonian fluids, when the pressure drop applied is greater than zero, there is flow in the system, for Bingham fluids, the situation is completely different.

When simulation in network-like porous media is considered, the flow of the fluid in a single throat (bond) can be expressed by the following equation [12]

$$q_i = \frac{\pi r_i^4}{8\mu_p l}\left(1 - \frac{4}{3}\left(\frac{\tau_0}{\tau_i}\right) + \frac{1}{3}\left(\frac{\tau_0}{\tau_i}\right)^4\right)\Delta p_i \quad \text{when } \tau_i > \tau_0 \tag{2}$$

and

$q_i = 0$ when $\tau_i \le \tau_0$

where q_i is the volumetric flow rate of the fluid in the throat , Δp_i is the pressure drop applied to the throat, and τ_i is the wall shear stress

$$\tau_i = \frac{\Delta p_i r_i}{2l}$$

Just for simplicity, we use the equation below in the algorithm, for throat i,

$$q_i = \Delta p_i - \frac{1}{r_i} \quad \text{when } \Delta p_i > \frac{1}{r_i} \tag{3}$$

and

$$q_i = 0 \quad \text{when } \Delta p_i \le \frac{1}{r_i}$$

where r_i, is distributed with a size distribution, $\alpha(r)$.

This condition (3) is similar to the one used by Roux and Herrmann [6] for a single resistor. So it can be described by Fig. 1, too. In equation (3), the variables are all in dimensionless form. It is clear from the simplified equation that the onset of the flow of the Bingham fluid in the network is controlled by the flow situation of each of the throats in the path. For the first path in the system, there is a minimum pressure difference between the two boundaries.

$$\Delta P_{\min} = \sum_i \frac{1}{r_i} \tag{4}$$

where the summation is over all of the throats in the first single path.

It is obvious that the first path in our algorithm is completely the same as the static one obtained by Kharabaf et al. But after that, the pressure drop of the system, which is needed to open a new path is not only determined by the throat radius (or $\frac{1}{r_i}$), but also by the flow, and more exactly the pressure distribution of the mobilized path, which is the factor that is not considered in Kharabaf's mobilization algorithm. In our new algorithm, the two factors, radius and pressure distribution are combined together to be τ_i, which is updated every time when a new path is open. In the following description, τ_{0i} is used, instead of $\frac{1}{r_i}$, and τ_{0i} is corresponding to the size distribution function $\beta(\tau_0)$.

The mobilization of the fluid is the same as finding the paths which connect one side of the network with the other. Each of the paths is corresponding to a specific pressure drop across the network. Here, the pressure at the left side of the network is fixed and equal to zero. As described in previous work, IPM is an effective method to find the minimum path from the right side of the network to the left side. After we find the first path and the critical pressure $\Delta P_{\min} = P_{\min}$, we need a little higher pressure to open a new path. The new path may be a branch or a loop connected to the old or a separate one. We should notice that when the new path is just opened, the flow rates in the newly mobilized throats in the paths are zero and they have no contribution to the total flow rate in the network. If the new path is just opened and connected to the old (AB) one at point C (Fig. 4), for any bond j in the path CD, the flow rate is

$$q_j = \Delta p_j - \tau_{0j} = 0$$

therefore, $\Delta p_j = \tau_{0j}$

For any bond in the path AC, the flow rate is

$$q_k = \Delta p_k - \tau_{0k}$$

If we let

$$\Delta p_k = q_k + \tau_{0k} = \tau_k^{'} \qquad (5)$$

the pressure drop between the two sides of the network for the new path ACD determined using IPM is

$$P_{ACD} = \sum_{AC} \tau_i^{'} + \sum_{CD} \tau_{0i} = \sum_{ACD} \tau_i^{*} \qquad (6)$$

which is the MTP with updated thresholds τ_i^{*}, in the new part CD, $\tau_i^{*} = \tau_{0i}$, and in the shared part AC, $\tau_i^{*} = \tau_i^{'}$.

For throats in the old path $\tau_i^{*} = \tau_i^{'}$, so for the old path ACB

$$P_{ACB} = \sum_{ACB} \tau_i^{'} = \sum_{ACB} \tau_i^{*} \qquad (7)$$

From all above, we can see that the apparent way to find the next path to be opened is to determine the MTP in IPM with updated thresholds. So, in our algorithm, we first use IPM to find MTP with all initial τ_0. Then we increase the pressure drop P_{ACB}, and at the same time update the thresholds of the bonds in opened paths to be $\tau^{'}$ according to Eq. (4). After that, we use IPM again to determine the MTP at this pressure drop to find the potential (P_{ACD}) of site D at the left boundary. If the pressure drop between the two boundaries is high enough, we can always find a new path ACD. Then decrease the pressure drop. These steps are repeated until the new path with smallest $P_{ACB} = P_{ACD}$ is found. Just as mentioned before, the new path is not necessarily connected to the old ones

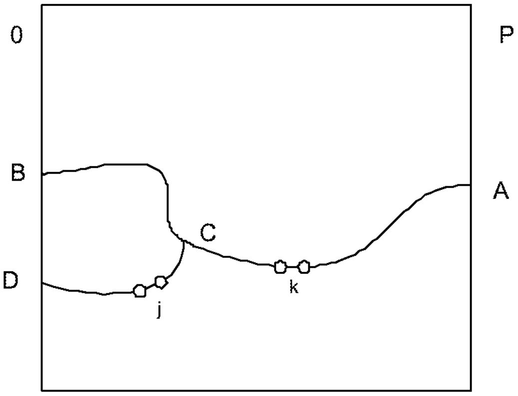

Fig. 4 The flow pattern when a new path (ACD) is open

like the one shown, it may be a loop or even a new path, but the algorithm is the same for all of the situations.

In determining the pressure distribution of the mobilized fluid, the fluid is assumed to be incompressible, and for any site i in the continuous path, the below equation is obeyed,

$$\sum_{j}^{Z} q_{ij} = 0 \tag{8}$$

where q_{ij} is the volumetric flow rate from site i to its neighbor site j, and Z is the coordination number, $Z = 4$ for 2-D system and $Z = 6$ for 3-D system. At a site, which is the intersection of the four bonds, there may no flowing fluid in several bonds, but because of viscous forces, the static fluid in the throat(s) left may make contribution to the flow of the fluid in the other throats. But if the Bingham number of the fluid is high enough, this contribution is negligible. Consequently, in our study, this effect is not considered. Flow rate in a bond is computed according to equation (3).

In 2-D and 3-D systems, fluids flow from right to left, and periodic boundary conditions are used for the other boundaries. The size distribution of τ_0 is β^n, where β is uniform in the region (0, 1). Then for τ_0, the probability density function (PDF), the arithmetic mean and standard deviation are

$$f(\tau_0) = \frac{1}{|n|}\tau_0^{(1/n)-1},\ \langle \tau_0 \rangle = \frac{1}{1+n},\ \sigma_{\tau_0} = \frac{n}{(1+n)\sqrt{1+2n}} \tag{9}$$

respectively. From Eq. (9), it is apparent that for the existence of the arithmetic mean we must have $n > -1$, while for that of the variance, $n > -1/2$. Therefore, for finite first and second moments of general threshold distributions, we must restrict Eq. (9) to $n > -1/2$. However, the problem with smaller n will also be considered.

Result and Discussion

The result for $n = 1$

The relation between the flow rate of the network and the pressure exerted across the network is shown in Fig. 5(a) and 5(b). At a certain pressure drop $P_{\min}$, the first path is open; this is the onset of the mobilization process. Then with the increase of the pressure, more and more bonds are mobilized and the flow rate increases as well. In Fig. 5(b), we found that

$$\frac{4u\mu}{r^*\tau_0} \sim \left(\frac{(\Delta P - \Delta P_{\min})}{2\tau_0 N}\right)^{\alpha}$$

α is about 1.9, which is close to 2. In Kharabaf's work, he showed the mobilized paths of network without flow. His results are much different from what we have here. Fig. 6 and Fig. 7 are the mobilized paths at different stages. Under the two situations, the first paths opened are the same. After that, the static ones have more compact patterns, while with the new algorithm, we need higher pressure to mobilize the same amount of bonds or to have the same amount of sites in continuous paths (Fig. 8).

$\frac{8\mu Q}{N\pi r^{*3}\Delta P}$, which is an indication of the permeability of the fluid, is increasing with the pressure across the network (Fig. 9a) and so is the fraction of pores in the continuous paths (Fig. 9b).

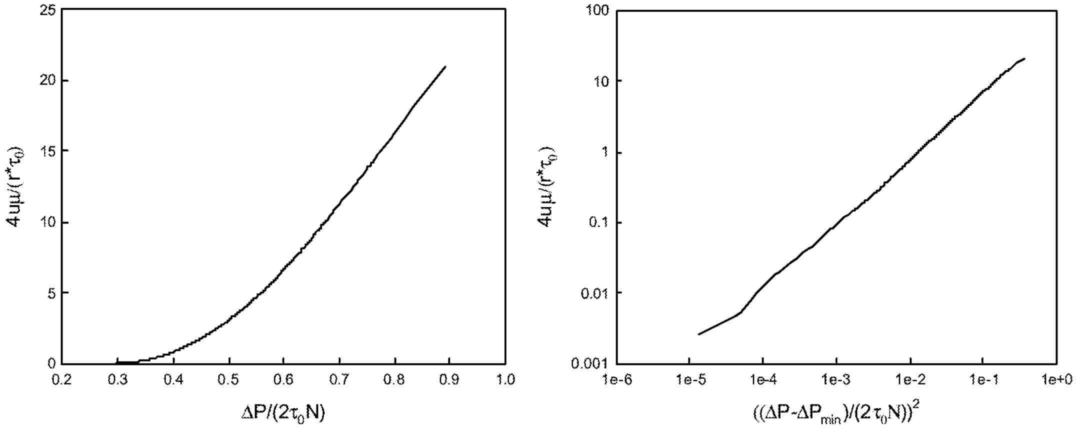

Fig. 5 a) the relation between $\frac{4u\mu}{r^*\tau_0}$ and $\frac{\Delta P}{2\tau_0 N}$; b) the relation between $\frac{4u\mu}{r^*\tau_0}$ and $\left(\frac{(\Delta P - \Delta P_{\min})}{2\tau_0 N}\right)^2$

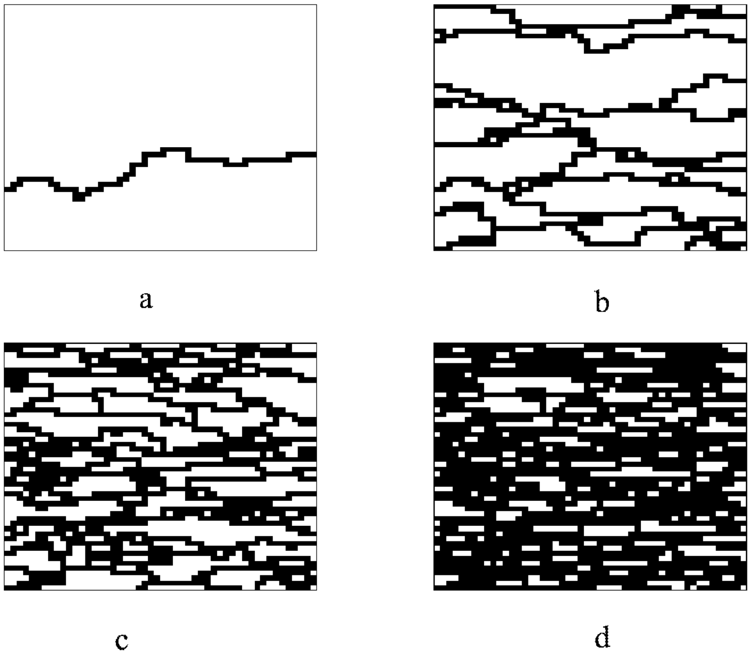

Fig. 6 Patterns with flow at different stages: (a) First path (MTP), (b) One fourth of the sites in continuous paths, (c) half, (d) three fourths.

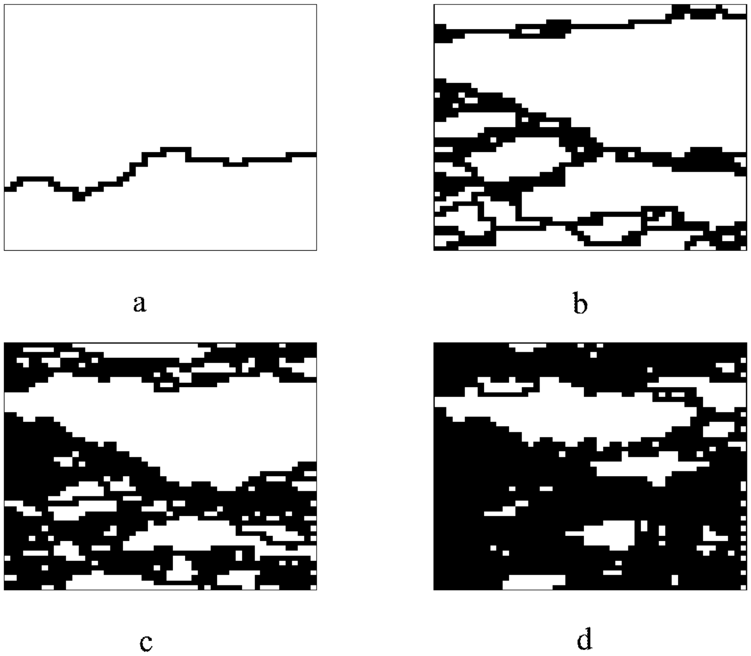

Fig. 7 The static situation:
(a) The first path (MTP) (b) One fourth of the sites are in continuous paths
(c) Half (d) Three fourths.

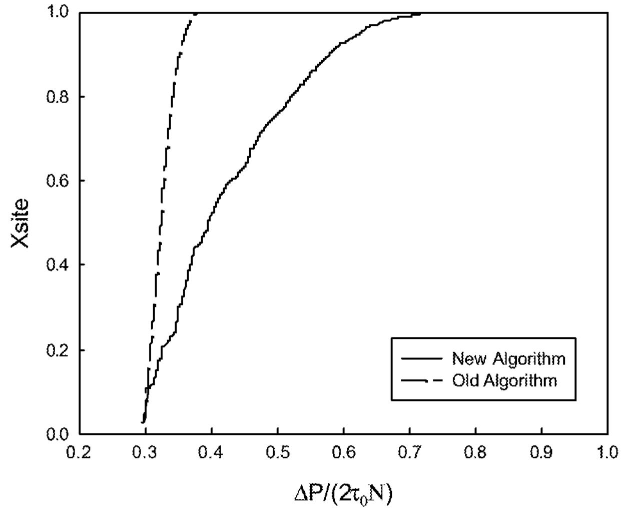

Fig. 8 Fraction of pores on the continuous path and the pressure drop exerted.

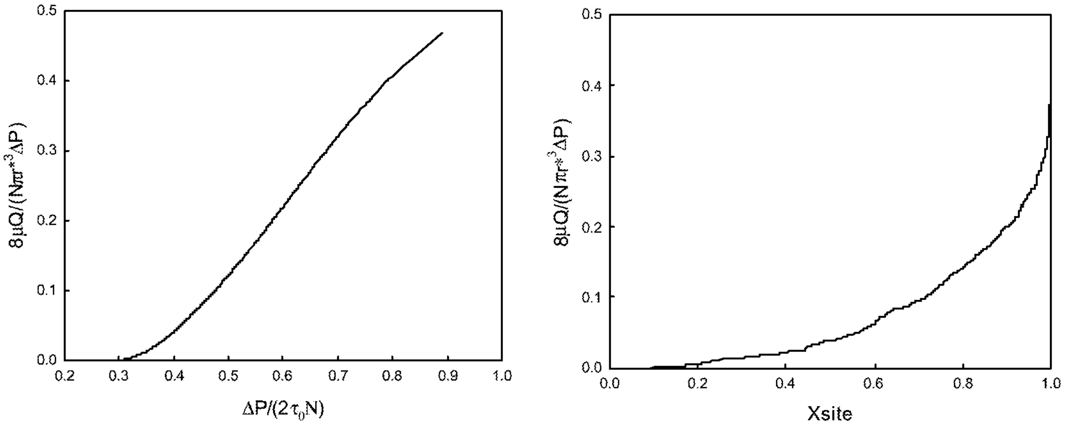

Fig. 9 a) ${}^{8\mu Q}\!/_{N\pi r^{*3}\Delta P} \sim {}^{\Delta P}\!/_{2\tau_0 N}$; b) ${}^{8\mu Q}\!/_{N\pi r^{*3}\Delta P} \sim X_{\text{site}}$

Because the first path in the system is MTP, the critical pressure to open the first path is increasing when the lattice gets larger and is totally determined by the threshold distribution. For different sizes of lattices, similar ${}^{4u\mu}\!/_{r^{*}\tau_0} \sim {}^{\Delta P}\!/_{2\tau_0 N}$ relation to those in Fig. 5 can be observed.

Other Situations for different n

For different values of n in β^n, the relations between the flow rate Q and pressure drop P are similar to that of $n=1$. The main difference is the flow pattern of the mobilized fluid. As shown in Fig. 10-Fig. 14, with increase of the absolute value of n, the flow paths are more tortuous. In Fig. 10 and Fig. 11, the paths are almost straight lines, this is because the τ_0 s are almost the same, close to 1, here we do not need much higher pressures to open new paths.

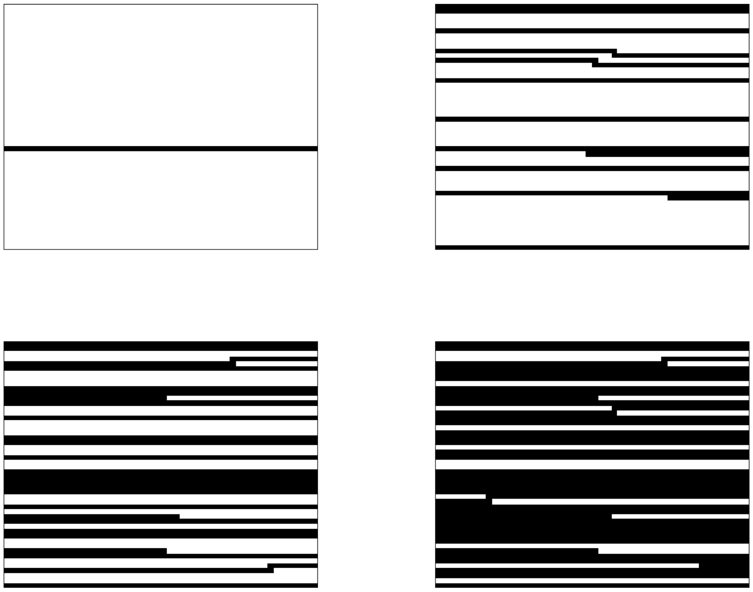

Fig. 10 Flow patterns at different stages, n=-0.1

Fig. 11 Flow patterns at different stages, n=0.1

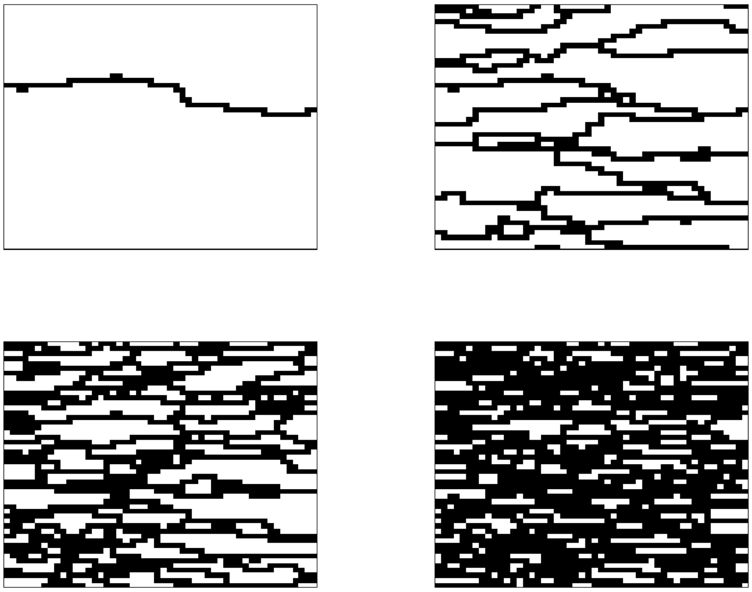

Fig. 12 Flow patterns at different stages, n=-1

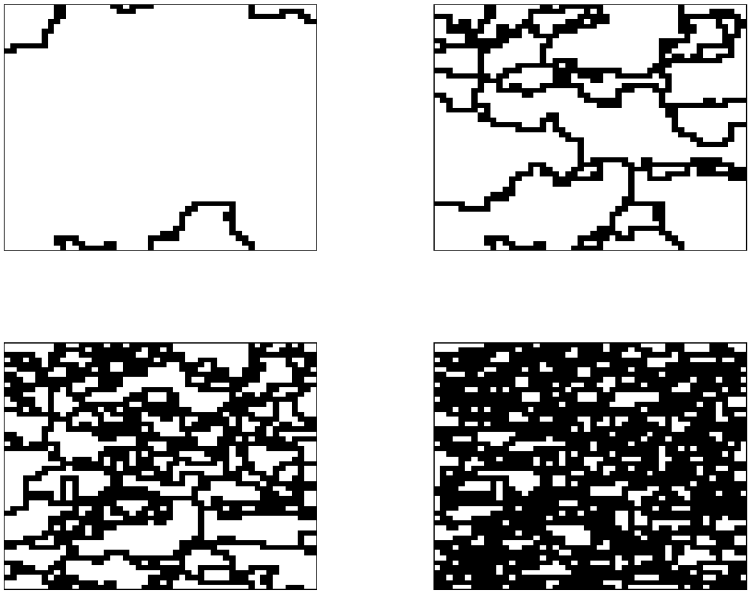

Fig. 13 Flow patterns at different stages, n=5

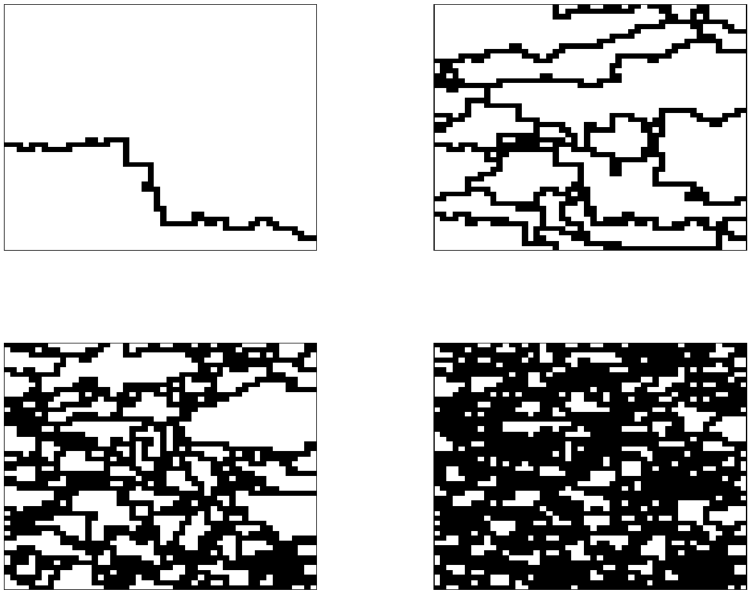

Fig. 14 Flow patterns at different stages, n=-5

In previous simulations, the volumetric flow rate in a bond is calculated based on equation (3). If we modify the equation to that shown below,

$$q_i = r_i^3\left(\Delta p_i - \frac{1}{r_i}\right)$$

We can see that the algorithm works well too.

Here, in the simulation process, τ_i is updated in the way shown below.

$$\tau_i^* = \Delta p_i = \frac{q_i}{r_i^3} + \frac{1}{r_i} = \frac{q_i}{r_i^3} + \tau_{0i}$$

Fig. 15 and Fig. 18 show simulation results and flow patterns. In Fig. 15, the ${}^{4u\mu}\!/_{r^*\tau_0}$ and ${}^{\Delta p}\!/_{2\tau_0 N}$ relation is not the same as the one we get for $n=1$, while the qualitative change of the curve is in agreement with Roux's result. At most of the part, the curve is more like a straight line, and there is an intermediate part, where the slope is different. In the previous discussion for $n=1$, the pressure need to mobilize the bonds after all of the pores are in continuous paths are incredibly high, while we can see in Fig. 17, with the new equation, all of the bonds in the system can be mobilized with relatively smaller pressures. The patterns in Fig. 18 are similar to the ones we present before.

In Fig. 19, the interesting patterns of mobilizing the fluid from the center are shown. As what we can expect, the paths to the corners are open later than other ones. We can see that even though the distance from the center is not the determinative factor, it still has obvious effect on the mobilization process.

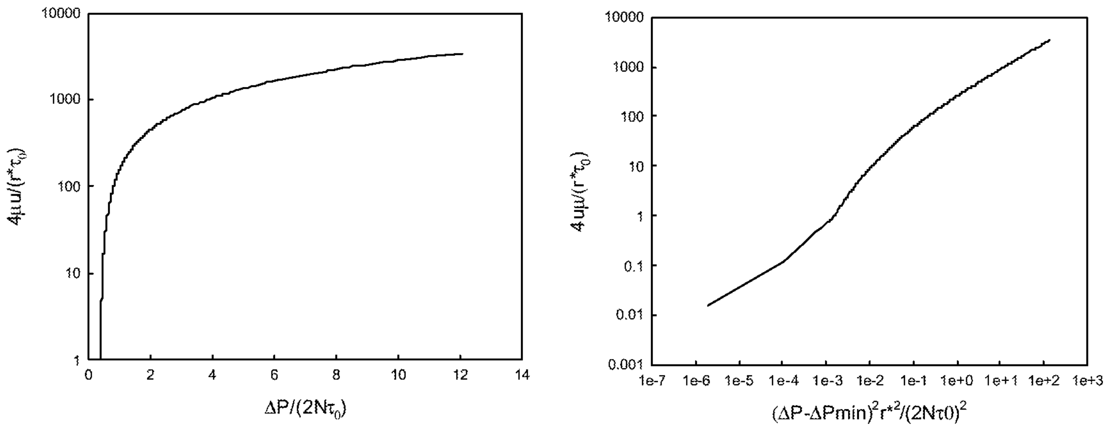

Fig. 15 Relation between $4u\mu/_{r^*\tau_0}$ and $\Delta P/_{2\tau_0 N}$;

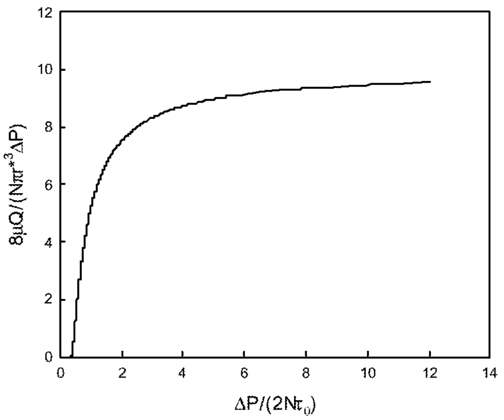

Fig. 16 $8\mu Q/_{N\pi r^{*3}\Delta P} \sim \Delta P/_{2\tau_0 N}$

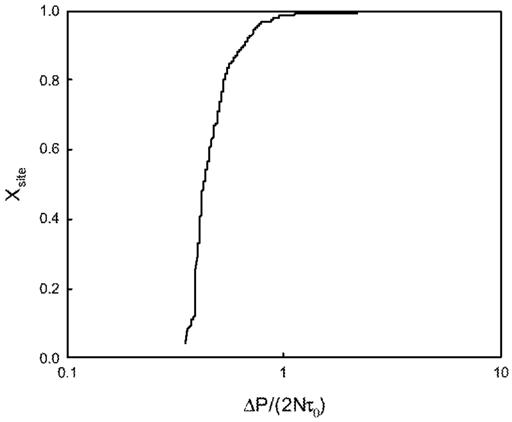

Fig. 17 $X_{site} \sim \Delta P/_{2\tau_0 N}$

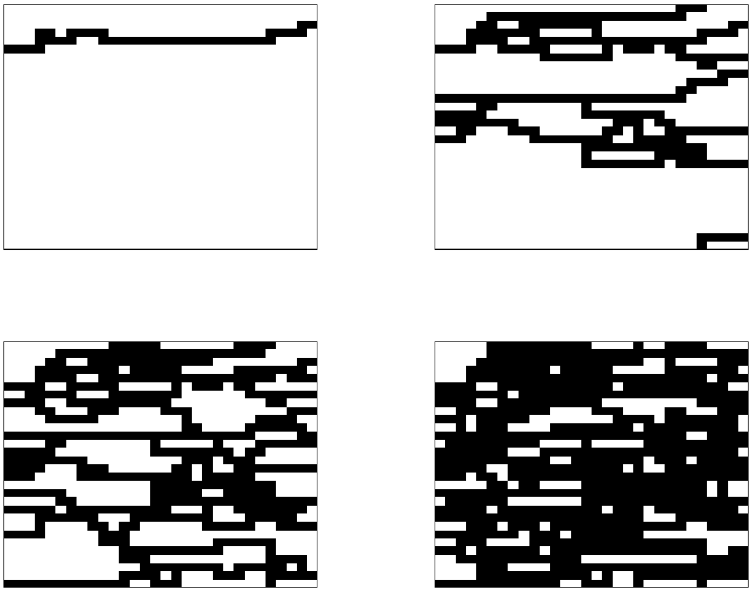

Fig. 18 Flow patterns of the fluid at different stages

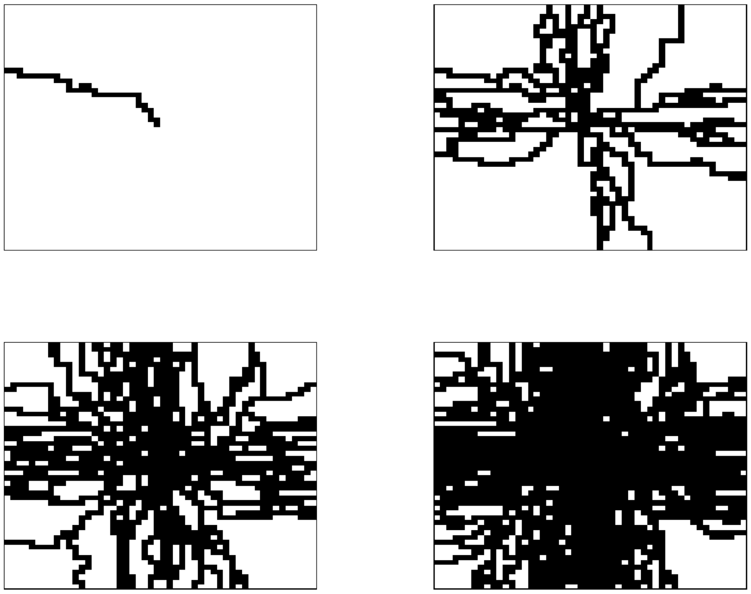

Fig. 19 Flow patterns of the fluid mobilized from the center of the network

Examples on mobilization of Bingham fluid in complex system

In our work, mobilizations of Bingham fluid in more complex system are also considered. The patterns of confined flows of Bingham fluids in converging and diverging networks at different stages are shown in Fig. 20 and Fig. 21. To compare the result to the flow process in complex geometries, the bond size in this part is evenly distributed in a very narrow interval, from 1.0 to 1.0001. From Fig. 20 and Fig. 21, we can find that the mobilization process is very similar to the ones shown in Fig. 10 and Fig. 11, where the bond sizes are very close to 1. The difference between the ones presented here and characteristics claimed by Lipscomb [13] is that the in our results yielding is not happening everywhere, which is understandable, because even though the bond size is very close to one, there is still difference between bond sizes and consequently the initial yields stresses which leads to the necessity that different paths need different minimum pressure drop to open. If bond sizes are completely the same, then yielding would occur over the entire flow field when the pressure difference applied is high enough to open a

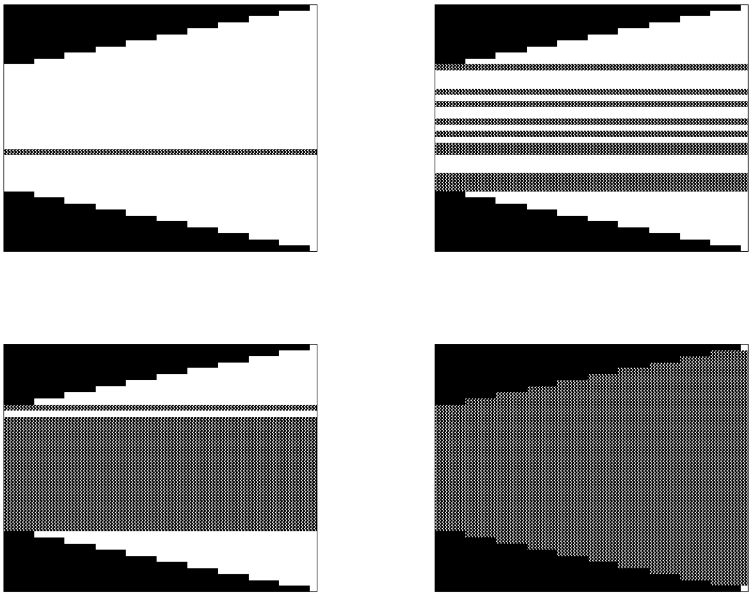

Fig. 20 Flow in converging network, first path; one quarter, half of all sites and almost all available sites are in continuous paths

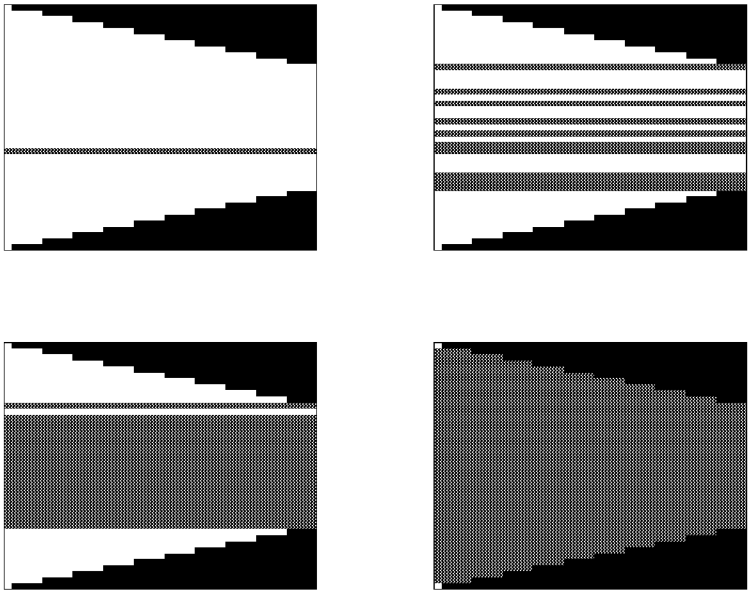

Fig. 21 Flow in diverging network, first path; one quarter, half of all sites and almost all available sites are in continuous paths

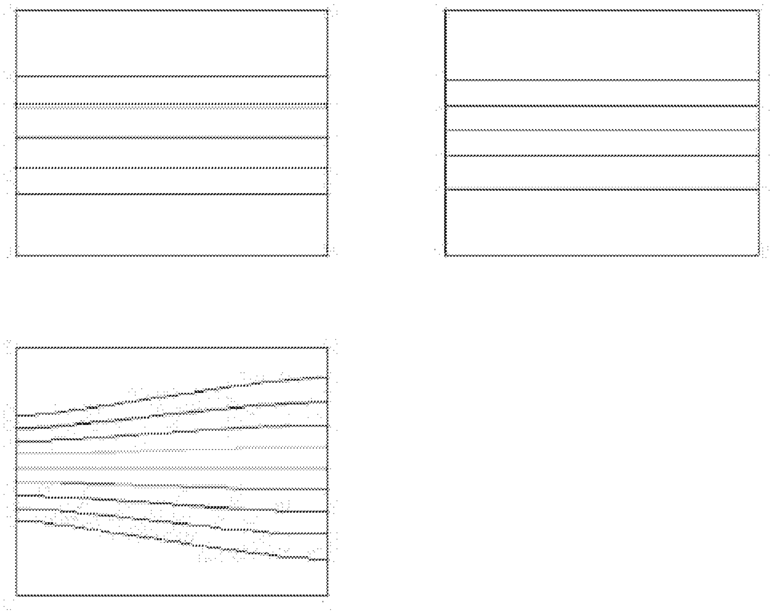

Fig. 22 Streamlines of the patterns in converging network

path. In these figures, black part is the walls, the gray part is the mobilized fluid and white part is static fluid. Fig. 22 shows the streamlines corresponding to the last three patterns in Fig. 20.

Next, flow of Bingham fluids in a network with an obstacle at the center is studied. The mobilization process in network is presented in Fig. 23. The black part at the center is an obstacle that cannot be mobilized, gray part is the sites with flowing fluid and white part is static fluid, except for the last figure, where white part is the mobilized fluid. Because of the size difference between bonds, the paths are open one by one and each at a certain pressure drop between the two boundaries. In Fig. 24, streamlines at some mobilization stages are plotted. Because of the Darcian property of the flow in the network, finally all of the available site in the system can be occupied by flowing fluid, even the ones next to the obstacle which is a bond away. This stands for the fact that there is no stagnant point in Fig. 23.

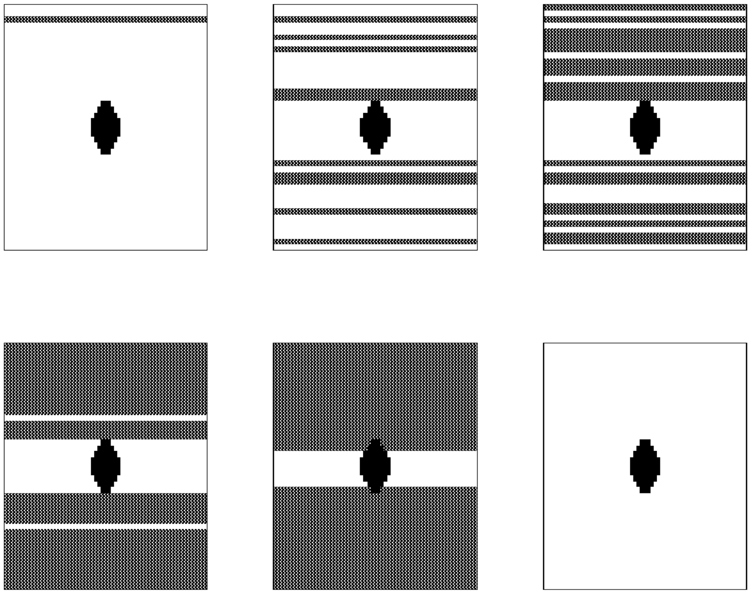

Fig. 23 Flow in a network with an obstacle at the center, first path; About one quarter, half, three quarters, 85% of all sites and all available sites are in continuous paths

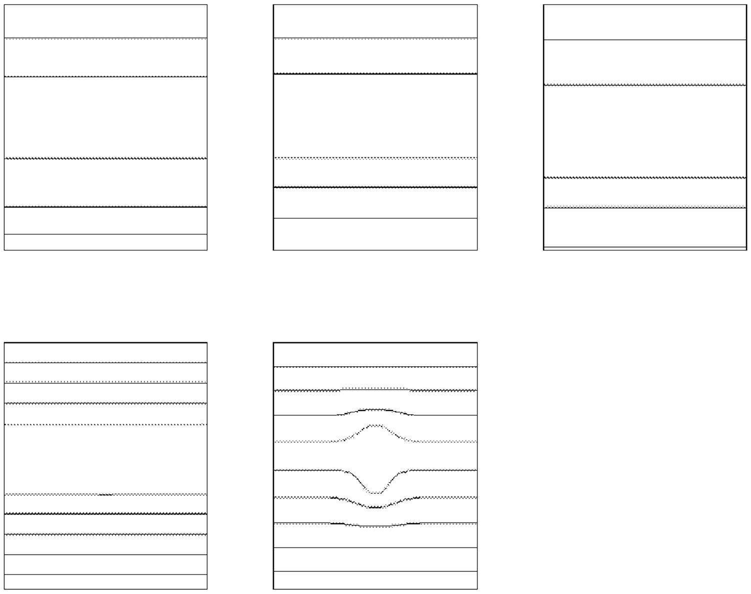

Fig. 24 Streamlines in a network with an obstacle at the center

Displacement of a Bingham fluid by a Newtonian fluid

The displacement of a Bingham fluid by a Newtonian fluid is encountered widely in oil recovery processes. The efficiency of the displacement is affected by the properties of the two fluids. This problem can also be tackled with our new algorithm. In this part, the capillary forces are neglected.

First, let's consider a case in which the Newtonian fluid has almost zero viscosity, this means that the pressure drop is almost zero in the part occupied by Newtonian fluid. Every time the interface advances, we choose the one which needs minimum amount of time to get to the next site. Every other interface moves a distance determined by its velocity and the minimum time known. If we use the same equation as (3) for the non-Newtonian fluid flow, calculating pressure distribution with the restriction of mass conservation at each pore in the mobilized path, we can get the following patterns at different stages, shown in Fig. 25. The algorithm is similar to the one discussed before. In this case, only the τ_i s of the non-Newtonian fluid are updated. In Fig. 25 and all the figures in this section, the white part is non-Newtonian fluid, gray part is the mobilized

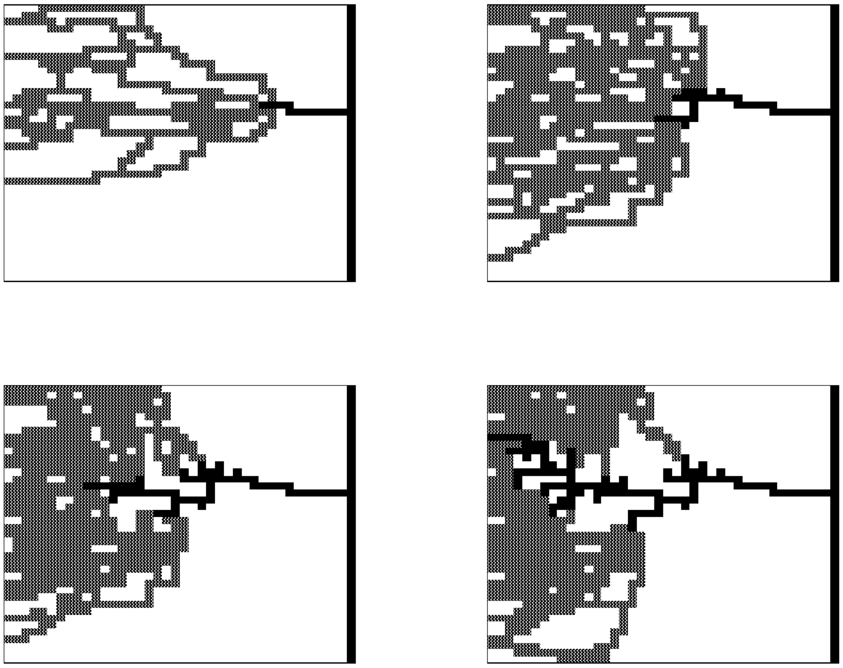

Fig. 25 Patterns of displacement process at different stages, viscosity ratio=0
non-Newtonian fluid and black part is occupied by Newtonian fluid. Before the breakthrough of the Newtonian fluid, the pressure is kept constant as the initial pressure to open the first path. With time increasing, more and more paths are open and the front of the Newtonian fluid moves deeply into the lattice gradually.

If we consider the situations with larger viscosity ratios (1 in Fig. 26 and 20 in Fig. 27), the number of mobilized paths in the system doesn't increase much. The patterns at larger viscosity are much different from the one with zero viscosity, while the latter one can have more mobilized paths. One reason accounting for this difference is the larger pressure drop in the former case, so the pressures are not enough to overcome the thresholds.

Mobilization of a Bingham fluid trapped in a Newtonian fluid

In oil recovery processes, waterfloods of Bingham rheology heavy oils are of much importance. During this kind of displacement process, the Bingham fluid may be trapped

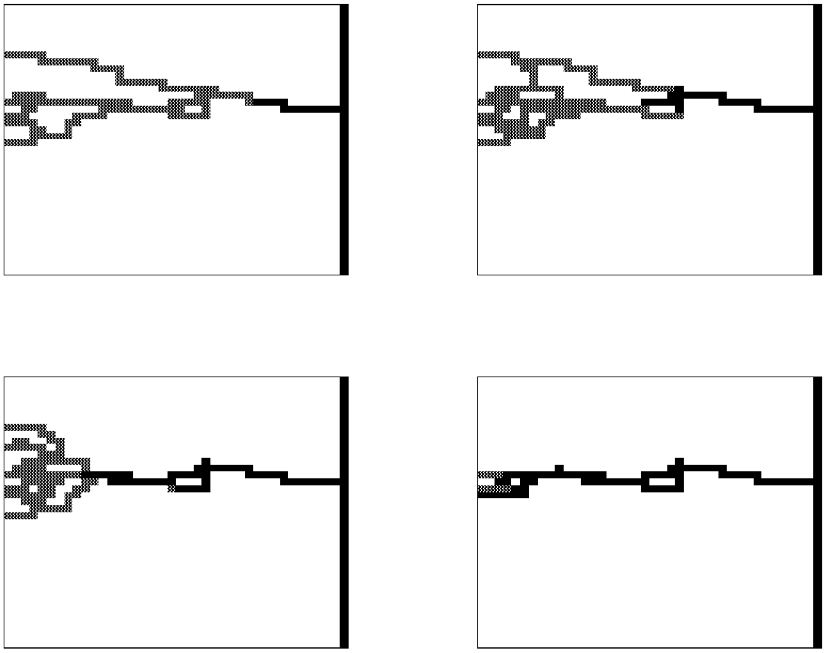

Fig. 26 Displacement patterns at different stages, viscosity ratio=1

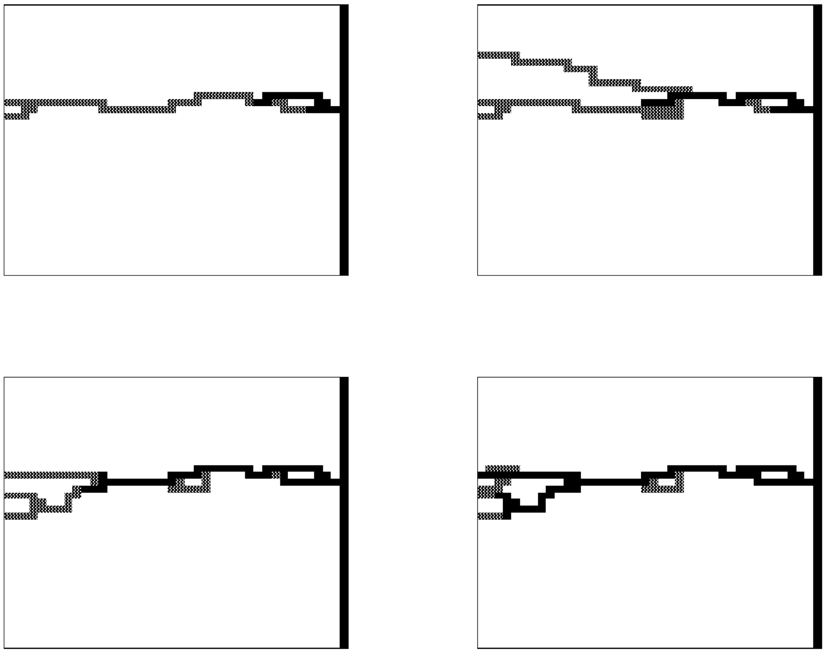

Fig. 27 Displacement patterns at different stages, viscosity ratio=20

and cannot escape until the pressure is high enough. The immiscible displacement involves not only the yield stress, but also the capillary forces. Viscous forces in the Bingham fluid are still neglected, assuming the displacement takes place very slowly.

To use the new algorithm developed to mobilize the trapped Bingham fluid, τ_i should be correspondingly updated every time. For Newtonian fluid, the initial value is $\tau_{0i} = 0$, and

$$\tau_i^* = \Delta p_i$$

For Bingham fluid, τ_{0i} keeps constant,

$$\tau_{0i} = \frac{1}{r_i}.$$

At the interfaces of the two fluids, the capillary condition should be considered,

$$P_c = \frac{2\gamma}{r}$$

In each bond occupied by Newtonian fluid,

$$q_i = \frac{\pi r_i^4}{8l\mu} \Delta p_i$$

First, consider the mobilizing process of a single point of Bingham point trapped. Fig. 28 shows the trace of the point. It starts from the right boundary of the network. This is a quasi-steady state process, if the pressure of the Newtonian fluid around the Bingham fluid is high enough to overcome the thresholds and the capillary effect, the Bingham fluid moves in the direction of decreasing pressure, otherwise, it stays and the pressure applied to the system increases. In every step, the pressure distribution of the Newtonian fluid is computed.

When a block of Bingham fluid trapped in Newtonian fluid is mobilized in the same approach as described above, the Bingham fluid would go through a spattering process, and become a bunch of points, which are mobilized almost one by one. This is because each time we find one path, and mobilize the Bingham fluid in that path. Fig. 29 shows some patterns of the mobilization process. It is possible that some trapped points can never be moved out the system.

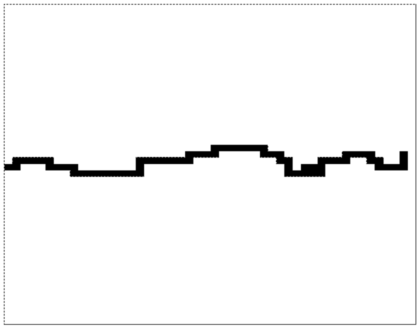

Fig. 28 Mobilization trace of a single point

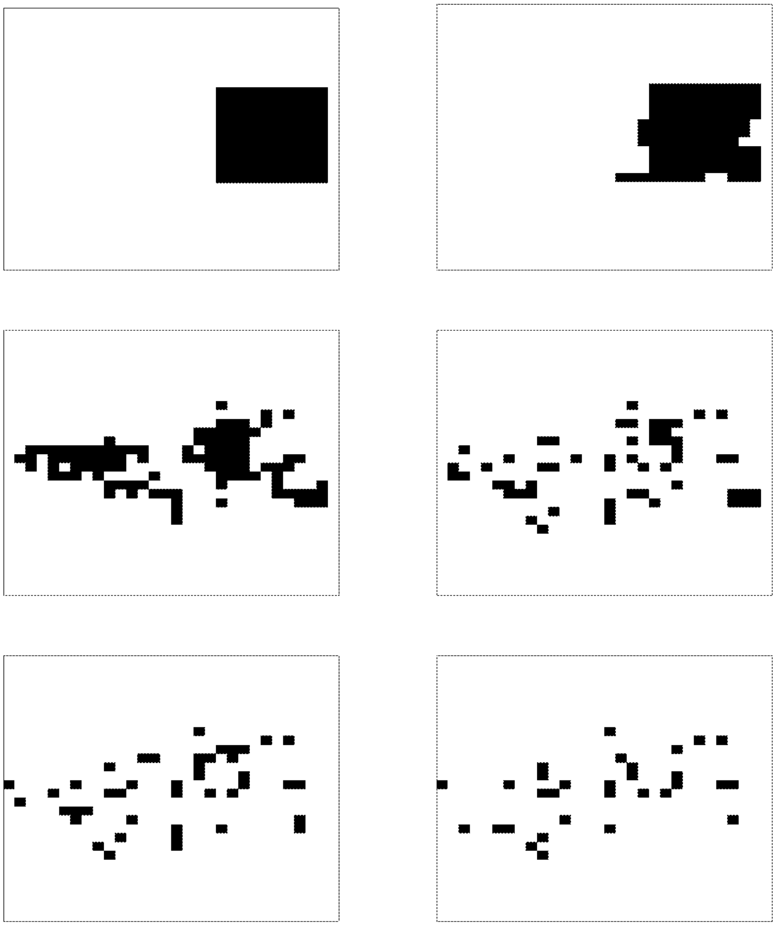

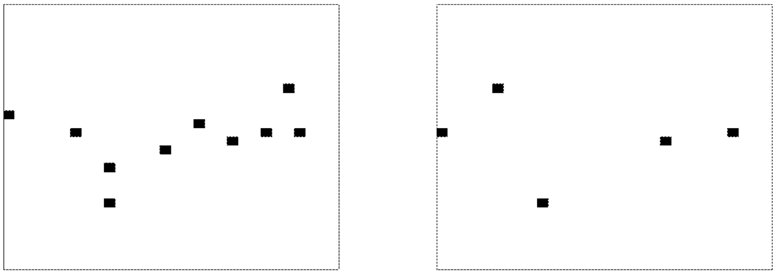

Fig. 29 Snapshots of mobilization process

Conclusion

A new algorithm is developed, which can effectively solve the problem of the mobilization of a single fluid with yield stress in a network. The simulation result is in good agreement with the work done by Roux et al. The model is successfully used in some different situations and the results are shown. The distribution of the yield stress has obvious effects on the mobilization process; with the increase of the power n, the paths are more tortuous. The results of mobilization processes are also obtained for complex networks.

In the displacement of a non-Newtonian fluid by a Newtonian fluid, patterns are affected by the viscosity ratio of the Newtonian fluid to the non-Newtonian fluid.

The model is also employed in the mobilization process of Bingham fluid trapped in Newtonian fluid. The Bingham fluid block is broken into small parts and mobilized one by one, which is the typical process found in experiments.

Reference

1 Barrenblatt, G.I., Entov, V.M., and Ryzhik, V.M.: Theory of fluid flows through natural rocks, Kluwer Academic Publishers, Netherlands, 1990.

2 Bedrikovetsky, P.: Principles of oil and gas production, Kluwer Academic Publishers, Netherlands, 1995.

3 Rossen, W. R. and Gauglitz, P.A.: "Percolation theory of creation and mobiliztion of foam in porous media", AIChE J., 36(8) Aug. 1990, pp. 1176-1188.

4 Wu, Y.S., Pruess, K., and Witherspoon, P.A., SPERE, (1992) 369.

5 Rossen, W.R. and Mamun,C.K.: "Minimal path for transport in networks", Phys. Rev. B 47(18) 1993-II, pp. 11815-11825.

6 Roux, S., and Herrmann, H.J.: "Disorder-induced nonlinear conductivity", Europhys. Lett., 4(11), 1987, pp. 1227-1231.

7 Sahimi, M.: "Non-linear transport processes in disordered media", AIChE J. 39(3) 1993, pp. 369-385.

8 Zhou, D. and Stenby, E.: "Displacement of trapped oil from water-wet reservoir rock", Transport in Porous Media, vol. 11, 1993, pp. 17-31.

9 Kharabaf, H. and Yortsos, Y.C.: "Invasion Percolation with memory," Phys. Rev. E (1997) 55, 7177.

10 Kharabaf, H. and Yortsos, Y.C.: "Pore Network Model for Foam Formation and Propagation in Porous Media", SPE J. March 1998 pp. 42-53.

11 Kharabaf, H.: PhD Dissertation, U. of Southern California, Los Angeles, California (1996).

12 Bird, R.B., Stewart, W.E., and Lightfoot, E.N.: Transport Phenomena, Wiley, New York (1960).

13 Lipscomb, G.G., and Denn, M.M.: "Flow of Bingham fluids in complex geometries," Journal of Non-Newtonian Fluid Mechanics 14(1984) 337-346.

$$\theta_j = 1 + c_3 e^{r_1\xi} + c_4 e^{r_2\xi} + c_5 e^{r_3\xi} + c_6 e^{r_4\xi} \tag{37}$$

III. Region III:

$$\begin{aligned}\theta_i = 1 + \left(1 + \frac{h_j}{\sigma}\right)\left(c_7 e^{r_3\xi} + c_8 e^{r_4\xi}\right) + \frac{1}{\sigma}\Big(A_j \Big(c_7 r_3 e^{r_3\xi} \\ + c_8 r_4 e^{r_4\xi}\Big) - c_7 r_3^2 e^{r_3\xi} + c_8 r_4^2 e^{r_4\xi} - h_j\Big)\end{aligned} \tag{38}$$

$$\theta_j = 1 + c_7 e^{r_3\xi} + c_8 e^{r_4\xi} \tag{39}$$

Application of the same jump conditions as before gives rise to a set of ten equations in terms of the ten unknowns (integration constants, the distance between the fronts and the front velocity). Details of the solution are found in [9].

3.3 Non-adiabatic, symmetric, three-layered porous medium

The same approach can be applied to the solution of a symmetric three-layered medium, when the two outer layers have the same properties. This type of geometry is useful in the investigation of the effect of a middle layer that plays the role of a permeable thief zone. Because of the symmetry assumed, velocity and temperature of the outer reaction fronts are taken to be identical, as shown in Figure 6.

Then, the governing energy balances become

$$A_i \theta_i' = \theta_i'' + \sigma_i(\theta_j - \theta_i) - h_i(\theta_i - 1) \tag{40}$$

$$A_j \theta_j' = \theta_j'' + \sigma_j(\theta_i - \theta_j) \tag{41}$$

Working as before, equation (41) gives θ_i,

$$\theta_i = \theta_j + \frac{1}{\sigma_j}(A_j \theta_j' - \theta_j'') \tag{42}$$

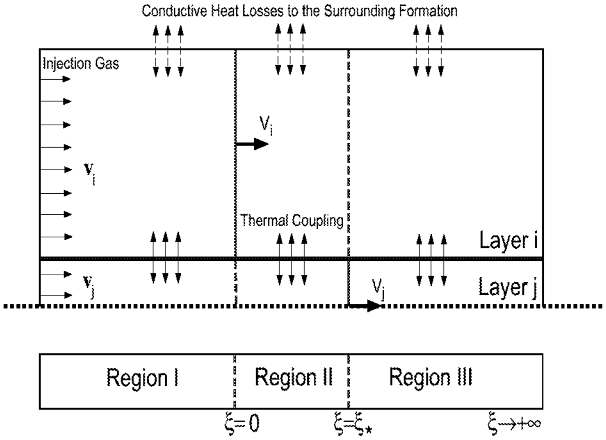

Figure 6: Schematic of the notation used for the propagation of combustion fronts in a two-layered porous medium.

Inserted into (40) gives

$$\theta_j^{(iv)} - B\theta_j''' + \bar{E}\theta_j'' + \bar{F}\theta_j' + \sigma h_i\theta_j - \sigma h_i = 0 \tag{43}$$

where

$$\begin{aligned} \bar{E} &= A_iA_j - \sigma_i - \sigma_j - h_i \\ \bar{F} &= B\sigma_j + A_jh_i \end{aligned}$$

the solution of which is obtained as before, in terms of a combination of exponentials, with exponents the real roots r_1, r_2 >0 and r_3, r_4 <0 of the characteristic equation

$$r^4 - Br^3 + \bar{E}r^2 + \bar{F}r + \sigma_jh_i = 0. \tag{44}$$

The mathematical procedure is similar to the previous and will not be repeated (see [9] for more details).

4 Results

The numerical solution was studied using typical in situ combustion data [7, 9]. Results were obtained for the temperature T_f and velocity V of the fronts as well as their distance $\tilde{\xi}_* = \xi_* \times l_*$, in terms of the velocity (hence, permeability) ratio $R = v_i/v_j$, the thermal coupling coefficient σ, the velocity of the layers, and, in the non-adiabatic cases, the layer thicknesses H_i and H_j. We considered two velocity cases, one in which the larger velocity is fixed to v_j=100m/day (case j), and another in which lower velocity v_i is fixed to v_i=100m/day (case i). In either case R was varied between its limits 0 and 1.

4.1 Adiabatic Two-layer Case

The procedure applied during the calculations is explained in detail in [9]. Figures 7 and 8 show the effect of R on the temperature profiles and the front velocity for constant σ, and case j. We note the following: The system recovers the single-layer solution (with V=1.7346 m/day) in the single-layer case $R = 1$ (Figure 7). Here the two fronts collapse, and their distance is nil. When $R = 0.5$ (Figure 8), the separation between the fronts is clear. The front in layer j has slowed down, and has a lower temperature than that of layer i, which has accelerated to a common velocity (equal to V=1.0033 m/day). The temperature profile is more diffuse than in the single-layer case, with heat being transferred from layer j to layer i downstream and from i to j upstream. Interestingly, the temperature profile in the lower-permeability layer has a peak, which is not present in the single-layer problem. Nonetheless, the far-field temperature upstream is equal to the adiabatic temperature. The common front velocity is much closer to the single-layer velocity for the lower-permeability layer (corresponding to an injection velocity of 50m/day, rather than the arithmetic average injection velocity of 75m/day). This reflects strong non-linear coupling effects. The effect of the thermal coupling parameter σ is shown in Figure 9. Interestingly, as σ decreases the coupling is not weakened, but rather enhanced. Clearly, the front separation has increases, the temperature peaks increased, while the common front velocity has further increased (V=1.0161 m/day).

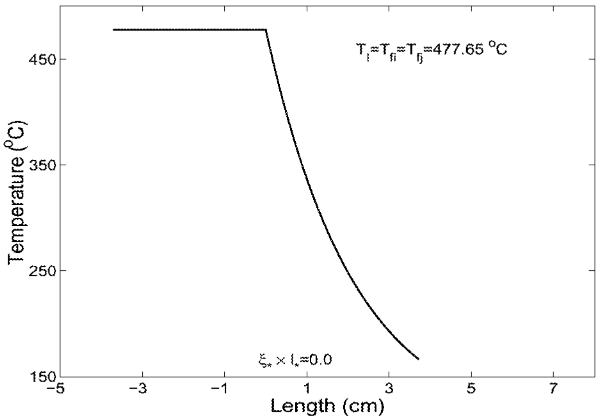

Figure 7: Temperature profiles for the two-layer adiabatic case. R=1.0, σ=0.01.

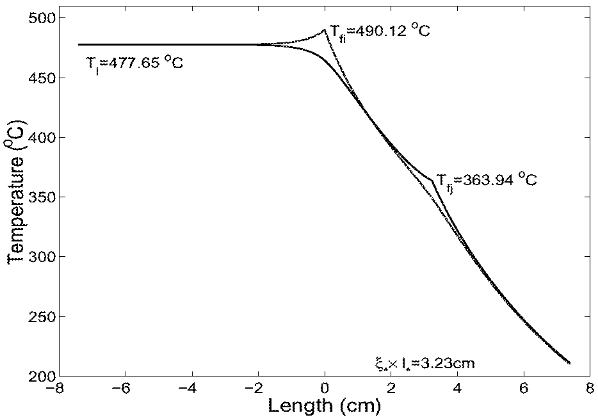

Figure 8: Temperature profiles for the two-layer adiabatic case. R=0.5, σ=0.01.

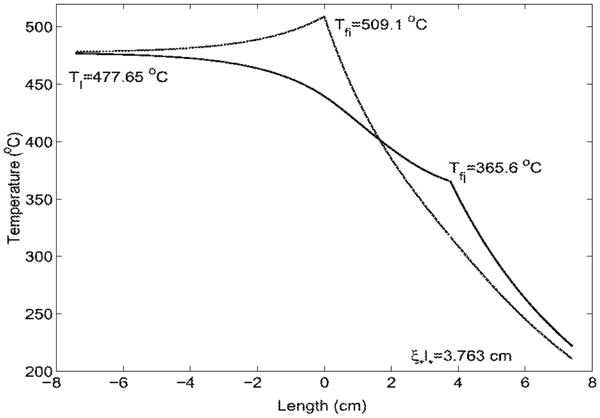

Figure 9: Temperature profiles for the two-layer adiabatic case. R=0.5, σ=0.001.

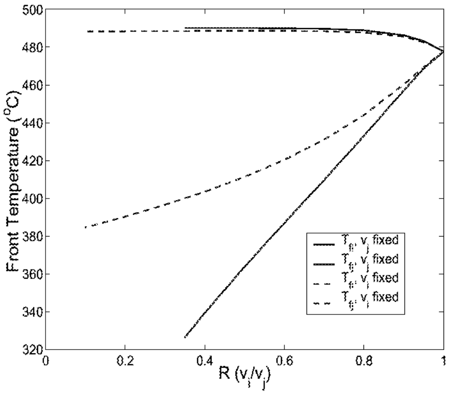

Figure 10: Front temperatures versus R for the two-layer adiabatic case. Solid lines denote case j, dashed lines denote case i.

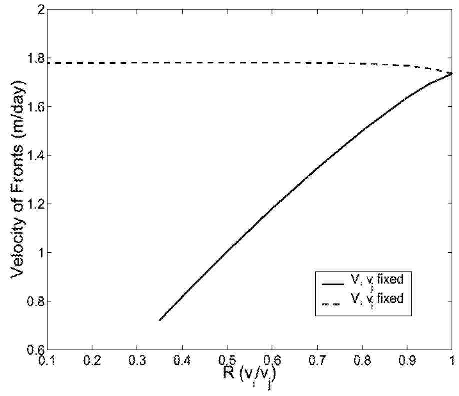

Figure 11: Front velocity versus R for the two-layer adiabatic case. Solid lines denote case j, dashed lines denote case i.

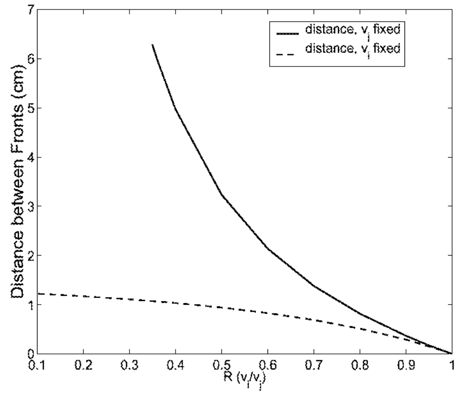

Figure 12: Distance between the fronts versus R for the two-layer adiabatic case. Solid lines denote case j, dashed lines denote case i.

While these results point out to an important effect of R, the latter also depends on the actual velocity values. Figures 10-12 show two sets of the front temperatures, front velocities and front distance, as a function of R for σ=0.01 and the two cases j and i, respectively. Recall that case j corresponds to fixed v_j=100 m/day, while case i to fixed v_i=100 m/day. Of course, ideally one would like to have a three-dimensional plot with v_i and v_j as the independent variables. However, these computations can be time consuming and in the present we will restrict ourselves to only a few slices of this diagram.

It is clear from Figure 10 that the effect of the actual velocity levels is not great on the front temperatures (except for that of the leading front at small values of R). In fact, the far-field temperature behind the two fronts is not influenced at all by the variations in R or σ as its value is always the adiabatic temperature, as pointed out above. Thus, for the adiabatic case, the temperature is roughly only a function of R. However, the effect is significant on the front velocities and the front distance. In case j, where it is the larger injection velocity which is kept fixed, the front velocity decreases as the smaller injection velocity decreases, almost proportionally to it, while in case i, where the smallest velocity is fixed, the variation is insignificant. Analogous is the effect on the front distance.

These results suggest that essentially the behavior of the system is controlled by the layer with the smallest injection velocity, with the front velocity in particular almost being a slave of that variable. The implications of this finding are important. For the adiabatic case they simply affect the rate of front propagation. However, for the non-adiabatic case, discussed below, they may have more dramatic consequences, regarding the possibility of process extinction.

4.2 Non-adiabatic Two-layer Case

Using the formulation described in the previous sections, numerical results were obtained for the non-adiabatic case in the two-layer system. Now, in addition to the previous, an important additional parameter is the layer thickness, which was taken in all simulations shown as the same for the two layers.

When the layer thickness is sufficiently large (approximately 2m, for the parameters shown here) the solution of the problem and its sensitivity to R and the velocities is qualitatively the same as in the adiabatic case. Unique solutions exist and the main difference is that the temperature profile is more spread out, has somewhat more structure and, of course, asymptotically tends to the initial value. Characteristic examples are shown in Figures 13-15. The observed similarity of the non-adiabatic model results when H=2m to the results of the adiabatic case is consistent with the results of single layer analysis – the combustion fronts propagate as if the system is in the adiabatic mode, given that sufficient gas is injected into the layers.

On the other hand, when the thickness becomes small, the qualitative picture changes. As in the single-layer case, the possibility of multiplicity arises. Figures 16 and 17 show features very similar to the single layer. Thus, for case j, where the lower injection velocity can become sufficiently small in magnitude, extinction and ignition limits arise. The multiplicity arises simultaneously in both fronts, and both fronts ignite and get extinct simultaneously. The corresponding curves for case j are similar both qualitatively and quantitatively to the single layer case. The results for case i are somewhat different. Here, because the lowest velocity remains fixed (at 100 m/day), multiplicity does not arise until the layer thickness is sufficiently small (contrast Figures 16 and 17). By comparing with the single-layer results, this effect is somewhat unexpected. If we were to assume that the front basically follows the front velocity corresponding to the lower injection velocity, the curves corresponding to case i could be interpreted from the single-layer results as those corresponding to the upper branch. This would mean that intermediate and lower branches would also exist. These do not appear in Figure 16, although they do in Figure 17, which corresponds to a smaller thickness layer. One infers that when the velocities are sufficiently large, the composite, two-layer system behaves as one with an effectively larger thickness, compared to the case when the layer velocities are relatively small. This interpretation is also supported in the velocity and front distance curves shown in Figures 18 and 19. However, and contrary to the adiabatic case, another effect is also present here, namely, an intrinsic heterogeneity effect through the parameter R. For example, the above figures illustrate through case i, that by increasing the heterogeneity of the layers, extinction will eventually set in, even though the lower-permeability layer has a fixed injection velocity. This effect is non-trivial and unexpected. For completeness, we examined the sensitivity of these results to the thermal parameter σ. Very small differences were found as σ was decreased by a factor of 10.

The implications of these results are important. They point out that increasing the permeability contrast between the layers can have dramatic effects on the propagation of a combustion front. Namely, given an overall injection rate, and for sufficiently small layer thickness, there is a sufficiently large permeability contrast, such that the process becomes extinct. Depending on the parameters, this contrast can be as low as 10. Strongly layered (and by extension, strongly heterogeneous) systems may thus be not good candidates for in-situ combustion. The above results gave only one indication of the ballpark values for this to occur. A more systematic analysis would require the development of 3-D plots using the two velocities as coordinates and the resulting identification of extinction and ignition limits.

4.3 Non-adiabatic Three-layer Case

For completeness, we also analyzed the symmetric, three-layer geometry. Now, the middle layer is shielded and does not lose heat directly to the surroundings. The results obtained were qualitatively similar to the previous non-adiabatic problem. In this geometry, we investigated the sensitivity of the results to the ratio of the thickness of the two layer, which here were taken unequal. In the calculations, we also kept the injection velocity of the surrounding layers fixed, and varied v_j (case i). Front temperature results are shown in Figure 20. It is shown that when the shielding layers are thick enough (dashed lines in Figure 20) the behavior approaches the adiabatic case, where there exists a unique solution. If the layer thickness decreases, then multiplicity sets in, with characteristics similar to the ones discussed above.

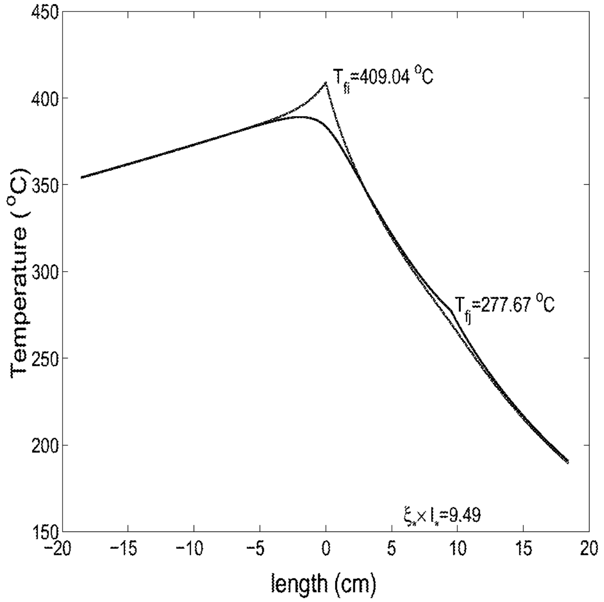

Figure 13: Temperature profiles for the non-adiabatic two-layer model. H_i=H_j=2m, R=0.20, σ=0.01, calculated V=0.4070 m/day.

5 Concluding Remarks

In this chapter we extended the approach of [7] to heterogeneous systems, by considering the simpler case of in-situ combustion in layered porous media. Two simple geometries were considered, a two-layer model and a symmetric three-layer model. Analytical models were developed to delineate the combined effects of fluid flow, reaction and heat transfer on the dynamics of combustion fronts in the layers, using as parameters the thermal coupling between the layers, the heat transfer to the surroundings and the permeability contrast. We find that in layered systems, the thermal coupling between layers leads to coherent traveling fronts, propagating at the same velocity. This coupling retards greatly fronts in the more permeable layer and accelerates only slightly those in the less permeable one, until a common front velocity is attained. In essence, the problem becomes slave to the injection velocity in the lower permeability layer. As in the single-layer case, there exists a unique solution, under adiabatic conditions, and multiple steady-state solutions, under non-adiabatic conditions. The latter lead to ignition and extinction conditions. Importantly, for a sufficiently large permeability contrast, relatively small layer thickness and under non-adiabatic conditions, steady-state

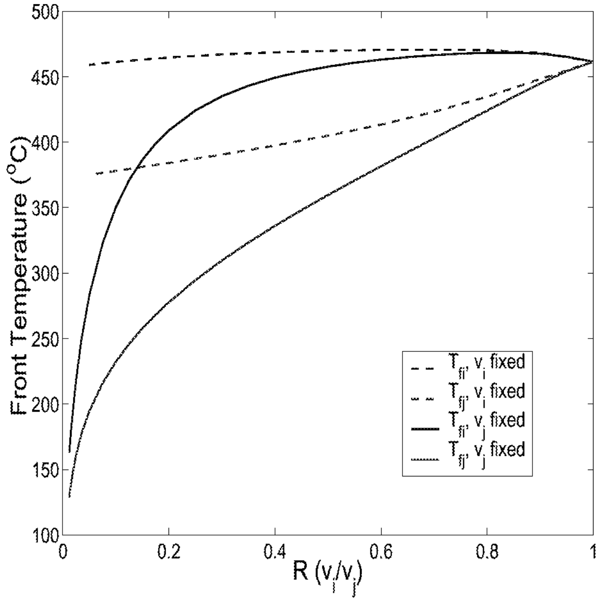

Figure 14: Front temperatures versus R for the non-adiabatic two-layer model. Solid lines denote case j, dashed lines denote case i. H_i=H_j=2m., σ=0.01.

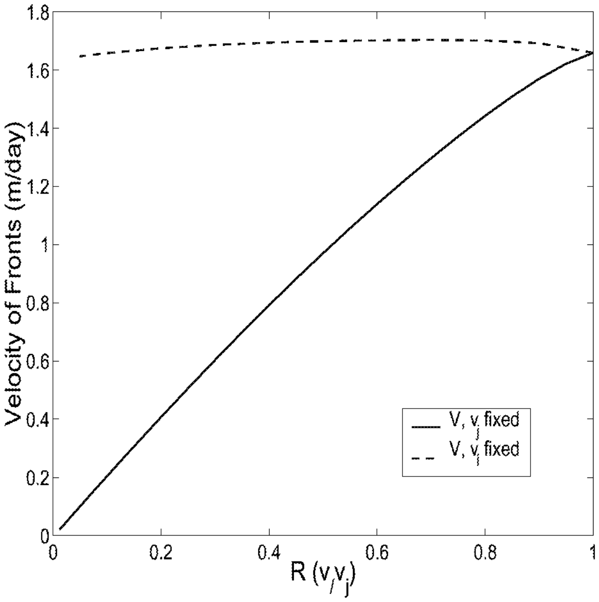

Figure 15: Velocity of the fronts versus R for the non-adiabatic two-layer model. Solid lines denote case j, dashed lines denote case i. H_i=H_j=2m., σ=0.01.

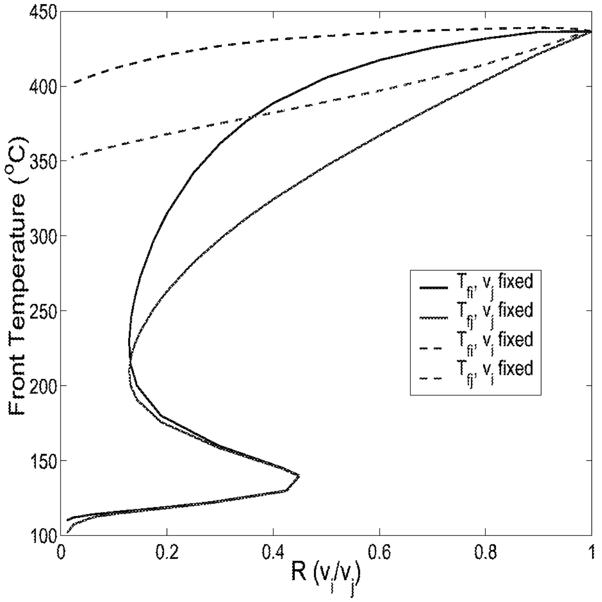

Figure 16: Nonadiabatic front temperatures for layers i and j versus R. Solid lines denote case j, dashed lines denote case i. H_i=H_j=0.8m., σ=0.1.

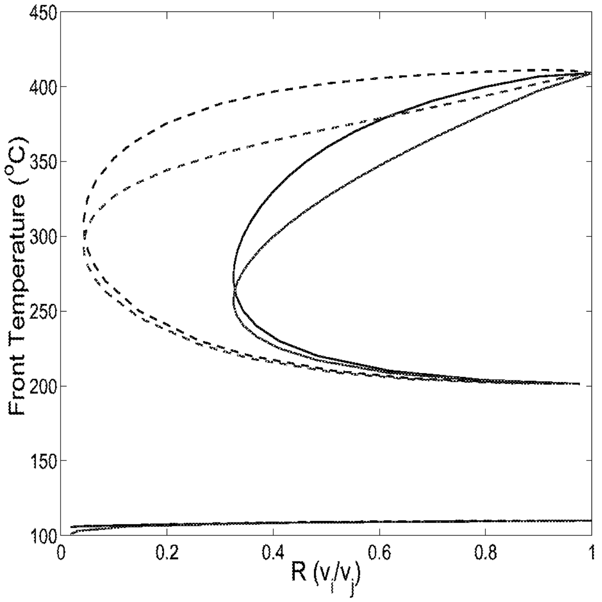

Figure 17: Nonadiabatic front temperatures for layers i and j versus R. Solid lines denote case j, dashed lines denote case i. H_i=H_j=0.5m., σ=0.1.

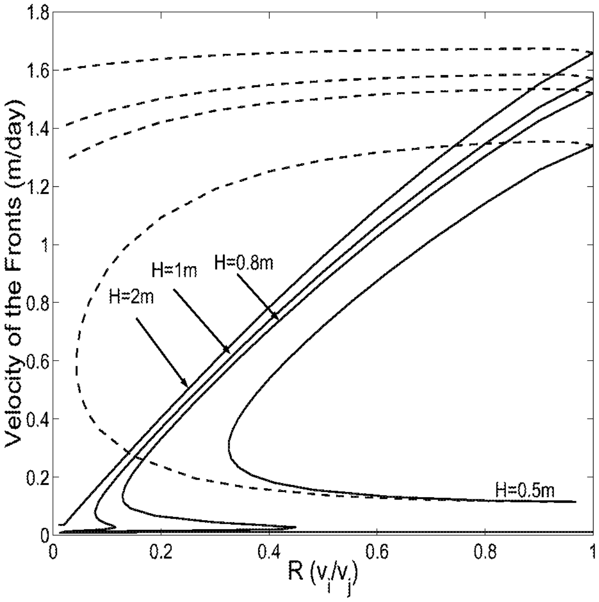

Figure 18: Nonadiabatic front velocity for layers i and j versus R for varying H. Solid lines denote case j, dashed lines denote case i. σ=0.1.

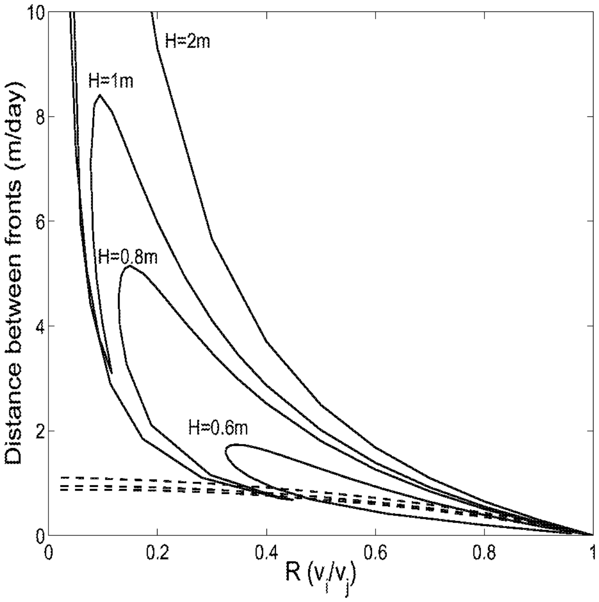

Figure 19: Distance between the fronts in layers i and j versus R for varying H and the non-adiabatic case. Solid lines denote case j, dashed lines denote case i. σ=0.1.

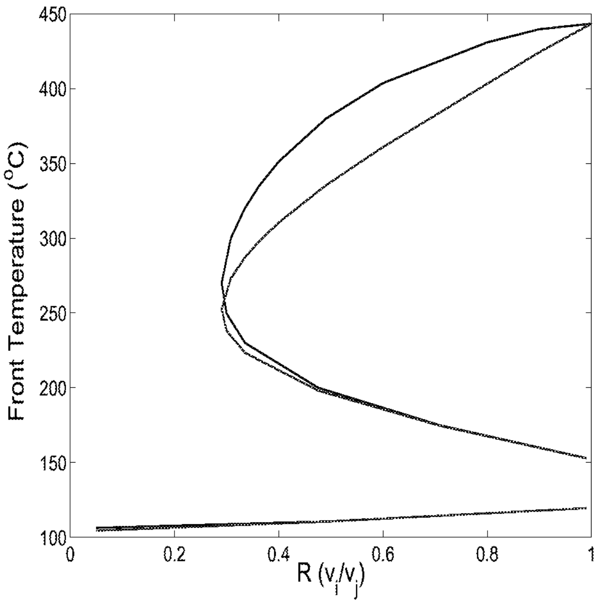

Figure 20: Front temperature versus R for the non-adiabatic symmetric, three-layer case. Solid line denotes thickness of the shielding layers equal to 0.5 m, dashed lines denote thickness equal to 2 m. σ_i=0.1

propagation in the two layers cannot be sustained, and the process becomes extinct, even though, under the same conditions, sustained propagation would have been predicted for the equivalent single-layer problem with the average injection velocity. In a sense, the problem becomes controlled by the extremes of the permeability distribution. Such behavior can be detrimental to the success of in-situ combustion in highly heterogeneous layered media. In addition, it raises serious questions on the ability of conventional reservoir simulators to capture it. Conventional models average flow and kinetic behavior over substantially large distances, where effects, such as the above, which are dominated by the extremes of the permeability field, cannot be adequately represented. Precise conditions for the delineation of the above behavior need to be further developed. We anticipate that similar conclusions will hold in the case of heterogeneous media. Work in this direction is currently in progress.

References

[1] Williams, F.A. *Combustion Theory*, Benjamin and Cummings Publishing Company Inc. (1985).

[2] Britten, J.A. and Krantz, W.B., *Combust. Flame*, 60:125 (1985).

[3] Britten, J.A. and Krantz, W.B., *Combust. Flame*, 65:151 (1986).

[4] Schult, D.A., Matkowsky, B.J., Volpert, V.A., and Fernandez-Pello, A.C., *Combust. Flame*, 104:1 (1996).

[5] Schult, D.A., Bayliss, A. and Matkowsky, B.J., *SIAM J. Appl. Math.*, 58:806 (1998).

[6] Chuan, L. and Yortsos, Y.C. *A Pore-Network Model of In Situ Combustion in Porous Media*, paper SPE 69705 presented at the Society of Petroleum Engineers International Thermal Operations and Heavy Oil Symposium, Santa Margarita, Venezuela, March 15-17 (2001).

[7] Akkutlu, I.Y. and Yortsos, Y.C. *Combust. Flame*, submitted (2001).

[8] Willhite, G.P. *Waterflooding*, SPE Textbook Series Vol. 3 (1986)

[9] Akkutlu, I.Y. *Dynamics of Combustion Fronts in Porous Media*, PhD Dissertation, U. of Southern California (2002, expected).

IV. FLOW AND DISPLACEMENT OF FLUIDS WITH YIELD STRESS

Many applications with heavy oils involve a non-Newtonian rheology. Specifically, the flow and displacements of fluids with yield stress are common. Examples include the flow of foams for oil recovery, where the mobilization of foam lamellae requires that a pressure threshold is exceeded; the flow of heavy oils containing asphaltenes, where a Bingham plastic-like behavior is exhibited; and the formation of wormholes during cold heavy oil production, where the flow of sand particles also requires that limiting yield stresses are overcome. In this section we report on our going efforts to understand these processes at the pore-network scale and to provide the necessary information for their representation at the macroscopic scale. The work reported builds on our previously developed models, including the algorithm of Invasion Percolation with Memory. We utilize this algorithm in order to facilitate the simulation of flow and displacements of Bingham plastics.

Mobilization and Displacement of Fluids with Yield Stress

Min Chen and Yannis C. Yortsos

Introduction

The flow or displacement of fluids with yield stress is an important research area of non-Newtonian fluid studies, which is also encountered in a variety of industry applications. Examples include the flow of heavy oils, which can be often represented as Bingham plastics, the production of sand during cold heavy oil production, and the flow and mobilization of foams in porous media.

Foams are a typical fluid of engineering interest appear to exhibit yield behaviors, which are widely used in the oil industry in various applications, to improve reservoir sweep efficiency, block swept channels, and in gas storage and acidizing operations. These applications rely on the substantial reduction of the gas mobility in rocks obtained in the presence of foams. Some issues in this regard include whether there exists a minimum pressure gradient or a critical gas velocity, above which the porous medium can be mobilized and the relation between the pressure gradient and the flow velocity

In the context of the flow of Bingham fluid, similar problems arise. Typical Bingham fluids include paint, slurries, pastes and food substances like margarine, mayonnaise and ketchup. Bingham fluids possess nonzero yield stresses, so that they flow when an applied stress exceeds some levels of stress, and they show little or no deformation up to the stresses. Because of the complex property of this kind of fluids, much effort has been made to study the flow and mobilization processes of these fluids. In addition, due to the complexity brought out by the combination of the non-Newtonian fluid rheology with the porous media geometry, the state of the art of Bingham fluid flow is not complete.

Many authors in the Russian literature have approximated the rheology of heavy oils as that of a Bingham fluid [1, 2]. Some other studies were also carried out, including flow of foams [3], ground water flow in certain clayey solids, and drilling and hydraulic-fracturing fluids [4]. Rossen and Mamun [5] proposed a percolation approach, consisting of occupying elements with thresholds below a certain value. In the study of the foam flow, Rossen and Gauglitz [3] developed a model for foam mobilization in porous media, for both continuous and discontinuous gas regimes. In the process, they employed percolation theory to find the cluster size, and verified the fact that a minimum pressure gradient is needed to displace lamellae out of a pore throat. Because of lack of data and also the complexity of the system, their conclusions are not complete.

Wu et al. [4] investigated the transient flow of Bingham fluids in porous media, including single- and multiphase flow, using an ad-hoc extrapolation of the single-capillary expressions for the Bingham flow. In the context of reservoir engineering, most existing studies are phenomenological and consist of solving effective continuum equations.

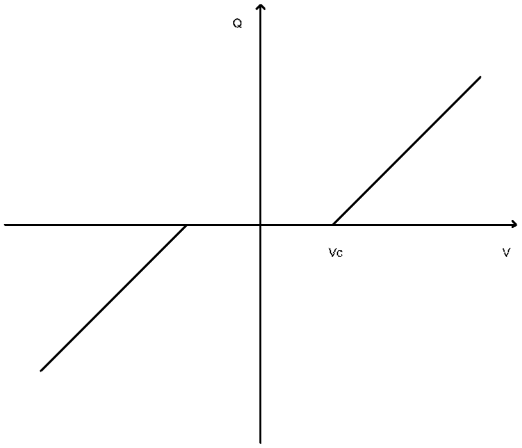

Fig. 1 Voltage – current relation of an individual resistor

A fundamental and now widely accepted work was done by Roux and Herrmann [6]. They used a 2-D network, which is composed of resistors. Each of the resistors has a threshold below which it becomes an insulator. The resistors are distributed randomly in a network. Their results show that the relation between current and the voltage is non-linear. The macroscopic current Q has the following relation with V and V_c,

$$Q \sim (V - V_c)^{\delta} \tag{1}$$

where $\delta = 2$ or $\delta \sim 0.5$ for intermediate part (if for each of the resistor, Q is linearly determined by V when $|V|$ is larger than threshold, as shown in Fig. 1, and V_c is the minimum voltage to have current in the network. In their studies, the thresholds of the resistors are distributed between 0 and 1.

Sahimi [7] used EMA to predict that in a certain range, Q depends quadratically on V. His Monte Carlo simulation results agree with the prediction quite well. Zhou and Stenby [8] studied the displacement of oil trapped in water-wet reservoirs using percolation theory. They obtained the CDC curve based on pore structure of the medium, which is in good agreement with the measured data.

Kharabaf et al. [9,10,11] developed a different algorithm for the construction of the minimum threshold path (MTP), based on which its properties can be studied, such as the connection of the threshold-lattice problem to percolation and also the relation of the MTP with the minimum path of percolation. The algorithm has a similar simulation process as that of an invasion process; the difference is that the advance of the front depends on the front history. It is referred as Invasion Percolation with Memory (IPM). They studied the mobilization of Bingham fluid, immiscible displacement of Bingham fluid by Newtonian fluid and also displacement of Bingham fluid by another kind of Bingham fluid. The same algorithm is used in the study of foam formation and propagation in porous media.

Even though some work has been done, the understanding of single- and multiphase flow of fluids with yield stress in porous media is still limited. In considering and simulating mobilization of fluids with yield stress, Kharabaf used a static model, which will be modified further here. In his work, the potential of a pore is only determined by thresholds, and the pressure distribution effect of the flowing fluid was not considered. In this paper, a new dynamic algorithm for mobilizing fluids with yield stress based on IPM is developed, in which the contribution of flowing fluid is taken into account. Simulation results for different yield stress distributions are compared and discussed. The difference between the new algorithm and Kharabaf's static model is shown.

Algorithm

1) Invasion Percolation with Memory (IPM)

Because the IPM process is the basis of the new algorithm, the algorithm of IPM is described with some details [9].

A network composed of bonds and pores are used, in which bonds have thresholds, τ_i, randomly assigned from a distribution in (0,1). The invading front invades one site at a time. An arbitrary site currently on the front is denoted by F, a site which is a neighbor of F by F', the site from which the front will advance by F_G, the site which will actually be invaded by F_G'. Each site that has been invaded has a value of $V_1(F)$. For a site F on the front and one of its neighbors F', a sum $S = V_1(F) + \tau_{FF'}$ can be formed.

The minimum one of all possible S can easily be found, the corresponding F and F' become F_G and F_G', respectively, and $V_1(F_G') = V_1(F_G) + \tau_{F_G F'_G}$. If the boundary condition $V_1(R) = 0$ for all sites R on the right boundary is applied, the first site invaded on the left boundary has the MTP value, which is $\sum_i \tau_i$. By this method, the MTP of the lattice can be found, and V_1 of each site is its smallest resistance to the starting side. The patterns before and after a growth step are shown in Fig. 2.

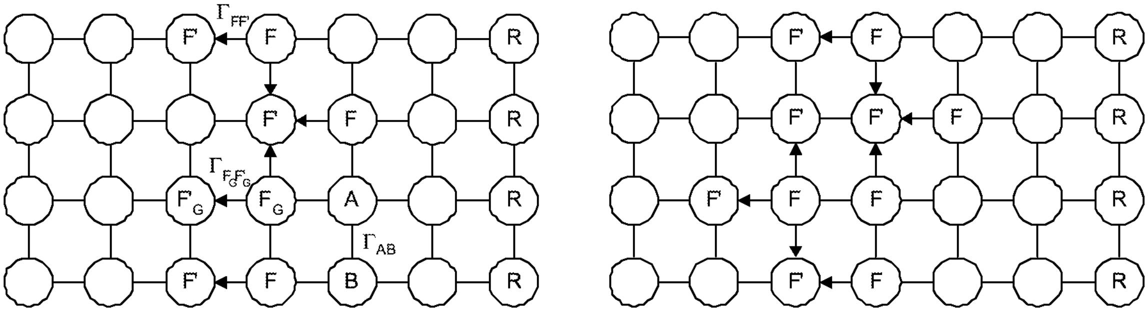

(a) (b)

Fig. 2 Description of the invasion rule, before (a) and after (b) a growth step.

2) New algorithm on mobilization of fluids with yield stress

Fluid with yield stress is a kind of special one, belonging to non-Newtonian fluids. A typical example is Bingham fluids, which exhibit a finite yield stress at zero shear rate and they correspond to the extreme case of pseudoplasticity. Bingham model is the most often used model for a Bingham material. The behavior of this kind of fluid described by Bingham model is shown in Fig. 3. For low stress values, the fluid does not deform, and above the critical value τ_0, it flows like an inelastic non-Newtonian fluid.

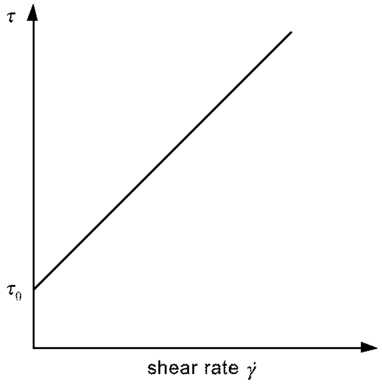

Fig. 3 Behavior of Bingham Fluid

$\tau = \tau_0 - \mu_p \dot{\gamma}$, when $\tau > \tau_0$

and

$\dot{\gamma} = 0$, when $\tau < \tau_0$

If the viscous forces are neglected for single-phase flow of a Bingham fluid, yield stress is the only force affecting its flow. While for Newtonian fluids, when the pressure drop applied is greater than zero, there is flow in the system, for Bingham fluids, the situation is completely different.

When simulation in network-like porous media is considered, the flow of the fluid in a single throat (bond) can be expressed by the following equation [12]

$$q_i = \frac{\pi r_i^4}{8\mu_p l}\left(1 - \frac{4}{3}\left(\frac{\tau_0}{\tau_i}\right) + \frac{1}{3}\left(\frac{\tau_0}{\tau_i}\right)^4\right)\Delta p_i \text{ when } \tau_i > \tau_0 \qquad (2)$$

and

$q_i = 0$ when $\tau_i \le \tau_0$

where q_i is the volumetric flow rate of the fluid in the throat , Δp_i is the pressure drop applied to the throat, and τ_i is the wall shear stress

$$\tau_i = \frac{\Delta p_i r_i}{2l}$$

Just for simplicity, we use the equation below in the algorithm, for throat i,

$$q_i = \Delta p_i - \frac{1}{r_i} \text{ when } \Delta p_i > \frac{1}{r_i} \qquad (3)$$

and

$$q_i = 0 \text{ when } \Delta p_i \le \frac{1}{r_i}$$

where r_i, is distributed with a size distribution, $\alpha(r)$.

This condition (3) is similar to the one used by Roux and Herrmann [6] for a single resistor. So it can be described by Fig. 1, too. In equation (3), the variables are all in dimensionless form. It is clear from the simplified equation that the onset of the flow of the Bingham fluid in the network is controlled by the flow situation of each of the throats in the path. For the first path in the system, there is a minimum pressure difference between the two boundaries.

$$\Delta P_{\min} = \sum_{i} \frac{1}{r_i} \tag{4}$$

where the summation is over all of the throats in the first single path.

It is obvious that the first path in our algorithm is completely the same as the static one obtained by Kharabaf et al. But after that, the pressure drop of the system, which is needed to open a new path is not only determined by the throat radius (or $\frac{1}{r_i}$), but also by the flow, and more exactly the pressure distribution of the mobilized path, which is the factor that is not considered in Kharabaf's mobilization algorithm. In our new algorithm, the two factors, radius and pressure distribution are combined together to be τ_i, which is updated every time when a new path is open. In the following description, τ_{0i} is used, instead of $\frac{1}{r_i}$, and τ_{0i} is corresponding to the size distribution function $\beta(\tau_0)$.

The mobilization of the fluid is the same as finding the paths which connect one side of the network with the other. Each of the paths is corresponding to a specific pressure drop across the network. Here, the pressure at the left side of the network is fixed and equal to zero. As described in previous work, IPM is an effective method to find the minimum path from the right side of the network to the left side. After we find the first path and the critical pressure $\Delta P_{\min} = P_{\min}$, we need a little higher pressure to open a new path. The new path may be a branch or a loop connected to the old or a separate one. We should notice that when the new path is just opened, the flow rates in the newly mobilized throats in the paths are zero and they have no contribution to the total flow rate in the network. If the new path is just opened and connected to the old (AB) one at point C (Fig. 4), for any bond j in the path CD, the flow rate is

$$q_j = \Delta p_j - \tau_{0j} = 0$$

therefore, $\Delta p_j = \tau_{0j}$

For any bond in the path AC, the flow rate is

$$q_k = \Delta p_k - \tau_{0k}$$

If we let

$$\Delta p_k = q_k + \tau_{0k} = \tau_k^{'} \tag{5}$$

the pressure drop between the two sides of the network for the new path ACD determined using IPM is

$$P_{ACD} = \sum_{AC} \tau_i^{'} + \sum_{CD} \tau_{0i} = \sum_{ACD} \tau_i^{*} \tag{6}$$

which is the MTP with updated thresholds τ_i^*, in the new part CD, $\tau_i^* = \tau_{0i}$, and in the shared part AC, $\tau_i^* = \tau_i^{'}$.

For throats in the old path $\tau_i^* = \tau_i^{'}$, so for the old path ACB

$$P_{ACB} = \sum_{ACB} \tau_i^{'} = \sum_{ACB} \tau_i^{*} \tag{7}$$

From all above, we can see that the apparent way to find the next path to be opened is to determine the MTP in IPM with updated thresholds. So, in our algorithm, we first use IPM to find MTP with all initial τ_0. Then we increase the pressure drop P_{ACB}, and at the same time update the thresholds of the bonds in opened paths to be $\tau^{'}$ according to Eq. (4). After that, we use IPM again to determine the MTP at this pressure drop to find the potential (P_{ACD}) of site D at the left boundary. If the pressure drop between the two boundaries is high enough, we can always find a new path ACD. Then decrease the pressure drop. These steps are repeated until the new path with smallest $P_{ACB} = P_{ACD}$ is found. Just as mentioned before, the new path is not necessarily connected to the old ones

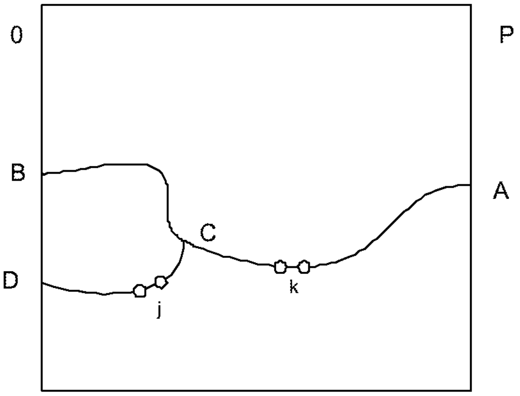

Fig. 4 The flow pattern when a new path (ACD) is open

like the one shown, it may be a loop or even a new path, but the algorithm is the same for all of the situations.

In determining the pressure distribution of the mobilized fluid, the fluid is assumed to be incompressible, and for any site i in the continuous path, the below equation is obeyed,

$$\sum_{j}^{Z} q_{ij} = 0 \tag{8}$$

where q_{ij} is the volumetric flow rate from site i to its neighbor site j, and Z is the coordination number, $Z = 4$ for 2-D system and $Z = 6$ for 3-D system. At a site, which is the intersection of the four bonds, there may no flowing fluid in several bonds, but because of viscous forces, the static fluid in the throat(s) left may make contribution to the flow of the fluid in the other throats. But if the Bingham number of the fluid is high enough, this contribution is negligible. Consequently, in our study, this effect is not considered. Flow rate in a bond is computed according to equation (3).

In 2-D and 3-D systems, fluids flow from right to left, and periodic boundary conditions are used for the other boundaries. The size distribution of τ_0 is β^n, where β is uniform in the region (0, 1). Then for τ_0, the probability density function (PDF), the arithmetic mean and standard deviation are

$$f(\tau_0) = \frac{1}{|n|}\tau_0^{(1/n)-1},\ \langle \tau_0 \rangle = \frac{1}{1+n},\ \sigma_{\tau_0} = \frac{n}{(1+n)\sqrt{1+2n}} \tag{9}$$

respectively. From Eq. (9), it is apparent that for the existence of the arithmetic mean we must have $n > -1$, while for that of the variance, $n > -1/2$. Therefore, for finite first and second moments of general threshold distributions, we must restrict Eq. (9) to $n > -1/2$. However, the problem with smaller n will also be considered.

Result and Discussion

The result for $n = 1$

The relation between the flow rate of the network and the pressure exerted across the network is shown in Fig. 5(a) and 5(b). At a certain pressure drop $P_{\min}$, the first path is open; this is the onset of the mobilization process. Then with the increase of the pressure, more and more bonds are mobilized and the flow rate increases as well. In Fig. 5(b), we found that

$$ {}^{4u\mu}\!/_{r^*\tau_0} \sim \left({}^{(\Delta P-\Delta P_{\min})}\!/_{2\tau_0 N} \right)^{\alpha} $$

α is about 1.9, which is close to 2. In Kharabaf's work, he showed the mobilized paths of network without flow. His results are much different from what we have here. Fig. 6 and Fig. 7 are the mobilized paths at different stages. Under the two situations, the first paths opened are the same. After that, the static ones have more compact patterns, while with the new algorithm, we need higher pressure to mobilize the same amount of bonds or to have the same amount of sites in continuous paths (Fig. 8).

${}^{8\mu Q}\!/_{N\pi r^{*3}\Delta P}$, which is an indication of the permeability of the fluid, is increasing with the pressure across the network (Fig. 9a) and so is the fraction of pores in the continuous paths (Fig. 9b).

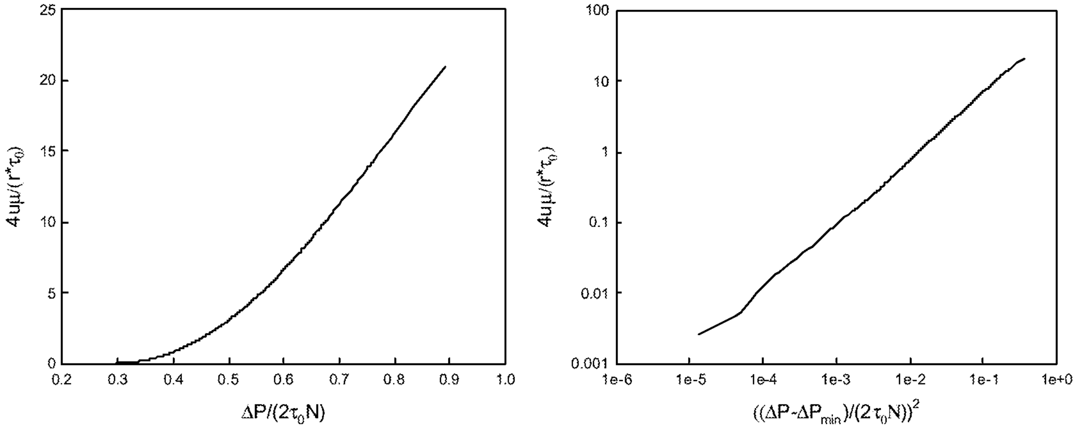

Fig. 5 a) the relation between ${}^{4u\mu}\!/_{r^*\tau_0}$ and ${}^{\Delta P}\!/_{2\tau_0 N}$; b) the relation between ${}^{4u\mu}\!/_{r^*\tau_0}$ and $\left({}^{(\Delta P-\Delta P_{\min})}\!/_{2\tau_0 N} \right)^{2}$

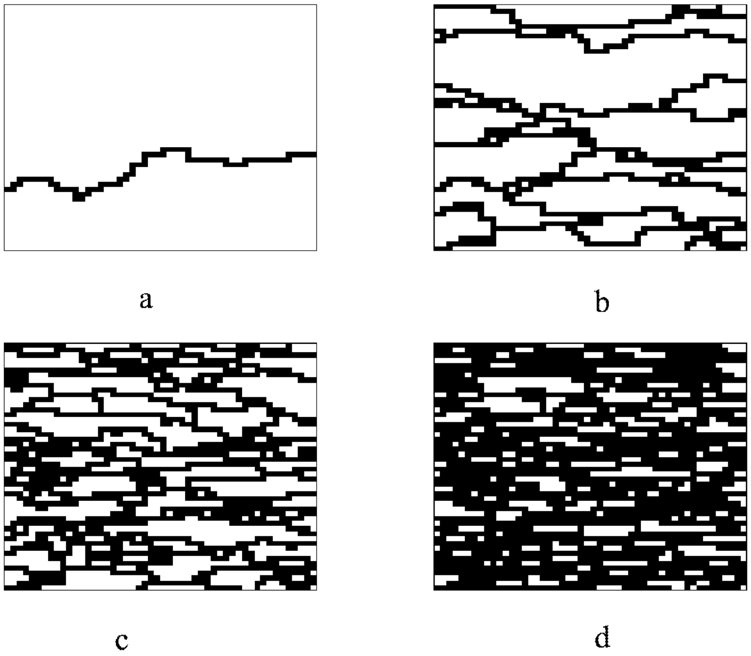

Fig. 6 Patterns with flow at different stages: (a) First path (MTP), (b) One fourth of the sites in continuous paths, (c) half, (d) three fourths.

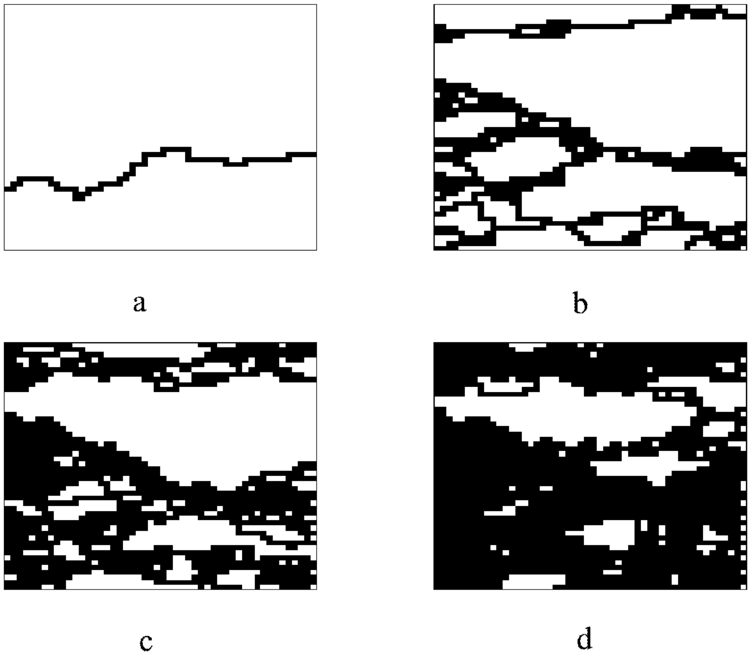

Fig. 7 The static situation:
(a) The first path (MTP) (b) One fourth of the sites are in continuous paths
(c) Half (d) Three fourths.

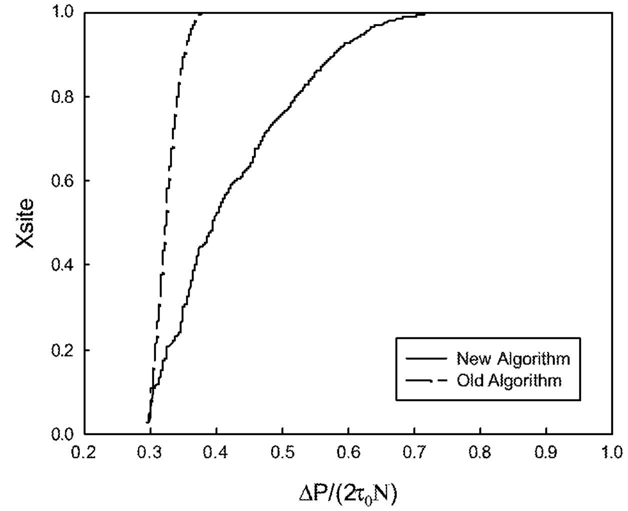

Fig. 8 Fraction of pores on the continuous path and the pressure drop exerted.

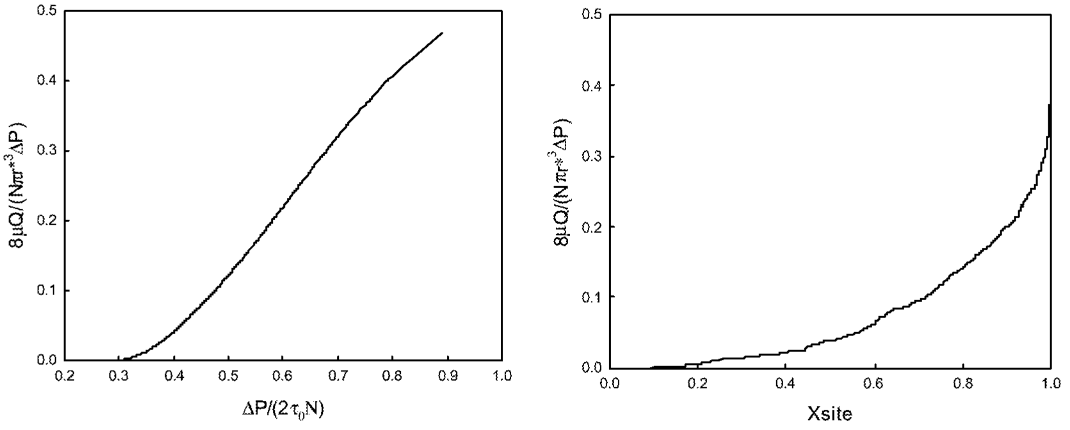

Fig. 9 a) ${}^{8\mu Q}/_{N\pi r^{*3}\Delta P} \sim {}^{\Delta P}/_{2\tau_0 N}$; b) ${}^{8\mu Q}/_{N\pi r^{*3}\Delta P}$ ~X_{site}

Because the first path in the system is MTP, the critical pressure to open the first path is increasing when the lattice gets larger and is totally determined by the threshold distribution. For different sizes of lattices, similar ${}^{4u\mu}/_{r^{*}\tau_0} \sim {}^{\Delta P}/_{2\tau_0 N}$ relation to those in Fig. 5 can be observed.

Other Situations for different n

For different values of n in β^n, the relations between the flow rate Q and pressure drop P are similar to that of $n = 1$. The main difference is the flow pattern of the mobilized fluid. As shown in Fig. 10-Fig. 14, with increase of the absolute value of n, the flow paths are more tortuous. In Fig. 10 and Fig. 11, the paths are almost straight lines, this is because the τ_0 s are almost the same, close to 1, here we do not need much higher pressures to open new paths.

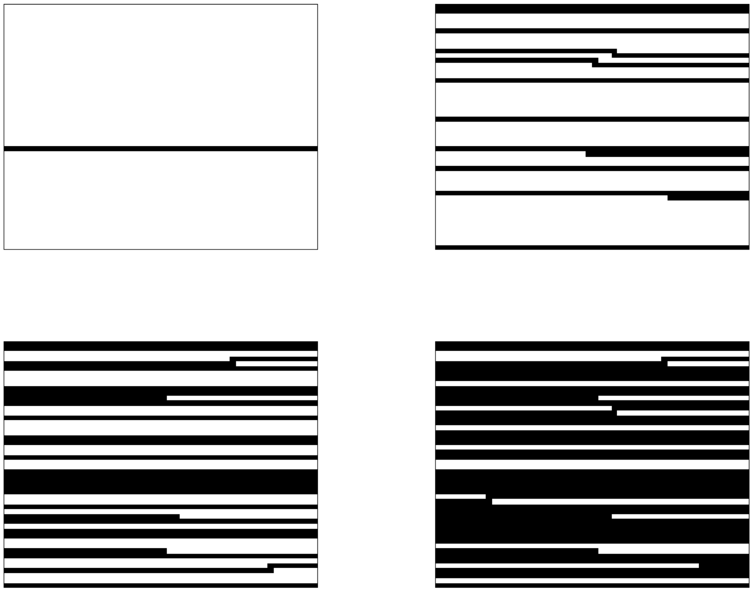

Fig. 10 Flow patterns at different stages, n=-0.1

Fig. 11 Flow patterns at different stages, n=0.1

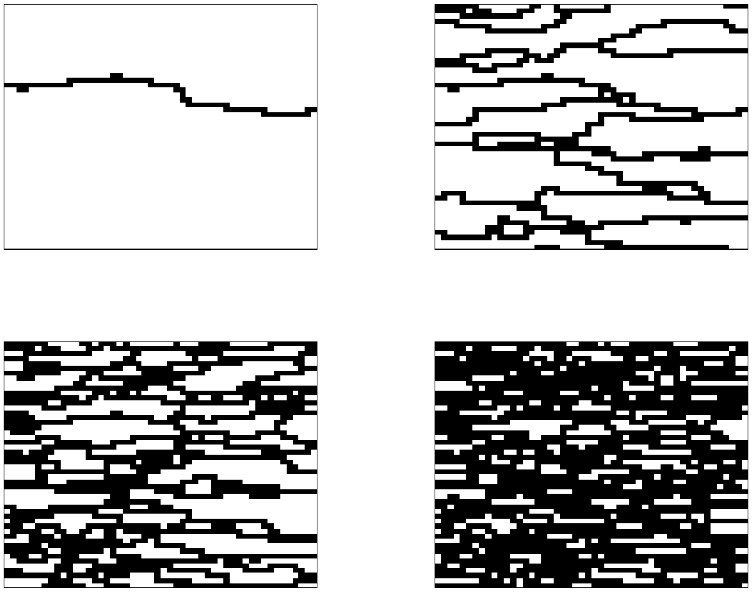

Fig. 12 Flow patterns at different stages, n=-1

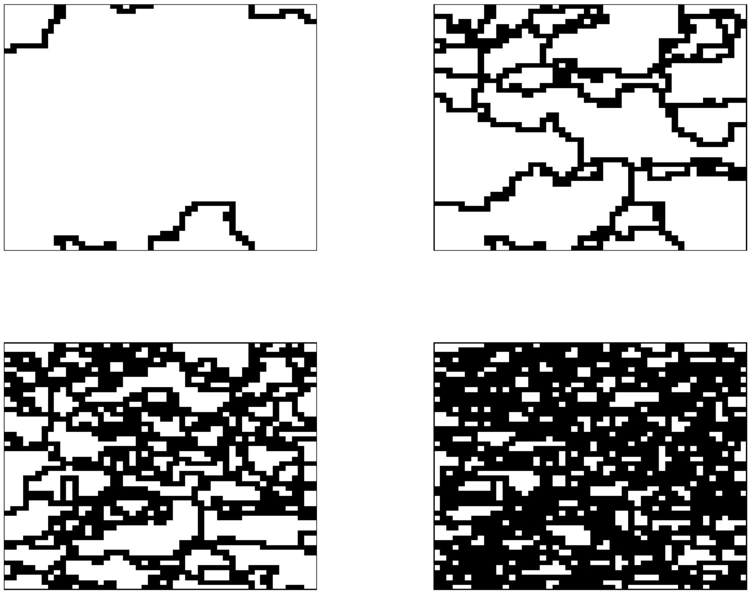

Fig. 13 Flow patterns at different stages, n=5

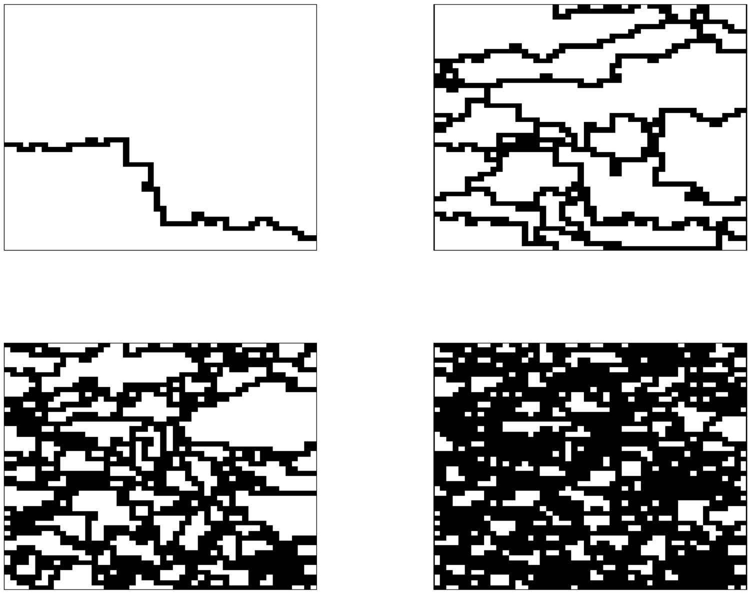

Fig. 14 Flow patterns at different stages, n=-5

In previous simulations, the volumetric flow rate in a bond is calculated based on equation (3). If we modify the equation to that shown below,

$$q_i = r_i^3 \left(\Delta p_i - \frac{1}{r_i} \right)$$

We can see that the algorithm works well too.

Here, in the simulation process, τ_i is updated in the way shown below.

$$\tau_i^* = \Delta p_i = \frac{q_i}{r_i^3} + \frac{1}{r_i} = \frac{q_i}{r_i^3} + \tau_{0i}$$

Fig. 15 and Fig. 18 show simulation results and flow patterns. In Fig. 15, the ${}^{4u\mu}/_{r^*\tau_0}$ and ${}^{\Delta P}/_{2\tau_0 N}$ relation is not the same as the one we get for $n=1$, while the qualitative change of the curve is in agreement with Roux's result. At most of the part, the curve is more like a straight line, and there is an intermediate part, where the slope is different. In the previous discussion for $n=1$, the pressure need to mobilize the bonds after all of the pores are in continuous paths are incredibly high, while we can see in Fig. 17, with the new equation, all of the bonds in the system can be mobilized with relatively smaller pressures. The patterns in Fig. 18 are similar to the ones we present before.

In Fig. 19, the interesting patterns of mobilizing the fluid from the center are shown. As what we can expect, the paths to the corners are open later than other ones. We can see that even though the distance from the center is not the determinative factor, it still has obvious effect on the mobilization process.

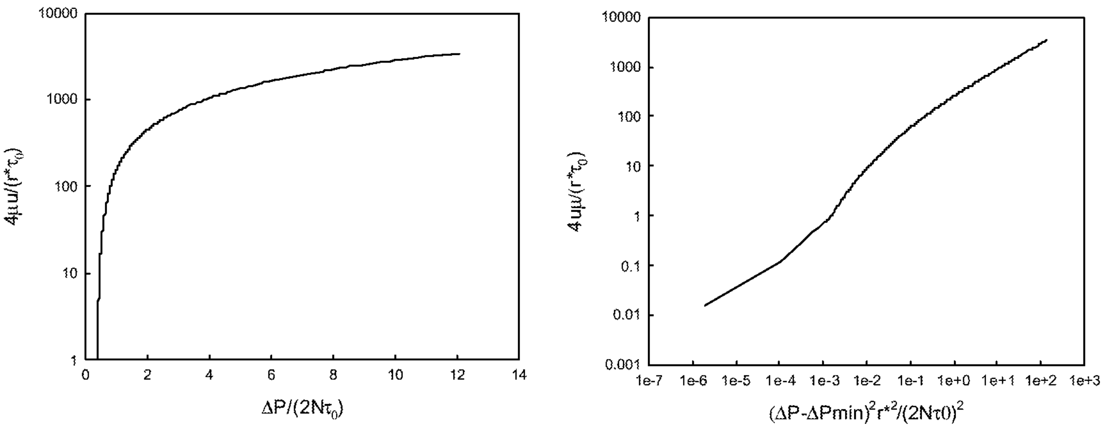

Fig. 15 Relation between $^{4u\mu}/_{r^*\tau_0}$ and $^{\Delta P}/_{2\tau_0 N}$;

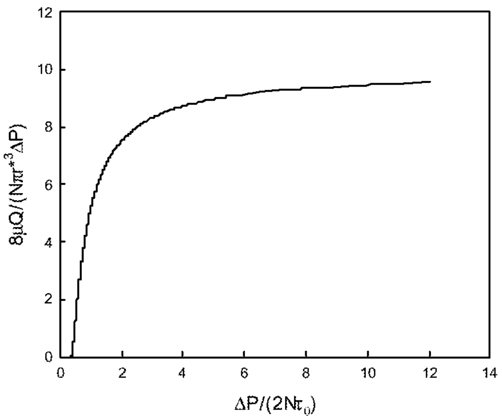

Fig. 16 $^{8\mu Q}/_{N\pi r^{*3}\Delta P} \sim {}^{\Delta P}/_{2\tau_0 N}$

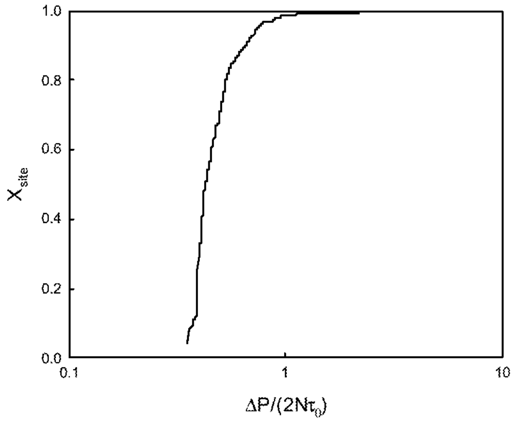

Fig. 17 $X_{site} \sim {}^{\Delta P}/_{2\tau_0 N}$

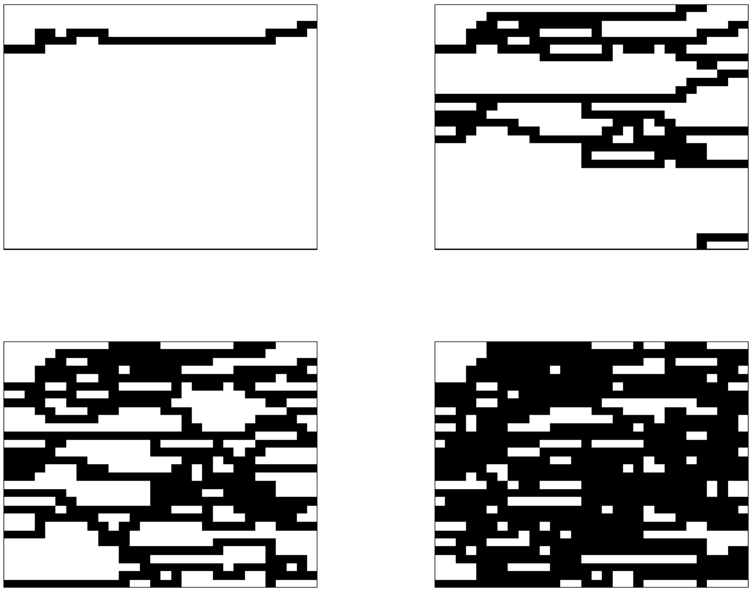

Fig. 18 Flow patterns of the fluid at different stages

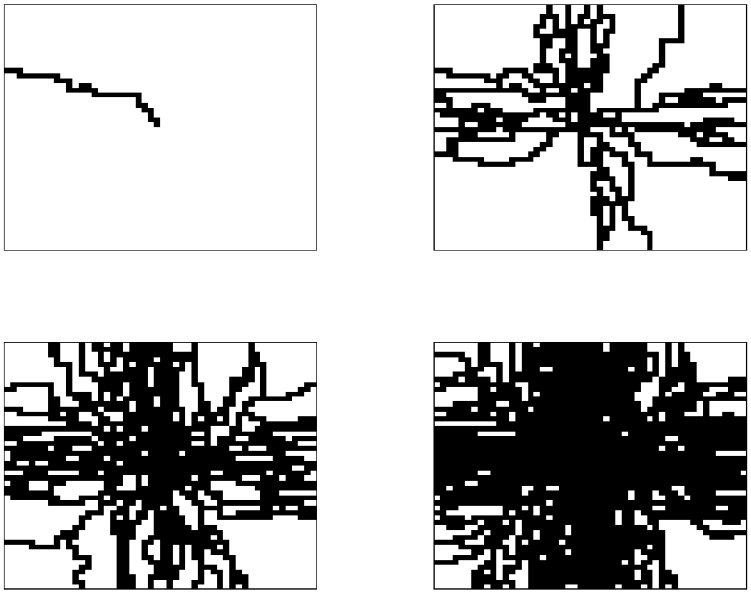

Fig. 19 Flow patterns of the fluid mobilized from the center of the network

Examples on mobilization of Bingham fluid in complex system

In our work, mobilizations of Bingham fluid in more complex system are also considered. The patterns of confined flows of Bingham fluids in converging and diverging networks at different stages are shown in Fig. 20 and Fig. 21. To compare the result to the flow process in complex geometries, the bond size in this part is evenly distributed in a very narrow interval, from 1.0 to 1.0001. From Fig. 20 and Fig. 21, we can find that the mobilization process is very similar to the ones shown in Fig. 10 and Fig. 11, where the bond sizes are very close to 1. The difference between the ones presented here and characteristics claimed by Lipscomb [13] is that the in our results yielding is not happening everywhere, which is understandable, because even though the bond size is very close to one, there is still difference between bond sizes and consequently the initial yields stresses which leads to the necessity that different paths need different minimum pressure drop to open. If bond sizes are completely the same, then yielding would occur over the entire flow field when the pressure difference applied is high enough to open a

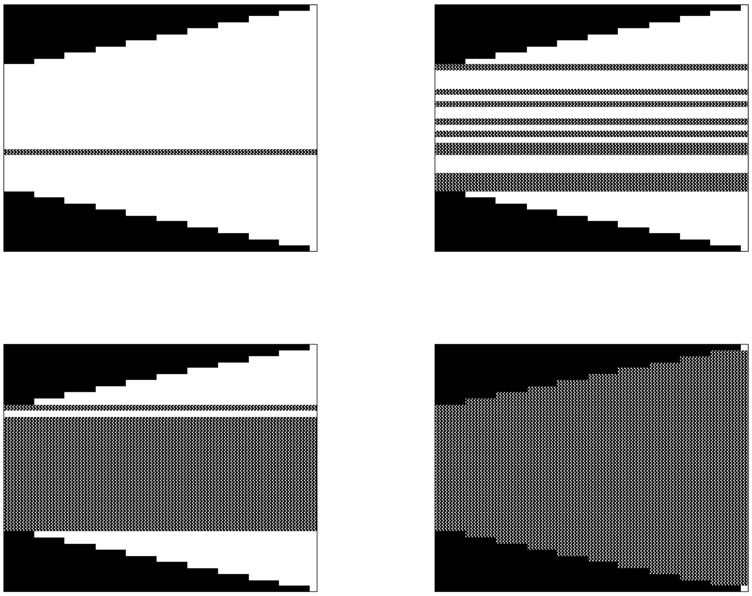

Fig. 20 Flow in converging network, first path; one quarter, half of all sites and almost all available sites are in continuous paths

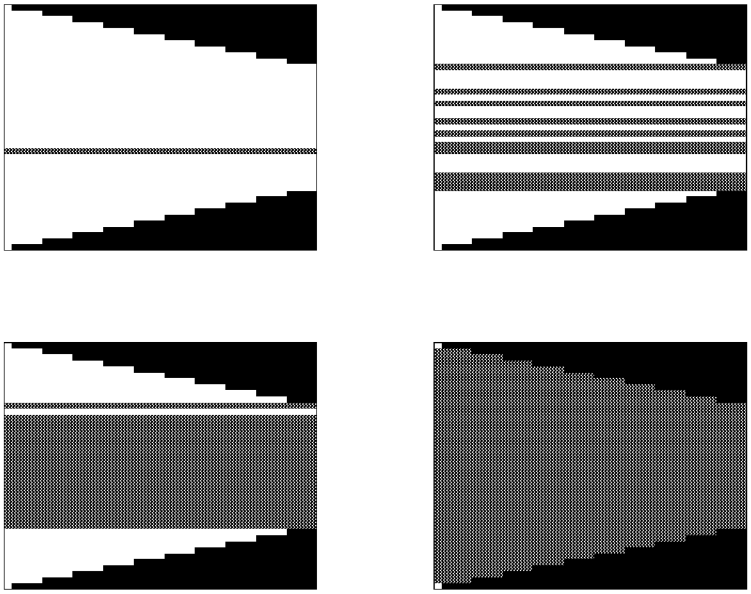

Fig. 21 Flow in diverging network, first path; one quarter, half of all sites and almost all available sites are in continuous paths

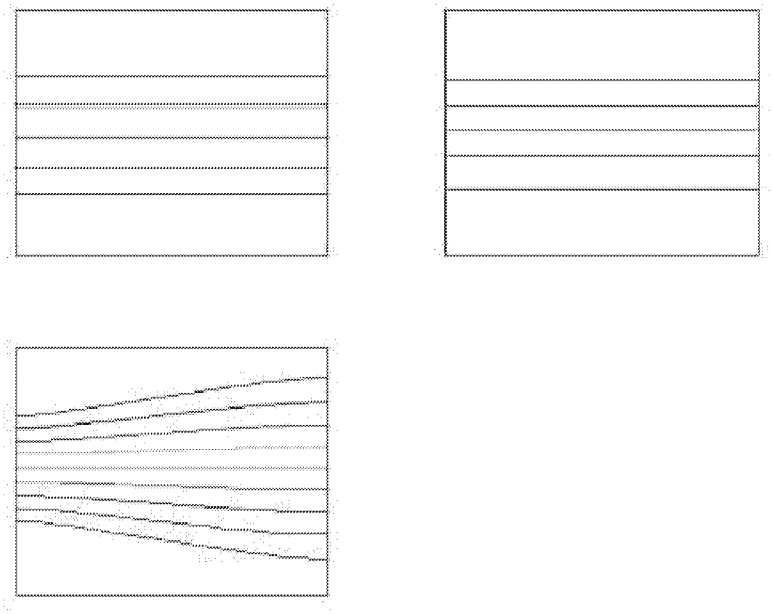

Fig. 22 Streamlines of the patterns in converging network

path. In these figures, black part is the walls, the gray part is the mobilized fluid and white part is static fluid. Fig. 22 shows the streamlines corresponding to the last three patterns in Fig. 20.

Next, flow of Bingham fluids in a network with an obstacle at the center is studied. The mobilization process in network is presented in Fig. 23. The black part at the center is an obstacle that cannot be mobilized, gray part is the sites with flowing fluid and white part is static fluid, except for the last figure, where white part is the mobilized fluid. Because of the size difference between bonds, the paths are open one by one and each at a certain pressure drop between the two boundaries. In Fig. 24, streamlines at some mobilization stages are plotted. Because of the Darcian property of the flow in the network, finally all of the available site in the system can be occupied by flowing fluid, even the ones next to the obstacle which is a bond away. This stands for the fact that there is no stagnant point in Fig. 23.

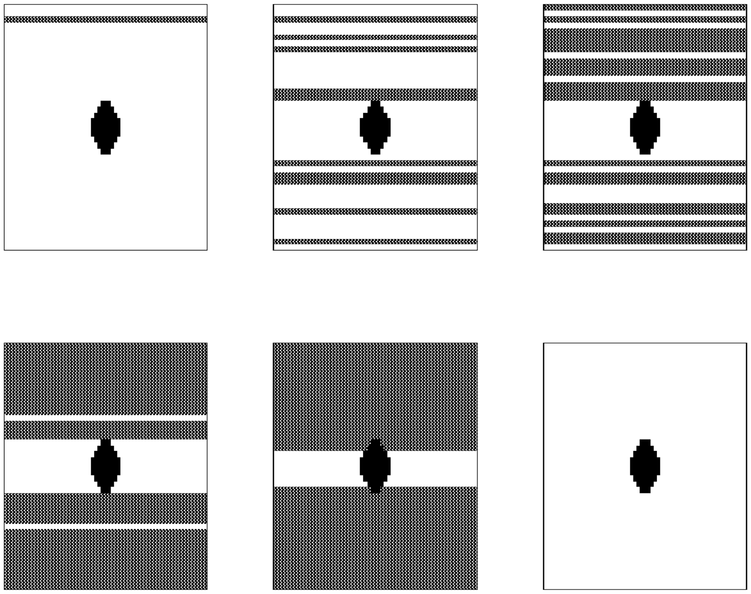

Fig. 23 Flow in a network with an obstacle at the center, first path; About one quarter, half, three quarters, 85% of all sites and all available sites are in continuous paths

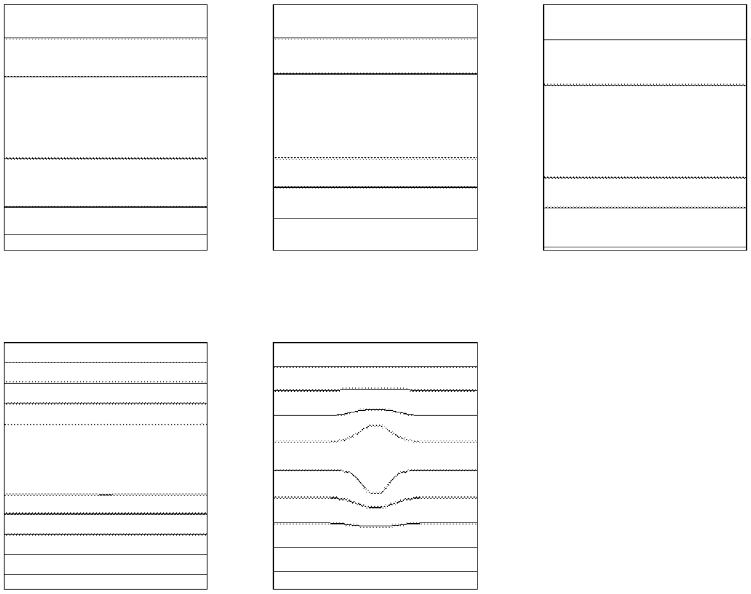

Fig. 24 Streamlines in a network with an obstacle at the center

Displacement of a Bingham fluid by a Newtonian fluid

The displacement of a Bingham fluid by a Newtonian fluid is encountered widely in oil recovery processes. The efficiency of the displacement is affected by the properties of the two fluids. This problem can also be tackled with our new algorithm. In this part, the capillary forces are neglected.

First, let's consider a case in which the Newtonian fluid has almost zero viscosity, this means that the pressure drop is almost zero in the part occupied by Newtonian fluid. Every time the interface advances, we choose the one which needs minimum amount of time to get to the next site. Every other interface moves a distance determined by its velocity and the minimum time known. If we use the same equation as (3) for the non-Newtonian fluid flow, calculating pressure distribution with the restriction of mass conservation at each pore in the mobilized path, we can get the following patterns at different stages, shown in Fig. 25. The algorithm is similar to the one discussed before. In this case, only the τ_is of the non-Newtonian fluid are updated. In Fig. 25 and all the figures in this section, the white part is non-Newtonian fluid, gray part is the mobilized

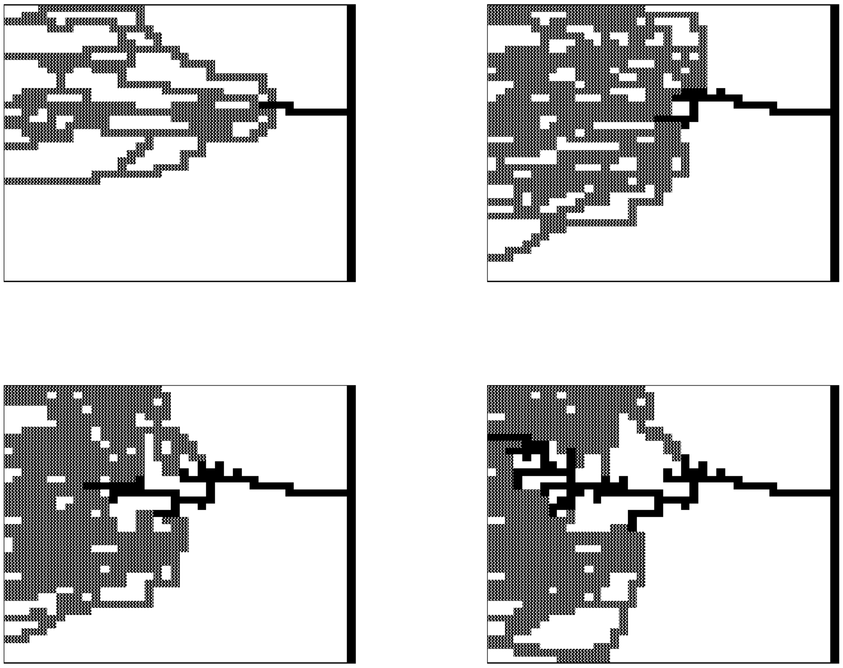

Fig. 25 Patterns of displacement process at different stages, viscosity ratio=0 non-Newtonian fluid and black part is occupied by Newtonian fluid. Before the breakthrough of the Newtonian fluid, the pressure is kept constant as the initial pressure to open the first path. With time increasing, more and more paths are open and the front of the Newtonian fluid moves deeply into the lattice gradually.

If we consider the situations with larger viscosity ratios (1 in Fig. 26 and 20 in Fig. 27), the number of mobilized paths in the system doesn't increase much. The patterns at larger viscosity are much different from the one with zero viscosity, while the latter one can have more mobilized paths. One reason accounting for this difference is the larger pressure drop in the former case, so the pressures are not enough to overcome the thresholds.

Mobilization of a Bingham fluid trapped in a Newtonian fluid

In oil recovery processes, waterfloods of Bingham rheology heavy oils are of much importance. During this kind of displacement process, the Bingham fluid may be trapped

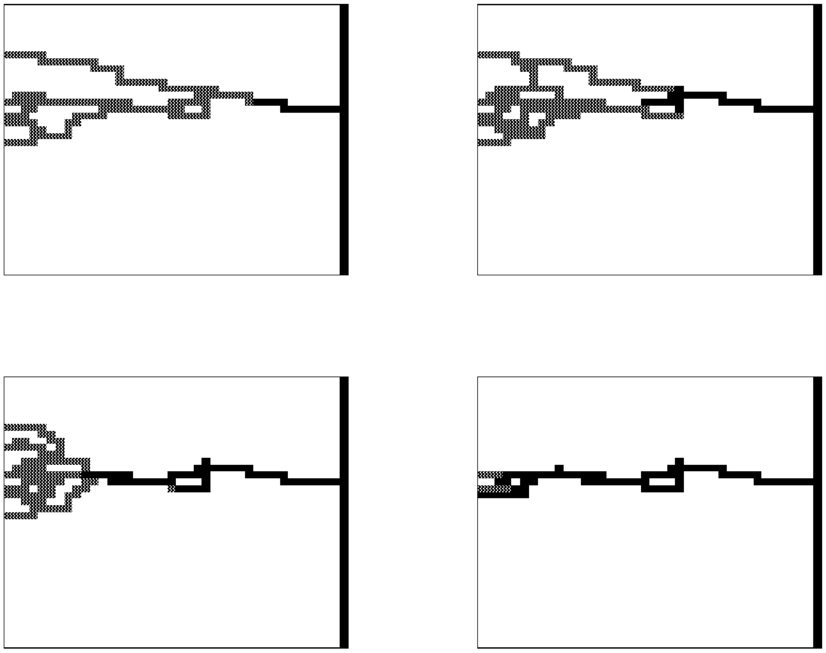

Fig. 26 Displacement patterns at different stages, viscosity ratio=1

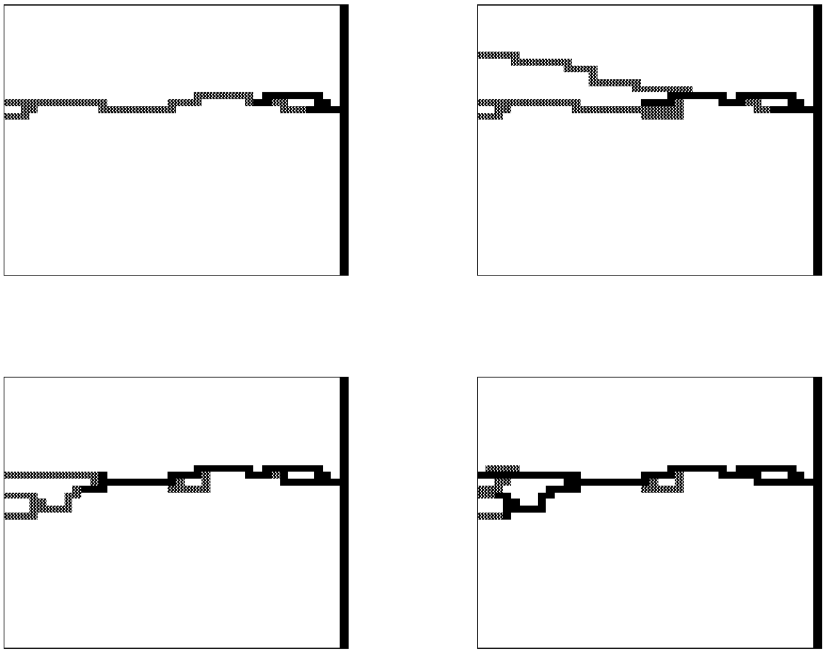

Fig. 27 Displacement patterns at different stages, viscosity ratio=20

and cannot escape until the pressure is high enough. The immiscible displacement involves not only the yield stress, but also the capillary forces. Viscous forces in the Bingham fluid are still neglected, assuming the displacement takes place very slowly.

To use the new algorithm developed to mobilize the trapped Bingham fluid, τ_i should be correspondingly updated every time. For Newtonian fluid, the initial value is $\tau_{0i} = 0$, and

$$\tau_i^* = \Delta p_i$$

For Bingham fluid, τ_{0i} keeps constant,

$$\tau_{0i} = \frac{1}{r_i}.$$

At the interfaces of the two fluids, the capillary condition should be considered,

$$P_c = \frac{2\gamma}{r}$$

In each bond occupied by Newtonian fluid,

$$q_i = \frac{\pi r_i^4}{8l\mu} \Delta p_i$$

First, consider the mobilizing process of a single point of Bingham point trapped. Fig. 28 shows the trace of the point. It starts from the right boundary of the network. This is a quasi-steady state process, if the pressure of the Newtonian fluid around the Bingham fluid is high enough to overcome the thresholds and the capillary effect, the Bingham fluid moves in the direction of decreasing pressure, otherwise, it stays and the pressure applied to the system increases. In every step, the pressure distribution of the Newtonian fluid is computed.

When a block of Bingham fluid trapped in Newtonian fluid is mobilized in the same approach as described above, the Bingham fluid would go through a spattering process, and become a bunch of points, which are mobilized almost one by one. This is because each time we find one path, and mobilize the Bingham fluid in that path. Fig. 29 shows some patterns of the mobilization process. It is possible that some trapped points can never be moved out the system.

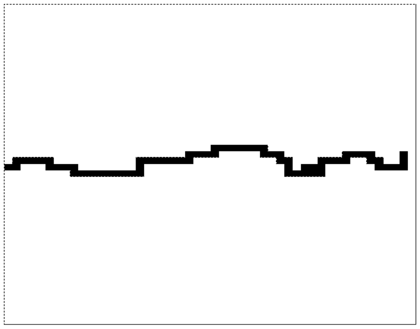

Fig. 28 Mobilization trace of a single point

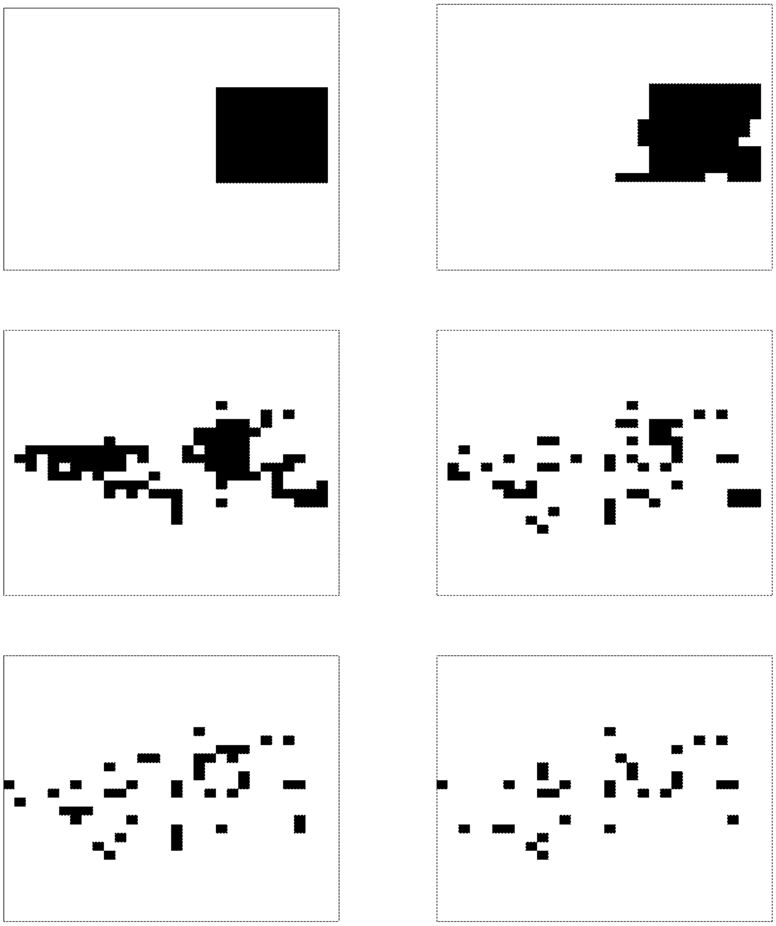

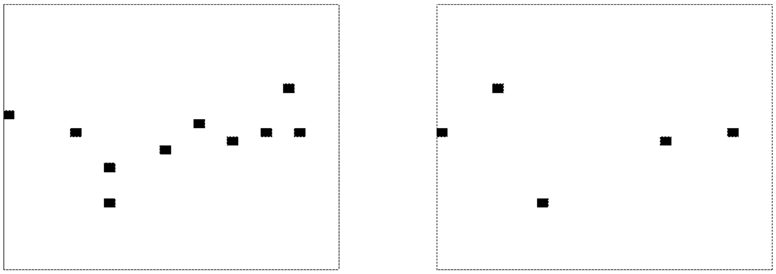

Fig. 29 Snapshots of mobilization process

Conclusion

A new algorithm is developed, which can effectively solve the problem of the mobilization of a single fluid with yield stress in a network. The simulation result is in good agreement with the work done by Roux et al. The model is successfully used in some different situations and the results are shown. The distribution of the yield stress has obvious effects on the mobilization process; with the increase of the power n, the paths are more tortuous. The results of mobilization processes are also obtained for complex networks.

In the displacement of a non-Newtonian fluid by a Newtonian fluid, patterns are affected by the viscosity ratio of the Newtonian fluid to the non-Newtonian fluid.

The model is also employed in the mobilization process of Bingham fluid trapped in Newtonian fluid. The Bingham fluid block is broken into small parts and mobilized one by one, which is the typical process found in experiments.

Reference

1 Barrenblatt, G.I., Entov, V.M., and Ryzhik, V.M.: Theory of fluid flows through natural rocks, Kluwer Academic Publishers, Netherlands, 1990.

2 Bedrikovetsky, P.: Principles of oil and gas production, Kluwer Academic Publishers, Netherlands, 1995.

3 Rossen, W. R. and Gauglitz, P.A.: "Percolation theory of creation and mobiliztion of foam in porous media", AIChE J., 36(8) Aug. 1990, pp. 1176-1188.

4 Wu, Y.S., Pruess, K., and Witherspoon, P.A., SPERE, (1992) 369.

5 Rossen, W.R. and Mamun,C.K.: "Minimal path for transport in networks", Phys. Rev. B 47(18) 1993-II, pp. 11815-11825.

6 Roux, S., and Herrmann, H.J.: "Disorder-induced nonlinear conductivity", Europhys. Lett., 4(11), 1987, pp. 1227-1231.

7 Sahimi, M.: "Non-linear transport processes in disordered media", AIChE J. 39(3) 1993, pp. 369-385.

8 Zhou, D. and Stenby, E.: "Displacement of trapped oil from water-wet reservoir rock", Transport in Porous Media, vol. 11, 1993, pp. 17-31.

9 Kharabaf, H. and Yortsos, Y.C.: "Invasion Percolation with memory," Phys. Rev. E (1997) 55, 7177.

10 Kharabaf, H. and Yortsos, Y.C.: "Pore Network Model for Foam Formation and Propagation in Porous Media", SPE J. March 1998 pp. 42-53.

11 Kharabaf, H.: PhD Dissertation, U. of Southern California, Los Angeles, California (1996).

12 Bird, R.B., Stewart, W.E., and Lightfoot, E.N.: Transport Phenomena, Wiley, New York (1960).

13 Lipscomb, G.G., and Denn, M.M.: "Flow of Bingham fluids in complex geometries," Journal of Non-Newtonian Fluid Mechanics 14(1984) 337-346.